RICE UNIVERSITY

Novel Dynamic Bioreactor and PEGDA Hydrogel Scaffolds for Investigation and Engineering of Aortic Valve Tissues

By

Christopher Atkinson Durst

A THESIS SUBMITTED
IN PARTIAL FULFILLMENT OF THE
REQUIREMENTS FOR THE DEGREE

Doctor of Philosophy

APPROVED, THESIS COMMITTEE

K. Jane Grande-Allen, Associate Professor
Committee Chair, Department of
Bioengineering, Rice University

Mary E. Dickinson, Associate Professor,
Department of Molecular Physiology and
Biophysics, Baylor College of Medicine

Jennifer L. West, Isabel C. Cameron
Professor of Bioengineering and Chair,
Department of Bioengineering, Rice
University

Kyriacos Zygourakis, A.J. Hartsook
Professor of Chemical Engineering and
Chair, Department of Chemical and
Biomolecular Engineering, Rice University

HOUSTON, TEXAS
MARCH 2011

Abstract

Tissue engineered heart valves (TEHV) will allow clinicians to have a high-quality prosthesis for patients that could eliminate many drawbacks of currently available treatments. Although there is great promise for TEHV, the field is still in its infancy; proper scaffolding materials and dynamic culture regimens that produce TEHV suitable for implantation in the aortic valve (AV) position have not yet been identified. Novel systems to apply biomechanical stimuli to developing engineered tissues and materials development and characterization will be necessary to progress towards an aortic TEHV. This thesis work aimed to address these issues in a parallel manner.

The thesis begins by describing the design and physical characterization of a bioreactor system capable of both AV organ culture and biomechanical conditioning of engineered AV tissues. This work demonstrated that the newly developed bioreactor system allows AV to be cultured dynamically in a simple system that scales to accommodate varying sample sizes. Evaluation of this bioreactor system showed that dynamic culture of AV maintained normal tissue phenotype for durations of up to seven days, which is to-date the longest *ex vivo* maintenance of normal AV tissue phenotype in a dynamic bioreactor system.

This thesis work also investigated the suitability of poly(ethylene glycol) diacrylate hydrogels to be used as a TEHV scaffold. These studies showed that flexural stiffness of the resulting scaffolds could be modulated by varying the formulation parameters chosen, and that valvular interstitial cells embedded and cultured within these gels (also containing incorporated bioactive moieties) maintained expression of several characteristic phenotypic markers. The thesis also describes studies in which advanced hydrogel scaffolds were fabricated using anatomically-inspired composite strategies, resulting in scaffolds that possessed unique material properties (anisotropic behavior and altered bending stiffness) compared to standard single component hydrogels. These studies were the first to show a biphasic, trilayered quasilaminate structure in a photopolymerized system. Additionally, these studies demonstrated the development of new anatomically-inspired patterns of reinforcement that allow hydrogels material behavior to more closely mimic tissue. The thesis closes with a description of the implications of these studies on heart valve tissue engineering and potential future directions using these techniques.

Acknowledgements

I am grateful to the numerous educators, mentors, friends, and family members who over the years have guided me along the path that ultimately has brought me to this point. I'd like to express my sincerest gratitude to my thesis advisor, Dr. Grande-Allen, for her enthusiastic mentorship and the knowledge that she passed to me. I would also like to thank my thesis committee for their guidance and support in the accomplishment of this thesis work. Also, I would like to extend my appreciation to Dr. Taby Ahsan, who was my mentor while an undergraduate researcher at Georgia Tech and was instrumental in my decision to pursue a PhD.

I'd like to thank the many students that came before me as well as those who are still in the Grande-Allen lab and the West lab, who have made this work possible. Special thanks should go to Dr. Nikhil Gheewala and Hubert Tseng for being my go-to guys when I had a mechanics or design question, Dr. Elizabeth Stephens for generally knowing the answer to *any question*, Dr. David Allison for helping show me the way to fulfill my entrepreneurial drive, and Dr. Stephanie Nemir and Michael Cuchiara for their hydrogel knowledge. Thanks should also go to the many undergrads that I have worked with, specifically Steve Xu and Alex Brewer for working with me on the physical design of the bending tester; Brad Otto, Liz Mansfield and Chris Lin for work with hydrogels and flexure.

Many thanks should go to my parents, both for having the patience to raise me (one of my many nicknames as a young child was "the man of a million questions"), but also providing an environment where education and ambition were strongly encouraged. My interest in science and engineering began early in my life, where my family tried to redirect how this interest manifested itself in disassembling every household item to “see how they work” to more productive pursuits. I should also thank my family, coaches, and religious leaders for instilling in me a sense of moral and ethical duty with the drive to accomplish something meaningful that is larger than oneself.

The National Institutes of Health, National Science Foundation, and March of Dimes funded most of the research presented in this thesis. I received personal funding from the NIH Biotechnology Training Grant of the Institute of Biosciences and Bioengineering at Rice.

TABLE OF CONTENTS

Abstract ii

Acknowledgements iv

TABLE OF CONTENTS vi

LIST OF FIGURES xi

LIST OF TABLES xvi

LIST OF EQUATIONS xvii

LIST OF ABBREVIATIONS xviii

Chapter 1: Introduction and Specific Aims 1

1.1 Introduction 1

1.2 Motivation and Global Objectives 4

1.3 Specific Aims 5

- 1.3.1 Specific Aim I: Design and evaluate a bioreactor capable of medium term culture of native and engineered aortic valves. 5
- 1.3.2 Specific Aim II: Optimize the composition of PEGDA hydrogels to achieve most favorable bending mechanics for use in a tissue engineered aortic valve. 5
- 1.3.3 Specific Aim III: Create an anatomically-inspired composite hydrogel structure that emulates the natural structure of the aortic valve leaflet. 6

Chapter 2: Background 8

2.1 Aortic Valve 8

- 2.1.1 Gross Anatomy 8
- 2.1.2 Aortic Valve Leaflets 8
- 2.1.3 Layered Structure of the Leaflet 10
- 2.1.4 Comparison of Animal and Human Aortic Valves 12

2.2 Aortic Valve Disease 12

- 2.2.1 Aortic Valve Stenosis 12

2.3 Clinical Relevance 14

- 2.3.1 Valve Homografts 15
- 2.3.2 Mechanical Valves 15
- 2.3.3 Bioprosthetic Valves 16

2.4 Valvular Tissue Engineering 17

- 2.4.1 Previous Tissue Engineered Heart Valve Paradigms 17

2.4.2 Current State-of-the-Art 18
2.4.3 Natural Scaffolds 19
2.4.4 Polymer Scaffolds 21
2.5 Poly(ethylene glycol) Diacrylate Hydrogels 23
2.5.1 Photopolymerization of Hydrogels 24
2.5.2 Previous Medical Applications of Poly(ethylene glycol) 25
2.5.3 Mechanical Properties of PEGDA Hydrogels 25
2.5.4 VIC Adhesion to PEG 27
2.5.5 Advanced Hydrogel Structures and Strategies 28
2.6 Bioreactors 29
2.6.1 Single Phenomena Systems 29
2.6.2 Complex Environment Systems 30
Chapter 3: Design and Physical Characterization of a Synchronous Multivalve Aortic Valve Culture System 34
3.1 Introduction 35
3.2 Physical Design of Bioreactor System 36
3.3 Computational Analyses 42
3.3.1 Computational Fluid Dynamics 42
3.4 Finite Element Analysis 45
3.5 Sterility Challenge 48
3.6 Potential Directions and Future Studies 48
3.7 Conclusions 49
3.8 Acknowledgements 51
Chapter 4: Phenotypic Evaluation of Aortic Valve Tissue Cultured in Synchronous Bioreactor System 53
4.1 Introduction 53
4.2 Study Design and Statistical Methods 54
4.3 Bending Tester Design 56
4.4 Materials and Methods 62
4.4.1 Preparation of Tissue and Bioreactor Loading 62
4.4.2 Static and Dynamic Culture 64
4.4.3 Mechanical Tests 64
4.4.4 Biochemical Assays 65
4.4.5 Histological Techniques 67

4.5 Results.. 70
    4.5.1 Mechanical Testing Results 70
    4.5.2 Biochemical Results 72
    4.5.3 Histological Characterization 74
4.6 Discussion 80
4.7 Conclusions 84
4.8 Acknowledgements 85
Chapter 5: Flexural Characterization of Cell-Encapsulated PEGDA Hydrogels 86
5.1 Introduction 86
5.2 Background 87
5.3 Materials and Methods 90
    5.3.1 Study Design 90
    5.3.2 Cell Culture 92
    5.3.3 PEGDA Synthesis 93
    5.3.4 Methacrylation of Heparin 94
    5.3.5 Hydrogel Polymerization 94
    5.3.6 Mechanical Testing 96
    5.3.7 Cellular Analyses 97
    5.3.8 Hydrogel Network Characterization 98
    5.3.9 Statistical Analysis 100
5.4 Results.. 101
    5.4.1 Characterization and Verification of Polymer Products 101
    5.4.2 Hydrogel Material Properties 101
    5.4.3 Network Properties of Acellular Hydrogels 107
    5.4.4 Cell Phenotype Assessment 108
5.5 Discussion 111
5.6 Acknowledgements 115
Chapter 6: Fabrication and Mechanical Evaluation of Anatomically-Inspired Advanced Hydrogel Structures 117
6.1 Introduction 117
6.2 Background 118
6.3 Materials and Methods 123
    6.3.1 Study Design and Statistical Analysis 123

6.3.2 Polymer Synthesis 124
6.3.3 Cell Culture 125
6.3.4 Interface Strength Testing 125
6.3.5 Layering 128
6.3.5.1 Serial Layering 128
6.3.5.2 Sandwich Layering 130
6.3.6 Photolithographic Patterning 130
6.3.7 Modeling of Photolithographically Patterned Gels 135
6.3.8 Flexure Testing of Quasilaminates 135
6.3.9 Mechanical Testing of Photolithographically Patterned Gels 136
6.4 Results.. 136
6.4.1 Layering Results 136
6.4.2 Behavior of Modeled Photolithographic Patterned Gels 140
6.4.3 Mechanical Properties of Photolithographically Patterned Gels 142
6.5 Discussion 146
6.5.1 Interface Testing 146
6.5.2 Development of Serial and Sandwich Layering Methods and Practical Setbacks 147
6.5.3 Interpretation of Quasilaminate Stiffness 149
6.5.3.1 Consideration of Swelling on State of the Hydrogel Network and Other Potential Causes of Increased Stiffness in Quasilaminates 150
6.5.4 Interpretation of Modeled Behavior in PLP Hydrogels 152
6.5.5 PLP Increases Bulk Stiffness and Allows Anisotropic Behavior 153
6.5.6 Applications and Utility of Layering and PLP Methods 155
6.6 Conclusions 156
6.7 Acknowledgements 156
Chapter 7: Conclusions and Future Directions 158
7.1 Thesis Summary 158
7.2 Conclusions 159
7.3 Future Directions 162
Chapter 8: Bibliography 164
Appendix I: Design Evolution of Bioreactor and Bending Tester 187
Appendix II: Additional Hydrogel Network Information 193
Appendix III: Confocal Tissue Strainer 199

Appendix IV: Computational Fluid Model of ELSIE Bioreactor 211
Appendix V: Mitral Valve Function on Substrates with Varying Stiffness 228
Appendix VI: Mathematical Models for Mechanical Testing of Leaflets.............237
Appendix VII: Custom MATLAB Code 250
Appendix VIII: Custom ImageJ Scripts 266

LIST OF FIGURES

Figure 2.1: Illustration of a dissected aortic root open to show the leaflets and coronary ostia. 9
Figure 2.2: Image showing the aortic valve in a closed (A) and open (B) position. When open, the leaflets undergo bending stresses while they experience a reversal of curvature.[9] 10
Figure 2.3: Hematoxylin and eosin (H&E) stain of an aortic valve showing the layered structure of the leaflet. V, S, F denote ventricularis, spongiosa, and fibrosa respectively.[10] 11
Figure 2.4: Retrospective study examining sources of aortic stenosis. Figure adapted from Passik *et al.*[21] 14
Figure 2.5: Bileaflet mechanical (upper row), stented bioprosthetic (left, lower row) stentless bioprosthetic (right, lower row) aortic valves. Source: STS. 16
Figure 2.6: System to apply cyclic flexure to strips of scaffold material.[52] 30
Figure 2.7: Flow Loop systems for aortic valve culture. A) Simple flow loop with approximated left ventricle. B) Complex flow loop with automatic resistance control.[33, 96] 31
Figure 2.8: Diastolic pulse duplicator that allows high numbers of replicates per system.[42] 32
Figure 3.1: A) Photograph of assembled prototype system. B) Photograph of assembled final design, showing revised drive assembly. C) Computer model of system configuration for six valves. D) Computer model of system showing revision to allow culture of up to twelve valves. System width is approximately forty cm. 39
Figure 3.2: A) Custom designed stent (left) and gasket (right) to secure the aortic root to the piston face (1.25 x 1.5 in dia x height) B) Porcine aortic root secured to stent with polypropylene sutures. 40
Figure 3.3: Assembled piston containing mechanical and porcine valves. 42
Figure 3.4: A) Pressure in the system calculated using a simplified model in Floworks (mechanical valve open, porcine valve closed). B) Pressure in the system calculated using a simplified model in Floworks (porcine valve open, mechanical valve closed). 44
Figure 3.5: Von Mises distribution of internal stresses in piston assembly demonstrating maximum stress is more than an order of magnitude under the yield stress of the material. 46
Figure 3.6: Resultant deformation plot produced (1100X magnification scale) by CosmosWorks, indicating peak deformation of ~20 μm in sliding components. Color scale is blue = 0 μm, green = 15 μm, red = 30 μm. 47
Figure 4.2: Isometric view of bending tester. Stepper motor (A) is coupled to a micropositioner (B), which is mounted to a linear stage (C) resulting in system linear displacement capability of 13 mm. Other loading rigs permitting various sample thicknesses and widths can be seen in the background. 58

Figure 4.3: Top-down view of AV leaflet loaded into bending tester. Letters denote (A) reference rod, (B) flexure bar, (C) loading posts. Leaflet is supported by loading posts and can freely slip, so rotation can occur (no tensile load applied). 59
Figure 4.4: Software interface for controlling bending tester. Total system displacement is input (in mm), along with shaft velocity (in counts per minute) and acceleration. 59
Figure 4.5: Illustration showing the use of a calibrated steel bar to measure load applied to a sample in three point bending. The flexure bar bends and the relative displacement to the reference rod is recorded. 60
Figure 4.6: Sample curve showing the moment-curvature relationship and the linear fit (from which the stiffness is calculated). 62
Figure 4.7: Porcine aortic root sutured to custom designed stent and silicone gasket (not visible). 63
Figure 4.8: Tensile stiffness of leaflets cultured for seven days. Statically cultured leaflets at day 14 were significantly stiffer than leaflets in either culture regimen at day 7 ($p < 0.01$). $N \geq 6$ for all groups. 71
Figure 4.9: Flexural stiffness of porcine aortic valve leaflets in dynamic culture (bioreactor) or static culture in comparison with freshly excised (baseline) tissue. Day 7 dynamic culture showed no difference from freshly excised tissue, and all other groups were significantly less stiff than freshly excised tissue. 71
Figure 4.10: Collagen content of porcine aortic valve leaflets, as measured by hydroxyproline content normalized to dry weight. In dynamic culture, the trend showed no change in hydroxyproline content at day seven and by day 14, hydroxyproline content was increased. There was virtually no change in the trend of collagen content across the duration of culture for statically cultured leaflets. * denotes statistically significant difference where $p < 0.05$. 73
Figure 4.11: Uronic acid content of porcine aortic valve leaflets, normalized to wet weight of the tissue. * denotes statistically significant difference with $p<0.001$. 73
Figure 4.12: Movat pentachrome stain of porcine aortic valve leaflets. Black corresponds to elastin, yellow to collagen, green/blue to proteoglycans and glycosaminoglycans, dark blue to cell nuclei, and red to muscle. Orientation of ventricularis, spongiosa, and fibrosa is the same across all samples (denoted by f, s, and v in high magnification inset). 75
Figure 4.13 - Relative intensity of elastin DAB staining in leaflets as a function of multiple days of culture. $N \geq 6$ for all groups and * denotes significance with $p < 0.05$. 76
Figure 4.14: Immunohistochemical staining for elastin in leaflets cultured in static and dynamic conditions. Distinct elastin staining can be seen in the fibrosa of all leaflets, but it is more distinct in the fibrosa of dynamically cultured samples than statically cultured samples. Orientation of ventricularis, spongiosa, and fibrosa is the same across all samples. A representative staining control (2° antibody only) is included—all samples had on-slide staining controls. 77

Figure 4.15 - Relative intensity of collagen DAB staining in leaflets as a function of multiple days of culture. N≥6 for all groups and * denotes significance with $p < 0.05$......78
Figure 4.16: Immunohistochemical staining for collagen type III in leaflets cultured in static and dynamic conditions. Distinct collagen staining is observed in all leaflets. At day 14 in statically cultured leaflets, it appears to be diffuse through the fibrosa and spongiosa and located mainly in the ventricularis. For dynamically cultured leaflets at day 14, the staining appears to be diffuse throughout the leaflet. Orientation of ventricularis, spongiosa, and fibrosa is the same across all samples. A representative staining control (2° antibody only) is included—all samples had on-slide staining controls......79
Figure 5.1: Diagram of experimental design. A full factorial design was chosen to investigate the effect of varied formulation parameters (molecular weight, weight fraction) on cell phenotype and hydrogel network and mechanical properties. Sample sizes were chosen from prospective power calculations......91
Figure 5.2: Diagram showing sub-studies investigating the effect of heparin inclusion on gels......92
Figure 5.3: Photograph with annotations depicting the method of operation of the bending apparatus. The linear motion of the bending tester stage pulls the hydrogel strip (secured against the loading posts (c)) against the flexure bar (b). Displacement of the flexure bar is determined relative to the immobile reference bar (a). Graphite particles (d) are visible atop the hydrogel strip. Arrow indicates the direction of motion......96
Figure 5.4: Flexural stiffness of base PEGDA hydrogels (unmodified; containing no Hep-MA). Hydrogels were all 10% PEGDA by weight. Samples marked with different letters are significantly different at $\alpha=0.05$. N=6 for all sample groups......102
Figure 5.5: Compressive stiffness of base PEGDA hydrogels. Flexural stiffnesses are on the same order of magnitude as compressive stiffnesses for the 10% weight fraction hydrogels. Samples marked with different letters are significantly different at $\alpha=0.05$. N=6 for all sample groups......102
Figure 5.6: Flexural stiffness of acellular gels containing 0.5 mM of Hep-MA. N=3-6 for all groups and samples marked with different letters are significantly different at $\alpha=0.05$......103
Figure 5.7: Flexural stiffness of representative groups of PEGDA hydrogels containing 0.5 mM unmodified heparin. N=3-6 for all groups and samples marked with different letters are significantly different at $\alpha=0.05$......104
Figure 5.8: Compressive stiffness of PEGDA discs with containing Hep-MA at concentrations of either 0.5 or 1.0 mM. N=3-6 for all groups and samples marked with different letters are significantly different at $\alpha=0.05$......105
Figure 5.9: Flexural stiffness of cell-seeded gels. N=3-6 for all samples. Samples marked with different letters are significantly different at $\alpha=0.05$......106

Figure 5.10: Representative immunostaining of (A) alpha smooth muscle actin and (B) prolyl-4-hydroxylase in cell-encapsulated hydrogels for each composition of hydrogel. 110
Figure 6.1: Dogbone punched hydrogel strips loaded in mechanical tester for interface strength determination. The stiff layer can be seen in purple at the top, and the soft layer has the faint violet tint at the bottom. 126
Figure 6.2: Schematic depicting interface strength testing of quasilaminates. Samples were imaged during testing and pulled to failure. 122
Figure 6.3: Schematic depicting multilayer quasilaminate scaffold fabrication with serial layering approach. This fabrication technique can be used to generate scaffolds with layers between 1.0-2.0 mm and differing composition 124
Figure 6.4: Schematic depicting trilayer quasilaminate scaffold fabrication with A-B-A composition. This fabrication technique can be used to generate thin (less than 1.5 mm thick) scaffolds with different stiffnesses and cellularity in each layer. 126
Figure 6.5: Photomask patterns tested for generating anisotropic gels. The first four linear patterns have the same level of total coverage, while varying the thickness of the patterned stripes (number shown in microns); as a result, spacing between stripes changes. The sinusoidal patterns have the same amplitude and period, but thickness of the pattern is varied 133
Figure 6.6: Schematic depicting photolithographic patterning of hydrogels to yield bulk anisotropy 129
Figure 6.7: Quasiaminates formed with serial layering method. Bilayer and trilayer quasilaminates could be formed with this method, however, they could not be formed with layers under 1.0 mm in thickness. "a" a higher molecular weight polymer, and "b" is a lower molecular weight polymer. Preferential cresyl violet staining can be seen in the higher stiffness layers. The top gel was formed in a steel mold, and the curving interface was a result of surface tension. 137
Figure 6.8: A) Representative images of tensile interface strength test demonstrating that failure does not occur at the interface between layers. The interface between layers is highlighted with the red arrow in the far right panel. B) Mean failure stress and bulk modulus for uniaxial tensile testing of quasilaminates. $N \geq 10$ for all samples. * denotes significance with $p < 0.0001$. 138
Figure 6.9: Flexure testing of quasilaminate hydrogels. The bulk flexural modulus of trilayer gels was higher than for the single layer bulk slab gels. The inclusion of cells did not significantly affect scaffold stiffness for either the softer single layer gels or the quasilaminate gels (in which cells were embedded in the softer inner layer only). Quasilaminates were significantly stiffer than both single layer gels and * denotes $p < 0.05$. 140
Figure 6.10: Simplified finite element analysis of scaffold deformation when reinforced with sinusoidal patterns of increased stiffness. The patterned regions bear the majority of the load applied to the bulk. 141
Figure 6.11: Simulated loads ranging from 9.81 x 10-3 to 3.92 N were applied to a FEA model of sinusoidally reinforced hydrogel. Bulk strain was calculated and

the resulting stress-strain curve was plotted. In contrast to expected results, no nonlinear behavior was observed (linear fit r2=0.99981) 142
Figure 6.12: Patterns used to investigate feature size and geometry. Pattern on right ("skewed fibers") was highlighted with red lines to aid in visualization. Patterns were generated with custom MATLAB code available in Appendix VII. Dark purple indicates regions of pattern reinforcement and light purple is unpatterned gel. 143
Figure 6.13: Stress strain curves for a variety of patterns used in pilot study to investigate feasibility of desired feature size and geometry. 143

LIST OF TABLES

Table 5.1: Table showing calculated network properties for acellular hydrogels. Table lists mean ± SEM for molecular weight between crosslinks, mesh size, and mass swelling ratio for acellular gels with 0 and 0.5 mM Hep-MA. In both heparinized and non-heparinized gels, with increasing weight fraction, molecular weight between crosslinks decreases. In non-heparinized gels, molecular weight between crosslinks increases with increasing molecular weight. In heparinized gels, this trend is observed from 3400 to 6000 Da, but is not seen at higher molecular weights. In both heparinized and non-heparinized gels, with increasing weight fraction, mesh size decreases. In non-heparinized gels, mesh size increases with increasing molecular weight. Samples marked with different letters are significantly different at $\alpha=0.05$ 108
Table 5.2: Percentage of cells expressing alpha smooth muscle actin (top item) and prolyl-4-hydroxylase (bottom item) in each composition of gel. N≥5 for all samples. 109

LIST OF EQUATIONS

Equation 4.1: Quadratic line equation 60
Equation 4.2: Curvature equation. Y is the quadratic fit. 60
Equation 4.3: Moment equation. M is moment, F_x and F_y are the x and y components of the applied load, respectively and x and y are the orthogonal distances from the point of applied force to the loading posts. 61
Equation 4.4: Bernouilli-Euler moment curvature equation, where E_{eff} is stiffness, I is moment of inertia, and K is change in curvature (Equation 4.2). 61
Equation 4.5: Moment of Inertia equation, where t is sample thickness and w is height. 61
Equation 4.6: Bernouilli-Euler equation rearranged to calculate stiffness. 61
Equation 5.1: Number of effective chains per unit volume, where v is the specific volume of the bulk PEG in amorphous state, V_1 is the molar volume of water, $V_{2,r}$ and $V_{2,s}$ are the polymer volume fraction in the relaxed and swollen state respectively, and u is the Flory-Huggins solvent interaction parameter. 99
Equation 5.2: Molecular weight between crosslinks equation, where Ve is number of effective chains per unit volume, υ is the specific volume of PEG in the amorphous state, and Mn is the number average molecular weight of the starting polymer. 99
Equation 5.3: Average end-to-end distance of polymer in unperturbed state. Mc is the number average molecular weight between crosslinks, Mr is the molecular weight of the repeat unit, and Cn is the characteristic ratio for PEG. 100
Equation 5.4: Crosslink density calculation, where Mc is the number average molecular weight between crosslinks and υ is the specific volume of PEG in the amorphous state. 100
Equation 5.5: Mesh size equation, where where r_0 is average end-to-end distance of the polymer, and $V_{2,s}$ is the polymer volume fraction in the swollen state. 100

LIST OF ABBREVIATIONS

ABAM	Antibiotic/Antimycotic
aSMA	Alpha Smooth Muscle Actin
BGS	Bovine Growth Serum
BSA	Bovine Serum Albumin
CCD	Charge Coupled Device
CFD	Computational Fluid Dynamics
DAB	Diaminobenzidine
DAPI	4',6-diamidino-2-phenylindole
FEA	Finite Element Analysis
GAG	Glycosaminoglycan(s)
Gel-MA	Gelatin Methacrylate
H&E	Hematoxylin and Eosin
Hep-MA	Heparin Methacrylate
HEPES	4-(2-hydroxyethyl)-1-piperazineethanesulfonic acid
HSD	Honestly Significant Difference
IHC	Immunohistochemistry
P4H	Prolyl 4-hydroxylase
P4HB	Poly-4-hydroxybutyrate
PBS	Phosphate Buffered Saline
PEG	Poly(ethylene glycol)
PEGDA	Poly(ethylene glycol) Diacrylate
PGA	Polyglycolic Acid
PHO	Polyhydroxyoctonoate
PLLA	Poly-L-lactic Acid
PLP	Photolithographic Patterning
s(GAG)	Sulfated Glycosaminoglycan(s)
TEHV	Tissue Engineered Heart Valve(s)
TPA	Two-photon Adsorption
VIC	Valvular Interstitial Cell(s)

Chapter 1: Introduction and Specific Aims

1.1 Introduction

Tissue engineering holds great promise for the repair or replacement of many diseased or damaged tissues, however, much work remains to be performed before suitable engineered tissues are a clinical reality. In particular, tissue engineered heart valves (TEHV) would allow clinicians to have a high-quality prosthesis for pediatric patients (whom frequently have malformed or diseased valves that require surgical intervention) that could eliminate many drawbacks of currently available treatments. Additionally, TEHV would give a higher quality option to adult patients who most commonly receive mechanical or bioprosthetic valves when they require valve replacement. Despite the promise, and the work over performed over the past 20 years by a few labs in this field, there has been limited clinical success of TEHV and even less when they are needed in the aortic position. Development of new systems to culture and study valves so that investigators can truly understand valve biology and stimulate tissue development will be necessary to realize progress towards a successful TEHV. Of equal importance will be the development of novel, advanced scaffolds capable of sufficient mechanical performance in the tissue's *in vivo* environment while supporting cells exhibiting valve-like phenotypes. This thesis work aimed to address these issues simultaneously. The thesis begins by describing the design, physical, and phenotypic characterization of a bioreactor system capable both of aortic valve organ and biomechanical conditioning of engineered aortic valve tissues. The newly designed system will permit investigators to examine valve biology in a more controlled environment than *in vivo* large animal studies. Data collected and interpreted for the purpose of bioreactor validation is incorporated in the development and testing of poly (ethylene glycol) diacrylate (PEGDA) hydrogel compositions in order to evaluate their suitability for use in valvular tissue engineering. Following these studies, development and characterization of anatomically inspired advanced hydrogel scaffolds are described, which further incorporate valve-tissue specific concepts, while having general applicability to the engineering of a diverse range of tissues.

The system designed and detailed in this thesis can be used to study valve disease states as provide dynamic mechanical stimulation to TEHV. The creation of a system that provides low-cost, scalable sterile culture of aortic valve tissues allowed for the determination of design criteria for engineered tissues (particularly flexure properties). Furthermore, this system has broad applicability for the study of valve biology and remodeling, as well as mechanical conditioning of tissue engineered heart valves.

The testing of PEGDA gels with primary concern placed on their material properties and ability to support valve cells is unique. Material characterization of PEGDA hydrogels has been predominantly limited to compression and tension, while bending (used synonymously in this thesis with flexure) has largely been unexplored. This work is the first to investigate bending behavior of single-layer (referring to formulation, standard in the literature) PEGDA hydrogels, which is of particular concern to TEHV. Additionally, this work investigated the mechanical consequences of adding heparin to hydrogel scaffolds. Novel methods for creating anatomically-inspired composite hydrogels were created. Quasilaminate structures and interpenetrating pattern reinforced composites that mimic the geometry of the native aortic valve leaflet were created, and allow for more biomimetic mechanical behavior of the resulting constructs.

This research has been presented in this thesis in seven chapters. The first chapter set ups the ideas to be explored in this document and serves as a conceptual map for the thesis. Next, an in-depth review of pertinent literature and background information follows (Chapter 2) in order to describe the work that has enabled this research as well as to frame this work in the context of the field of heart valve tissue engineering. The first specific aim will be detailed in the subsequent two chapters (Chapters 3 and 4). The design, physical evaluation, and ability of the bioreactor system to provide a sterile medium-term culture environment will be detailed in the first of these chapters. Next, medium-term organ culture of native tissues in this system will be detailed. The following two chapters will detail the hydrogel investigation that comprises aims II and III. The composition optimization and bending evaluation of single layer hydrogels is detailed in Chapter 5. The following chapter describes the novel methods used for creating the anatomically-inspired structures that mimic native valve tissue. Finally, the thesis closes with a discussion that frames the global results achieved through this research and delineate the unique contribution of this work to valvular tissue engineering. Additionally, the thesis contains eight appendices that detail physical design of systems, new source code created in system design or image processing, and the doctoral candidate's contributions to projects outside the scope of this thesis.

1.2 Motivation and Global Objectives

While TEHV have been researched in a variety of materials and dynamic culture conditions, the ideal material and dynamic culture regimen has yet to be realized. Low-cost, scalable, simple systems to dynamically stimulate the valve will aid both investigation of native tissues, but also rapidly accelerate development of engineering tissues. The use of a hydrogel that can be extensively modified both biochemically and biomechanically, like PEGDA, is very attractive for applications such as TEHV. Despite the obvious potential benefits PEGDA has as a TEHV scaffold, it has not been extensively studied as a potential scaffold for heart valve tissue engineering, most likely due to initial reports that growing valvular interstitial cells on PEG surfaces was unsuccessful.[1] However, recent studies showed that by modifying PEGDA gels with methacrylated heparin, VIC growth and normal phenotype could be supported.[2] **The objective of these studies was two-fold: (i) to develop a novel bioreactor that can be used for the *ex vivo* culture and dynamic conditioning of engineered and native heart valves and (ii) to develop composite PEGDA scaffolds with composition and architecture most suitable for tissue engineered aortic valve leaflets.** The development of the novel bioreactor will enable application of dynamic biomechanical stimuli to engineered valves in the future. Exploration of PEGDA gels with primary concern placed on their bending properties will aid in the translation of hydrogels towards more biomimetic scaffold fabrication and realistic *in vitro* testing of hydrogel-based TEHVs. This objective has been realized through the investigation of the following specific aims.

1.3 Specific Aims

1.3.1 Specific Aim I: Design and evaluate a bioreactor capable of medium term culture of native and engineered aortic valves.

Hypothesis: A system that cyclically opens and close an aortic valve will maintain the normal phenotype of aortic valve tissue for longer culture durations than will static culture.

Approach: A simple, scalable system has been developed that provides a method to culture aortic valves under repeatable sterile conditions. The dynamically cultured valves have been compared with valves cultured under static conditions for the same duration and assessed for their mechanical, biochemical, and histological characteristics.

Significance: This new system to maintain valves *ex vivo* has applications not only for development of tissue-engineered valves, but for also studying disease models in the aortic valve. Furthermore, this study developed the bending mechanics criteria for the following specific aim.

1.3.2 Specific Aim II: Optimize the composition of PEGDA hydrogels to achieve most favorable bending mechanics for use in a tissue engineered aortic valve.

Hypothesis: Altering the molecular weight and weight fraction of PEGDA chains used to develop hydrogels will significantly affect their material properties. Such parameters can be tuned to achieve bending properties similar to native aortic tissue.

Approach: PEGDA hydrogels have been created with a range of compositions and the effect of each parameter on the bending mechanics of the hydrogel has been investigated with a custom designed bending tester.

Significance: While PEGDA hydrogels have been widely used in various applications, their bending behavior has not been reported. These studies augment the current understanding of PEG hydrogels as well as detail their suitability for use in tissue engineered heart valves. This characterization of bending behavior has applications in fields beyond heart valve tissue engineering, such as orthopedics.

1.3.3 Specific Aim III: Create an anatomically-inspired composite hydrogel structure that emulates the natural structure of the aortic valve leaflet.

Hypothesis: After characterizing bending properties of PEGDA hydrogels, layered and patterned structures can be created to mimic the natural structure of the aortic valve leaflet and exhibit unique bulk material properties when compared with standard hydrogel scaffolds.

Approach: Quasilaminate structures and interpenetrating pattern-reinforced composites were created using a range of PEGDA hydrogel compositions. Photolithographic patterning and layering was used generate gels with material properties that were distinct from single component gels (exhibition of anisotropy and altered bending stiffness).

Significance: The developed layering techniques are novel for photopolymerized systems regardless of application, and both advanced scaffold fabrication techniques are unique in the field of heart valve tissue engineering. These methods allow the scaffold to more closely mimic the material properties of native tissue. Layering allows a very simple, quick way of controlling cell distribution throughout the construct, as well as control of the pericellular mechanical environment, without compromising overall scaffold material properties. Photolithographic patterning allows the creation of anisotropy in what is fundamentally an isotropic, elastic material.

Chapter 2: Background

2.1 Aortic Valve

2.1.1 Gross Anatomy

The aortic valve is one of four valves in the heart, and is one of two arterioventricular valves. The aortic valve is composed of three semilunar leaflets and aortic sinuses and is located between the left ventricle and the aorta (Figure 2.1). It functions as a one-way valve, allowing oxygenated blood to flow from the left ventricle to the aorta. Each leaflet attaches to the sinus wall, thus creating the cavity between them, referred to as the sinuses of Valsalva. The walls of these sinuses become continuous with their respective leaflets at the fixed lower edge. The sinus wall is seen as a dilation of the aortic wall, and the left and right sinuses contain the ostia of their respective coronary arteries. The leaflets meet at the closing line, and overlap in the area of coaptation.[3]

2.1.2 Aortic Valve Leaflets

The shape of the leaflets have been determined to be cylindrical, which enables them to withstand more stress in the circumferential direction than the radial direction.[4] Additionally, during opening and closing of the valve, a cylindrical leaflet can undergo a reversal of curvature more easily than could a multiply curved leaflet (Figure 2.2). The aortic valve experiences its maximal load during diastole, when the leaflets are fully pressurized and bulge back towards the heart. Maximum stress is found in two areas of the leaflet; the point of leaflet attachment and the line of leaflet coaptation. Maximum stress is due to flexion due to the high bending deformations at these areas. It is generally accepted that high local stresses lead to tissue damage and disease (calcification).[3, 5-8]

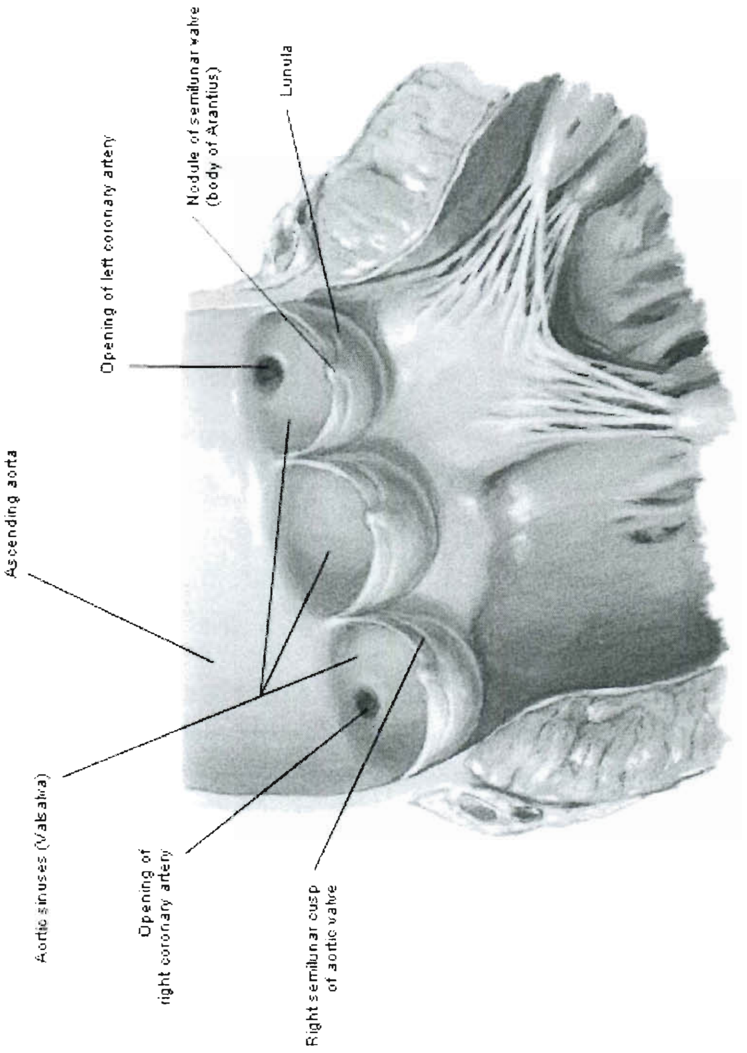
Opening of left coronary artery
Nodule of semilunar valve (body of Arantius)
Lunula
Ascending aorta
Aortic sinuses (Valsalva)
Opening of right coronary artery
Right semilunar cusp of aortic valve

Figure 2.1: Illustration of a dissected aortic root open to show the leaflets and coronary ostia.

The area where the leaflets join the aortic wall is called the commissure, and the peaks of these commissures are in the sinotubular junction. When the valve is open, the diameter of the opening is roughly equivalent to that of the sinotubular junction. While the valve is open, the length of the closing edge can be observed to be much greater than the straight-line distance between commissures. This is thought to be necessary for nonstenotic opening of the valve and nonregurgitant closure.[9]

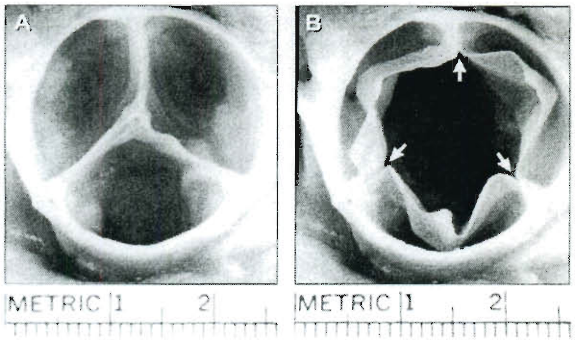

Figure 2.2: Image showing the aortic valve in a closed (A) and open (B) position. When open, the leaflets undergo bending stresses while they experience a reversal of curvature.[9]

2.1.3 Layered Structure of the Leaflet

The aortic valve is composed of a layered structure, with the endothelium on the surface. Three distinct layers can be seen below the endothelium (Figure 2.3). They are, in order from the aortic to the ventricular side:

1. Fibrosa – comprised of tightly packed collagen bundles
2. Spongiosa – loose, GAG rich tissue
3. Ventricularis – elastin rich layer

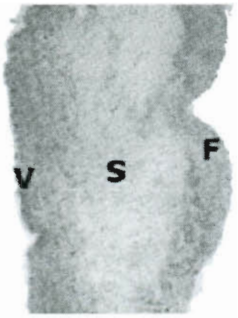

Figure 2.3: Hematoxylin and eosin (H&E) stain of an aortic valve showing the layered structure of the leaflet. V, S, F denote ventricularis, spongiosa, and fibrosa respectively.[10]

These layers are present in both the coaptational and non-coaptational areas of the leaflet, however in the coaptational area there is a lower degree of organization. These layers give the tissue its strength, and the orientations of the elastic fibers and collagen bundles contribute to the anisotropic behavior of the leaflet. In the circumferential direction, the collagen bundles bear the brunt of the load, in contrast to the radial direction, where the elastic fibers bear the majority of the load.[11] The *lamina fibrosa* is composed of parallel collagen fibers, oriented in the circumferential direction. Additionally, the increased extensibility of this layer is probably due to the "corrugated" nature of the collagen fibers in the relaxed state.[12] This structure bears the brunt of the stress experienced in diastole. The next layer up is called the *lamina spongiosa*, which is primarily composed of glycosaminoglycans and water. It has been hypothesized that this layer acts as a damper during leaflet closing.[11] The *lamina ventricularis* is found on the ventricular side of the spongiosa. The ventricularis is composed of both elastic and collagen fibers. The elastic fibers ensure that the collagen is organized into a folded contractile state.[12] This layer varies in thickness, and is considerably thicker at the transition between loaded and unloaded portions of the leaflet.[3] However, the mean thickness of this layer is roughly half that of the fibrosa.[12]

2.1.4 Comparison of Animal and Human Aortic Valves

Various animal and human heart valves have been compared extensively, and in both dimension and anatomical characteristics (points of leaflet attachment), the porcine valve has been shown to be the most similar.[13] As a result, porcine valves have been long considered to be a suitable experimental model for human valves.[14]

2.2 Aortic Valve Disease

The most common incidences of aortic valve disease are congenital defects and aortic valve stenosis.[9] Congenital defects in valve formation are responsible for numerous types of valvular dysfunction, including regurgitation and valve stenosis.[15] A wide variety of causes for aortic valve stenosis have been proposed, but the root causes of this condition are not necessarily known.

2.2.1 Aortic Valve Stenosis

Aortic valve stenosis is fairly common, and affects patients with congenitally malformed valves as well as patients with normal valves.[16] It is a condition resulting in the hindrance of blood flow from the left ventricle to the aorta. In aortic valve stenosis, the valve orifice is frequently reduced to a small triangular opening that is not only stenotic, but may also be regurgitant (leaky).[9] Aortic valve stenosis can be divided into two classes, congenital and acquired. Congenital stenosis is uncommon (however when it does occur, it frequently is due to a bicuspid aortic valve), and when stenosis is seen young patients it usually becomes symptomatic after birth.[15] [17]Acquired stenosis can be further subdivided into stenosis of a normally formed valve and stenosis of a malformed valve.[10] In normally formed valves, this pathology can be caused by rheumatic fever or calcific degeneration, as well as by congenital defects.

Aortic stenosis that results from rheumatic fever is due to the formation of adhesions and the fusion of the commissures and cusps. In rheumatic fever, the tissue becomes fibrotic leading to stiffening.[9] Calcific degeneration of the valve tissue also is a significant cause of aortic stenosis. This calcification results from a variety of causes including osteogenic and inflammatory reactions, and may be linked to atherosclerosis.[18, 19] Congenital bicuspid valves, he most common malformed valve, produce turbulent flow patterns that also lead to fibrosis and increased calcification of the valve.[20]

Regardless of the cause of aortic stenosis, the effect on the heart is the same. If untreated, this condition results in an increased afterload for the heart. In turn, the heart compensates by increasing the muscle mass of the left ventricle. Ultimately, left ventricular hypertrophy leads to clinical heart failure. For this reason, a large number (> 100,000) patients undergo valve replacement surgery each year.[9]

Patients with normally formed tri-leaflet valves constitute the bulk of aortic valve stenosis cases in the 65+ age group. In these patients, calcific deposits are uniformly distributed across the cusp. The commissures are rarely fused; as such, it is uncommon for these patients to experience aortic valve regurgitation.

As previously discussed, the bicuspid valve is the most common type of malformed aortic valve. In a retrospective study of aortic valve stenosis, the largest percentage (47%) of patients aged 15-56 had bicuspid valves (Figure 2.4). In contrast, when patients over the age of 65 were studied, nearly all cases of stenosis were in normal tri-leaflet valves.[10] These results suggest that when aortic stenosis is seen in younger patients, the root cause is most likely some kind of malformed valve, but when it is observed in elderly patients, the cause is typically calcific degeneration.

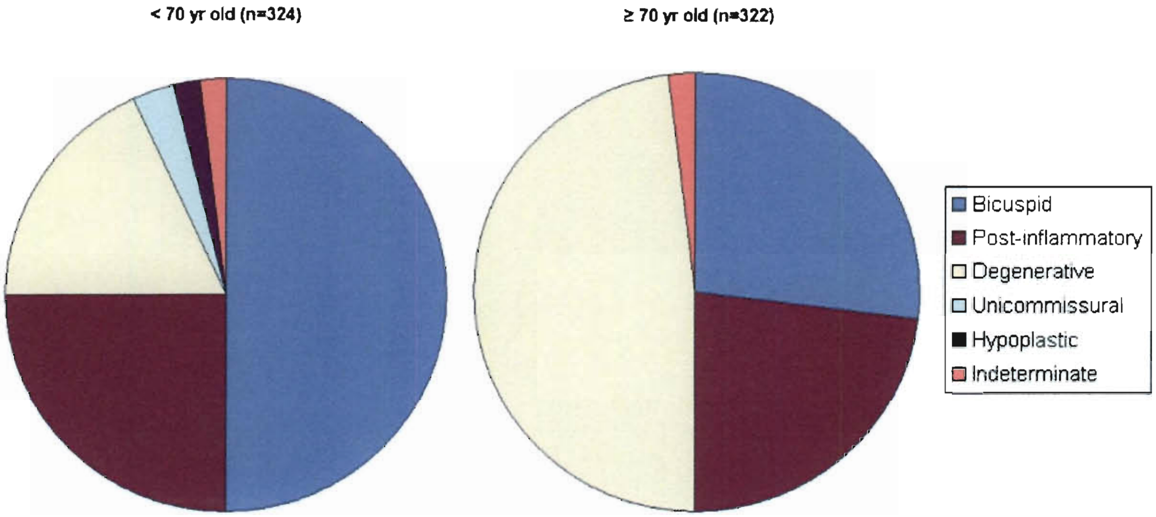

Figure 2.4: Retrospective study examining sources of aortic stenosis. Figure adapted from Passik *et al.*[21]

2.3 Clinical Relevance

Cardiovascular disease and more specifically, valvular disease is very common in the United States. Roughly 95,000 people undergo some form of treatment each year for valvular disease, and over half of these patients have an aortic valve disorder. The mortality associated with aortic valve disorders is over 26,000 patients per year in the United States.[22] The most common treatment for valvular dysfunction is replacement, with either a mechanical or bioprosthetic valve.[8] Neither replacement option is ideal for pediatric patients. Mechanical valves require systemic anticoagulation, which can be dangerous in children.[23] In young patients bioprosthetic valves tend to calcify very quickly and require frequent replacement surgeries.[24]

2.3.1 Valve Homografts

Mechanical and prosthetic valves are equally susceptible to endocarditis and nonstructural dysfunction.[8] Furthermore, since neither of these treatments have the ability to grow; they are not ideal for a pediatric patient. Additionally, pediatric patients experience much quicker degradation of bioprosthetics than do elderly patients.[24, 25] As an alternative, the Ross procedure (pulmonary autograft and replacement of the pulmonary valve) is used commonly in pediatric patients in the hope that the transplanted valves may grow with the child. This has been used successfully for many years and is most successful when the pulmonary valve is replaced by a homograft.[26] Currently, the Ross procedure is the gold standard of care for suitable patients, and offers potential for valve growth in pediatric patients.[27, 28] However, in many cases the procedure proves to be too risky, since the operation more than doubles in complexity (one valve to two valve), there are a limited number of homografts, and an artificial valve is used. [27]

2.3.2 Mechanical Valves

While valve replacements have been successfully performed for many years, there is no “silver bullet” solution to treating valve dysfunction. A plethora of designs for the mechanical valve exist, and some have been used clinically for as long as 40 years. The most common mechanical valve used today is a bileaflet valve composed of two tilting disks (Figure 2.5 A & B). These prostheses are very durable and have desirable central flow properties. The downside of mechanical valves is that they typically require the use of anticoagulant therapy for the remainder of the patient's life (regardless of the patient's age), which puts the patient at risk for adverse hemorrhagic effects.[29]

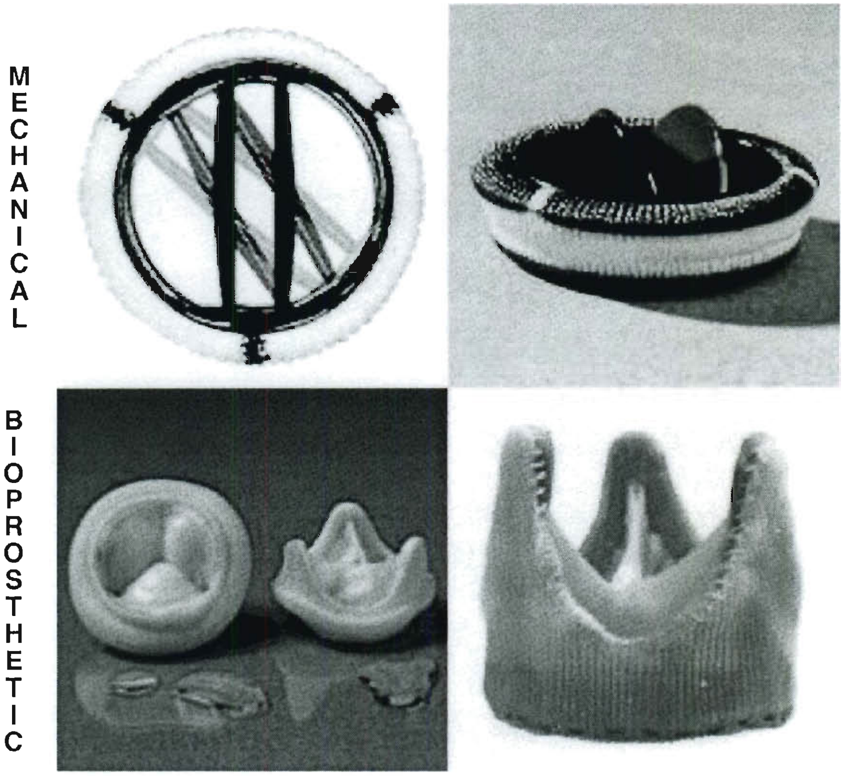

Figure 2.5: Bileaflet mechanical (upper row), stented bioprosthetic (left, lower row) stentless bioprosthetic (right, lower row) aortic valves. Source: STS.

2.3.3 Bioprosthetic Valves

Bioprosthetic valves do not require systemic anticoagulation, but they are significantly less durable than mechanical prostheses.[24, 25] These valves are typically created by glutaraldehyde fixation of a porcine valve, which is then mounted to a stent for implantation (Figure 2.5 C & D). A major problem with bioprosthetic valves is the durability. These valves are only expected to last 10-15 years after implantation due to structural valve degeneration, and are most commonly used in patients who are older than 70.[25] This strategy is used because the patient is not expected to need a subsequent surgery, since the lifespan of the valve exceeds the patient's life expectancy.[30] When these valves are used in patients under the age of 65, they frequently need to be replaced (this replacement frequency increases with decreasing patient age).[25] The risk and trauma associated with multiple valve replacement surgeries further justifies the need for a tissue engineered valve.

2.4 Valvular Tissue Engineering

A tissue engineered heart valve offers a solution to the limitations of currently available treatments for aortic valve dysfunction. In addition, a tissue engineered heart valve could serve as a robust model to understand the mechanisms of valve biology and disease. An ideal tissue engineered valve would be able to grow and remodel as a pediatric patient grows. The ability to create a valve with a natural architecture will minimize the problems of hemolysis and incomplete closing associated with current vale prostheses. Valvular tissue engineering is emerging as an established field, and has been an active area of research for the past 20 years.

2.4.1 Previous Tissue Engineered Heart Valve Paradigms

There is no definitive solution to the problem of creating a tissue engineered valve, however, there are two main approaches being investigated:

i. decellularization of xenograft or human valve tissues and repopulation with the patient's own cells

ii. population of engineered scaffolds with cells

The promise of using the first method, a decellularized valve that would then be repopulated by the patient's own cells, was initially very popular due to the aortic valve's complex nature and our relative lack of knowledge about this process.[31] This method has yet to yield any success in a human model, and typically fails due to a severe inflammatory response and structural failure encapsulation.[32] The second method, population of engineered scaffolds with cells, is the more common "tissue engineering paradigm," which refers to the population of a 3D scaffold with cells then the subsequent application of biochemical and biomechanical cues to guide tissue formation. A variety of approaches to the second paradigm will be discussed below, however this chapter will focus primarily on the application of physical stimuli and scaffold material choice, since those conditions are of primary importance to this work.

2.4.2 Current State-of-the-Art

The current state-of-the-art tissue engineered valve has been detailed in the literature and has been developed in a number of collaborative labs.[33-54] The general technique employed by Hoerstrup *et al.*,[44] that yielded a functional tissue engineered valve was to create a valve-shaped mesh scaffold composed of polyglycolic acid/polylactic acid (PGA/PLLA) copolymer, which is then dip-coated in poly-4-hydroxybutarate (P4HB). The valve was then seeded with human saphenous vein cells and mechanically conditioned in a bioreactor. Their method has yielded a layered microstructure that mimics that of a native valve. However, this approach is not yet ideal, due to the compaction of the mesh scaffold. This compaction leads to the loss of coaptation of the valve leaflets, and leakage across the valve. Additionally, the degradation of this scaffold is uncontrolled and produces potentially cytotoxic acidic byproducts.[40] Finally, the created valve is not of a suitable strength for use in the aortic position. Other groups are investigating this approach with slight variation in the polymer or cell types used, but this approach is essentially the state-of-the-art.[38, 45-47, 50-54]

2.4.3 Natural Scaffolds

A variety of natural scaffold materials for use in a tissue engineered heart valve (TEHV) have been investigated. These range from gels comprised of fibrin, collagen, gelatin, hyaluronic acid and other glycosaminoglycans (GAG) to decellularized tissues. Collagen and fibrin gels exhibit compaction when seeded with mesodermal cells, and the compaction of the scaffold can be tuned by altering the matrix protein concentration.[55] Additionally, pure fibrin gels have been used to make bileaflet valve equivalents, which when cultured in a bioreactor in a valve shaped demonstrate anisotropy and show good cellularity through 5 weeks of culture.[56] While these scaffolds show promise for a clinical therapy, they suffer from leaflet thinning, are much less stiff than native tissues, and lack the intrinsic "bio-inertness" and customization potential of synthetic scaffolds. Modified gelatin has recently been investigated as a potential scaffold material for TEHV. This modified gelatin shows tunable mechanical properties, controllable porosity, biodegradability, and maintenance of valvular interstitial cell (VIC) phenotype throughout culture. Additionally, since the gelatin modified with methacrylate moieties (gel-MA), it is possible to photopolymerize the scaffold. These gel-MA scaffolds, however are two orders of magnitude less stiff than native tissues.[57, 58] Hyaluronic acid based hydrogels have also been investigated as a potential scaffold material. These gels are similar in composition to the cardiac jelly present in heart development, can be photopolymerized, and have bioactive degradation products, but they too are significantly weaker than native tissue, and until recently, there was little control over the degree of modification required for crosslinking.[59] Decellularized valve tissues have also been explored as a natural TEHV scaffold and take advantage of significant industrial development of processing techniques used in the manufacture of bioprosthetic valves. Decellularized valve tissues can be fixed to stents, a common practice for bioprosthetic valves. These stented valves can easily be loaded into bioreactor systems and subjected to dynamic cell seeding environments.[31] Despite the advantages of dynamic seeding, it was shown by one group that when using human cells, cellularity in the TEHV remained less than half that of native tissues even after 8 weeks of culture. GAGs were deposited by the seeded cells; however, it has been difficult to ascertain the degree of matrix production by the reseeded cells that are retained in these constructs.[60] Furthermore, the decellularization process considerably weakens the construct, particularly in the radial direction. Cell seeding and dynamic culture for 16 days allows the recovery of tensile strength.[31] While constructs generated from decellularized natural tissues have shown *in vitro* success, they failed quickly and catastrophically when used *in vivo* in pediatric patients.[32] Three patients died (two suddenly), and one patient showed severe inflammation within 2 days of the implant. As a result, decellularized tissues are undergoing more extensive laboratory testing to elucidate the root causes of the observed clinical failures.

2.4.4 Polymer Scaffolds

Biodegradable synthetic scaffolds are the other primary area of TEHV scaffold research, and they have been used extensively in a wide variety of applications. Many engineered tissues both in development and in clinical use employ this paradigm.[61] The majority of these TEHV investigations have used non-woven fiber mesh or salt-leached foam scaffolds generated from polyglycolic acid, poly (lactic-co-glycolic acid), and polyhydroxyalkanoates, to-date, hydrogels have received far less attention for TEHV applications.[35, 37, 40, 51, 53] The open structure of the mesh or foam allows cell migration throughout the scaffold, and their material properties can be engineered to be sufficient for the mechanical environment of the valve, which involves flexure, tension, compression, and shear varying throughout cardiac cycle. Additionally, these materials are degradable and have been FDA approved for many years. However, these materials have shown certain limitations, namely their high initial stiffnesses compared to native tissues and the substantial length of time required for the polymer to undergo hydrolysis-governed degradation.[52] Polyhydroxyoctonoate (PHO), when cell seeded and subjected to physiologic flows results in functional flexible leaflets, with synchronous opening and closing, however, studies by Sodian *et al.* demonstrated that this material did not resorb completely over 4 months, and does not lead to full tissue development.[33, 35, 36, 62] Polyglycolic acid (PGA) meshes were also investigated as a TEHV scaffold, and when used alone, were far too stiff and thick for functional leaflet creation.[63] Constructs with

PGA meshes surrounding a nonporous PHO film were successfully implanted in the pulmonary position, and showed no thrombus formation when cell-seeded, although when acellular meshes were implanted, they constructs developed thrombi.[50] Both PGA and poly l-lactic acid (PLLA) have been modified by dip coating with poly 4-hydroxybutyrate (P4HB) to improve the mechanical properties of these non-woven meshes. PGA/P4HB shows appropriate degradation kinetics, however in a study by Hoerstrup *et al.* the valves are regurgitant after 16 weeks of implantation.[34] PLLA/P4HB valves are of higher stiffness than leaflets and complete degradation can take longer than two years.[53, 64] Both of these materials were shown to have much quicker degradation when subjected to cyclic flexure.[53] Furthermore, these materials lack intrinsic biological functionalization, meaning that they do not present any functional biological moieties that could direct cell signaling, ECM production, or enzyme-governed degradation. These materials can be modified to present these motifs, however, there is no control over functional molecule localization, in contrast to the patterned localization achievable in hydrogels via photolithographic or two-photon adsorption methods (described in section 2.5 and Chapters 5 and 6).[65-67]

Both non-woven fiber mesh and salt-leached foam scaffolds use cytotoxic processing conditions to generate their architecture. Since the polymer processing conditions are cytotoxic, cell seeding must be performed after the scaffold is fabricated. Cell seeding has been one of the most significant challenges in use of these scaffold materials. Seeding methods have often resulted in inhomogeneous cell distribution, low cell densities, and long seeding times before the scaffold was fully populated. Initially, cells were incubated atop the scaffolds under static conditions for up to 4 days in order to allow cell migration into the interior of the scaffold.[34] Dynamic seeding methods were developed that yielded homogenous and slightly more efficient seeding, but the dynamic nature of the seeding environment was reported to cause small cracks in the scaffold material.[68] Encapsulation has been shown to be the most efficient and homogeneous method of cell seeding. For example, the use of a viscous fibrin "cell carrier" gel resulted in fast, high yield, homogenous seeding of valvular interstitial cells (VICs) into fiber matrices. The use of fibrin as the basis for the gel, however, alters the seeded cell's local biochemical and biomechanical environment. It does this both through its structure (cell-substrate) as well changing the diffusivity of the cell's pericellular environment.[43, 69] While these previous mesh-based approaches hold promise, the ability to encapsulate cells coupled with the customization potential of polymeric biomaterials makes photopolymerizable hydrogels very appealing as scaffold systems.

2.5 Poly(ethylene glycol) Diacrylate Hydrogels

Hydrogels are a class of polymer networks that are comprised of hydrophilic cross-linked polymer chains. Due to the hydrophilicity of the chains, these structures swell in the presence of water. Monomers that are in solution undergo anionic, cationic, or photoinitiated polymerization methods that yield a solution of uncrosslinked polymer chains. These polymer chains are then modified with a reactive group at the chain ends which enable crosslinking.[70] When hydrogels are created for tissue engineering purposes, the method of crosslinking a solution of polymer chains is most common, since most monomers are cytotoxic.[71]

The near infinite biochemical and biomechanical tunability of poly(ethylene glycol) diacrylate (PEGDA) hydrogels makes them very attractive potential scaffold materials for TEHV. PEGDA hydrogels are intrinsically biocompatible, since the base (unmodified) gels are biologically neutral, resist protein adsorption, do not release acidic products during their degradation and can be crosslinked with low cytotoxicity allowing for high density 3D cell encapsulation. Furthermore, these hydrogels can be modified by crosslinking a large number of bioactive moieties (peptides, glycosaminoglycans, growth factors) to achieve a high degree of specific bioactivity.[2, 72, 73] Indeed, it is widely reported that peptides tethered to either the surface or bulk phase of PEGDA gels will retain their bioactivity after this modification.[74-76] Additionally, since these materials can be rapidly photopolymerized, spatial control of functional moieties is possible in both 2D and 3D, due to the emerging field of two-photon stereolithographic fabrication techniques.[66]

2.5.1 Photopolymerization of Hydrogels

Photopolymerization exploits the use of a light-irradiated photoinitiator to produce a radical initiating species that can create crosslinked hydrogels. Photopolymerization has many advantages that establish its value for tissue engineered applications. This method offers spatial, temporal, and rate control of polymerization.[77] The spatial control of crosslinking allows for two and three dimensional patterning to be achieved in hydrogel structures with the use of photolithography patterning (PLP) and two photon adsorption (TPA).[65, 66, 78, 79] In addition to the high level of control realized via photopolymerization, this technique is desirable for use *in vitro* since crosslinking can be completed quickly without the presence of monomers or organic solvents. Polymerization conditions that are sufficiently gentle to allow this procedure to be performed in the presence of cells have been achieved.[71]

2.5.2 Previous Medical Applications of Poly(ethylene glycol)

The very low toxicity of poly(ethylene glycol) (PEG) permitted it to become FDA approved, which has been a significant stumbling block for other biomaterials. As such, PEG has been used in a variety of medical applications, whose function can often be grouped into two major categories: 1) improvement of biocompatibility and 2) controlled release of a bioactive molecules. When used to improve biocompatibility, PEG is most often linked to the surface of another object. This technique is commonly referred to as PEGylation, which most typically refers to the tethering of single chains of PEG to a surface.[80] There are several commercially available products that use PEG to improve local biocompatibility. Vigilon is a hydrogel sheet that is used as a wound dressing to improve healing. The use of PEG as a mechanism for rate controlled drug delivery has been explored for many years. This schema has been successful in the delivery of both proteins and genes.[81, 82] Even though PEG has been used in other medical products, PEG hydrogels are only beginning to be explored for use as a TEHV scaffold.

2.5.3 Mechanical Properties of PEGDA Hydrogels

The tunable mechanics of PEGDA hydrogels has been reported in the literature and it has been demonstrated that a wide range of material properties can be readily achieved by varying the prepolymer composition. It has been shown that by varying the polymer chain's weight fraction, the modulus of elasticity can be altered significantly.[75, 83] In the 1 to 10% strain range, fully swelled PEGDA hydrogels have been shown to behave with near purely elastic behavior, and no significant difference between tensile and compressive moduli was shown.[75] Moreover, it has been hypothesized that the elasticity of PEG will enable more efficient transfer of dynamically applied mechanical loads to cells than current fiber based scaffolds. Molecular weight of the PEG chain is also a significant modifier of the modulus. At higher magnitudes of strain (up to 30% in compression), the behavior of hydrogels is nonlinear, and dependent on the molecular weight of PEG chains.[84] Although the tensile and compressive properties of PEG hydrogels have been investigated, there is little to no work that has been reported on the bending and fatigue characteristics of these hydrogels.

The physical properties of PEGDA gels can be modified across a continuum of magnitudes that are biologically relevant in terms of recapitulating both tissue function and the pericellular environment. Hydrogel physical properties such as stiffness, degree of swelling and effective diffusivity can be controlled by manipulating the molecular weight of the macromer, the weight fraction of macromer in solution and the crosslinking time.[85, 86] It has been further demonstrated that crosslinking density affects the strain experienced by the cell, and certain formulation parameters can translate nearly 100% of bulk strain to individual cells.[83] Cells seeded in fiber mesh scaffolds can be in contact with either a singular fiber, or many fibers, which may have varying degrees of displacement at the microstructure due to macrostructural strain. Thus, mechanotransduction in hydrogels appears to be more efficient than in fiber meshes.

2.5.4 VIC Adhesion to PEG

Valvular interstitial cells are the primary cell type found in the heart valve. VICs are myofibroblasts that produce vast amounts of ECM and are contractile. Therefore, it is a natural choice to select this cell type when attempting to create a tissue engineered heart valve. The ability of PEG to be customized with particular functional groups is also desirable to ensure specific cell adhesion and retention. In one of the initial studies examining VIC seeding on PEG surfaces (Masters *et al.*), gels were created with covalently linked GRGDS and/or EILDV and VICs were seeded on these surfaces. These gels did not show much improvement with respect to adhesion over the unmodified PEGDA hydrogels.[1] In an effort to improve adhesion and cell morphology on hydrogels in a later work by Cushing *et al.*, PEGDA gels were fabricated with both the RGD adhesive ligand as well as methacrylated heparin. VICs seeded on these gels did not show a significant increase in adhesion, however there were pronounced morphological and phenotype differences. The VICs seeded on heparinized gels had a more spread shape and significantly higher levels of αSMA expression. This behavior was shown to be specific to heparin and dose dependent.[2] Since these gels have been shown to support VIC adhesion and growth, as well as having high potential for mechanical and biochemical modification, they are a natural choice for investigation as a TEHV scaffold. Recent work investigating other hydrogel materials (including methacrylated gelatin and hyaluronic acid) has shown promise for the maintenance and proliferation of VICs, however these materials are not fundamentally inert (in contrast to PEG-based hydrogels) and therefore can influence cell behavior in unexpected ways. Additionally, it is more difficult to modify the material properties of these gels across a continuum, since the molecular weight of the prepolymer is not directly controllable.[57, 87]

,

2.5.5 Advanced Hydrogel Structures and Strategies

In addition to being able to modify bulk PEGDA gels biochemically and biomechanically, the ability to photopolymerize these materials permits the fabrication of advanced structures. Since the prepolymer can be crosslinked via radical initiating species, patterns can be crafted in the gel with unique geometries. Photolithographic patterning, as described by Hahn *et al.* can be used to craft a variety of two dimensional patterns.[65, 78] Furthermore, using rapid prototyping methods (two-photon adsorption based stereolithography), 3D patterns can be created within the gel.[66] These structures can result in the creation of anisotropy in what is fundamentally a linearly elastic, isotropic material. Other groups are investigating inducement of anisotropy in hydrogels by application of strain while polymerizing (using freeze-thaw crosslinking)[88], control of secondary crosslinking by patterning [89], and direct embedding of fibers[90, 91], however, many of these methods prohibit the direct encapsulation of cells.

Layered hydrogel structures have been investigated in a range of hydrogel materials, exploiting a variety of "lamination" strategies. Several groups have demonstrated the ability to create quasilaminate hydrogel structures where each layer is composed of the same material and formulation.[79, 92, 93] Temenoff *et al.* was the first to demonstrate the ability to laminate hydrogels with distinct formulations in each layer, and was able to demonstrate a strong interface by using thermal crosslinking.[85] While quasilaminate hydrogels have been successfully fabricated by labs in the past, no one has demonstrated the ability to create a quasilaminate layered structure with distinct formulations in each layer in a photocrosslinked system.

2.6 Bioreactors

Tissue engineering has had limited success in attempts to regrow tissues that can withstand the mechanical demands of the *in vivo* environment.[94] This failure could be due to the original tissue engineering paradigm, which was the combination of cells, three dimensional scaffolds, and exogenous agents. Recently, studies have shown that mechanical stimuli play a very large role in the architecture of tissues.[95] As a result of these findings, various bioreactor systems have been designed to apply specific mechanical stimuli to constructs. These systems have a vast range of complexity and capability. Several bioreactor systems have been designed for heart valve tissue engineering. These include strain-based systems, flexure based systems, and flow loops. The majority of these systems are flow loops that approximate the behavior of the ventricle, and permit the engineered tissues to be cultured under a wide variety of conditions.

2.6.1 Single Phenomena Systems

A system to evaluate scaffold materials and their use in TEHV was designed by Englemayr *et al.* (Figure 2.6).[52] This system is a device that will apply dynamic three point bending to strips of scaffold material. The rationale for its design is that by isolating a particular source of mechanical stimuli, a greater understanding of the effect can be achieved. This system has been used to test the fatigue properties of acellular PGA/P4HB and PGA:PLLA/P4HB. Substantial decreases in stiffness were observed for scaffolds that were dynamically flexed in comparison with controls. This finding substantiates the hypothesis that fatigue may significantly accelerate weakening of the construct in a culture environment. This system is useful for preliminary material research, although, it cannot be used for valve shaped constructs.

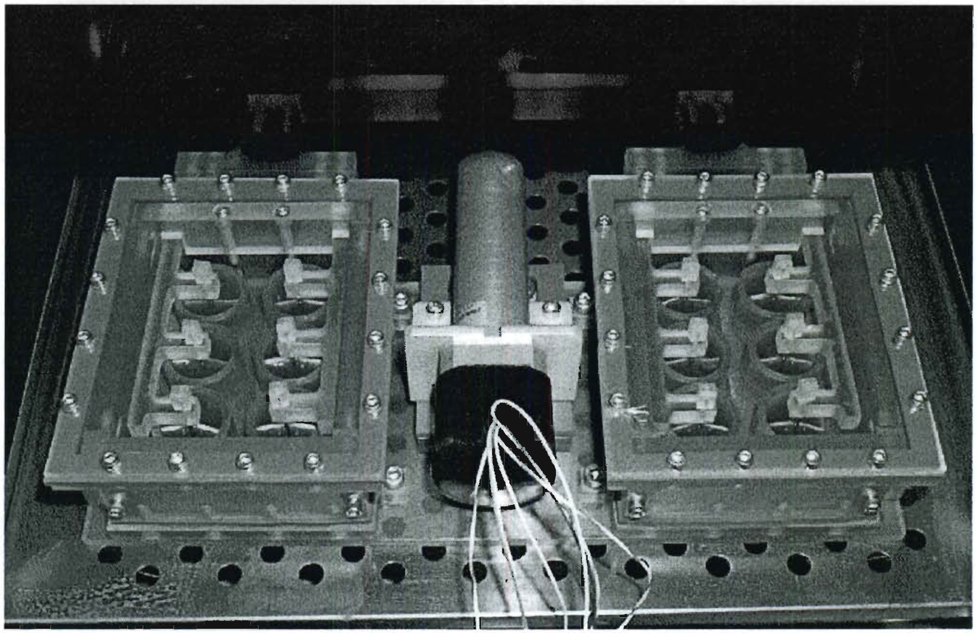

Figure 2.6: System to apply cyclic flexure to strips of scaffold material.[52]

2.6.2 Complex Environment Systems

The vast majority of bioreactors designed for use in heart valve tissue engineering have been flow loops. These systems (Figure 2.7) range from simple systems to approximate the pumping of the left ventricle to very complex setups that include variable resistance and the ability to maintain long-term sterile culture.[33, 96-98] Flow loop systems, while robust, require complicated controls and do not easily scale to allow for higher sample size studies.

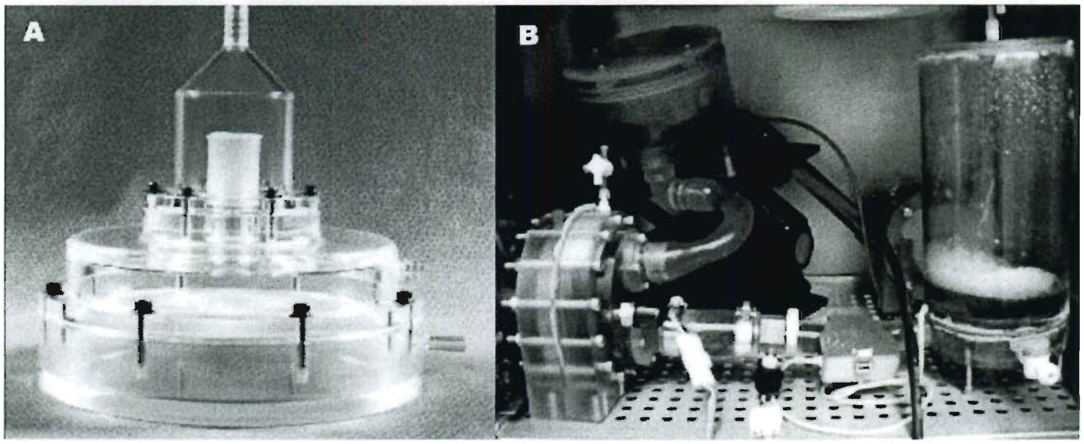

Figure 2.7: Flow Loop systems for aortic valve culture. A) Simple flow loop with approximated left ventricle. B) Complex flow loop with automatic resistance control.[33, 96]

The last type of existing bioreactor for use in tissue engineered heart valves is the diastolic pulse duplicator (Figure 2.8). The aortic valve experiences maximum stresses during the diastolic phase, and this system was designed to replicate that phenomena. The system exploits the use of low flow rates (sub-physiologic) in the early stages of stimulation. It further develops the idea of strain based conditioning of TEHV constructs, and is modular for scalability. Ultimately, implementation of this system is complicated and setup is time consuming.[42]

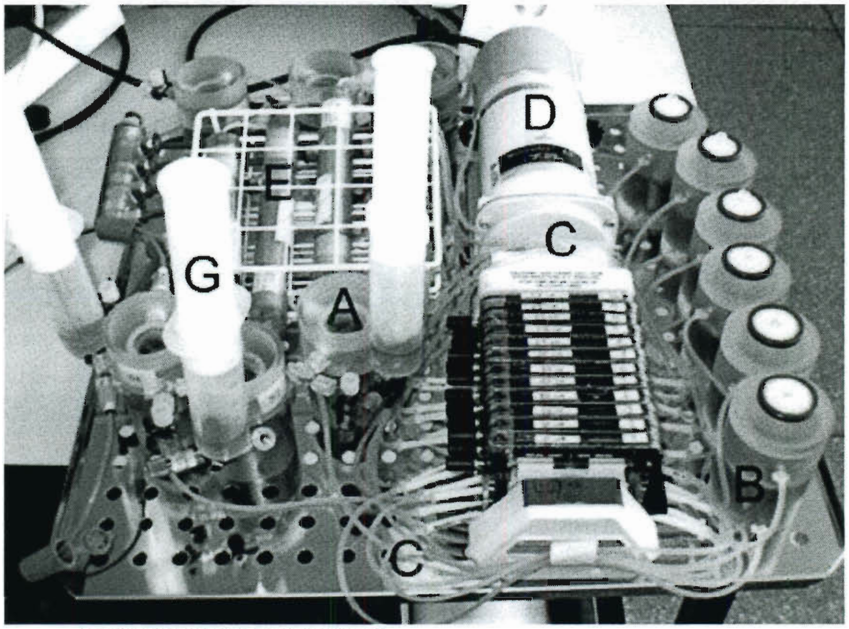

Figure 2.8: Diastolic pulse duplicator that allows high numbers of replicates per system.[42]

Tissue engineered heart valves have yet to be successful in the aortic position regardless of the methodology employed. The most appropriate material for TEHV has not been identified, due to the complex mechanical environment that these scaffolds must endure. Furthermore, the necessary biochemical and biomechanical cues for *in vitro* development of a TEHV are not yet fully known. We believe that since passive, inert prostheses have shown clinical success in valve replacement for over 40 years, and that structural valve degradation significantly reduces the useful life of inert bioprosthetics, the mechanical characteristics of the TEHV scaffold are of primary importance. Without adequate material properties, any TEHV will fail when implanted. Furthermore, it has been clearly demonstrated in the literature that biomechanical conditioning (with the goal of driving tissue formation) is necessary for any TEHV prior to implantation. In the following chapters, a system that can provide biomechanical stimuli to explanted tissue or engineered aortic valves is detailed (Chapter 3), and the *ex vivo* culture of valves in this system is described (Chapter 4). Using criteria obtained from these studies, an optimization and characterization of the flexural properties of a range of PEGDA formulations is explained (Chapter 5). The flexural properties determined in those studies drove the interest in creating anatomically-inspired composite hydrogels, which are described in Chapter 6.

Chapter 3: Design and Physical Characterization of a Synchronous Multivalve Aortic Valve Culture System*

For many tissues, cyclic mechanical stimulation is necessary to maintain the normal morphology *in vitro*. This need motivated the design of a simple, scalable aortic valve organ culture system capable of medium-term (more than 2 weeks) culture of native and engineered aortic valves. The system consists of three pistons in separate cylindrical chambers that are simultaneously driven through the culture medium by a crank and~ cam assembly. The faces of these pistons have unidirectional valves mounted in opposing orientations that permit flow from one side of the face to the other. A custom designed stent was employed to secure either native or engineered trileaflet valves to the pistons. Computational fluid dynamics and finite element modeling was used to assist selection of materials and components in the system. Finally, sterility testing using base culture medium was performed to verify the ability of the system to retain sterile conditions. The current design permits the cyclic opening and closing of three aortic valves, however this device can be modified to accommodate up to 12 valves simultaneously. This chapter will discuss the physical design and performance characterization of the system and effects of culture in this system will be discussed in Chapter 4.

---

* This majority of this chapter was published as: Durst CA, Grande-Allen KJ. Design and physical characterization of a synchronous multivalve aortic valve culture system. Annals of Biomedical Engineering, 2011 Jan; 7(1):75-82.

3.1 Introduction

The aortic valve consists of three leaflets continuous with three aortic sinus walls and is located between the left ventricle and the aorta. It functions as a one-way valve, allowing oxygenated blood to flow from the left ventricle to the aorta. The normal *in vivo* mechanical loading of aortic valves is responsible for varied biosynthetic responses of valvular cells and heterogeneous distribution of extracellular matrix throughout the leaflets.[99] For example, protein and glycosaminoglycan synthesis is greater at locations in the leaflet demonstrating the greatest functional stresses.[100] Furthermore, mechanical stimulation has been shown to be necessary for the maintenance of tissue phenotype as well as regulating matrix synthesis for a variety of tissues when cultured *in vitro.*[101-103] Cultured valve leaflets respond to hydrostatic pressure in a magnitude dependent manner by altering their sulfated glycosaminoglycan (sGAG), collagen, and DNA contents.[104] Similarly, engineered tissue surrogates containing valvular interstitial cells (VICs) react to cyclic stretch in a reversible manner by altering their GAG and proteoglycan production.[105] The need to improve our understanding of the true role that mechanical stimuli play on the extracellular matrix of the aortic valve has motivated the design and creation of the *in vitro* mechanical environment. The effects of varied mechanical stimuli on valves have only been studied in the past few years, and further investigations in this area will have far ranging impacts from advancing knowledge of basic valve biology to understanding valve disease progression.

Mechanical stimulation culture systems have wide utility not only as systems to study models of valve disease and remodeling, but also for use in the development of tissue engineered heart valves.

A number of bioreactor systems have been designed to provide physical stimuli to engineered aortic valve tissues. These systems vary greatly in complexity, from very simple models that provide an isolated mechanical stimulus[52, 105] to very complex flow loops with automated resistance and feedback controls.[42, 96, 97, 106] Engelmayr *et al.* have detailed a system that allows the application of flexure thereby elucidating the effect of the mechanical stimulus.[52] In contrast, the flow loop described by Hildebrand *et al.* allows robust control over the physiologic environment, with control of both pressure and flow rates, which are achieved with computer controlled pumps and flow resistors.[96] Previously developed bioreactors and flow loops each serve a specific purpose and are well-characterized in the literature,[33, 42, 52, 96, 97, 105, 106] however, these systems generally fail to address the need for a simple, scalable design. The newly developed bioreactor described here lacks the robust level of control achieved in the most complicated flow loops, but can be easily scaled to allow a large number of valves to be cultured in pseudo-physiologic conditions. The design objectives of this aortic valve culture system were simple operation, high efficiency multivalve culture, low-cost, and a sterile culture environment.

3.2 Physical Design of Bioreactor System

The custom designed bioreactor system provided mechanical stimulation to aortic valves through a cyclic opening and closing action (Figure 3.1). This action, caused by fluid flow, was accomplished by raising and lowering a piston containing a securely mounted aortic root through culture medium. Motion was achieved using a Parker BE233FJ servo motor (Parker Compumotor, Rohnert Park, CA) coupled to a 25:1 planetary gearbox (Parker Compumotor, Rohnert Park, CA), which in turn drove a cam-crank (cam diameter 9.0 cm) assembly. The servo motor was chosen for its capacity for high torque (4.48 Nm) in a relatively small frame (5.7 x 5.7 x 14 cm, 1.9 kg). This servo provided sufficient torque to operate the system across a range of 0-110 equivalent BPM. The crank was attached to a cross-member (40 x 2.54 x 6.35 cm), which can slide in one dimension along two hardened steel alignment shafts. The drive components (cam, crank, cross-member) were made of 316L steel for high corrosion resistance as well as durability and low deformation under continuous load. The structural components of the bioreactor were made from anodized 6061 aluminum, chosen for its combination of low weight, strength and corrosion resistance. By varying the crank length and shaft speed of the motor, stroke volume (651 mL) and frequency (0-110 BPM) were controlled. For example, with the current cam and crank, a flow rate of 5 L/min was be achieved with a cam speed of 7.7 rpm. The system has been run at 5 rpm resulting in 3.3 L/min of flow through the valves. These flow rates were comparable to the current state-of-the-art flow loop described by Hildebrand *et al.*[96] With a simple Pouiselle flow-based calculation, we determined that shear stress on the ventricular side of the leaflets was approximately 0.249 dynes/cm^2. With no modification to the system, it can deliver shear stresses of up to ~0.4 dynes/cm^2. This is substantially lower than physiologic shear stresses (up to ~80 dynes/cm^2 during systole), and if it becomes apparent that application of physiologic shear stress is necessary for *ex vivo* maintenance, other strategies such as increasing the system viscosity with dextran could be used to increase imparted shear stresses.[107]

Motion of the three valve-containing pistons ensured that the valves open and close during each cycle (Figure 3.1). The piston formed a tight seal with the wall of the culture chamber to ensure all flow was through the valve. The piston faces were attached to the driven cross-member with steel shafts and a double seal was used at the air/chamber interface. The piston faces were machined from polycarbonate and were able to be autoclaved with the connecting shafts partially assembled. Each piston had one tissue valve mounted for flow in the positive z-direction, and one mechanical valve (Carbomedics, Austin, TX) mounted opposite to the tissue valve to allow flow in the negative z-direction.

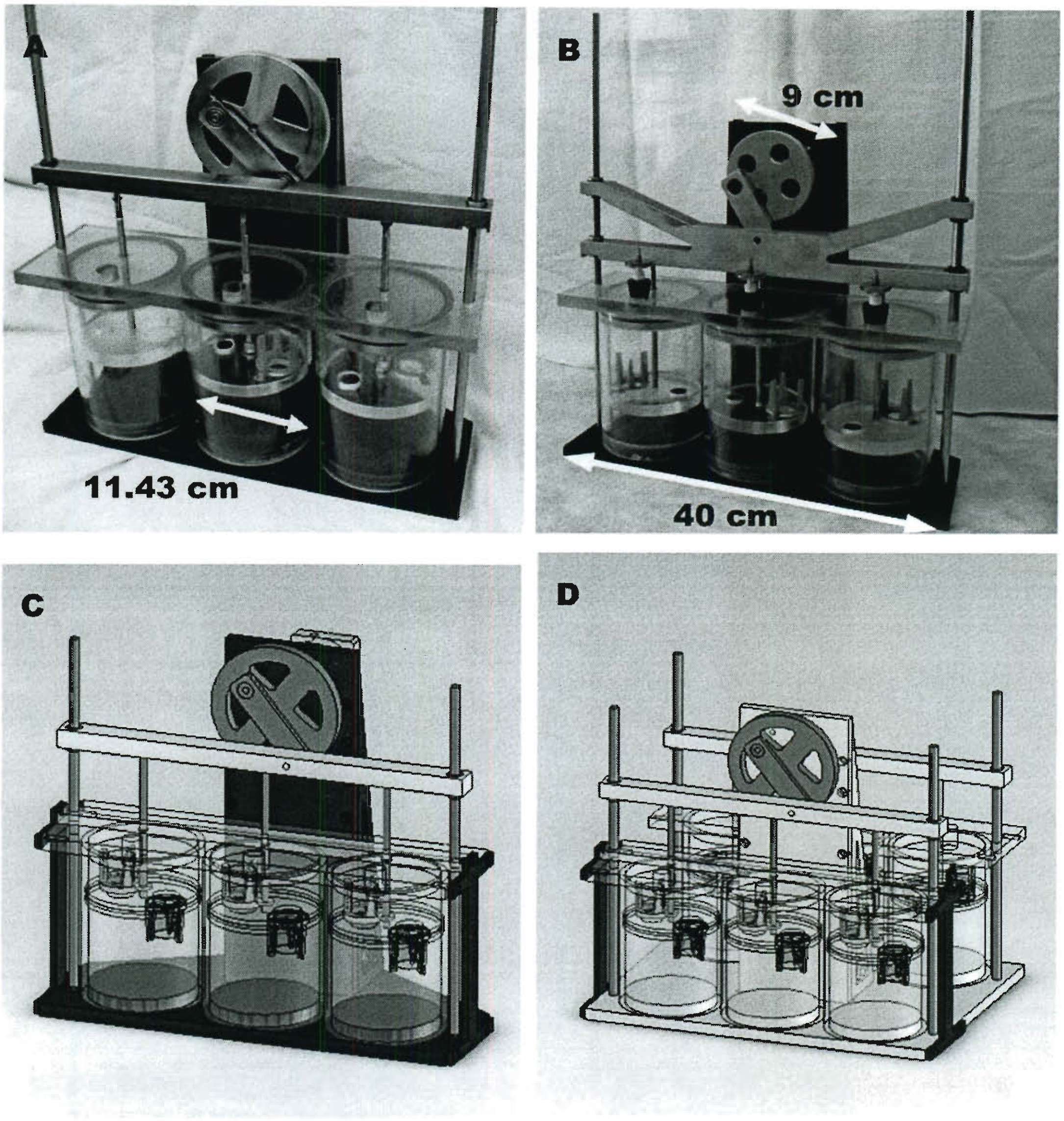

Figure 3.1: A) Photograph of assembled prototype system. B) Photograph of assembled final design, showing revised drive assembly. C) Computer model of system configuration for six valves. D) Computer model of system showing revision to allow culture of up to twelve valves. System width is approximately forty cm.

A method of securing the aortic valve to the piston was established by adapting a concept put forth by Hildebrand et al.[96] An aortic root (prepared as described in the following paragraph) was sutured to a custom designed stent-like device (Figure 3.2), which consists of three arms, each containing holes that allow a swaged suture needle to pass through. These holes were curved to match the radius of curvature of a 2-0 suture needle. Due to the complex geometry of the arms, this stent was fabricated using stereolithography (Laser Reproductions, Columbus, OH) from a high temperature nanoparticle filled polyurethane resin (Nanoform 15120, DSM Somos, Elgin, IL) to ensure both sufficient mechanical and thermal stability at high temperatures (autoclave 121°C). The base of the stent contained a recess for a silicone rubber gasket (thickness 0.125") that ensured a tight seal between the piston and aortic root.

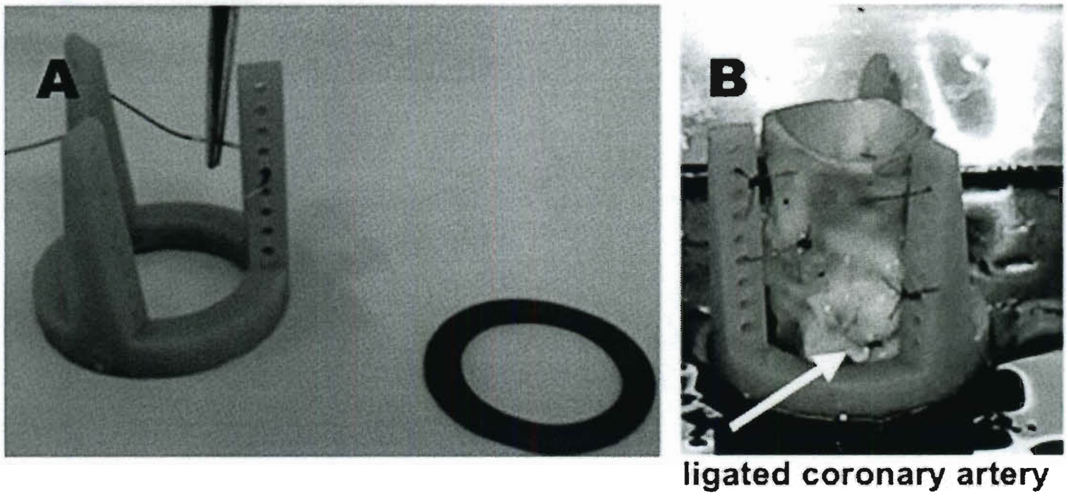

Figure 3.2: A) Custom designed stent (left) and gasket (right) to secure the aortic root to the piston face (1.25 x 1.5 in dia x height) B) Porcine aortic root secured to stent with polypropylene sutures.

The dissection and preparation of the aortic root allowed the tissue to be efficiently loaded into the organ culture system with minimal contamination for cyclic culture. First, the root was grossly dissected from porcine hearts obtained from a local abattoir. The root complete with valve was rinsed in PBS containing 2% antibiotic/antimycotic for 15 minutes. Next, the coronary arteries were ligated, and the root is then sutured to the stent using 2-0 Prolene sutures (Ethicon, Cincinnati, OH). After the root had been secured to the stent, the ventricular annulus was sutured to the silicone gasket. The aortic valve/stent assembly was then locked into the piston face with spring clips (Figure 3.3). This valve was mounted to allow flow in an opposite direction to a permanently installed bileaflet mechanical valve (Carbomedics 19 mm aortic valve, Sulzer Carbomedics, Austin, TX). The oppositely oriented valves both function in one direction only, thereby ensuring that flow proceeded entirely through one valve per half revolution of the cam. During the first half of the cam revolution (the "downstroke"), culture medium was be present on both sides of the piston surface and flowed from the bottom portion of the culture vessel to the top. Once the second half of the revolution began (the "upstroke"), the mechanical valve opened, the tissue valve closed, and fluid flowed from the top portion of the culture vessel to the bottom.

The pistons were located inside the cylindrical culture chambers, each of which was filled with 1.3 L of culture medium (Dulbecco's Modified Eagle's Medium (DMEM) supplemented with 2% antibiotic/antimycotic solution and 10% bovine growth serum (BGS); Mediatech, Manassas, VA and Thermo Scientific, Waltham, MA respectively).[108] The culture chambers were sealed by a rubber plug with an in-line 0.2 μm syringe filter that allowed adequate gas exchange. Silicone o-rings were used to create a seal between sterile, fluid-filled areas and non-sterile areas of the bioreactor.

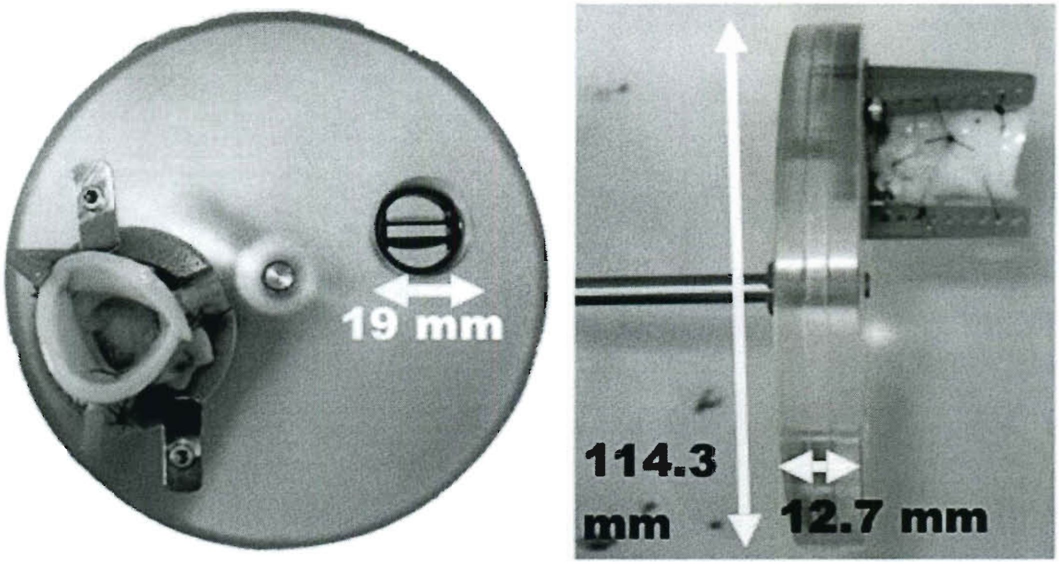

Figure 3.3: Assembled piston containing mechanical and porcine valves.

3.3 Computational Analyses

3.3.1 Computational Fluid Dynamics

Computational models were used to investigate the forces due to fluids contained within the cylindrical culture chambers, which ultimately guided the selection of materials and the servo motor. Basic computational fluid dynamic (CFD) models of each direction of flow were performed using a simplified culture chamber in Floworks (Solidworks Corporation, Concord, MA), which will approximate solutions to Navier-Stokes equations under specific boundary conditions and initial values. Models representing several states of the system were developed. In state 1, an open 19 mm Carbomedics aortic valve was modeled, and the porcine valve was assumed to be completely closed, with no leakage between chambers. The flow was modeled as an internal flow (Q=0.193 L/s), with static pressure (761 mmHg) and flow rate input as boundary conditions. This flow rate was chosen to be more than two times higher than physiologic or roughly 2.5 times what would be used experimentally[109] in order to generate a “safety factor” for load presented to the motor and to prevent material failure. Additionally, this state was modeled as an adiabatic system, and water was used as the test medium. Average transvalvular pressure was measured from areas on either side of the valve where laminar flow was observed (Figure 3.4A). In state 1 this value was approximately 61.658 mmHg. The highest normal force due to fluid resistance in state 1 was 168.087 N. This system was recalculated in state 2 of the model—in which the porcine valve was open, and the mechanical valve was closed (Figure 3.4B) but conditions were otherwise identical to state 1. It was assumed that the orifice area of the porcine valve was identical to the aortic cross-sectional area, and the mechanical valve was completely closed with no leakage. Both average transvalvular pressure and normal force on the piston were lower in state 2 – 18.394 mmHg and 28.484 N respectively. Based on the calculated normal force exerted on the piston face, materials were selected to ensure consistent mechanical performance under load. An estimate of the maximum torque required to complete a stroke was calculated from the state 1 data, and was subsequently used in selection of the servo motor and gearbox.

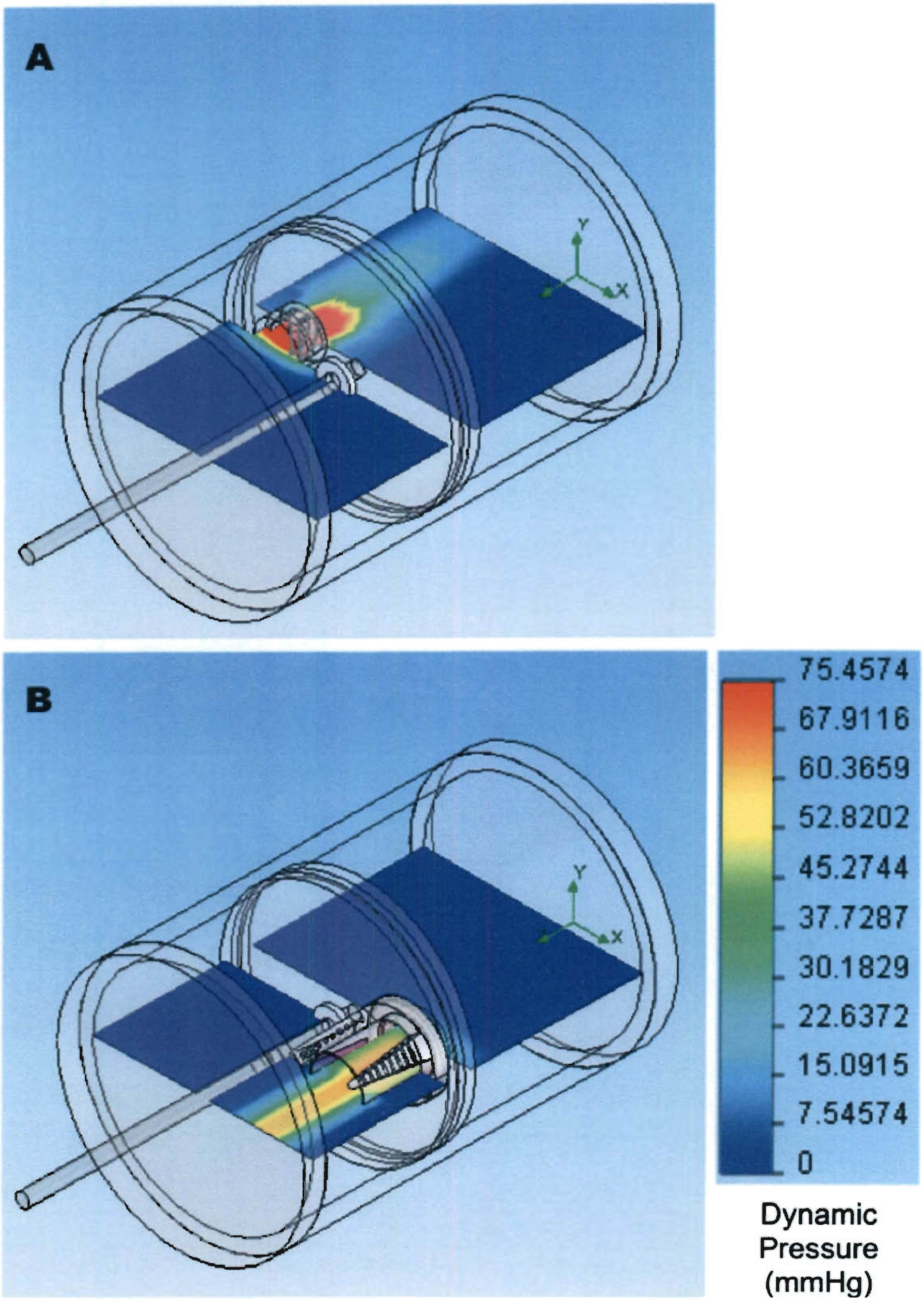
A
Y
X
B
Y
X
75.4574
67.9116
60.3659
52.8202
45.2744
37.7287
30.1829
22.6372
15.0915
7.54574
0
Dynamic Pressure (mmHg)

Figure 3.4: A) Pressure in the system calculated using a simplified model in Floworks (mechanical valve open, porcine valve closed). B) Pressure in the system calculated using a simplified model in Floworks (porcine valve open, mechanical valve closed).

3.4 Finite Element Analysis

Results obtained from CFD studies were entered into a finite element analysis (FEA) of the behavior of the system under loaded conditions. The maximum calculated normal force on the disc was applied to a simplified internal model of the piston assembly. Material parameters for polycarbonate and steel were obtained from ASTM specifications provided by the supplier (McMaster-Carr, Atlanta, GA) and input into the model of the piston face and the connecting threaded shaft, respectively. The steel shaft was assumed to be fixed, which was used as a boundary condition. Von Mises stress and material deformations for these components were then calculated. Upon analysis of the von Mises stress resulting from a normal force on the piston face of 168.087 N, it was determined that the interface of the steel and polycarbonate threads resulted in an unacceptably high value, and would likely crack during loading. A design revision was made using a steel washer to distribute the load, and then fix the axial location of the disc with a steel nut. This revision was modeled and the system was recalculated. This revision minimized the von Mises stress to more than an order of magnitude below the yield strength of polycarbonate (71-120 MPa, Figure 3.5). Deformation of the disk was also investigated since the alignment of the system is crucial to ensure no stiction between the circumferential surface of the piston and the inner wall of the culture chamber. There was no detectable bending deformation at modeled loads of the disc therefore the design was deemed acceptable.

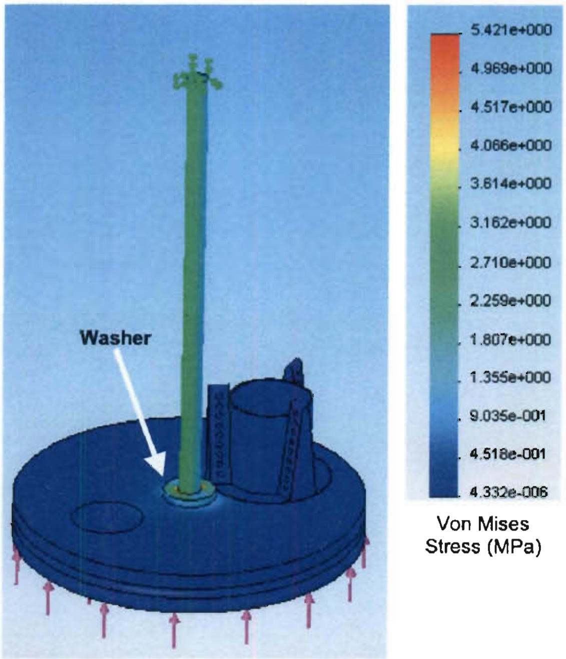
5.421e+000
4.969e+000
4.517e+000
4.066e+000
3.614e+000
3.162e+000
2.710e+000
2.259e+000
1.807e+000
1.355e+000
9.035e-001
4.518e-001
4.332e-006
Von Mises Stress (MPa)
Washer

Figure 3.5: Von Mises distribution of internal stresses in piston assembly demonstrating maximum stress is more than an order of magnitude under the yield stress of the material.

Bearing lock-up was observed frequently when evaluating the prototype design (Figure 3.1A). In response to these problems, CosmosWorks (Dassault Systèmes, Concord, MA) was used to analyze displacement and deformation of drive components using a finite element model of the system throughout a complete revolution of the cam. First, the peak torque required as a function of the stroke was calculated using a motion study with a 1 RPS shaft speed. The system was then virtually "assembled" in this configuration and deformation and displacement studies were performed. It was observed that purely due to the size of the link, placement of the cam, and location where these parts were pinned, there was a significant bending moment placed upon the sliding plate. The system was redesigned to increase the length:diameter ratio spanned by the bearings on the alignment shaft. Additionally, the link was thickened from 0.25 to 0.5 inches and the location for pinning to the sliding plate was changed to be located in the center, rather than on the face of the part. Lastly, the cam's diameter was reduced to decrease the force exerted on the drive assembly. This new design (Figure 3.1B) was then subjected to the same analysis in CosmosWorks, where the maximum resultant displacement was observed to be reduced from 0.075 to ~0.035 mm (Figure 3.6).

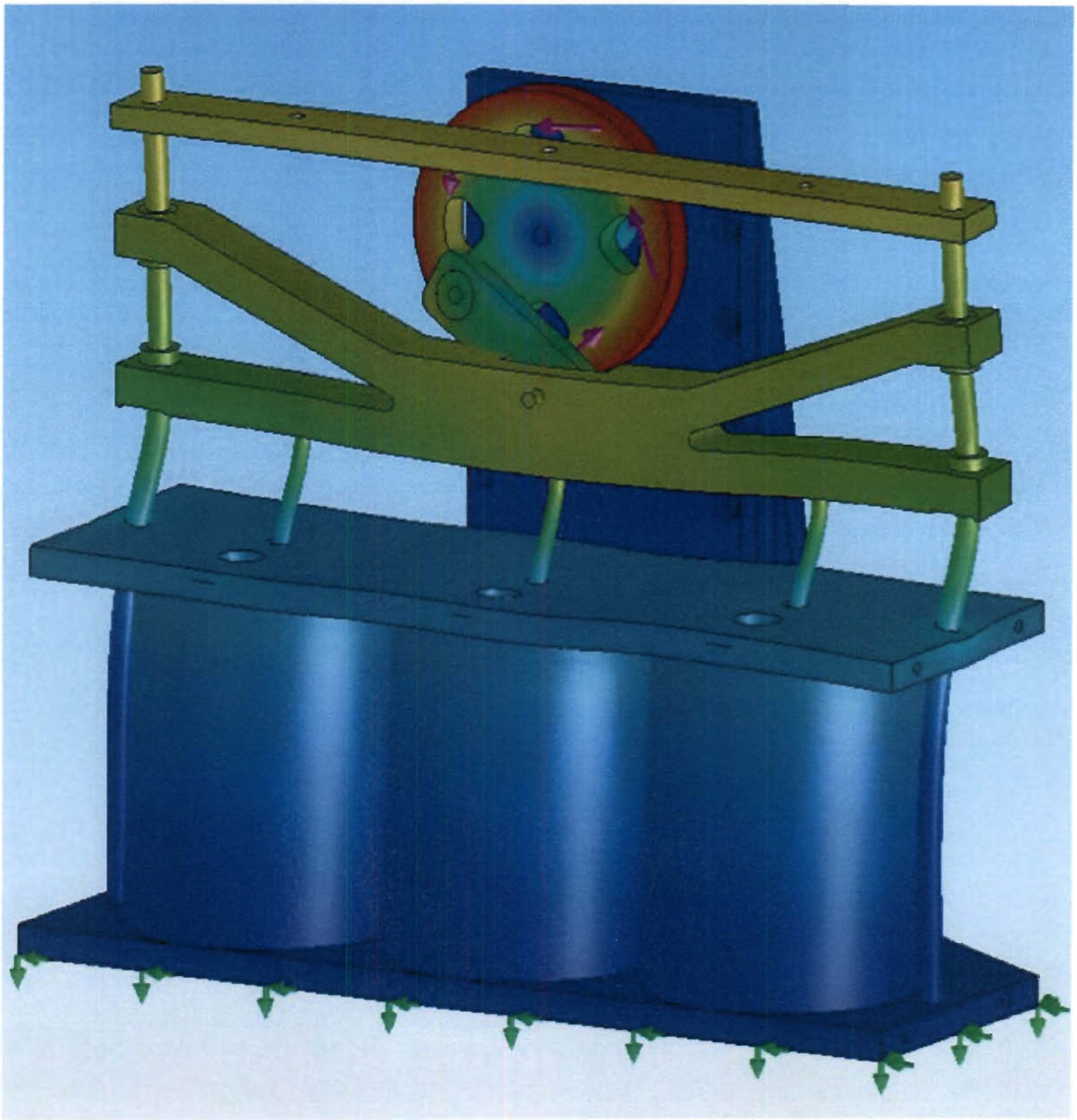

Figure 3.6: Resultant deformation plot produced (1100X magnification scale) by CosmosWorks, indicating peak deformation of ~20 μm in sliding components. Color scale is blue = 0 μm, green = 15 μm, red = 30 μm.

3.5 Sterility Challenge

The final design criterion was that the system provide a sterile culture environment for valves throughout the duration of stimulation. Thus, all developed components of the bioreactor are able to be steam sterilized. After all components of the bioreactor are removed from the autoclave, the system is assembled in a laminar flow hood using autoclaved tools and sterile gloves. The ability of the bioreactor system to provide a sterile culture environment was tested by filling the chambers with culture medium, placing the system in a humidified incubator (37° C with 5% CO_2), and enabling the drive. No valves were mounted in the system for the purposes of sterility evaluation. Medium samples were taken at one, two and four days and were plated on agar gels. Gels were inspected visually for colony formation at seven days post inoculation. No colony formation was observed indicating that no contamination of the culture environment occurred. Subsequently, the system has been run for up to 3 weeks (10 bpm, 4.2 L/min) with porcine valves loaded, and no visible signs of contamination have been observed.

3.6 Potential Directions and Future Studies

Scalability was a major motivating factor in the design of this system; therefore, the described organ culture system can easily accommodate six tissue valves. In order to accommodate large sample sizes, the mechanical valve can be replaced with another tissue valve, wherein each culture chamber would have two biologic valves mounted in opposite directions, thus permitting cyclic stimulation of six valves per bioreactor (Figure 3.1C). Furthermore, with the addition of a twin-output gearbox and an additional three culture chambers, this system will permit the culture of up to 12 tissue valves per run. This configuration has a small footprint (40 x 40 cm) for the number of samples, and even with a doubled number of culture chambers will still fit on a standard incubator shelf (Figure 3.1D). Furthermore, since the system is primarily composed of primarily two-dimensional parts, rapid fabrication of the components can be achieved using either waterjet or electrical discharge machining techniques at very low cost. Since its design, this system has been evaluated for its ability to maintain the normal state of valves *ex vivo* (described in Chapter 4). This system also will find utility for the study of tissue engineered heart valves, most likely at first with the fiber-mesh based technology employed by many labs pursuing TEHVs [33-37, 41-48, 50-54]; however, the design can be adapted to accommodate any current trileaflet TEHV scaffold, including the variety of hydrogel based scaffolds being pursued.[1, 2, 57, 69, 87, 88, 90, 110-113]) Finally, this system will find use as an organ culture system to elucidate the effects of specific biochemical agents on trileaflet valve biology and tissue remodeling, analogous to the studies on the mitral valve described in the thesis of Gheewala.[98] This wide range of bioreactor applications thus has implications for both the study of valve pathologies as well as the tissue engineering of heart valves.

3.7 Conclusions

The design of the system evolved as prototypes were fabricated and empirical results on system performance were obtained. The initial design of the system allowed the bearings to freeze, which ultimately resulted in sheared or bent parts. This failure was due to two design flaws. First, variability between the porcine valves meant that slightly different forces were exerted on the sliding plate as a result of resistance in each culture chamber, resulting in an unbalanced load. Second, the prototype of the system did not have an optimal design to prevent bearing lockup in sliding and the pinning geometry contributed to an unbalanced bending moment. This failure was examined by studying the system using the CosmosWorks software package, thus leading to the redesign of the pinning geometry and location of alignment shaft bearings. After the new design was tested in the software package, the system was fabricated and run for 3 weeks, with no lockup problems observed.

The design of a simple bioreactor system that can perform both organ culture and tissue engineering duties has yet to be realized. Many designs exist, but are inadequate for the design objectives listed here due to complicated mechanical designs, high implementation costs, lengthy setup times, low sample numbers, and complicated loading procedures. Flow loops offer the most precise control over culture conditions due to their use of pulsatile pumps and closed-loop feedback systems (both pressure and flow rate), however these systems require custom software to be created. These sorts of feedback systems require nontrivial software to both acquire and process signals before integrate them into meaningful changes in the pump's output. Furthermore, pulsatile pumps are more complicated than rotating shafts to design and maintain. Lastly, this system is the first to allow rapid loading of aortic valve roots due to the use of the spring-locked stent. This system can be pre-assembled and left under UV light in a BSC before dissection of the tissue. Since the system does not need to be completely disassembled to load the samples, it can be loaded and operational in minutes after tissue dissection.

The bioreactor presented here is simple to replicate, has the ability to scale to accommodate varying sample sizes, and uses very simple drive and control mechanisms. Limitations of this system include the lack of robust flow control and feedback systems, the requirement that all valves are subjected to the same stroke volume and flow rate, and imprecise waveform control. Improvements to controls could incorporate the inclusion of pressure or flow-based feedback sensors that would allow the servo to adjust the motion profile to achieve a desired physiologic condition. Furthermore, this system requires large volumes of media and an entire half-height incubator to run. Nonetheless, potential uses for a simple, scalable aortic valve organ culture system are wide ranging and the presented system will find many applications for study of valve biology and tissue engineering. In the subsequent chapter, the biological validation of this system will be described. Evaluation of the effect of the dynamic environment on porcine aortic valves cultured in this system helped determine if the imparted pseudophysiologic dynamic regimen was suitable for the *ex vivo* maintenance of aortic valve tissues.

3.8 Acknowledgements

This work was funded by NIH HL080080 and the Rice University NIH Biotechnology Graduate Training Program (5T32 GM008362). Thanks to Dr. R.E. Phillips at Carbomedics, Inc. for generously providing the mechanical heart valves. Thanks to Dwight Dear for aiding in fabrication. Thanks to Mike Allen for discussion on how to identify and correct the bearing lockup problem.

Chapter 4: Phenotypic Evaluation of Aortic Valve Tissue Cultured in Synchronous Bioreactor System

4.1 Introduction

Mechanical stimulation has been shown to be necessary during *in vitro* culture to promote or maintain the normal phenotype of a variety of tissues.[114, 115] Furthermore, many engineered tissues show better functional, anatomical, or mechanical development when subjected to sub- or near-physiologic mechanical cues.[53, 54, 102, 105, 116-118] Organ culture systems (also frequently referred to as bioreactors) are one such method of imparting mechanical stimuli to both engineered and *ex vivo* native tissue. Organ culture has emerged as an exciting method for the study of tissue biology, since normal tissue architecture can be readily maintained as in an *in vivo* configuration, while having a culture environment that is more controlled than it would have been in an animal model.

In contrast with monolayer or engineered tissue studies, organ cultures allow a much closer mimic of native tissue environment, since they enable 3D culture and the application various mechanical stimuli. Furthermore, the high cost, ethical concerns, and potential variability of animal studies can be substantially mitigated by the use of organ culture. Organ culture has been applied to a wide variety of cardiovascular tissues, including mitral and aortic valves.[96, 98, 115, 119, 120] Most organ culture systems, however, have been used for short durations (usually 24, 48, or 96 hours) or non-sterile investigations of tissue mechanics.[97, 103, 104, 109, 121-124] However, culture of portions of the valve leaflet has been performed for longer durations (up to fourteen days).[116] The system designed in the course of this research (as described in Chapter 3) has been shown to provide sterile culture well past the previous 48-hour mark and has scalability to accommodate large sample sizes with low cost and low experimental setup time. In the previous chapter, the design and physical characterization of a novel piston-based bioreactor system for synchronous stimulation of aortic valves was described. In this chapter, the effect of cyclic mechanical stimulation on the tissue phenotype of aortic valves cultured in this system for up to fourteen days is detailed using mechanical, biochemical, and histological evaluations.

4.2 Study Design and Statistical Methods

In order to determine the effect of dynamic culture of porcine aortic valves in the designed bioreactor, three groups were prepared. Porcine valves were chosen due to their anatomic similarity to human valves and the relative ease of acquiring sufficient samples (in comparison with human valves). Two experimental groups, static culture and dynamic culture, were compared with a control group of freshly excised tissue. This setup allowed the establishment of "baseline" values of the experimentally measured parameters for native valve tissues that could be used to benchmark the effect of *ex vivo* aortic valve leaflet culture. Using these groups, pairwise comparisons elucidating the relative effect of static culture vs. dynamic culture could be determined as well as the changes from

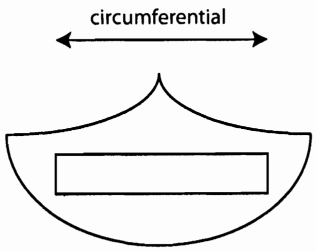

Figure 4.1: Illustration of leaflet showing direction of strips taken for mechanical testing.

normal tissue. One leaflet per aortic valve was retained for histology, leaving the other two leaflets for mechanical testing and biochemical evaluations. The leaflets used for mechanical testing were cut into circumferential strips and subjected to flexure testing or tensile testing. After mechanical evaluation, the leaflet strips were enzymatically digested and subjected to biochemical evaluation of the ECM components. Sample sizes were calculated using an on-line statistical power calculator[125], with detectable change set at 40%, assumption of sample population standard deviation set at 25% (calculated from literature investigating flexural stiffness of bioprosthetic and native AV) and power threshold set at 80%.[126, 127] This level of detectable change was calculated from reported stiffness values from mechanical testing studies of aortic valve leaflets.[108] Statistical analyses of quantative and semi-quantative data were performed using JMP (SAS Software, Cary, NC). Where appropriate (flexural & tensile stiffness, biochemical analyses), either one- or two-factor ANOVA was performed and data was fit to a least squares model. Sample group means were compared with post-hoc Tukey-Kramer HSD (Honestly Significant Difference) or Dunnett's comparison with control where α=0.05. When significance was not seen, but the p value was less than 0.2, it was commented on as a trend. When data was non-normally distributed (semi-quantative IHC analyses), ordinal logistic regression was performed simultaneously to Kruskal-Wallis tests to verify the consistency of results obtained from Kruskal-Wallis tests. Ordinal logistic regression did not show differences from Kruskal-Wallis tests, therefore post-hoc means comparisons were carried out with Wilcoxon or Steel Methods (non-parametric pairwise means comparisons, all pairs or with control, respectively). When represented visually, data is expressed as mean ± standard error.

4.3 Bending Tester Design

One of the primary objectives of this thesis work was to evaluate the flexure stiffness of hydrogel materials in comparison with native tissues in order to determine their suitability as a tissue engineered heart valve scaffold, since hydrogel flexure was unreported. In order to measure the flexure properties of native tissue and hydrogel samples, a three-point bending tester was designed. Before testing hydrogel materials (described in Chapter 5), native leaflets were tested to establish design criteria for the hydrogel scaffolds. For the organ culture phase of the research, the tester was also used to investigate the effect of the dynamic (bioreactor) culture environment on the bending properties of aortic valve leaflets. The design of the bending tester and general method of bending stiffness calculation is described here.

A custom fabricated bending tester (design adapted from Gloeckner *et al.*) was used to conduct 3-point bending tests on tissue samples (Figure 4.2 and Figure 4.3).[126] The physical design of this system was performed in conjunction with two undergraduate students, Alex Brewer and Steve Xu. Further detail of the design evolution of this system can be found in Appendix I. This system consists of a stepper motor (Figure 4.2A) coupled to a micropositioner (Figure 4.2B, Newport SM-13), which was fixed to a linear stage (Figure 4.2C, Newport 460A) that together allowed 13 mm of total system linear displacement. Motion of the system was achieved through a custom LabView program that allowed control of the system displacement, acceleration, deceleration, and strain rate via RS-232 communication to the stepper controller (Figure 4.4).

The system was visualized with a varifocal lens (Computar Ganz, Commack, NY) mounted to a CCD camera (DFC 320, Leica Microsystems, Bannockburn, IL) that captured images every 25 ms using Image-Pro Express (Media Cybernetics, Bethesda, MD). Optical tracking was used to detect sample deformation and the location of the loading and reference rod. Deformation tracking was achieved by sifting small graphite particles onto the top of the sample with a grid mesh, reference rod and a calibrated flexure bar (Figure 4.3).[52] Since the stiffness of the flexure bar was known, by calculating its displacement relative to a fixed reference point (reference rod) the force applied to the sample could be determined (Figure 4.5).[128-132]

Bending stiffness of all samples was calculated by application of Bernouilli-Euler beam bending theory. This bending theory has been routinely used to measure the stiffness of heart valve prostheses and tissues.[52, 58, 126, 127, 133-139] The characteristic assumptions of Bernoulli-Euler beam bending theory include the following:

1. The beam is in pure bending, with no shear force or torsional or axial loading.
2. The material is isotropic and homogeneous.
3. The material is linearly elastic.
4. The beam is straight with a homogenous cross section.
5. The beam has an axis of symmetry in the plane of bending.
6. The proportions of the beam are such that it will fail by bending rather than crushing, wrinkling, or buckling.
7. Cross sections of the beam remain in plane (no shear) during bending.[140]

While heart valve leaflets do not satisfy all of these characteristic assumptions (particularly number 2), this model has successfully been applied to aortic valve tissues and biomaterials.[52, 58, 126, 127, 133-139] Shearing of cross sections is neglected in Bernoulli-Euler theory, and Timoshenko theory would account for this shearing of beam cross-sections. Application of Timoshenko theory may ultimately be needed for thicker, laminate structures; however results would no longer be directly comparable with the literature if this analysis model is chosen.

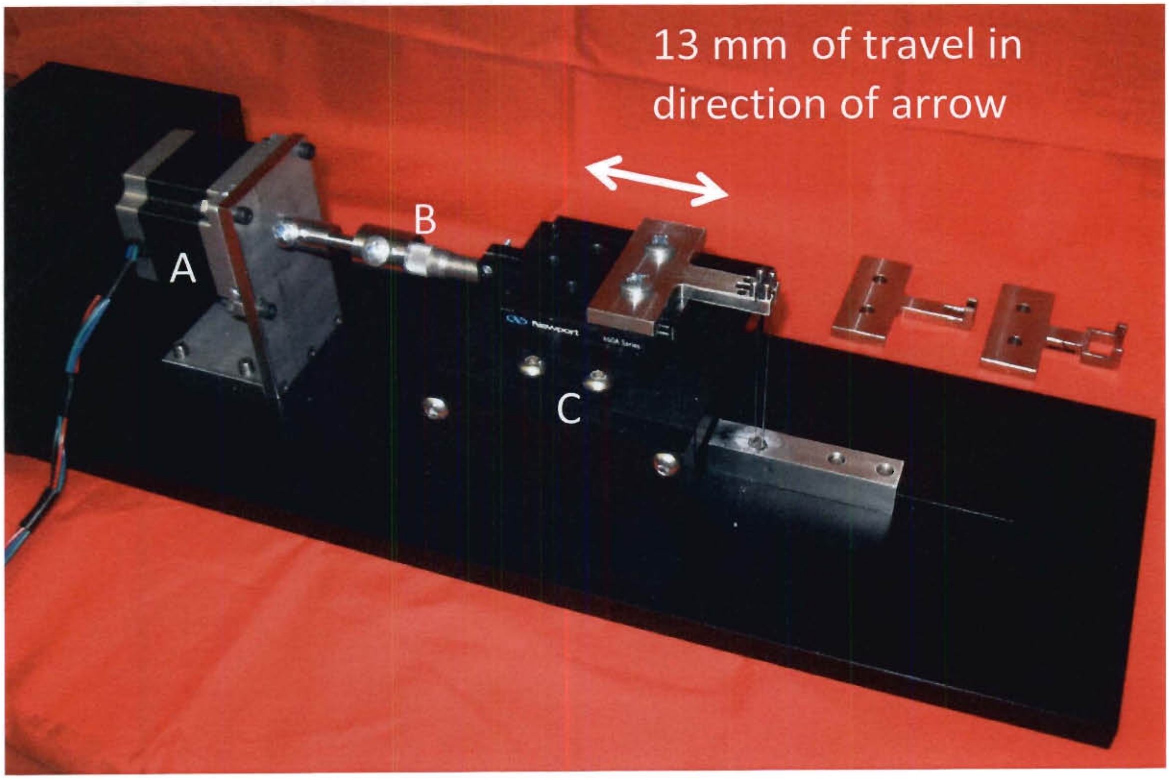

Figure 4.2: Isometric view of bending tester. Stepper motor (A) is coupled to a micropositioner (B), which is mounted to a linear stage (C) resulting in system linear displacement capability of 13 mm. Other loading rigs permitting various sample thicknesses and widths can be seen in the background.

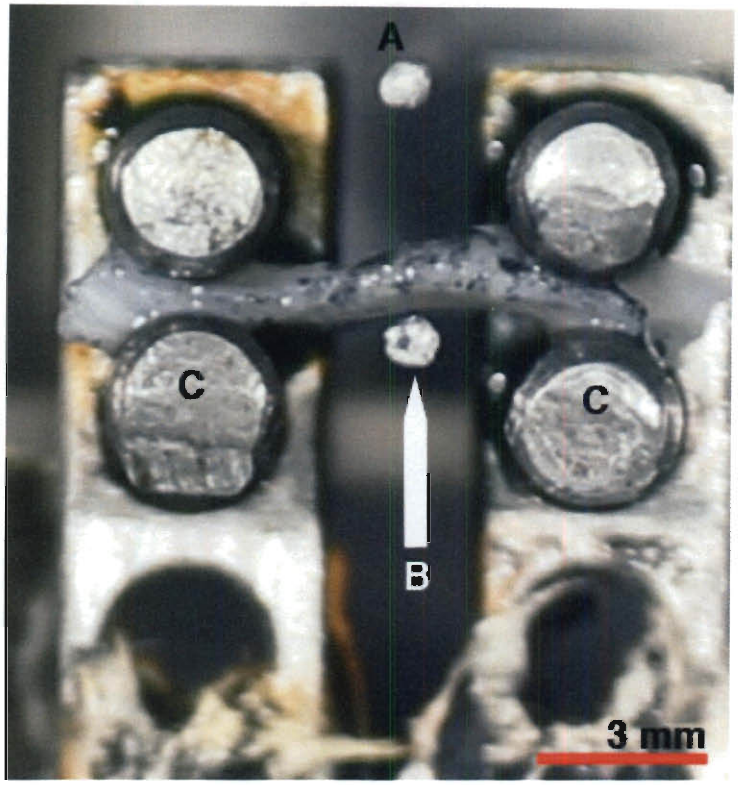

Figure 4.3: Top-down view of AV leaflet loaded into bending tester. Letters denote (A) reference rod, (B) flexure bar, (C) loading posts. Leaflet is supported by loading posts and can freely slip, so rotation can occur (no tensile load applied).

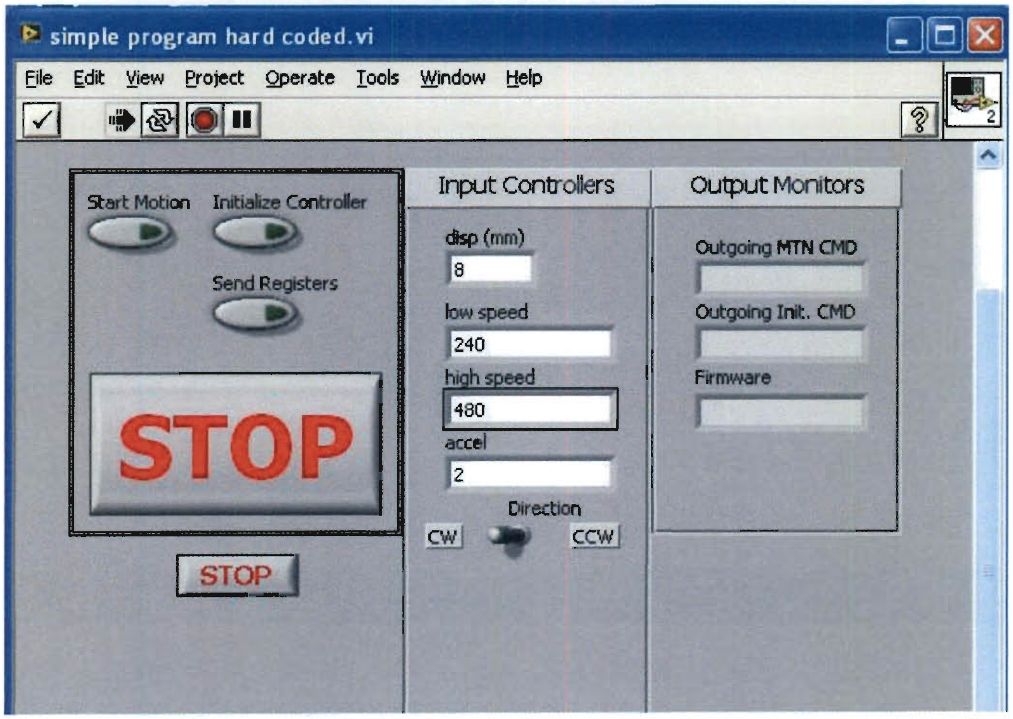
simple program hard coded.vi
File Edit View Project Operate Tools Window Help
Start Motion
Initialize Controller
Send Registers
STOP
STOP
Input Controllers
Output Monitors
Outgoing MTN CMD
Outgoing Init. CMD
Firmware
Direction
CW
CCW

disp (mm) 8
low speed 240
high speed 480
accel 2

Figure 4.4: Software interface for controlling bending tester. Total system displacement is input (in mm), along with shaft velocity (in counts per minute) and acceleration.

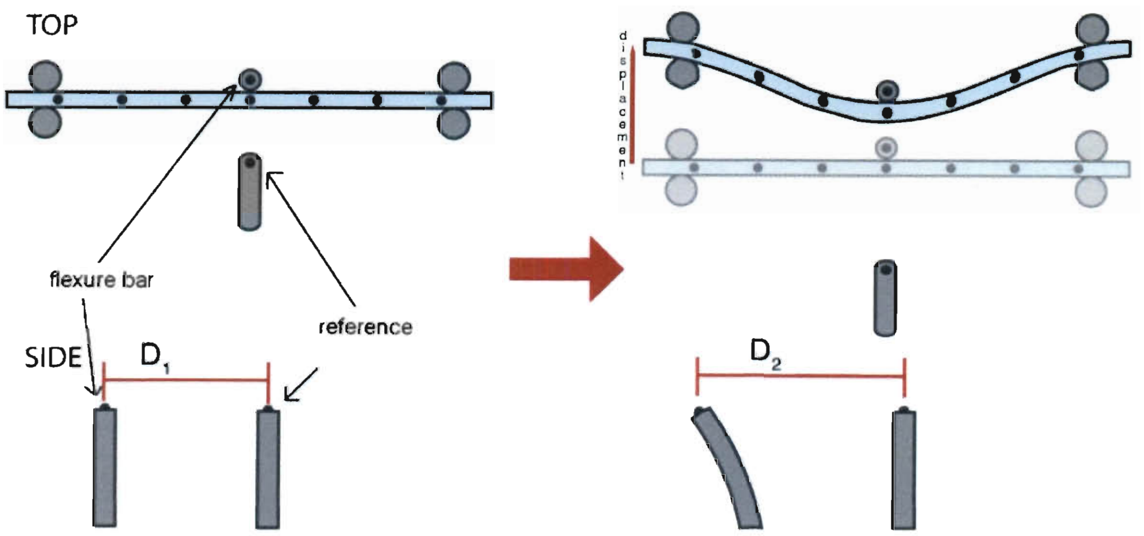

Figure 4.5: Illustration showing the use of a calibrated steel bar to measure load applied to a sample in three point bending. The flexure bar bends and the relative displacement to the reference rod is recorded.

A custom Matlab program, adapted from digital image correlation code by Chris Eberl *et al.*, was used to track the locations of markers applied to the sample, flexure bar, and reference rod (data processing script available in Appendix VII).[141] After determining X-Y coordinates for the markers on the sample, a least-squares regression to a quadratic line was performed to quantify the deformation of the sample in each image.

Equation 4.1: Quadratic line equation.

$$y = ax^2 + bx + c$$

Using derivatives of this line, the curvature of the sample was calculated using the following equation:

Equation 4.2: Curvature equation. Y is the quadratic fit.

$$k = \frac{y''}{[1 + (y')^2]^{\frac{3}{2}}}$$

The deflection of the calibrated flexure bar was also determined from each image and used to calculate the force applied to bend the sample. The maximum radius of curvature used was 4 mm, which corresponded to a maximum applied force of ~12 mN. It is important to note that in all samples (native tissue, single layered PEGDA, and quasilaminates), this resulted in large deformations, for which neither Bernouilli-Euler nor Timoshenko analysis account. The moment was then calculated using reaction forces at the arms:

Equation 4.3: Moment equation. M is moment, F_x and F_y are the x and y components of the applied load, respectively and x and y are the orthogonal distances from the point of applied force to the loading posts.

$$M = F_x y + F_y x$$

Finally, the calculated moment and sample deformation were used in the Bernoulli-Euler moment curvature relationship, and the effective stiffness of the sample was calculated (Figure 4.6).

Equation 4.4: Bernouilli-Euler moment curvature equation, where E_{eff} is stiffness, I is moment of inertia, and K is change in curvature (Equation 4.2).

$$M = E_{eff} I \Delta K$$

where the moment of inertia of a beam in bending is used (the thickness of the sample is greater than 1/10th of the length)

Equation 4.5: Moment of Inertia equation, where t is sample thickness and w is height.

$$I = \frac{1}{12} t^3 w$$

Rearranging the above equations gives:

Equation 4.6: Bernouilli-Euler equation rearranged to calculate stiffness.

$$E_{eff} = 12 \frac{M \Delta K}{t^3 w}$$

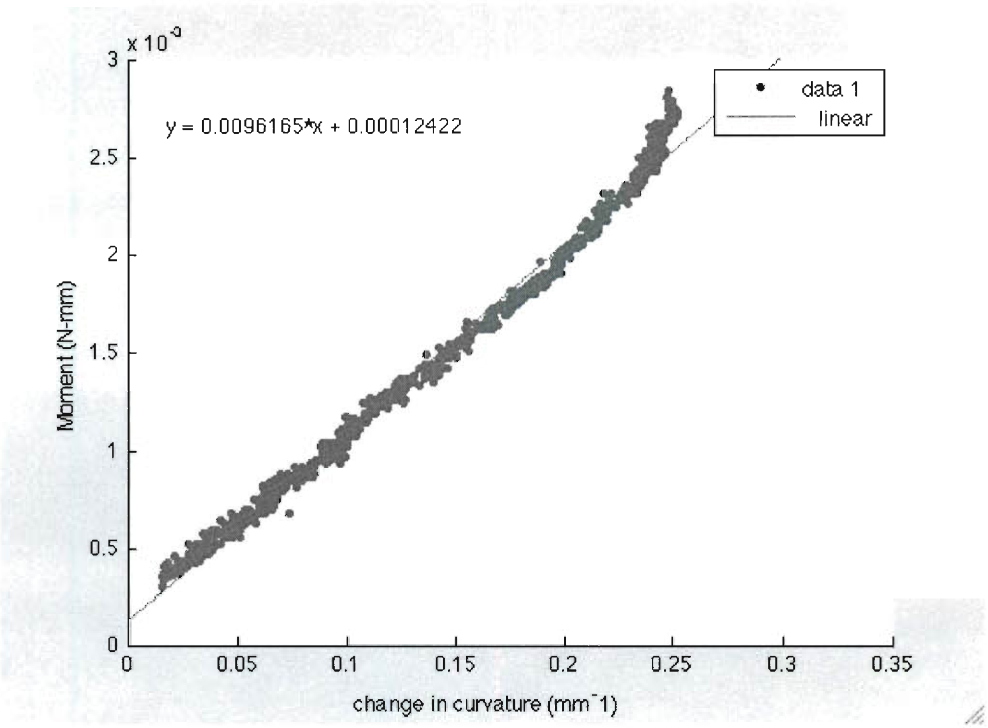

Figure 4.6: Sample curve showing the moment-curvature relationship and the linear fit (from which the stiffness is calculated).

4.4 Materials and Methods

All chemicals were purchased from Sigma-Aldrich unless otherwise noted.

4.4.1 Preparation of Tissue and Bioreactor Loading

The bioreactor system was preassembled in a biological safety cabinet using sterile tools and gloves before obtaining tissues. By preassembling the bioreactor into two main subassemblies (the base, motor support, and culture chambers on the bottom piece; the lid, alignment shafts, pistons, and cam-crank on the top) the system was ready for quick loading. After preassembly, the bioreactor was placed under UV light until the tissues were prepared for loading. Whole porcine hearts (from adult pigs) were obtained from a local abattoir (Fisher Ham and Meat, Spring, TX). The hearts were sprayed superficially with 70% ethanol and then extensively rinsed with sterile PBS to remove any remaining blood clots. Whole aortic roots were dissected from the hearts using sterile instruments and aseptic technique. After the root was dissected, each root was rinsed extensively and soaked in a solution of sterile PBS supplemented with 10% penicillin-streptomycin-amphotericin (Cellgro, Manassas, VA). For the "baseline" group, leaflets were then dissected out of the root and immediately subjected to the battery of tests and assays described in the sections 4.4.3, 4.4.4, and 4.4.5. For both the static culture and dynamic culture groups, the roots were sutured to the custom designed stent (described in section 3.2) with 2-0 Prolene sutures (Ethicon, Minneapolis, MN) and a custom fabricated silicone gasket was sutured around the ventricular annulus of the root. Next the root/stent assemblies (Figure 4.7) were either placed in culture flasks or snap-fit into the piston of the bioreactor system, respectively, depending on their culture group. At least 6 aortic roots were used for each group (n ≥ 6 valves or 18 leaflets per group for all culture conditions).

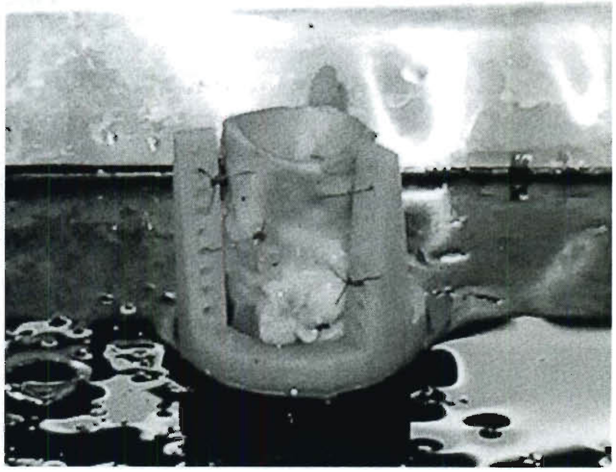

Figure 4.7: Porcine aortic root sutured to custom designed stent and silicone gasket (not visible).

4.4.2 Static and Dynamic Culture

Culture medium was prepared with DMEM supplemented with 10% bovine growth serum (BGS, Hyclone, Logan, UT) and 2% penicillin-streptomycin-amphotericin B solution (Cellgro, Manassas, VA). The static culture specimens were placed in culture flasks containing 250 mL of culture medium; for this group, medium was changed every 3-4 days. Dynamic culture specimens were placed in the bioreactor culture chambers, each of which was then filled with 600 mL of medium. For this group, medium was changed every seven days. After the bioreactor assembly was placed in the humidified incubator (37°C, 5% CO_2), the motor was enabled. The motor was controlled through a simple custom program that communicated with the servo drive via RS232 or Ethernet networking. A move profile was created with constant velocity and fixed acceleration and deceleration parameters. The software was set to produce a 2.1 rpm cam revolution, that when coupled with the 6.8 cm stroke length from the mechanical design of the system, corresponded to a ~1.5 L/min flow rate through the valve.

4.4.3 Mechanical Tests

After completion of the culture period (7 or 14 days), the roots were removed from their respective culture chambers and the aortic valve leaflets were dissected from the aortic root. Baseline values were established from freshly dissected tissues. Mechanical characterization of the tissue was performed using uniaxial tensile testing as well as three-point bending.

Uniaxial tensile testing was performed with a Bose Enduratec ELF 3200 system. A load cell (Honeywell Sensotec, Morristown, NJ) with capacity of ± 50 N was used to acquire load data while displacement data was obtained from the crosshead position. Data was acquired at 1kHz. Samples were preconditioned for 25 cycles at 0.5 Hz, allowed to rest for 15 s, and cycled again for 3 cycles at the same rate. The samples were then pulled to the maximum displacement of the system (12 mm) at a strain rate of 0.1 mm/s and the Young's modulus of the tissue was measured from the linear region curve corresponding to the final crosshead extension. This preconditioning regimen allows for the aortic valve leaflet's material memory to reset and repeatable measurement of material properties.[142, 143]

Flexural testing of the tissue was performed using the previously described three-point bending apparatus (section 4.3) and digital image correlation to determine the instantaneous effective bending stiffness of the tissue. This apparatus was used to deform the sample by pulling the center of the sample against a flexure bar at a strain rate of 0.02 mm/s to a displacement of 8 mm. Images of the sample deformation and graphite particles' movement were captured at 5 frames per second by a CCD camera (Leica DFC320) mounted over the apparatus. $N \geq 5$ for all flexure groups. After mechanical testing, samples were enzymatically digested for biochemical assays (described below).

4.4.4 Biochemical Assays

Samples used in biochemical assays were first assessed for wet weight, lyophilized for 48 hours and then assessed for dry weight. The samples were subsequently rehydrated with 100 mM ammonium acetate solution, minced, then digested with 100 uL of proteinase K solution (EMD Pharmaceutical, Durham, NC, 10 mg/mL in 100 mM ammonium acetate) for 16-48 hrs at 60 °C. The enzyme solution was then deactivated by immersing the tubes in a 100 °C water bath for 5 minutes. After tissue digestion, quantative assays to determine hydoxyproline content and total glycosaminoglycan content were performed.

Collagen content was indirectly measured using a hydroxyproline assay, since hydroxyproline is a major component of the collagen triple helix.[144, 145] Significant variability observed with more modern biochemical collagen assays was observed, so a reliable hydroxyproline assay was chosen as a proxy for collagen content. It is known that in collagen type I heterotrimer ($[\alpha_1]_2[\alpha_2]_1$), hydroxyproline constitutes roughly 10.4% of total residues. In collagen type III ($[\alpha_1]_3$), hydroxyproline constitutes a slightly higher amount of total residues, ~12.5%, therefore hydroxyproline content is a good proxy for total collagen content.[146, 147] Aliquots of proteinase K digested leaflets were hydrolyzed with 6 N HCl at 115 °C for 4 hours in glass vials sealed tightly with Teflon caps. After hydrolyzing the samples, the vials were removed from the heating block, allowed to cool, and uncapped, and then the HCl was boiled off at 115 °C for 2 hours. The hydrolyzate was then dissolved in ddiH_2O and samples and standards (prepared from a 1.0 mg/mL stock solution of trans-4-hydroxy-L-proline in ddiH_2O) were added to glass tubes in duplicate. Chloramine T (30 mM *N*-Chloro-*p*-toluenesulfonamide sodium salt hydrate, 10% v/v n-propanol in 0.16 M citric acid, 0.8 % glacial acetic acid, 0.58 M sodium acetate, 0.4 M NaOH, 20% n-propanol) was added to samples at room temperature, vortexed, and incubated for 20 minutes. Aldehyde/Perchloric acid solution (1.17 M p-dimethyl-amino-benzaldehyde in 70% v/v n-propanol and 70% perchloric acid solution) was added to all samples and standards, vortexed until no *schlieren* were visible and incubated at 60 °C for 15 minutes. Samples and standards were then vortexed again, aliquoted in triplicate into a 96-well plate and read on a spectrophotometer (Spectramax M2, Molecular Devices, Sunnyvale, CA) with absorbance read at 558 nm. Experimental absorbance measurements were compared with a standard curve derived from hydroxyproline standards, and were statistically analyzed to compare groups.

Glycosaminoglycan (GAG) content was assessed using an uronic acid assay for total GAGs.[148] GAG content has been shown to be a good indicator of the leaflet's synthetic ability in response to mechanical stimuli.[104] The uronic acid assay was used to colorimetrically quantify GAG amounts. Aliquots of digested leaflets were added to sulfuric acid tetraborate (12.5 mM sodium tetraborate in concentrated sulfuric acid) at 4 °C. This solution was then heated for 5 minutes at 100°C in a heating block. Samples were then cooled using a room temperature water bath for 5 minutes. 250 uL of solution was then removed from each sample to serve as a blank. The remainder of the solution was treated with 10 μl of hydroxyphenyl solution (0.15% m-hydroxyphenol in 0.5% NaOH). Blanks and samples were aliquoted in triplicate into a 96-well plate and read on a spectrophotometer (Spectramax M2, Molecular Devices, Sunnyvale, CA) with absorbance read at 532 nm and background subtraction performed at 750 nm. A standard curve of using known quantities of glucuronic acid was created and experimental sample concentration was back calculated from this curve.

4.4.5 Histological Techniques

Leaflets retained for histology and immunohistochemistry were fixed with 10% formalin, dehydrated through a series of graded alcohols and xylene (VWR, Radnor, PA), embedded in paraffin, and sectioned into 5 μm slices using a microtome. Sections were affixed to glass slides for Movat pentachrome staining and immunohistochemistry (IHC). Movat pentachrome staining was accomplished using serial baths of Alcian Blue (1% w/v Alcian Blue and 0.09% v/v acetic acid in ddiH_2O, Acros Organics, Geel, BE), alkaline alcohol (10% ammonium hydroxide, 4.5% ddiH_2O, 85.5% ethanol), Voerhoff's Hemotoxylin (5% w/v hemotoxylin in ethanol; 2% w/v iodine, 4% potassium iodide in ddiH_2O; 10% w/v ferric chloride hexahydrate in ddiH_2O; mixed 2:1:1 volumetrically, respectively), ferric chloride (2% w/v in ddiH_2O), aqueous sodium thiosulfate (5% w/v in ddiH_2O), Crocein Scarlet (0.1% w/v Brilliant Crocein MOO and 0.5% v/v acetic acid in ddiH_2O; 0.1% w/v acid fuschin and 0.5% v/v acetic acid in ddiH_2O; mixed 1:1 volumetrically; Acros Organics), 0.5% acetic acid, two changes of phosphotungstentic acid (5% w/v in ddiH_2O), pure ethanol, Safran (6% w/v in ethanol, Poly Scientific, Bay Shore, NY), and pure ethanol. This protocol stains ECM components as follows: elastic fibers – black, collagen – yellow, GAG – blue, fibrin – red, muscle – red. Movat staining was used to identify the relative location of ECM components and layer structure of the leaflet.

The presence of elastin and collagen type III was verified by immunohistochemistry. All samples were run concurrently for all semi-quantative IHC analyses to eliminate batch-to-batch variance in observed intensity. Antigen retrieval pretreatment was performed at 80 °C for 30 minutes with citrate antigen decloaker solution (Biocare Medical, Concord, CA) for collagen type III or 0.1% chymotrypsin and 0.1% $CaCl_2$ (w/v) in diH_2O for elastin. Peroxidases were then quenched with 3% H_2O_2 (this step is unnecessary for elastin and was skipped) and the samples were blocked with 0.1% goat serum buffer for 1 hour at room temperature. Primary antibodies were added in buffer with 0.1% bovine serum albumin and incubated for 1 hour at 37 °C (collagen III: 1:100 dilution Rb Anti-Col III; elastin: 1:150 Ms Anti-Elastin, Abcam, Cambridge, MA). Primary antibodies were removed with two PBS rinses and then biotinylated secondary antibodies were added at 37 °C for 1 hour (collagen III: 1:1000 Goat Anti-Rb; elastin: 1:500 Goat Anti-Ms, Jackson ImmunoResearch Laboratories, West Grove, PA). A chromogen reaction showing antibody location was visualized using Elite Vectastain ABC and diaminobenzidine kits (Vector Laboratories, Burlingame, CA). A hematoxylin counterstain was performed after the chromogen reaction and slides were sealed with mounting media and a coverslip. Slides were then imaged on a Leica microscope and images acquired from a Leica DFC320 CCD in Image Pro Express (Media Cybernetics, Bethesda, MD).

Image analysis was performed with a series of custom ImageJ scripts to eliminate the need for slide blinding and to mitigate potential viewer bias. First, slides were scanned with a Pathscan Enabler IV (Meyer Instruments, Houston, TX) at 7200 DPI in RGB color space. Semi-automated image processing and analysis was performed with ImageJ64. A brief description of the protocol follows, more detail can be found in Appendix VIII. First, background subtraction and color correction were performed using the built-in rolling ball method (pixel radius 50 mm, light background, sliding paraboloid). Next, the hematoxylin and DAB colors were deconvolved into separate images with only one color.[149, 150] Single-color images were converted to 8-bit greyscale images. Each image was then thresholded using with the upper bound of brightness from the on-slide negative control. A mask from the thresholded image was created and intensity (DAB) was measured within the mask area. These results were exported to Microsoft Excel, where the intensity was then binned into 5 bins across the dynamic range of intensities (e.g., if the darkest staining observed had a luminosity of 100, the dynamic range was 255-100, or 155; which resulted in a bin width of 51 intensity units).

4.5 Results

4.5.1 Mechanical Testing Results

At seven and fourteen days, there was no difference in tensile stiffness between the static and dynamic culture regimens (Figure 4.8, all mechanical testing was in the circumferential direction). However, at fourteen days, the statically cultured leaflets were significantly stiffer than either culture condition at seven days ($p < 0.01$). In addition, the stiffness values obtained here are much lower than recently published results (~10 MPa) by other groups, but test method and preconditioning can greatly affect the observed modulus.[58]

Flexural stiffness of freshly excised (baseline) leaflets showed no difference from the samples cultured in the bioreactor at seven days (Figure 4.9). Statically cultured samples at seven days were significantly less stiff than baseline tissue and dynamic samples ($p < 0.05$ and $p < 0.001$, respectively). However, at fourteen days, both the dynamic and static culture regimens resulted in lower flexural stiffness than baseline samples ($p < 0.05$). Additionally, at this time point, stiffness in dynamic and statically cultured samples was no longer different.

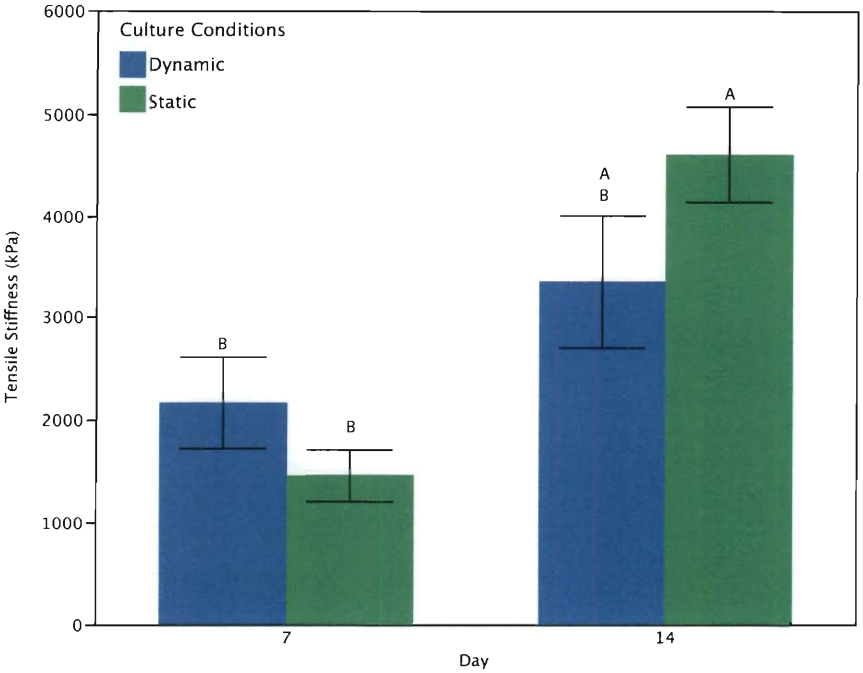

Figure 4.8: Tensile stiffness of leaflets cultured for seven days. Statically cultured leaflets at day 14 were significantly stiffer than leaflets in either culture regimen at day 7 ($p < 0.01$). $N \geq 6$ for all groups.

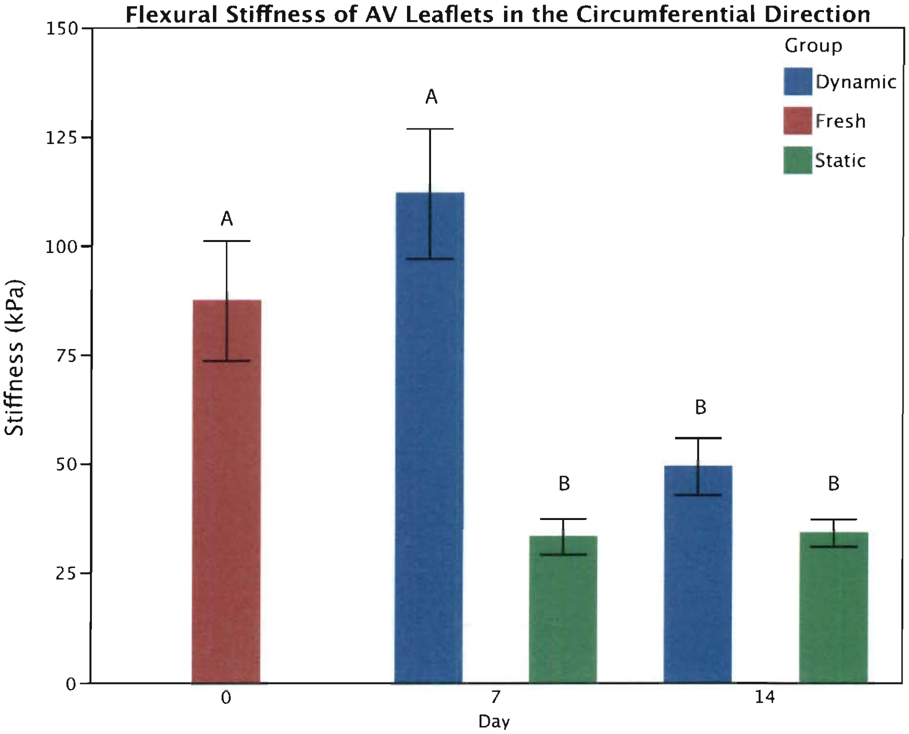

Figure 4.9: Flexural stiffness of porcine aortic valve leaflets in dynamic culture (bioreactor) or static culture in comparison with freshly excised (baseline) tissue. Day 7 dynamic culture showed no difference from freshly excised tissue, and all other groups were significantly less stiff than freshly excised tissue.

4.5.2 Biochemical Results

Hydroxyproline content (normalized to dry weight of sample) of valves in static culture for one week decreased in comparison to freshly excised valves ($p < 0.05$), however, valves exposed to dynamic culture showed no change in hydroxyproline content in comparison with freshly excised tissue (Figure 4.10). At two weeks, there was a trend showing that hydroxyproline content decreased in statically cultured samples compared with baseline values ($p < 0.13$). In contrast, samples cultured in the bioreactor (dynamic culture) showed significantly more hydroxyproline content at day fourteen than all other groups ($p < 0.05$).

Total glycosaminoglycan content was unchanged in comparison with baseline for either culture condition at seven days (Figure 4.11). Both dynamic and static cultured samples showed higher total GAG content at day fourteen than at baseline and at day seven values ($p < 0.001$), although there was no difference between the statically and dynamically cultured samples.

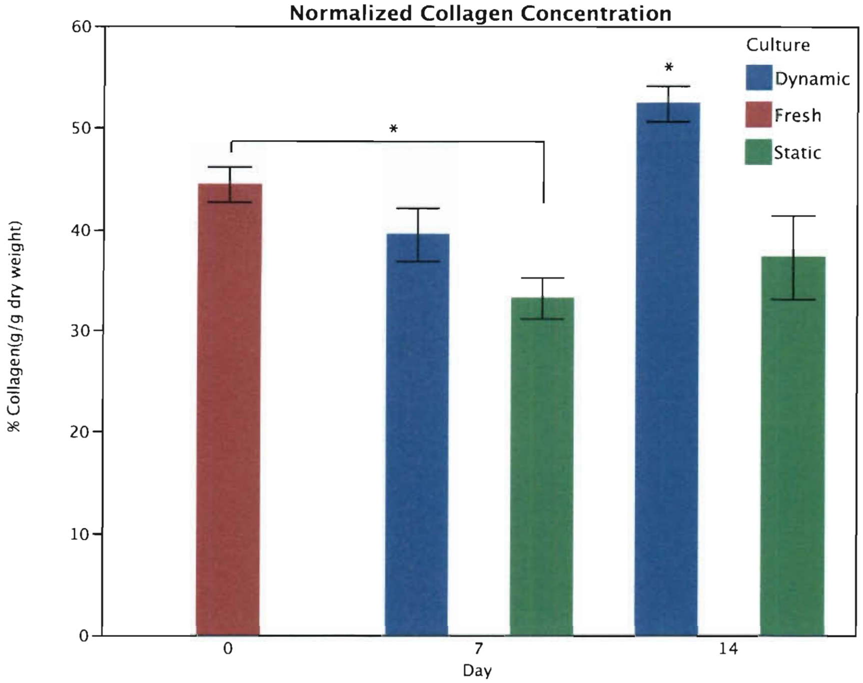

Figure 4.10: Collagen content of porcine aortic valve leaflets, as measured by hydroxyproline content normalized to dry weight. In dynamic culture, the trend showed no change in hydroxyproline content at day seven and by day 14, hydroxyproline content was increased. There was virtually no change in the trend of collagen content across the duration of culture for statically cultured leaflets. * denotes statistically significant difference where p < 0.05.

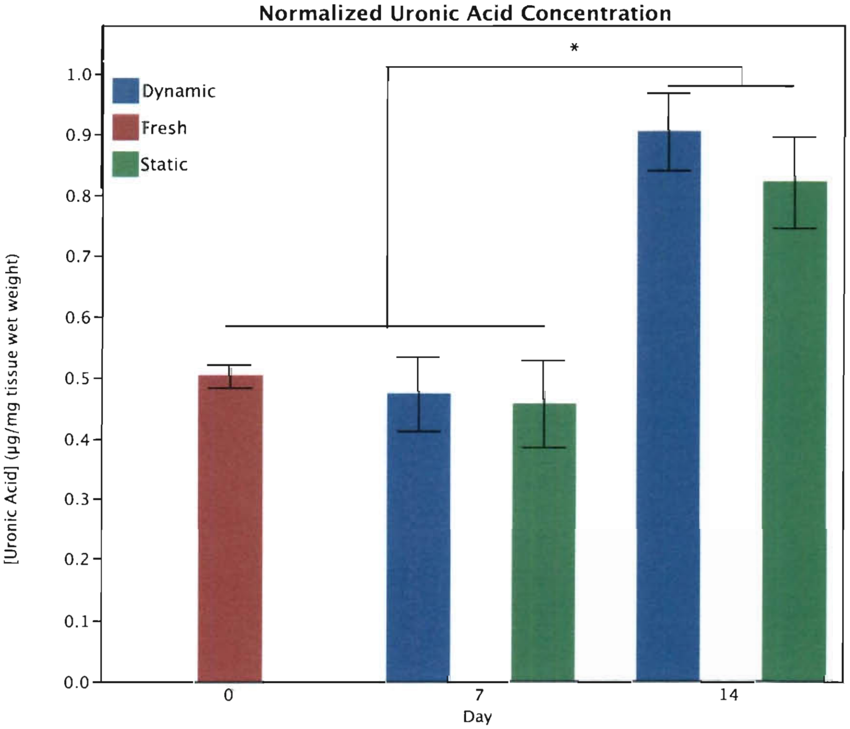

Figure 4.11: Uronic acid content of porcine aortic valve leaflets, normalized to wet weight of the tissue. * denotes statistically significant difference with p<0.001.

4.5.3 Histological Characterization

Movat staining was used to reveal the distribution of ECM components throughout the leaflet (Figure 4.12). Freshly excised tissue showed distinct collagen staining in the fibrosa (yellow), a GAG-rich spongiosa (blue), and distinct elastin banding in the fibrosa (black). During static culture, the leaflet showed collagen distributed throughout the layers at both seven and fourteen days. At both time points, the statically cultured leaflets maintained distinct staining for elastin (black) in the ventricularis. Statically cultured leaflets maintained GAG staining (blue) at day seven and fourteen, however it appeared less intense at day seven than fourteen. Both of these effects were noted by Barzilla *et al.* in static organ culture of mitral valve leaflet strips.*[115]* Additionally, GAG staining appeared primarily in the spongiosa of statically cultured leaflets. In the dynamically cultured leaflets, collagen was seen across all three layers of the leaflet at seven and fourteen days and it appeared to be mainly located in the fibrosa, however, the layered structure appeared less distinct at day fourteen. Furthermore, at day seven, it appeared that dynamic culture resulted in the appearance of elastin staining in the fibrosa, which did not appear to be maintained at day fourteen. Distinct blue GAG staining was seen in both day seven and fourteen dynamically cultured samples. Morphologically, the leaflets appeared to thin at day fourteen of either culture regimen, particularly in the cusp. Additionally, they appeared to be less intact than earlier time points. The location and abundance of elastin and collagen type III was further characterized by immunohistochemical techniques.

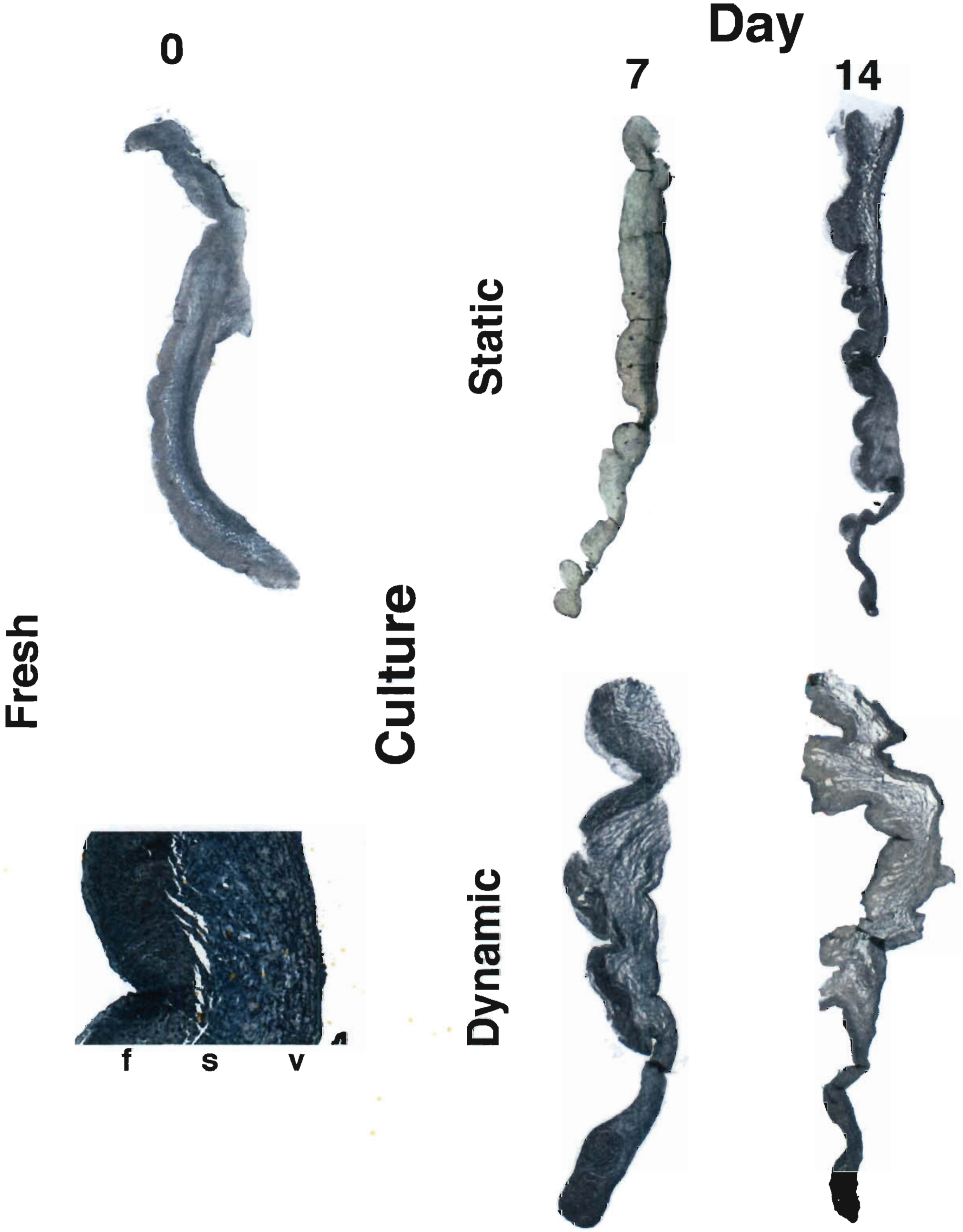
Day
0
7
14
Fresh
Culture
Static
Dynamic
f
s
v

Figure 4.12: Movat pentachrome stain of porcine aortic valve leaflets. Black corresponds to elastin, yellow to collagen, green/blue to proteoglycans and glycosaminoglycans, dark blue to cell nuclei, and red to muscle. Orientation of ventricularis, spongiosa, and fibrosa is the same across all samples (denoted by f, s, and v in high magnification inset).

Immunohistochemical staining revealed the presence of elastin across all layers of the valve during seven days of dynamic culture, however, at fourteen days of dynamic culture, it appeared to be localized to the ventricularis, where it is normally most abundant (Figure 4.14). Semi-quantitative analysis revealed that elastin staining intensity was significantly decreased at both seven and fourteen days in dynamic culture in comparison with baseline tissue (Figure 4.13). Static controls showed significantly lower elastin (by intensity) at day fourteen ($p < 0.05$ for all significant comparisons). The primary location of elastin in statically cultured samples appeared to be in the ventricularis.

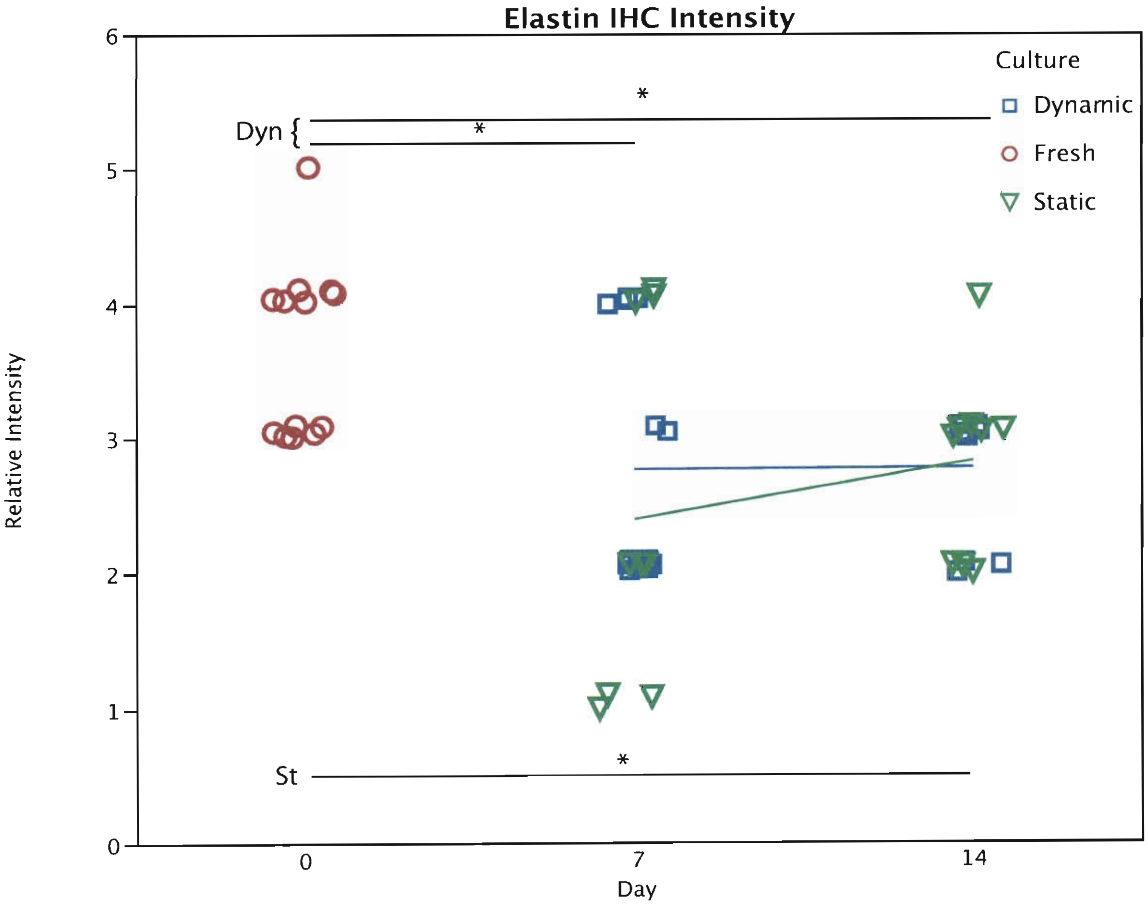

Figure 4.13 - Relative intensity of elastin DAB staining in leaflets as a function of multiple days of culture. N≥6 for all groups and * denotes significance with $p < 0.05$.

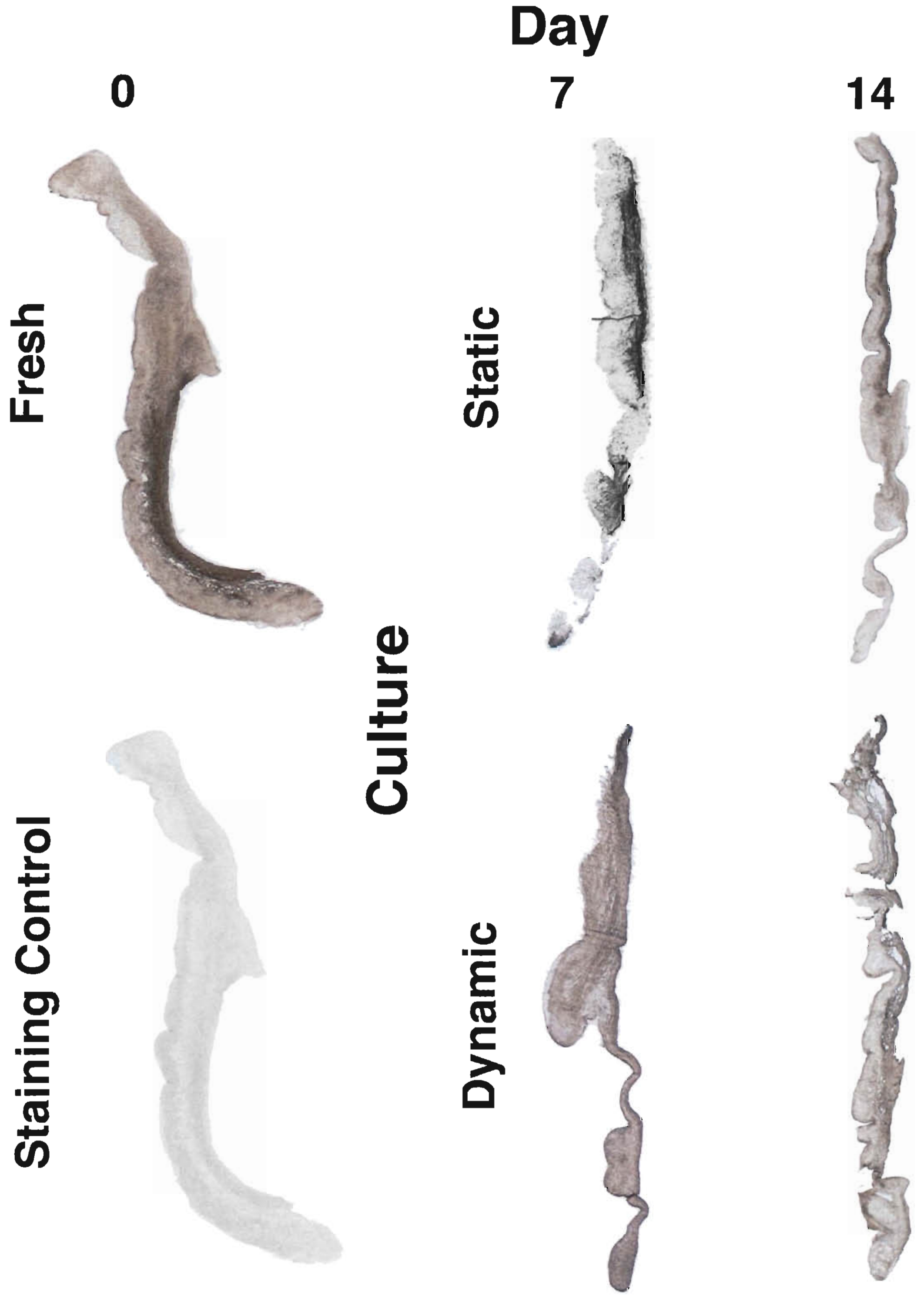
Day
0
7
14
Fresh
Static
Culture
Staining Control
Dynamic

Figure 4.14: Immunohistochemical staining for elastin in leaflets cultured in static and dynamic conditions. Distinct elastin staining can be seen in the fibrosa of all leaflets, but it is more distinct in the fibrosa of dynamically cultured samples than statically cultured samples. Orientation of ventricularis, spongiosa, and fibrosa is the same across all samples. A representative staining control (2° antibody only) is included—all samples had on-slide staining controls.

Immunohistochemical staining revealed intense collagen type III staining across all layers of the valve during seven days of dynamic culture (Figure 4.16) and at fourteen days it appeared more diffuse. Staining appeared to be most intense in the fibrosa (where it is typically seen). Semi-quantitative analysis revealed that collagen type III staining intensity was significantly decreased at both seven and fourteen days in dynamic culture in comparison with baseline tissue (Figure 4.15). Static controls showed significantly more collagen III (by intensity) at day seven than baseline tissue, however at day fourteen, this difference was no longer observed. ($p < 0.05$ for all significant comparisons). Furthermore, at day seven, statically cultured samples showed significantly higher collagen III staining intensity than dynamically cultured samples.

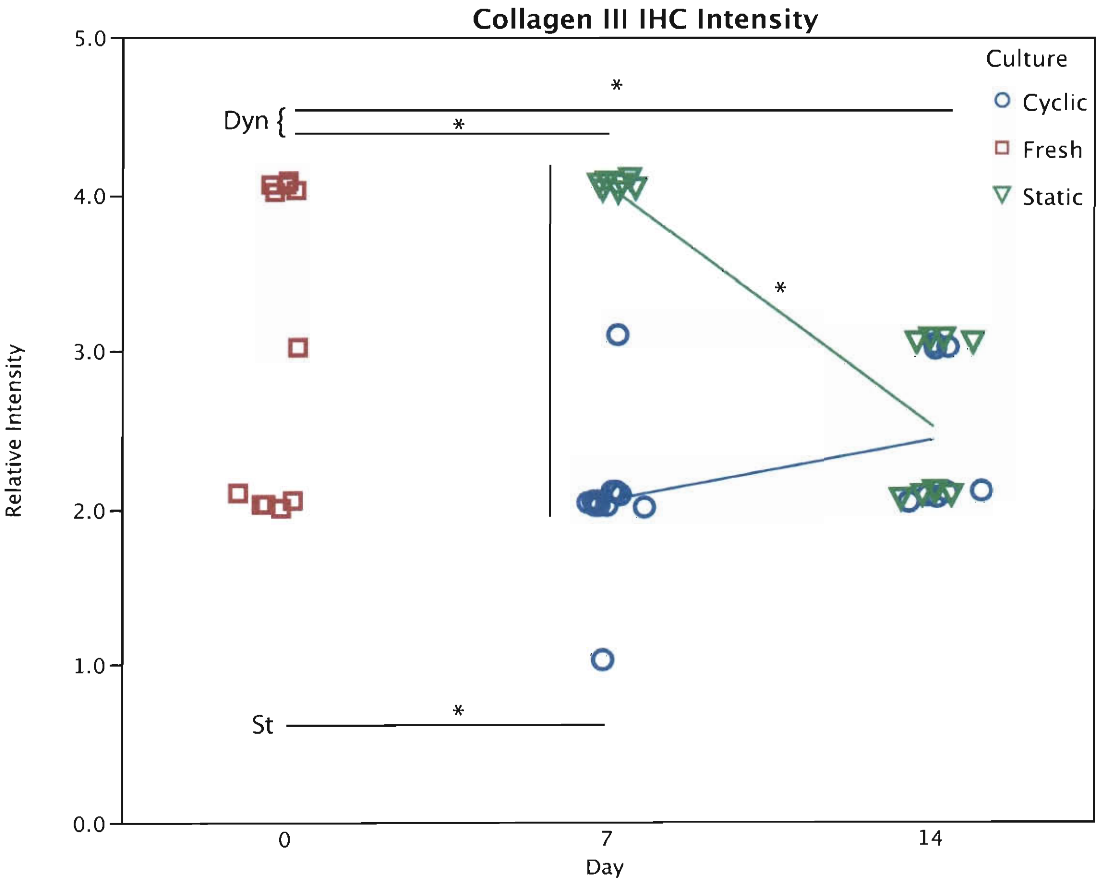

Figure 4.15 - Relative intensity of collagen DAB staining in leaflets as a function of multiple days of culture. N≥6 for all groups and * denotes significance with $p < 0.05$.

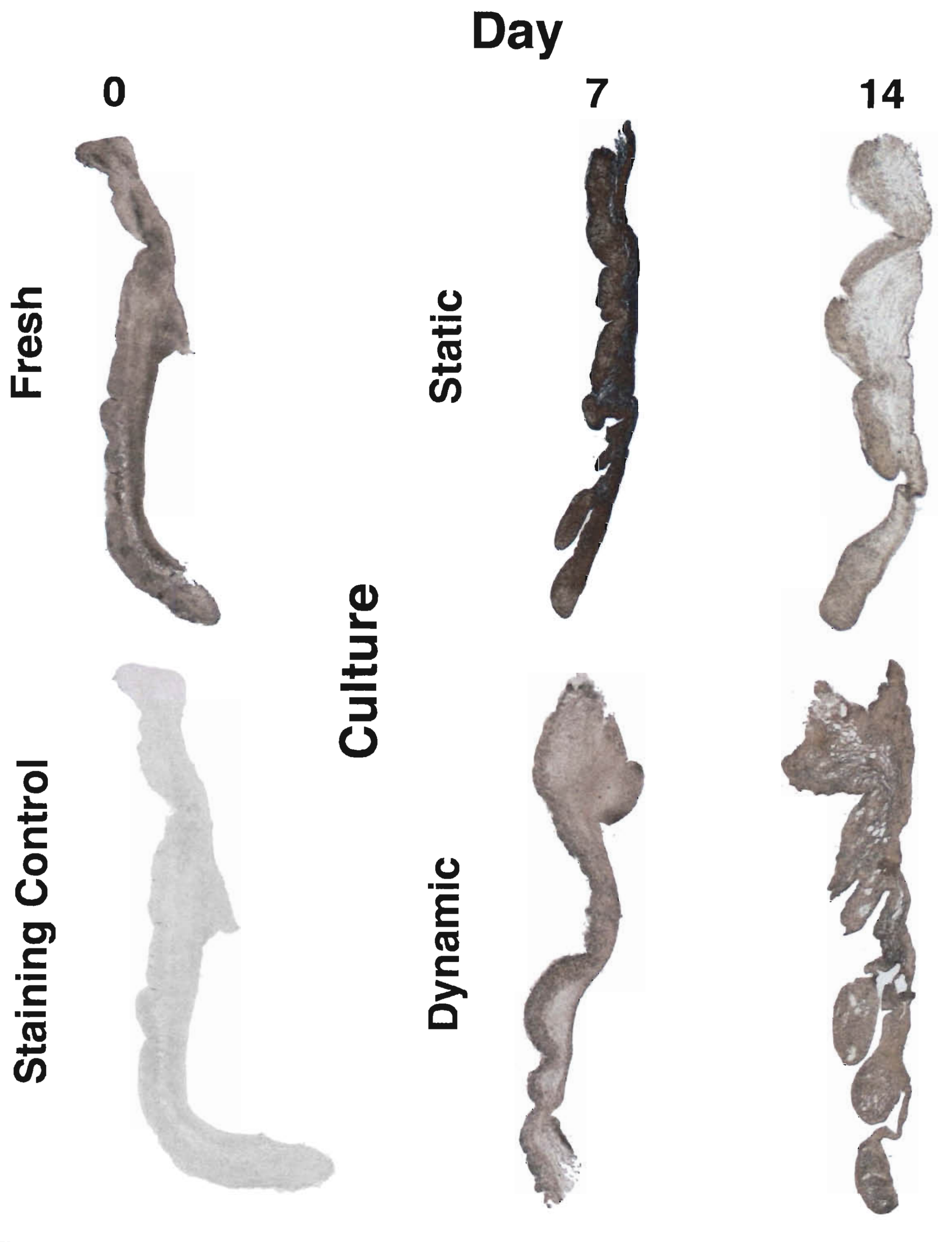

Figure 4.16: Immunohistochemical staining for collagen type III in leaflets cultured in static and dynamic conditions. Distinct collagen staining is observed in all leaflets. At day 14 in statically cultured leaflets, it appears to be diffuse through the fibrosa and spongiosa and located mainly in the ventricularis. For dynamically cultured leaflets at day 14, the staining appears to be diffuse throughout the leaflet. Orientation of ventricularis, spongiosa, and fibrosa is the same across all samples. A representative staining control (2° antibody only) is included—all samples had on-slide staining controls.

4.6 Discussion

This newly developed organ culture system was evaluated for use to determine its applicability for future studies of aortic valve biology, remodeling, and disease as well as for evaluation of tissue engineered heart valve scaffolds. It can be concluded that compared to static cultures (no mechanical stimulation), bioreactor culture provides the superior culture environment for aortic valve tissue maintenance for durations up to one week. This conclusion is evidenced by the mechanical testing and biochemical results at seven days. The flexural stiffness of the leaflets at day seven in dynamic culture is maintained at baseline levels, as is both the hydroxyproline and uronic acid content of the leaflets. Both biochemical assays measured total quantity present, normalized to tissue weights. It is unknown if tissue weights were substantially changing as a function of culture duration, since a defined volumetric sample of tissue was not used at all timepoints – instead one half of a leaflet was measured. If the leaflets are changing in size significantly (and correspondingly, in weight), then the conclusions drawn from the biochemical data would not be valid. However, the tissues did not appear to be grossly changing in either size, thickness or weight (of one half a leaflet), therefore the trends interpreted from the biochemical assays provide likely insight as to remodeling and synthetic capacity of the leaflets. Statically cultured leaflets showed a significant decrease in hydroxyproline content (a proxy for collagen content) and a corresponding decrease in flexural stiffness at this time point (both in comparison with dynamic culture and baseline leaflets). However, it is important to note that at this time point, uronic acid (a proxy for total GAGs) was unchanged from baseline levels in both dynamically and statically cultured leaflets, and that tensile modulus of the dynamically and statically cultured leaflets was identical. The discrepancy between measured hydroxyproline content and material properties could further investigated by examining the alignment of the collagen fibers with picrosirius red. For example, if the collagen network is becoming less aligned by day seven, that could explain why the tensile modulus is not significantly higher for the dynamically cultured leaflets, even though their hydroxyproline content is higher. Additionally, the extent of collagen crosslinks could be probed with IHC analysis of lysyl oxidase, since as crosslinking increases, stiffness of the tissue will increase correspondingly.

The histological characterization provides further support that bioreactor culture is preferable to static culture for this one week duration. The leaflets appear to retain their layered structure more distinctly in the dynamically cultured leaflets (as shown by Movat staining). While leaflets appeared thinner at later time points, it is difficult to determine this purely from tissue sections, since section thickness depends on microtome technique and orientation of the tissue within the paraffin block. In the future, leaflet thickness should be quantified before beginning the fixation and dehydration process. While the overall amount of elastin is lower in the dynamically cultured leaflets compared to baseline levels (from both visual interpretation of images and semi-quantative IHC analyses), the distribution of elastin appears to be properly retained in the normal layer (ventricularis) at seven days. By semi-quantative analysis, collagen type III content at day seven was lower than both baseline and statically cultured leaflets in the bioreactor samples. Furthermore, the visual interpretation of the collagen type III distribution within the stained sections shows that it is more layer specific in bioreactor cultures than in static cultures. This distribution suggests that statically cultured leaflets are undergoing remodeling in a manner that would generate more collagen III throughout the bulk of the leaflet. These findings could be investigated more quantitatively by using a fluorescently tagged secondary antibody, however, it is more difficult to visualize the whole sample when using fluorescence (microscope images must be tiled) and the stain could no longer be maintained for long term storage.

Analysis of the data from all assays indicates that the benefit of dynamic culture in the bioreactor was less apparent by day fourteen. Tensile stiffness of samples cultured to day fourteen in this system show no significant difference from control, although they were less stiff than statically cultured leaflets at this time point. Furthermore, there was no difference in flexural stiffness between dynamically or statically cultured leaflets at day fourteen, and both of these culture regimens resulted in significantly less stiff leaflets than baseline controls. At day fourteen, hydroxyproline concentration in bioreactor samples significantly increased in comparison with baseline valves, as did uronic acid concentration in both dynamic and statically cultured leaflets. This overall pattern indicates that remodeling was occurring by day fourteen, and the leaflets' ECM composition was significantly changed from native tissue conditions. Histological analyses confirmed these observations. In contrast to day seven, the day fourteen samples that were subjected to static culture conditions show better retention of the layered structure than dynamically cultured leaflets. Furthermore, morphologically, the dynamically cultured leaflets appeared more degenerated than statically cultured leaflets. IHC analyses showed that elastin concentration significantly decreased in both dynamically and statically cultured leaflets at day fourteen, when compared with baseline elastin intensity. Elastin did appear to be retained in the ventricularis of leaflets exposed to either culture regimen. Collagen III concentration at day fourteen was significantly lower in bioreactor samples than baseline values, and statically cultured samples showed a corresponding drop at this time point, although they were not significantly different than baseline controls, likely due to the spread of the data. Although the tensile and flexure moduli do not increase in dynamic culture at day fourteen, the data suggests that collagen type I content could be increased in bioreactor samples at day fourteen, since collagen III content decreased while hydroxyproline content increased. It may be that a mature, crosslinked, and oriented collagen network is not present at this time point.

From the data exhibited in this chapter, one can conclude that the imparted dynamic culture regimen provides clear benefit to the culture of aortic valves for one week, but does not appear to be appropriate for durations exceeding one week. However, since the bioreactor can indeed provide extended-duration sterile culture of aortic valve leaflets in a pseudo-physiologic environment, it is expected medium to long term (fourteen days and beyond) *ex* vivo maintenance can be achieved with proper optimization of the imparted dynamic regimen. The dynamic environment can be controlled by varying flow rate and frequency with the software and physical design of the cam-link assembly. Other studies of *ex vivo* organ culture of whole aortic valves have been limited to 96 hours and they have only showed data from 48 time points.[97, 109]. These studies have demonstrated the necessity of a dynamic culture regimen to maintain VIC phenotype and proper ECM composition. Organ culture systems using portions of valve tissue (AV or mitral valve) have been performed to durations as long as fourteen days.[103, 116, 121, 133] These studies demonstrated the need for the appropriate mechanical culture regimen, as several cyclic stretch investigations have shown VIC activation and degradation of ECM.[116, 133, 151, 152] Furthermore, altered shear stresses have been shown to have a profound effect on cells synthetic activity. The low shear stresses imparted in this system could be stimulating the cells to synthesis matrix metalloproteinases, of which increased synthesis could explain the decrease in tensile stiffness. As the system continues to be used for organ culture studies of valve biology, it will be important to characterize the collagen network for collagen quantity, alignment, and cross-linking. Additionally, since the system is clear, video analysis could be used to determine if valves remain competent during extended culture durations. Furthermore, the dynamic regimen could be optimized for tissue growth, since this system can also be used for the mechanical conditioning of a TEHV. Sub-physiologic flow rates have been shown to be very useful in these types of applications, and this system can easily generate these types of dynamic culture environments.[42] Lastly, the bulk bending stiffness of AV leaflets determined in this chapter serves as design criteria for the following chapters that deal with the optimization of hydrogel formulations for use in TEHV.

4.7 Conclusions

The dynamic culture regimen imparted by the bioreactor shows a clear benefit for *ex vivo* culture of aortic valves for one week when compared to static culture. At seven days, the flexural stiffness, hydroxyproline content and GAG content were unchanged from fresh tissue. Additionally, this culture regimen showed that when compared to statically cultured leaflets at the same time point, the dynamic regimen resulted in significantly better retention of flexural stiffness and hydroxyproline content. At durations longer than one week, this dynamic culture regimen does not appear to be appropriate. Despite the unclear benefit of the imparted regimen for durations of fourteen days, this is the longest *ex vivo* organ culture of whole aortic valves to date. Histologically, leaflets cultured in the dynamic environment showed better retention of their characteristic layered structure, and proper distribution of collagen III and elastin at both time points. The bending stiffness of native AV leaflets determined in this chapter served as design criteria for investigations of PEGDA scaffold bending stiffness.

4.8 Acknowledgements

The authors would like to thank Dr. Glen Leverson at Department of Surgery, University of Wisconsin for assessment of appropriate statistical methods.

Chapter 5: Flexural Characterization of Cell-Encapsulated PEGDA Hydrogels[*]

5.1 Introduction

The limitations of the current clinical options for valve replacements inspire development of enabling technologies to create a tissue engineered heart valve (TEHV). Poly(ethylene glycol) diacrylate (PEGDA) hydrogel scaffolds permit greater biological and biomechanical customization than do non-woven mesh scaffold technologies. However, the material characterization of PEGDA hydrogels has been predominantly limited to compression and tension, as opposed to bending. Since large flexural deformations result in points of maximum stress in native valves as well as TEHVs, it is crucial to evaluate any potential scaffold material in this mode. The effect of formulation parameters on the bending mechanics of cell-seeded PEGDA hydrogels were investigated with a custom designed bending tester. Three molecular weights (3.4, 6, or 8 kDa) and three weight fractions (5, 10, 15 %, w/v) were subjected to three-point bending tests and the flexural stiffness was calculated. Manipulating the composition of the hydrogels resulted in flexural stiffnesses comparable to native tissues (15-220 kPa) with varied mesh sizes and swelling ratios. Hydrogels containing encapsulated valve cells, methacrylated heparin (Hep-MA), or both were substantially less stiff than acellular hydrogels. In conclusion, PEGDA hydrogels are an attractive potential scaffold system for TEHVs because they are not only cytocompatible and modifiable but can also withstand bending deformations. These studies were the first to explore the encapsulation of valvular interstitial cells in pure PEGDA hydrogels as well as to investigate the bending properties of PEGDA gels.

---

[*] The majority of this chapter will be published as: Durst CA, Cuchiara MP, Mansfield EG, West JL, Grande-Allen KJ. Flexural Characterization of Cell Encapsulated PEGDA Hydrogels with Applications for Tissue Engineered Heart Valves. Acta Biomaterialia 2011: in press.

5.2 Background

The near infinite biochemical and biomechanical tunability of hydrogels makes them very attractive potential scaffold materials for tissue engineered heart valves (TEHVs). Hydrogels have received far less attention than other scaffolding materials, with the majority of TEHV investigations being performed using non-woven fiber mesh or salt-leached foam scaffolds generated from polyglycolic acid, poly(lactic-co-glycolic acid), and polyhydroxyalkanoates.[35, 37, 40, 51, 53] Thus far, these materials have been used as scaffolds for the most successful TEHV to-date (in both in vitro and in vivo evaluation).[47] Their open structure allows cell migration throughout the scaffold, and their material properties can be engineered to be sufficient for the mechanical environment of the valve, which involves flexure, tension, compression, and shear varying throughout cardiac cycle. Additionally, these materials are degradable and have been FDA approved for many years. However, these materials have shown certain limitations, namely their high initial stiffnesses compared to native tissues and the substantial length of time required for the polymer to undergo hydrolysis-governed degradation.[52] Furthermore, these materials lack intrinsic biological functionalization, meaning that they do not present any functional biological moieties that could direct cell signaling, ECM production, or enzyme-governed degradation. These materials can be modified to present these motifs, however, there is no control over functional molecule localization (in contrast to the patterned localization achievable in hydrogels via photolithographic or two-photon adsorption methods).[65-67]

Both non-woven fiber mesh and salt-leached foam scaffolds use cytotoxic processing conditions to generate their architecture. Since the polymer processing conditions are cytotoxic, cell seeding must be performed after the scaffold is fabricated. Cell seeding has been one of the most significant challenges in use of these scaffold materials. Seeding methods resulted in inhomogeneous cell distribution, low densities, and long seeding times before the scaffold was populated. Initially, cells were incubated on the scaffolds under static conditions for up to 4 days in order to allow cell migration to the interior of the scaffold.[34] Dynamic seeding methods were developed that yielded homogenous and slightly more efficient seeding, but the dynamic nature of the seeding environment was reported to cause small cracks in the scaffold material.[68] Encapsulation has been shown to be the most efficient and homogeneous method of cell seeding. For example, the use of a viscous fibrin “cell carrier” gel resulted in fast, high yield, homogenous seeding of valvular interstitial cells (VICs) into fiber matrices. The use of fibrin as the basis for the gel, however, alters the cell’s local biochemical environment through both its structure (cell-substrate) as well as retention of bioactive molecules within the gel.[43, 69] While these previous approaches hold promise, we believe that the ability to encapsulate cells coupled with the customization potential of polymeric biomaterials makes hydrogels very appealing as scaffold systems.

Poly(ethylene glycol) diacrylate (PEGDA) hydrogels are intrinsically biocompatible, since the base (unmodified) gels are biologically neutral, resist protein adsorption, do not release acidic products during their degradation and can be crosslinked with low cytotoxicity allowing for high density 3D cell encapsulation. Furthermore, PEG hydrogels can be modified by crosslinking a large number of bioactive moieties (peptides, glycosaminoglycans, growth factors) to achieve a high degree of specific bioactivity.[2, 72, 73] Indeed, it is widely reported that peptides tethered to either the surface or bulk phase of PEGDA gels will retain their bioactivity after this modification.[74-76] Additionally, since these materials can be rapidly photopolymerized, spatial control of functional moieties is possible in both 2D and 3D, due to the emerging field of two-photon stereolithographic fabrication techniques.[66]

The physical properties of PEGDA gels can be modified across a continuum of magnitudes that are biologically relevant in terms of recapitulating both tissue function and the pericellular environment. Hydrogel physical properties such as stiffness, degree of swelling and effective diffusivity can be controlled by manipulating the molecular weight of the macromer, the weight fraction of macromer in solution and the crosslinking time.[85, 86] Stiffness was of primary interest in this study, and construct stiffness achieved ranged from very low (~5 kPa, similar to a 1% HA gel[153], which could mimic the gelatinous spongiosa[154]) to several orders of magnitude higher (400 kPa, similar to bovine pericardium[127]). It has been further demonstrated that crosslinking density affects the strain experienced by the cell, and certain formulation parameters can translate nearly 100% of bulk strain to individual cells.[83] Cells seeded in fiber mesh scaffolds can be in contact with either a singular fiber, or many fibers, which may have varying degrees of displacement at the microstructure due to macrostructural strain. Thus, mechanotransduction in hydrogels appears to be more efficient than in fiber meshes.

While polymer hydrogels have been well studied in tension and compression, the flexural properties of these gels have yet to be investigated. Since flexure represents a major mode of deformation of heart valve leaflets, the purpose of this study was to investigate the behavior of these gels in three-point bending. We hypothesized that cell encapsulated PEGDA gels could be formulated to approximate the flexural stiffness of fresh porcine aortic valve leaflets, and that these gels would support short-term maintenance of the VIC phenotype and ECM synthesis. This exploration of PEGDA gels with respect to their capacity for the mechanical requirements of engineered heart valve leaflets will aid in the translation of hydrogels towards more biomimetic scaffold fabrication and realistic in vitro testing of hydrogel-based TEHVs.

5.3 Materials and Methods

All chemicals were purchased from Sigma unless otherwise noted.

5.3.1 Study Design

The primary concern of this study was to investigate the effect of hydrogel formulation parameters on flexure properties of TEHV scaffolds. As a result, the experiment employed a full factorial design for the flexural testing and immunofluorescence studies of cell seeded gels, and flexural, compression and network property characterization of acellular gels (Figure 5.1).

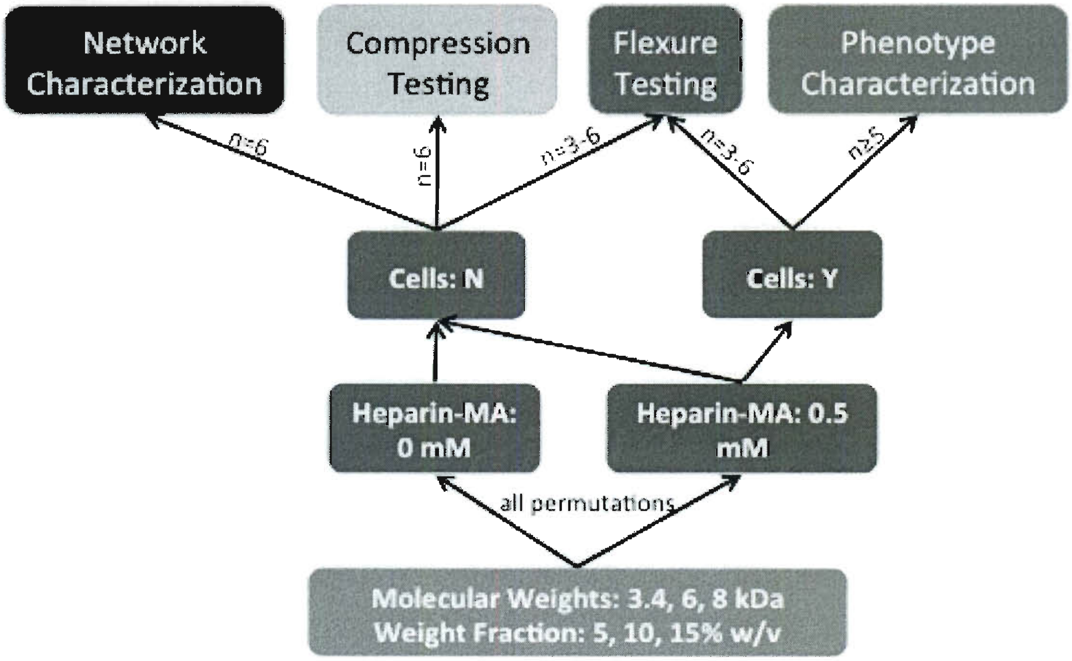
Network Characterization
Compression Testing
Flexure Testing
Phenotype Characterization
n=6
n=6
n=3-6
n=3-6
n≥5
Cells: N
Cells: Y
Heparin-MA: 0 mM
Heparin-MA: 0.5 mM
all permutations
Molecular Weights: 3.4, 6, 8 kDa
Weight Fraction: 5, 10, 15% w/v

Figure 5.1: Diagram of experimental design. A full factorial design was chosen to investigate the effect of varied formulation parameters (molecular weight, weight fraction) on cell phenotype and hydrogel network and mechanical properties. Sample sizes were chosen from prospective power calculations.

Sample sizes were chosen based on prospective statistical power calculations. Using two-way ANOVA comparison of the row*col means, where detectable contrast is set at 0.4, standard deviation at 0.15 (on the upper bound of what is reported in hydrogel compression testing [83, 84]), and n=5, statistical power was observed to be 0.8. As the study was underway, it became evident that heparin altered the gels' properties in an unexpected way, and subgroups were added to attempt to address the effect of heparin incorporation on gel mechanical properties (Figure 5.2). These subgroups were tested using lower sample sizes than the samples used in the primary focus of the chapter.

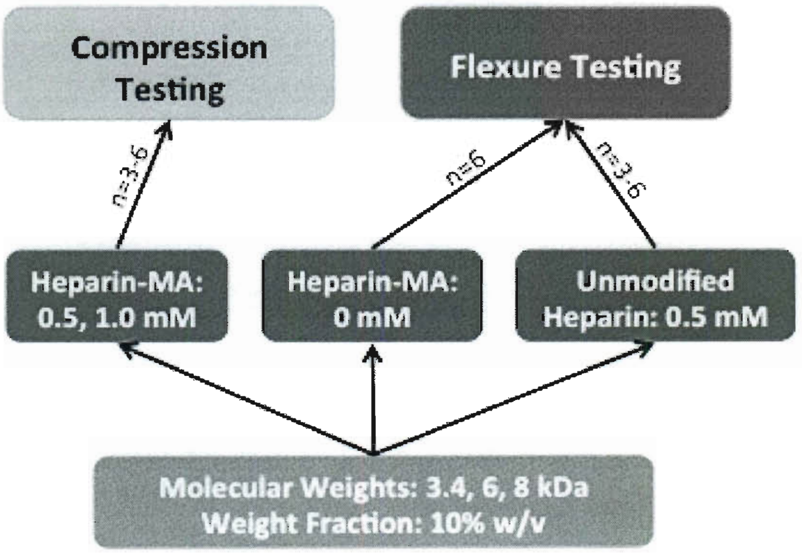
Compression Testing
Flexure Testing
n=3-6
n=6
n=3-6
Heparin-MA: 0.5, 1.0 mM
Heparin-MA: 0 mM
Unmodified Heparin: 0.5 mM
Molecular Weights: 3.4, 6, 8 kDa
Weight Fraction: 10% w/v

Figure 5.2: Diagram showing sub-studies investigating the effect of heparin inclusion on gels.

5.3.2 Cell Culture

Primary cultures of valvular interstitial cells (VICs) were isolated from aortic valve leaflets from 6-month-old pigs obtained from a local abattoir (Fisher Ham and Meat, Spring, TX) within 6 hours of slaughter. The valve leaflets were dissected using sterile technique and rinsed with sterile phosphate-buffered saline (PBS) supplemented with 5% antibiotic-antimycotic solution (ABAM, Cellgro, Manassas, VA). The leaflets were then placed in a flask containing serum-free DMEM (Cellgro) supplemented with 2 mg/mL of collagenase type II (Worthington, Lakewood, NJ) and 2.5% ABAM. The flask was incubated at 37°C in an incubated shaker for 30 minutes. Next, the leaflets were removed from solution and the endothelial cells were removed by rubbing the surface of the valve with a cotton swab. The leaflets were then minced using a #10 scalpel and digested using 2 mg/mL of collagenase type III, 0.1 mg/mL testicular hyaluronidase

(Worthington), 2 mg/mL protease, 2.5 % (v/v) HEPES, and 2.5% (v/v) ABAM in serum-free DMEM for 4 hours on an incubated shaker (150 rpm). The cell suspension was filtered using a 70 μm pore size cell strainer (BD Falcon, Franklin Lakes, NJ), pelleted, and cultured on TCPS in DMEM supplemented with 10% bovine growth serum (BGS, Hyclone, Logan, UT) and 1% ABAM. VICs were maintained in a humidified incubator at 37°C with 5% CO_2. Medium was changed every 2 days. All experiments were performed using cells between passages 4 and 8.

5.3.3 PEGDA Synthesis

PEGDA was prepared using previously described methods.[73] Briefly, 0.1 mM dry poly(ethylene glycol) with molecular weight of either 3400, 6000, or 8000 Da was combined with 0.4 mM acryloyl chloride, 0.2 mM triethyl amine, in anhydrous dichloromethane. The reaction was stirred proceed overnight under argon at 22 °C. The solution was washed with 2 M K_2CO_3 in order to remove HCl. Gravity-based phase separation was used to separate the solution into an aqueous and organic phase. The organic (PEGDA containing) phase was removed the next day and dried with anhydrous $MgSO_4$. PEGDA was then precipitated with cold diethyl ether, filtered, and dried under vacuum. ^{1}H-NMR was used to verify acrylation of the PEG chains by the presence of peaks at 3 ppm. MALDI-TOF was used to verify molecular weight of the synthesized PEGDA. PEGDA was stored at -20 °C under argon until use.

5.3.4 Methacrylation of Heparin

Heparin was methacrylated using previously described methods for the methacrylation of polysaccharides.[2, 155] In short, the procedure involved dissolving heparin in ddH_2O at 2% (w/v), reacting the solution with a 20 times molar excess of methacrylic anhydride, and adjusting the pH to 7.5 using 4N NaOH. This solution was stirred on ice for 24 hours while maintaining pH at 7.5. The methacrylated heparin (Hep-MA) was precipitated from solution with 4 °C ethanol, then dialyzed for 48 h using a 1000 Da MWCO filter (Spectrum Laboratories, Rancho Dominguez, CA). The solution was then dialyzed and the powder was stored under argon at -20°C until use. ^{1}H-NMR was used to determine methacrylation per disaccharide repeat unit.

5.3.5 Hydrogel Polymerization

In order to test the effects of a wide range of hydrogel formulation parameters on bending mechanics, a full factorial design was employed. Because molecular weight and weight fraction of the macromer are known to affect the material behavior of the resulting hydrogels,[85] three different molecular weights (3.4, 6, or 8 kDa) and three weight fractions (5, 10, or 15%, w/v) were investigated in a combinatorial study (nine permutations). For each permutation, a specific molecular weight of PEGDA was dissolved in PBS to a specific weight fraction, after which Hep-MA was added to obtain a final concentration of 0.5 mM Hep-MA in the prepolymer solution. The photoinitiator 2-Hydroxy-4′-(2-hydroxyethoxy)-2-methylpropiophenone was dissolved in ethanol at 10% (w/v) and added to the prepolymer solution at 3% (v/v). The resulting solution was sterile filtered and VICs were added to the solution at a concentration of 22×10^6

cells/mL. All cellularized gels used Hep-MA since it had previously been shown to be necessary for the maintenance of VIC phenotype when VICs were seeded on PEGDA gels (in 2D studies).[2]

Prior to polymerization, the prepolymer solution was poured into custom molds. The molds were created from glass slides separated by comb-shaped polycarbonate spacers, resulting in seven 6 x 44 x 0.8 mm (width x height x thickness) wells per mold assembly. Prior to molding, the glass slides and polycarbonate spacers were coated with Sigmacote (Sigma-Aldrich, St. Louis, MO) to ease removal of the crosslinked hydrogels from the molds. The molds were steam sterilized assembled and after cooling, the prepolymer was loaded into the molds. Subsequently the gels were crosslinked with longwave UV light (365 nm, 10 W/cm^2) for 10 minutes. The hydrogels were removed from the molds and cultured separately in well plates for 48 hours in a humidified incubator before mechanical testing.

To determine the impact of cell inclusions on hydrogel bending behavior, acellular gels were created in the same manner as above for all nine permutations of molecular weight and weight fraction. In order to elucidate the effect of methacrylated heparin subsets of hydrogel formulations were created in the same manner as above, except that either (i) the heparin used was not methacrylated (10% WF for all MW plus 15% for 8 kDa) or (ii) the concentration of Hep-MA was varied (10% WF for all MW). An additional control set of "base" PEGDA hydrogels (all nine permutations of MW and WF) was prepared without any Hep-MA.

5.3.6 Mechanical Testing

The hydrogel strips were loaded into a custom built bending tester (design adapted from [126]) and subjected to 3-point bending tests. The general method of flexure testing is the same as described in section 4.3, and the methods will be briefly summarized here. Optical tracking of hydrogel deformation was achieved by sifting small graphite particles over the hydrogel test strip, the reference rod, and a calibrated flexure bar (Figure 5.3).[52]

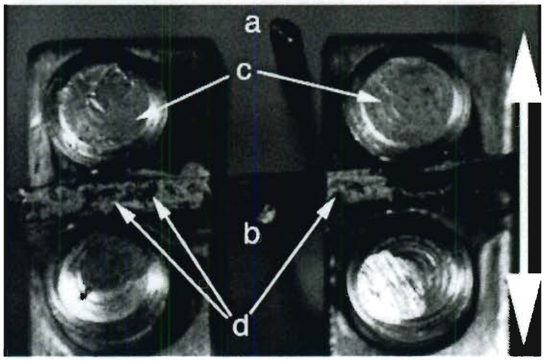

Figure 5.3: Photograph with annotations depicting the method of operation of the bending apparatus. The linear motion of the bending tester stage pulls the hydrogel strip (secured against the loading posts (c)) against the flexure bar (b). Displacement of the flexure bar is determined relative to the immobile reference bar (a). Graphite particles (d) are visible atop the hydrogel strip. Arrow indicates the direction of motion.

The sample was deformed at a rate of 1.5 mm/min until a maximum change in curvature (ΔK) of 0.3 mm^{-1} was achieved. Images of the sample deformation and graphite particles movement were captured at 5 frames per second by a CCD camera (Leica DFC320) mounted over the apparatus. Calculation of stiffness was identical to the method presented in Chapter 4. Sample size for all flexure groups was 3-6 per hydrogel permutation. After flexure testing, the cellularized gels were retained for immunocytochemical staining.

In order to verify stiffness results obtained from bending, several additional sets of PEGDA hydrogels were tested in compression. PEGDA slabs with initial thickness of 3 mm were created (as in section 2.4, with the exception of using 3 mm spacer), punched with a 3 mm biopsy punch, swollen in medium, and compressed. The gels were compressed to 50% strain at 0.1 mm/s between stainless steel platens in a Bose-Enduratec ELF3200 (Bose Electroforce, Eden Prairie, MN). After converting load-displacement data to stress-strain data, stiffness was measured from the linear portion of the stress-strain curve at 15-30% strain. Compression testing was also performed to determine whether there was an influence of Hep-MA concentration (0.5 or 1.0 mM) on hydrogel stiffness. All compressive testing groups had a sample size of 5-6 for each hydrogel formulation.

5.3.7 Cellular Analyses

To assess the viability of the VICs following encapsulation, freshly prepared cell-seeded hydrogels were stained with a Live/Dead kit (Molecular Probes, Carlsbad, CA). After staining for 30 minutes, the hydrogels were imaged using a Zeiss LSM 510 confocal microscope (Carl Zeiss Microimaging, Thornwood, NY) to assess the abundance and location of live cells (green calcien AM) or dead cells (red ethidium homodimer-1).

To assess the VIC phenotype and capacity for collagen synthesis, the gels were cultured for 2 days in static culture (using same medium and conditions as 2D culture explained in 5.3.2) and then stained with rabbit anti-α-smooth muscle actin (Abcam, Cambridge, MA) and mouse anti-prolyl-4-hydroxylase (Chemicon, Billerica, MA).[2, 156] Primary antibodies were used at 1:100 dilution in 0.1 % (w/v) BSA in PBS and allowed to diffuse into the hydrogel for 16 hours at 4°C on a rocker table at room temperature. Gels were then washed with 0.1% BSA in PBS for 4 hours on a rocker table. After washing, gels were incubated simultaneously for 16 hours with fluorescently tagged secondary antibodies (AF-488 conjugated donkey anti-mouse, AF-633 conjugated goat anti-rabbit secondary, Molecular Probes, Carlsbad, CA) at 4° C on a rocker table. Secondary antibodies were used at 1:1000 dilution in 0.1% BSA in PBS. Finally, gels were washed with 0.1% BSA in PBS for 4 hours on a rocker table and subsequently imaged.

The proportion of αSMA and P4H positive cells was determined in order to assess the maintenance of the myofibroblast phenotype. First, the channels from the confocal images were separated in ImageJ. Next, the background was subtracted using a rolling ball method with radius of 25 pixels. The images were thresholded from with values above the background intensity obtained from secondary-only controls. Lastly, the analyze particles algorithm was used to count cells with particle size greater than 5 μm^2 and circularity ranging from 0.5-1.0. The total count for αSMA or P4H positive cells was normalized to the total cell count (from DAPI) in each frame and at least five images were used for each group.

5.3.8 Hydrogel Network Characterization

The hydrogel network was characterized using Flory-Rehner theory. The wet mass of the gels was measured after cellular analyses and mechanical testing. After the gels were lyophilized for 48 hours, their dry mass was measured. From this information and the formulation parameters the number of effective chains per unit volume (Equation 5.1), molecular weight between crosslinks (Equation 5.2), average end-to-end distance of the unperturbed state (Equation 5.3), crosslink density (Equation 5.4), mesh size (Equation 5.5), and mass swelling ratio were calculated as previously described by Cruise *et al.*[157] The number of effective chains per unit volume, Ve, used in calculation of molecular weight between crosslinks, was calculated using the equation below (Equation 5.1)

Equation 5.1: Number of effective chains per unit volume, where *v* is the specific volume of the bulk PEG in amorphous state, V_1 is the molar volume of water, $V_{2,r}$ and $V_{2,s}$ are the polymer volume fraction in the relaxed and swollen state respectively, and u is the Flory-Huggins solvent interaction parameter.

$$V_e = \frac{\frac{v}{V_1}\left[ln\left(1 - V_{2,s}\right) + V_{2,s} + \mu V_{2,s}^2\right]}{V_{2,r}\left[\left(\frac{V_{2,s}}{V_{2,r}}\right)^{\frac{1}{3}} - \frac{1}{2}\left(\frac{V_{2,s}}{V_{2,r}}\right)\right]}$$

After the number of effective chains per unit volume was solved, molecular weight between crosslinks was calculated using the equation below (Equation 5.2)

Equation 5.2: Molecular weight between crosslinks equation, where Ve is number of effective chains per unit volume, u is the specific volume of PEG in the amorphous state, and Mn is the number average molecular weight of the starting polymer.

$$M_c = \left(V_e + \frac{2}{M_{n(0)}}\right)^{-1}$$

Equation 5.3: Average end-to-end distance of polymer in unperturbed state. Mc is the number average molecular weight between crosslinks, Mr is the molecular weight of the repeat unit, and Cn is the characteristic ratio for PEG.

$$(r_0^{-2})^{\frac{1}{2}} = l\left(2\frac{M_c}{M_r}\right)^{\frac{1}{2}} C_n^{\frac{1}{2}}$$

Equation 5.4: Crosslink density calculation, where Mc is the number average molecular weight between crosslinks and u is the specific volume of PEG in the amorphous state.

$$X_d = \frac{1}{M_c v}$$

Equation 5.5: Mesh size equation, where where r_0 is average end-to-end distance of the polymer, and $V_{2,s}$ is the polymer volume fraction in the swollen state.

$$\zeta = (r_0^{-2})^{\frac{1}{2}} V_{2,s}^{\frac{-1}{3}}$$

5.3.9 Statistical Analysis

Statistical analyses of stiffnesses and network parameters were performed using JMP (SAS Software, Cary, NC). Where appropriate, either one- or two-factor ANOVA was performed and fit to a least squares model. Subgroup means were compared with post-hoc Tukey's HSD testing with an $\alpha=0.05$. When represented visually, data is expressed as mean ± standard error. Significance is denoted in figures with letters. Groups are significantly different if they do not share a letter.

5.4 Results

5.4.1 Characterization and Verification of Polymer Products

The molecular weight of the synthesized PEGDA was verified by mass spectrometry to be within 150 Da of the specified MW of the precursor (PEG) for all MW of PEG. The polydispersity index was calculated to be 1.053, 1.007, and 1.0574 for 3400, 6000, and 8000 Da PEGDA, respectively. Acrylation efficiency was verified by the presence of peaks at 3 ppm with NMR for all PEGDA samples. Percent methacrylation for heparin was 6.8% (spectra in Appendix II).[158]

5.4.2 Hydrogel Material Properties

As expected, decreasing the molecular weight of the PEGDA in unmodified, acellular hydrogels (containing no Hep-MA) resulted in stiffer gels in flexure (Figure 5.4). For equivalent weight fractions, gels in compression (Figure 5.5) showed similar modulus to that of gels in flexure, so it was concluded that the stiffnesses measured by the flexure device were valid. Compressive stiffness of the unmodified, acellular hydrogels was observed to increase with increasing weight fraction and to decrease with increasing molecular weight.

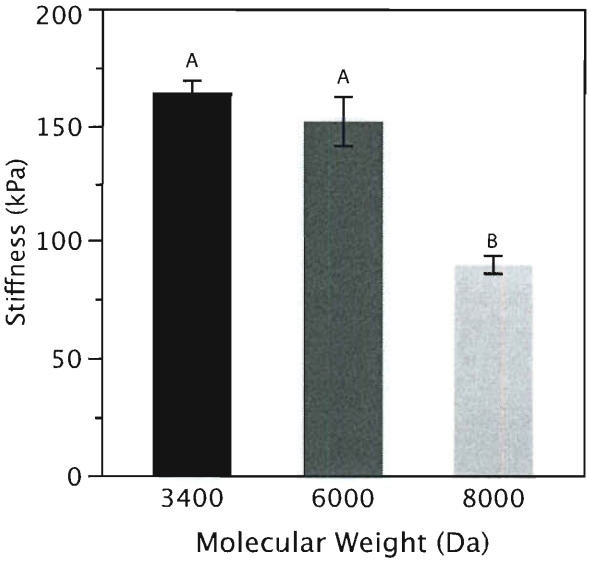

Figure 5.4: Flexural stiffness of base PEGDA hydrogels (unmodified; containing no Hep-MA). Hydrogels were all 10% PEGDA by weight. Samples marked with different letters are significantly different at $\alpha=0.05$. N=6 for all sample groups.

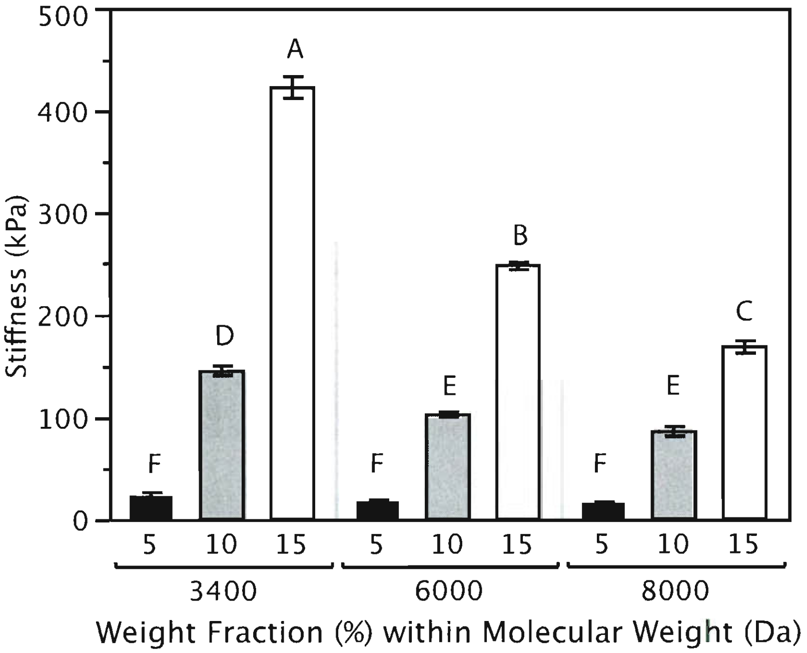

Figure 5.5: Compressive stiffness of base PEGDA hydrogels. Flexural stiffnesses are on the same order of magnitude as compressive stiffnesses for the 10% weight fraction hydrogels. Samples marked with different letters are significantly different at $\alpha=0.05$. N=6 for all sample groups.

Since heparin is a charged molecule, inclusion of heparin was expected to alter the swelling properties of the gel, although it was unknown what impact there would be on the material properties. In acellular gels containing 0.5 mM Hep-MA (Figure 5.6), stiffness again showed the pattern of being significantly increased with increasing weight fraction within each molecular weight ($p < 0.05$).

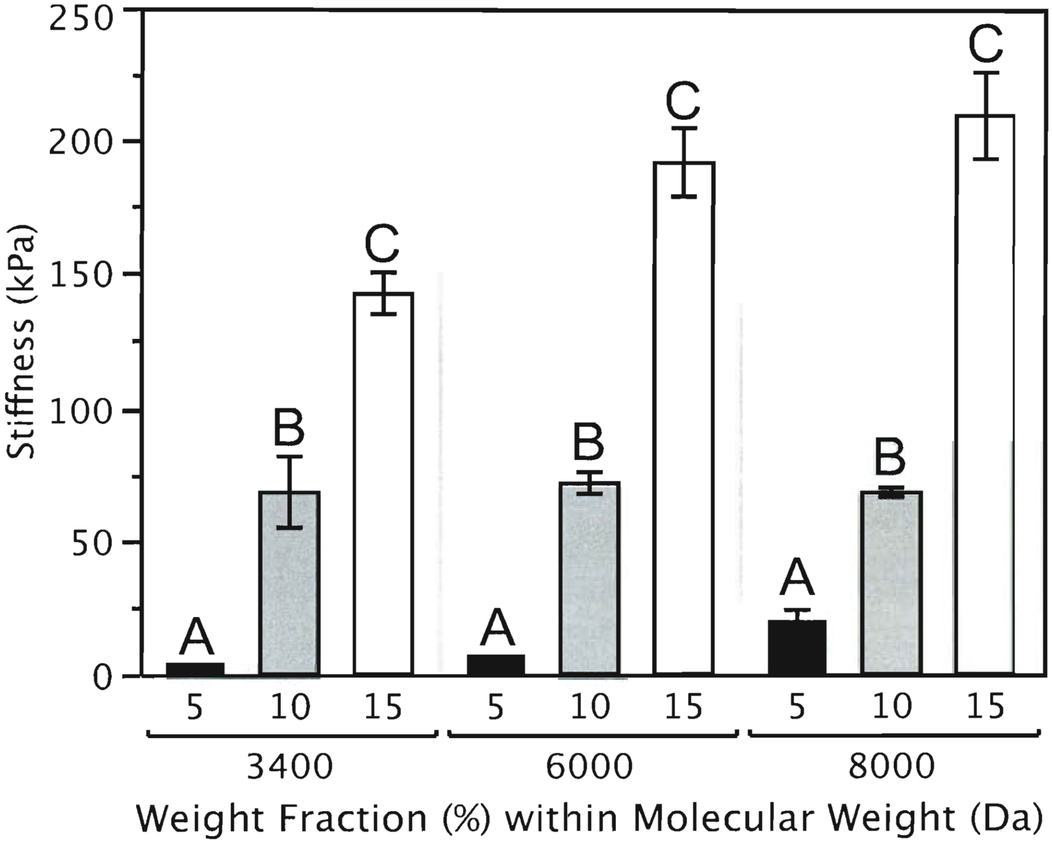

Figure 5.6: Flexural stiffness of acellular gels containing 0.5 mM of Hep-MA. N=3-6 for all groups and samples marked with different letters are significantly different at α=0.05.

Interestingly, there was either no change in stiffness or a trend of increasing stiffness with increasing molecular weight, which was opposite from what was expected given the data patterns from testing of unmodified PEGDA hydrogels (Figure 5.4 and Figure 5.5). To evaluate whether this deviation from the expected pattern was due to the methacrylation of heparin, PEGDA hydrogels containing unmodified heparin (0.5 mM) were tested in flexure (Figure 5.7).

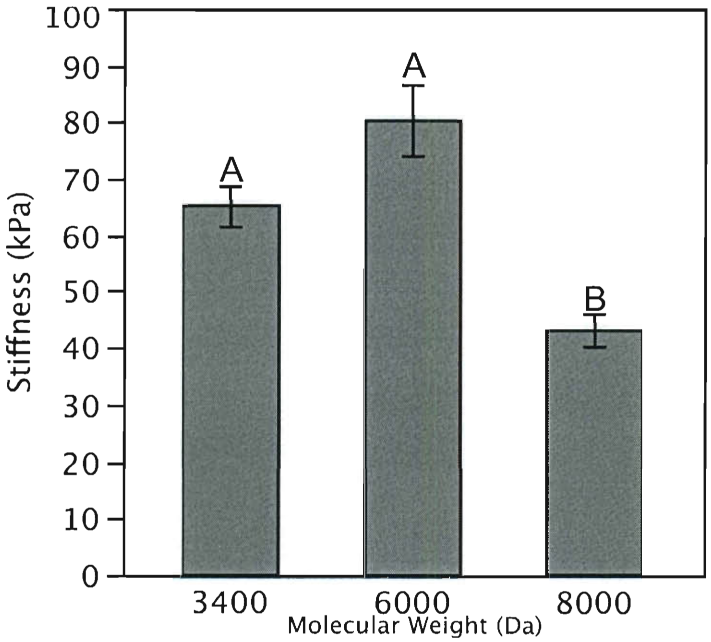

Figure 5.7: Flexural stiffness of representative groups of PEGDA hydrogels containing 0.5 mM unmodified heparin. N=3-6 for all groups and samples marked with different letters are significantly different at α=0.05.

Although there was no difference in hydrogel flexural stiffness between entangled unmodified heparin and Hep-MA for the lower molecular weights of PEG, stiffness of the 8 kDa PEGDA hydrogels was significantly lower for the unmodified heparin case, at PEGDA weight fractions of both 10% (Figure 5.7, $p < 0.01$) and 15% (70 kPa for unmodified heparin vs. 209.7 kPa for Hep-MA, results not shown on figure, $p < 0.01$). To determine whether Hep-MA interfered with stiffness in a concentration-dependent manner, hydrogels containing either 0.5 or 1.0 mM Hep-MA were tested in compression. The 3.4 kDa PEGDA hydrogels with greater Hep-MA concentration were less stiff

(Figure 5.8), but there was no significant effect of Hep-MA concentration at the higher molecular weights of PEGDA.

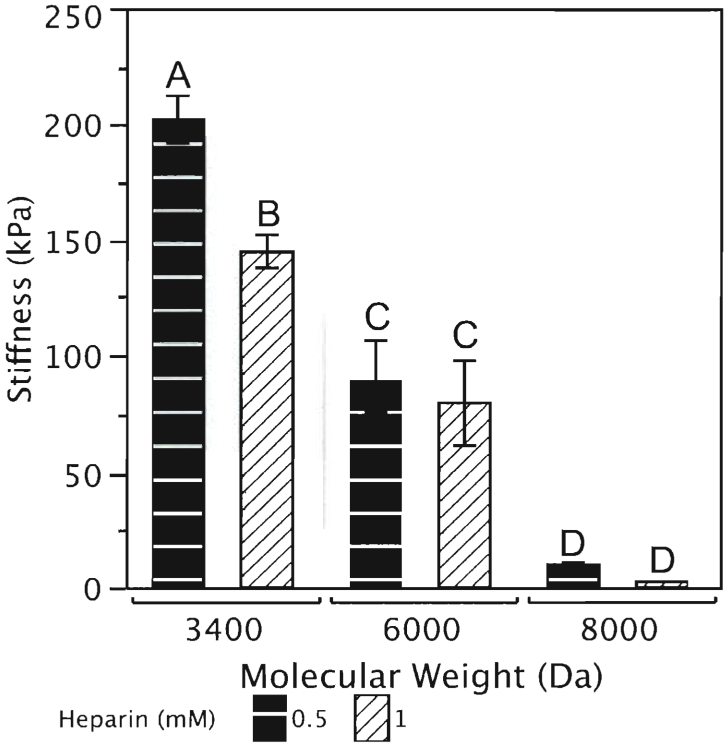

Figure 5.8: Compressive stiffness of PEGDA discs with containing Hep-MA at concentrations of either 0.5 or 1.0 mM. N=3-6 for all groups and samples marked with different letters are significantly different at α=0.05.

It was also noteworthy that for these hydrogels tested in compression, the inverse relationship between stiffness and molecular weight was again present, i.e., the addition of heparin to PEGDA hydrogels affected the flexural characteristics more than the compressive behavior.

Finally, cell seeded PEGDA gels with 0.5 mM Hep-MA were tested in flexure (Figure 5.9). These samples demonstrated trends that were very similar to the flexural stiffnesses of acellular hydrogels containing Hep-MA (Figure 5.6).

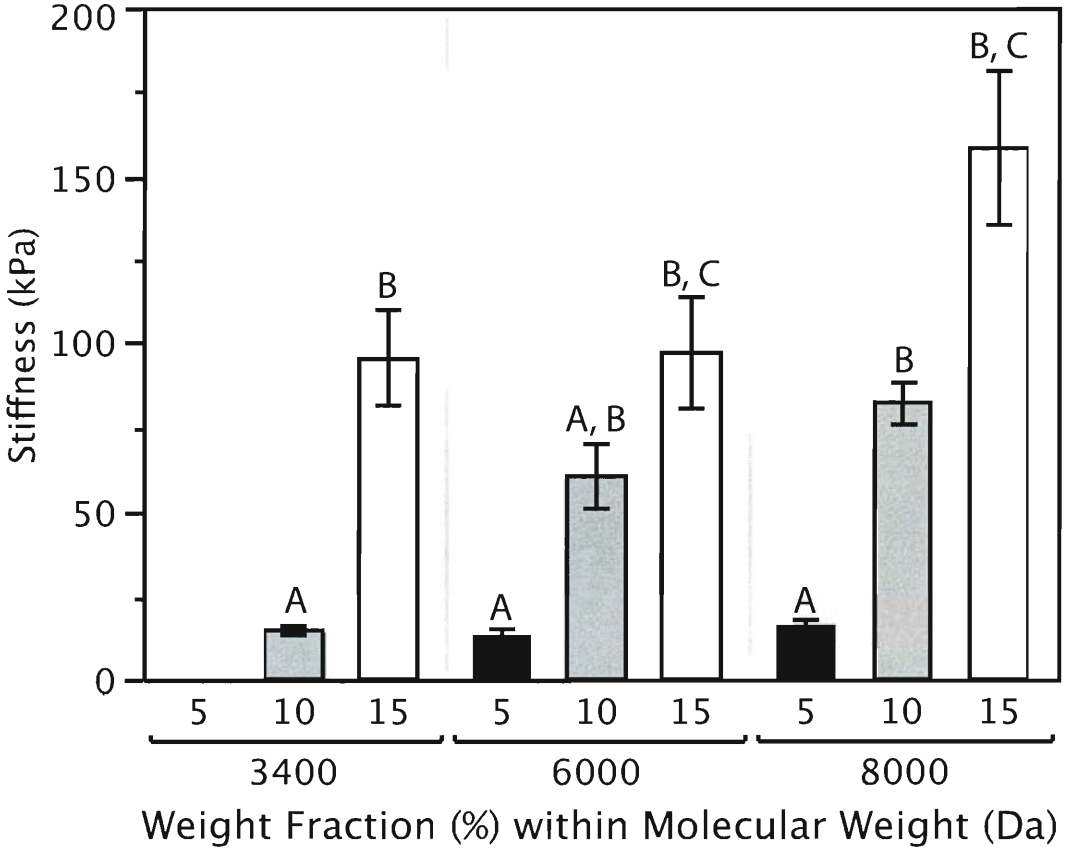

Figure 5.9: Flexural stiffness of cell-seeded gels. N=3-6 for all samples. Samples marked with different letters are significantly different at α=0.05.

Within each molecular weight, stiffness increased with increasing weight fraction ($p<0.05$). Additionally, stiffness was either unaffected or generally increased with increasing molecular weight, in contrast to the patterns shown in Figure 5.5 and Figure 5.8. It was also evident that the inclusion of cells reduced the hydrogel stiffness for all formulations compared with the acellular gels ($p<0.05$).

5.4.3 Network Properties of Acellular Hydrogels

The network properties of the gel were investigated to verify observed mechanical phenomena, and to ensure that diffusional properties were sufficient for cell viability and immunostaining. For hydrogels prepared without heparin, molecular weight between crosslinks decreased with increasing weight fraction and increased with increasing MW, as expected (Table 5.1). Adding Hep-MA to these gels resulted in a similar pattern at 3.4 and 6 kDa, however this trend was lost at the highest molecular weight (8 kDa). Decreasing molecular weight between crosslinks typically results in a stiffer gel, so these results were consistent with the material behavior of the unmodified (base) hydrogels. For the hydrogels containing Hep-MA, this relationship between molecular weight between crosslinks and stiffness was only evident for the lowest molecular weight PEGDA hydrogels (3.4 kDa). As shown in the table, mesh sizes in the base and heparinized hydrogels demonstrated the same data patterns, or lack thereof, as found with molecular weight between crosslinks. Swelling ratios for the various hydrogel formulations slightly increased with PEG molecular weight, but this effect was much less pronounced than for the other network properties. Swelling ratios decreased with increasing weight fraction of PEGDA. Finally, the overall magnitude of mesh sizes, and swelling ratios were lower for the heparinized hydrogels compared with the base hydrogels. However, molecular weight between crosslinks was only significantly lower in the heparinized gels than the base gels within at the 6000 kDa, 5% and 8000 kDa, 5% formulations. The impact of formulation on network parameters described in is illustrated visually with three figures along with omitted network property data in Appendix II.

Group	Molecular Weight (Da)	Weight Fraction (%)	Molecular Weight Between Crosslinks (Da)	Mesh Size (Å)	Mass Swelling Ratio (%)
Heparinized	3400	5	859.73 ± 118.89	99.42 ± 10.52	19 ± 1.96
		10	647.03 ± 63.29	71.11 ± 5.06	10.56 ± 0.61
		15	481.77 ± 22.06	54.54 ± 1.68	7.34 ± 0.17
	6000	5	1461.13 ± 93.54	137.52 ± 6.76	22.32 ± 1.13
		10	1103.05 ± 154.46	99.58 ± 10.22	13.11 ± 1.32
		15	1054.92 ± 32.86	90.64 ± 2.02	10.39 ± 0.21
	8000	5	1140.73 ± 153.82	111.8 ± 10.56	17.71 ± 1.25
		10	1324.46 ± 202.6	110.29 ± 12.54	13.68 ± 1.32
		15	898.89 ± 142.44	79.4 ± 8.8	9.03 ± 0.75
Non-heparinized	3400	5	1065.56 ± 50.6	117.83 ± 5.02	22.53 ± 1.29
		10	677.23 ± 10.83	73.61 ± 0.84	10.81 ± 0.11
		15	546.42 ± 4.2	59.43 ± 0.31	7.85 ± 0.03
	6000	5	1471.94 ± 45.61	138.2 ± 3.32	22.35 ± 0.58
		10	1143.68 ± 17.69	102.17 ± 1.14	13.18 ± 0.14
		15	941.97 ± 20.85	83.68 ± 1.3	9.69 ± 0.13
	8000	5	2051.76 ± 121	172.35 ± 8.15	26.41 ± 1.4
		10	1505.62 ± 78.13	121.7 ± 4.61	14.78 ± 0.55
		15	1421.79 ± 49	109.84 ± 2.75	11.82 ± 0.27

Table 5.1: Table showing calculated network properties for acellular hydrogels. Table lists mean ± SEM for molecular weight between crosslinks, mesh size, and mass swelling ratio for acellular gels with 0 and 0.5 mM Hep-MA. In both heparinized and non-heparinized gels, with increasing weight fraction, molecular weight between crosslinks decreases. In non-heparinized gels, molecular weight between crosslinks increases with increasing molecular weight. In heparinized gels, this trend is observed from 3400 to 6000 Da, but is not seen at higher molecular weights. In both heparinized and non-heparinized gels, with increasing weight fraction, mesh size decreases. In non-heparinized gels, mesh size increases with increasing molecular weight. Samples marked with different letters are significantly different at

5.4.4 Cell Phenotype Assessment

In gels with weight fractions of 5 and 10 percent (irrespective of molecular weight), the majority of cells were positive for αSMA (Table 5.2). This was maintained in the 15% w/v-3400 Da gel, but lost in the 15% w/v-6000 and 8000 Da gels. P4H positive cells were sparse in all gels, and were not seen at all in the 15% w/v, 6000 and 8000 Da gels (Figure 5.10).

Table 5.2: Percentage of cells expressing alpha smooth muscle actin (top item) and prolyl-4-hydroxylase (bottom item) in each composition of gel. N≥5 for all samples.

Molecular Weight (Da)	Weight Fraction (%)	Percentage of cells expressing marker ± standard error	
		αSMA	P4H
3400	5	0.68 ± 0.06	0.01 ± 0.02
	10	0.70 ± 0.06	0.14 ± 0.02
	15	0.71 ± 0.05	0.02 ± 0.01
6000	5	0.90 ± 0.05	0.06 ± 0.01
	10	0.47 ± 0.06	0.00 ± 0.02
	15	0.72 ± 0.05	0.03 ± 0.01
8000	5	0.56 ± 0.06	0.02 ± 0.01
	10	0.12 ± 0.06	0.00 ± 0.02
	15	0.11 ± 0.06	0.00 ± 0.02

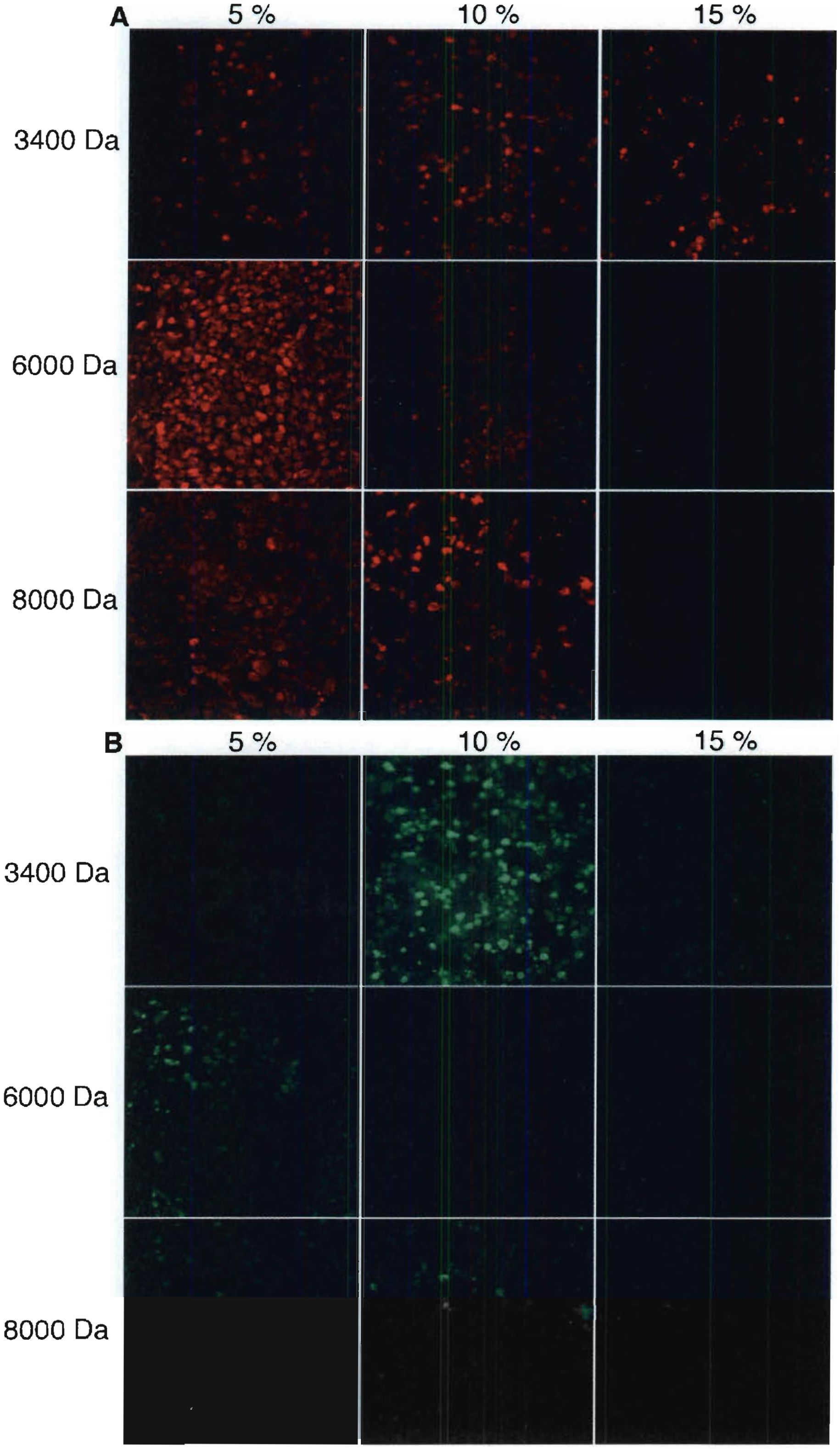
A
5 %
10 %
15 %
3400 Da
6000 Da
8000 Da
B
5 %
10 %
15 %
3400 Da
6000 Da
8000 Da

Figure 5.10: Representative immunostaining of (A) alpha smooth muscle actin and (B) prolyl-4-hydroxylase in cell-encapsulated hydrogels for each composition of hydrogel.

5.5 Discussion

Hydrogels are rapidly garnering interest within the valve community as potential scaffolds for TEHVs, but further investigation is needed about the ability of hydrogels to support the culture of VICs and about their material behavior, particularly in flexure. In contrast to the large body of information about TEHVs generated using polymer meshes or foams, the study of VIC encapsulation within hydrogels is in the nascent stage, with only three studies currently published, albeit with some differences to the hydrogels materials presented in this chapter.[57, 69, 112] The function of VICs encapsulated in PEG hydrogels was investigated in a recent paper by Benton et al.[87] Although previous work has focused on the important characteristics of cell phenotype and function, it is just as relevant to examine material properties, due to both the mechanical demands of the in vivo environment as well as the impact of pericellular substrate stiffness on cell function. Furthermore, since flexure constitutes a major mode of deformation for heart valves, and it is reported that maximum sites of stress are due to flexure in the in vivo environment[3], it is prudent that any potential TEHV scaffold undergoes flexural characterization in vitro. It has been reported that the incorporation of heparin into hydrogels is necessary to maintain the normal phenotype of VICs (in 2D culture), however, recently published data has demonstrated methods to preserve VIC phenotype by careful choice of gel formulations.[2, 87] This data was the motivation for the use of methacrylated heparin in this manuscript. By methacrylating heparin, it can be covalently bonded to the hydrogel bulk and its bioactivity can be retained. The tests performed in this study demonstrated that functionalizing the gels with immobilized heparin caused flexural stiffness to decrease. However, the resulting range of flexural moduli (up to 400 kPa), even in the hydrogels containing Hep-MA (up to 200 kPa) and encapsulated cells (up to 160 kPa), while lower than that of native tissue (703.05 kPa against curvature, 491.69 kPa with curvature[133]; we performed 3-point bending on a limited number of AV leaflets with our tester and obtained results on the same order of magnitude), was on the order of magnitude of both bovine pericardium (400 kPa cross fiber [127], commonly used in bioprosthetic valves) and virgin PGA/PLLA meshes (~250 kPa [53], commonly used for valvular tissue engineering).

The network properties, which were calculated to characterize these hydrogels further, suggested that the incorporation of Hep-MA disrupted network formation by the crosslinked PEGDA. For example, it was expected that lower values for molecular weight between crosslinks would correspond to stiffer gels. Indeed, when considering each hydrogel class (i.e., heparinized) separately, molecular weight between crosslinks followed the expected trends of decreasing with increasing weight fraction and increasing with increasing molecular weight. When comparing gels with and without heparin, the incorporation of heparin did not statistically impact the molecular weight between crosslinks of the resulting gels (with the exception of 6 kDa, 5% and 8 kDa, 5%). This result indicates that there are additional phenomena that govern gel stiffness when heparin is immobilized within the network. One potential explanation is that the negative charge or size of the heparin molecule could be interfering with network formation, thus inhibiting complete crosslinking of the PEGDA gel. This explanation was tested by varying the concentration of Hep-MA in gels in compression and it was confirmed that gels containing 1.0 mM Hep-MA were less stiff than gels containing 0.5 mM Hep-MA (Figure 5.8). To investigate whether this was a size dependent phenomena, gels were doped with unmodified heparin. Gels doped with 0.5 mM heparin were less stiff than gels functionalized with the same concentration of Hep-MA, suggesting that the potential multiple crosslinking sites per heparin molecule increase stiffness, and that chain entanglement is not the only means of retaining the heparin molecule. Collectively, these studies indicate that the negative charge of the heparin molecule is likely inhibiting the formation of radical polymerization sites, and that incomplete crosslinking is obtained when either Heparin or Hep-MA is included. The number of potential reactive sites per heparin-MA chain was calculated to be 2.5. This inhibition of complete crosslinking, however, appears to be mitigated by the inclusion of Hep-MA due to its ability to crosslink with PEGDA (through the reactive sites on the molecule). The other network properties (swelling ratio, mesh size) showed trends that were comparable with molecular weight between crosslinks. Mesh size was additionally investigated to ensure that molecules could diffuse through the gel. Mesh size ranged from ~50-180 Å, which is sufficiently large enough to allow the diffusion of molecules such as IgG.[159]

The finding that the addition of heparin or Hep-MA reduced the flexural stiffness of PEGDA hydrogels was in contrast to the results of Beamish et al., who reported that the incorporation of PEGylated moieties into the gel actually increased the bulk material stiffness.[160] Their finding was also surprising, given that it was expected that these additions would decrease the stiffness due to network interruption. Together, these works emphasize the importance of investigating the mechanical consequences of adding monoacrylated PEG or other functional sequences (peptides, glycosaminoglycans) to these hydrogels, in addition to the effects of these biofunctional moiety inclusion on cell phenotype and synthetic ability, which has received far more attention. The effect of bioactive moiety incorporation on hydrogel mechanics is important, and significant enough to merit its own study.

The incorporation of cells into the hydrogels profoundly decreased flexural stiffness, which was most likely caused by their cytoskeletal stiffness and total volume fraction.[161] This decrease in stiffness seen in cellularized gels could also be due to the high cell concentrations causing UV scattering, thereby decreasing crosslinking efficiency. It is unlikely that cells are either degrading or synthesizing matrix in the amount of time between encapsulation and mechanical testing (48 hours). Because the concentrations of cells typically used in TEHVs are rather high, it is necessary to plan for their effects on hydrogel mechanics.[87, 112] Furthermore, the impact of hydrogel swelling on cells has been understudied. Gel swelling could potentially "prestrain" the encapsulated cells, however, for compositions chosen in this chapter, this effect of swelling was likely modest due to both the small volumetric swelling (the resulting strain is substantially lower than what is typically imparted in a mechanical conditioning study) exhibited by the chosen formulations and the immaturity of adhesions between embedded ligands and cells during the swelling period. Gel formulations with very high molecular weight (20 and 35 kDa, results unpublished) demonstrate very high volumetric swelling and it will be necessary to characterize the mechanical forces imparted due to the cells by swelling phenomena.

The concentration of cells used in this study (22 million cells/ml) is representative of the range of cell concentrations employed in other hydrogel studies.[43, 57, 87, 112] In the future, it will be of interest to evaluate the impact of cell encapsulation on hydrogel mechanics in a concentration-dependent manner. Furthermore, the immunofluorescence showed that as gel stiffness increased, the proportion of cells positive for αSMA decreased. The stiffest gel compositions tested (15% w/v with 6000 and 8000 Da PEGDA, 100 and 150 kPa respectively) showed the lowest proportion of cells expressing αSMA. P4H expression was low throughout all gel compositions, which potentially was due to the short culture duration.

In conclusion, since bending is a major mode of deformation for valves, it is crucial to investigate the flexural properties of the materials being considered as TEHV scaffolds. This study is the first to examine flexure of cell-seeded hydrogels. Understanding the bending behavior of cell-seeded, homogeneous hydrogels will permit the creation and characterization of scaffolds with more complicated architectures in the drive to mimic heart valve tissue mechanics more closely. It is important to note that the hydrogels used in this study lacked any cell-degradable motifs, however these incorporations will be necessary to include as the scaffold architecture becomes more complex to enable the cells to synthesize matrix, migrate, and remodel the scaffold prior to implantation. Furthermore, this work adds to the recent publication by Beamish et al.[160] in demonstrating that the addition of other crosslinkable groups to PEGDA can radically change the mechanical behavior of the hydrogel. It will be important to consider and account for all of these effects in the design of more complex biomaterials.

5.6 Acknowledgements

The authors thank Maude Rowland and Christy Franco for assistance with polymer synthesis and Dr. Elizabeth Stephens for assistance with phenotypic assessment of encapsulated cells. The authors also thank Dr. Sean Moran for assistance with the ^{1}H-

NMR evaluation of samples. The authors would like to thank Alex Brewer and Steve Xu for assistance with development of the physical design of the bending tester. This research was funded by the March of Dimes.

Chapter 6: Fabrication and Mechanical Evaluation of Anatomically-Inspired Advanced Hydrogel Structures[*]

6.1 Introduction

As described in the previous chapter, many traditional hydrogel materials are being investigated for use in heart valve tissue engineering. These materials include natural gel materials such as fibrin, collagen, and hyaluronic acid as well as synthetic materials, such as poly (ethylene glycol) diacrylate (PEGDA). The synthetic class of materials is particularly interesting because they are intrinsically biologically compatible and permit the rapid encapsulation of cells in a cytocompatible environment. Furthermore, synthetic hydrogels can be modified extensively to tune their biochemical and biomechanical characteristics. However, generally these hydrogels do not yet possess sufficient mechanical strength for use in animal models or clinical applications of heart valve replacement. Furthermore, PEGDA hydrogels are fundamentally elastic, isotropic materials, whereas heart valve leaflets are layered, viscoelastic, and demonstrate anisotropic material behavior. These unique material characteristics of the valve leaflet allow the valve to undergo many loading-unloading cycles and a complete reversal of curvature upon opening.[3, 9] Moreover, the layered structure of the leaflet is believed to aid in shielding the cells in the interior layer from high stresses.[134] This chapter will discuss newly developed methods to fabricate quasilaminate structures with each layer having distinct cellularity and material properties. The resulting gels have different bulk material properties than single-component, single-layer (slab) gels. Additionally, this chapter will discuss the incorporation of valve anatomy-inspired patterns of reinforcement into hydrogel slabs. This work forms the basis for fabrication of truly advanced leaflet scaffolds that could address the current physical limitations of basic hydrogels when applied as scaffolds for valve leaflet engineering.

---

[*] The majority of this chapter is being prepared for submission to *Advanced Materials* and will be published as: Durst CA, Cuchiara MP, Lin CJ, West JL, Grande-Allen KJ. Fabrication and Mechanical Evaluation of Anatomically-Inspired Advanced Hydrogel Structures.

6.2 Background

Anisotropy, which refers to something having different properties depending on the direction of measurement, is widely observed in biological tissues, and arises due to the specific mechanical demands placed on the tissue. It is commonly seen in load bearing tissues such as heart valve leaflets, aortic tissue, intervertebral discs, cartilage, and connective tissue (e.g. tendons and ligaments). Most tissues exhibiting anisotropy behave in a similar manner as soft fiber-reinforced composites, in which the fiber and matrix can dissipate energy by large inelastic deformations[162]. The anisotropy of valve leaflets allows them to withstand the complex mechanical environment imparted by the heart. During the cardiac cycle, leaflets are exposed to shear, tension, compression, flexure, or a combination of any of these phenomena. The valve undergoes large radial elongations and a complete reversal of curvature during opening and closing, and the layered, anisotropic nature of the leaflet permits this movement.[9] In the aorta, the high circumferential strength of the tissue is governed by the preferential orientation of fibers and multiple lamina, permitting the aorta to withstand high pressure without failure.[163] Intervertebral discs are comprised of the annulus fibrosus (fibrocartilage) which surrounds the nucleus pulposus (gelatinous).[164] The annulus fibrosus is anisotropic and comprised of concentric layers of aligned collagen fibers and proteoglycans.[165] The gelatinous nature of the nucleus pulposus gives resistance to compression (dissipation of energy hydrostatically).[166] This geometry yields a tissue that is able to distribute and absorb the large complex loading (a combination of tension, shear, compression, and bending) imparted by the spine.[164, 167] In general, native tissues demonstrate anisotropy as part of a unique material behavior that allows the tissue to maintain proper function in its *in vivo* mechanical environment.

The aortic valve is a multilayered structure, with each layer possessing distinct ECM components (described in Section 2.1.3). The orientation and mechanical characteristics of these components gives each layer unique material properties, in addition to giving the overall leaflet anisotropic, viscoelastic behavior. For example, the corrugations found in fibrosa layer give the leaflet its characteristic high extensibility when strained in the radial direction, while the circumferential orientation of crimped collagen fibers allows for some extension (while the collagen is uncrimping) before the load is primarily borne by the collagen fibers.[167-169] Crimp period and amplitude corresponds to the degree of circumferential extensibility exhibited by the leaflet.[170] Furthermore, since each layer has distinct ECM components, the stiffness of each layer is distinct.[12] The varying stiffness found in the valve (with the center layer, the *spongiosa* exhibiting the lowest stiffness) is thought to shield the cells within from the majority of the significant stresses generated during valve opening and closure.[134]

Furthermore, the highly hydrated nature of the spongiosa (due to its rich proteoglycan content), gives the valve its compressive load-bearing ability.[154] These layer-specific properties allow the valve to undergo many cyclic loading-unloading cycles during the cardiac cycle. The purpose of this study was to implement methods for generating (i) a range of bio-mimetic anisotropic features and (ii) layered structure within poly(ethylene glycol) diacrylate hydrogels. We hypothesized that developing methods to mimic these microstructural features would create an improved scaffold for valve tissue engineering, as well as having broad applicability to engineering of other layered or anisotropic tissues.

Anisotropic tissues have been modeled as soft fiber-reinforced composites.[162, 167, 171, 172] In this case, we have assumed that the essential anisotropic aspects of the valve behavior are generated by collagen embedded within a softer matrix, which inspired our experimental hydrogel architecture. We hypothesized that the bulk anisotropic behavior of valve leaflets could be mimicked by the combination of a soft hydrogel matrix (8 kDa MW, 5% w/v) with stiff hydrogel reinforcements (3.4 kDa MW, 15% w/v). The reinforcements were designed to replicate collagen fibers, with reinforcement thicknesses of either 88 or 176 μm, a crimp period of 10 mm, and a crimp amplitude of 2 mm.[173] This reinforcement was accomplished using 2D photolithographic patterning (PLP) techniques that were initially developed for semiconductor fabrication and recently applied to soft hydrogels in Dr. Jennifer West's laboratory.[65, 78] Other potential ways of creating true fiber reinforcements could include directly embedding polycaprolactone (PCL) fibers in hydrogels, which our group is also beginning to pursue. While this latter approach will yield a true fiber-reinforced soft material, it employs electrospinning. Electrospinning permits the fabrication of anisotropic meshes, but is highly sensitive to operating parameters.[174] In addition, electrospinning operating conditions can be damaging to cells, so cells must be seeded post-fabrication.[118, 174, 175] Other groups are investigating inducement of anisotropy in hydrogels by application of strain while polymerizing (using freeze-thaw crosslinking)[88], control of secondary crosslinking by patterning [89], and direct embedding of fibers[90, 91], however, many of these methods prohibit the direct encapsulation of cells.

In contrast, PLP is an inexpensive, fast method that can control spatial diffusion of a secondary interpenetrating polymer network within a hydrogel. This patterning technique has been previously used to create high fidelity patterns with distinct edges in hydrated PEGDA gels.[78] This technique employs the use of a photomask, which is printed on acetate from a traditional high-resolution printer. The mask is then laid on a hydrogel soaked in the unpolymerized secondary polymer solution, and re-exposed to UV light. In the previous study, a variety of complex geometries with high fidelity were achieved, with minimum feature size of ~40 μm.[78] This technique was originally used for creation of distinct patterns of bioactivity, but has since been used to create distinct patterns of elasticity.[65] Nemir *et al.* showed that significant differences in bulk modulus could be achieved between the reinforcement direction and the lateral direction (0° and 90° to pattern direction, respectively). The PLP technique was similarly employed in this work to generate anisotropic patterns generally mimicking those found in heart valve leaflets.

Layered hydrogel structures have been reported infrequently in the literature over the previous 15 years, exploiting a variety of "lamination" strategies. Lu *et al.* demonstrated a multilayer fabrication technique using poly(hydroxyethyl methacrylate) and diethylene glycol methacrylate that allowed photocrosslinking of multilayered hydrogel structures where each layer had the same formulation.[92, 93] These studies were performed to characterize a drug delivery technology, where material properties were not a primary concern. As a result, no mechanical data was available from these initial reports. The studies performed by Lu *et al.* informed the design of the serial layering method described in Section 6.3.5.1. The first (and to our knowledge, only) published study demonstrating hydrogel layering where each layer had distinct composition was performed by Temenoff *et al.* using a oligo(PEG fumarate) with molecular weights of 860, 3900 and 8900 Da chemically crosslinked with PEGDA (molecular weight of 575 Da).[85] The 1st OPF:PEGDA mixture was injected into a mold, allowed to crosslink for 15 minutes at 22 °C, and then the second layer was added and crosslinking was completed at 60 °C for an additional 15 minutes. Temenoff *et al.* showed that a strong interface between layers with different compositions could be achieved. Furthermore, these studies showed that differential swelling as a result of using varying formulations in each layer was a significant problem that needed to be accounted for, since it frequently resulted in gel tearing. More recently, Cuchiara *et al.* demonstrated that PEGDA could be serially molded with PDMS to produce microfluidic channels. This method demonstrated that PEGDA of the same composition could be self-layered using a photocrosslinking method. The method used in this chapter is analogous to the sandwich layering method described in Section 6.3.5.2 and was developed in parallel with the methods published in the manuscript by Cuchiara *et al.*[79] These methods served as the foundation for both the developed serial and sandwich layering techniques described in this chapter. While these studies served as a guide for the work performed in our studies, the research presented in this chapter represents the first successful efforts to: (i) fabricate trilayer composite hydrogels, (ii) rigorously test the interface strength of multilayer photopolymerized hydrogel structures, (iii) mechanically characterize multilayer PEGDA scaffolds with layer-specific composition.

6.3 Materials and Methods

6.3.1 Study Design and Statistical Analysis

The objective of this study was to apply advanced hydrogel fabrication techniques to mimic the anatomic features of the aortic valve that promote the unique material behavior of the leaflets. We believe that by incorporating properties that allow the hydrogel to approximate more closely the behavior of the native tissue, a superior TEHV scaffold will be realized. Furthermore, development of these techniques will have applicability to diverse tissues, such as those listed in Section 6.2.

For an overview of the research design, this work was divided into two studies: layering and patterning. First, the layering method was evaluated by preparing hydrogels with layers of distinct composition (quasilaminate gels). These gels were then subjected to interfacial failure testing to find the optimal formulation for a quasilaminate gel. The "stiff-soft-stiff" quasilaminate gels were prepared both with and without cells, tested in flexure, and compared with acellular and cellular single layer controls. Additionally, cells encapsulated in quasilaminates were imaged with a confocal microscope to verify that viable cells remained after the layering procedure. Second, patterned gels were prepared across a sample space that contained a variety of feature thicknesses, while holding fixed the total amount of patterned material. These gels were then subjected to uniaxial tensile testing to determine the presence of anisotropy and the relative contribution of the pattern to the material behavior. Sample sizes were chosen based on prospective statistical power calculations. Using two-way ANOVA comparison of the row*col means, where detectable contrast was set at 0.4, standard deviation was set at 0.2 [83, 84], and n=10, statistical power was observed to be 0.9296.

Statistical analyses of stiffness and interface strength were performed using JMP (SAS Software, Cary, NC). Where appropriate, either one- or two-factor ANOVA was performed and fit to a least squares model. Sample group means were compared with post-hoc Tukey-Kramer HSD and $\alpha=0.05$. When represented visually, data was expressed as mean ± standard error.

6.3.2 Polymer Synthesis

PEGDA was prepared using previously described methods (Section 5.3.3). Gels were polymerized from pure PEGDA and did not contain any additional bioactive moieties. The photoinitiator 2-Hydroxy-4′-(2-hydroxyethoxy)-2-methylpropiophenone was dissolved in ethanol at 10% (w/v) and added to the prepolymer solution at 3% (v/v).

The resulting solution was sterile filtered before use and polymerized as described below (Sections 6.3.5.1, 6.3.5.2, and 6.3.6).

6.3.3 Cell Culture

Cell culture was performed in the same manner as in Section 5.3.2.

6.3.4 Interface Strength Testing

To ensure that the layering technique yielded robust interfaces that would remain bonded during handling and culture, the strength of the interface was tested. Additionally, it was necessary to investigate what "soft" formulation would yield the strongest bond. For the purposes of this chapter, the higher stiffness polymer formulation will be referred to as prepolymer A, and the lower stiffness hydrogel formulation will be referred to as prepolymer B. Prepolymer A was selected to have a molecular weight of 3.4 kDa and a weight fraction of 12.5%. Previous experiments (Table 5.1) showed that this formulation swells compatibly with a range of other PEGDA formulations. Prepolymer B was either 6 kDa, 10% (w/v) or 8 kDa, 5% (w/v). Layered gels were prepared by filling a 1" x 3" mold halfway with prepolymer A, exposing for 4.5 minutes, and then filling completely with prepolymer B and re-exposing for 10 minutes. The resulting gels were swollen for 48 hours in cresyl violet acetate in PBS (0.4 mg/mL) to visualize the stiffer (top) layer (Figure 6.1). The gels were punched into a dogbone shape for uniaxial tensile testing where the interface was placed at the center of the dogbone (Figure 6.2). The punched dogbone-shaped strips were then glued to 1 x 1 cm pieces of paper with Loctite 401

(Loctite, Dusseldorf, Germany). The pieces of paper were then loaded into the grips of an Instron Model 3340 (Instron, Norwood, MA) uniaxial mechanical tester and pulled to failure at a rate of 6 mm/min. The maximum stress of the 5 samples acquired by the software prior to failure was averaged to obtain the failure stress value for each hydrogel specimen. All experiments were recorded with high-speed videos, which were later analyzed to ensure that the samples did not fail at the layer interface.

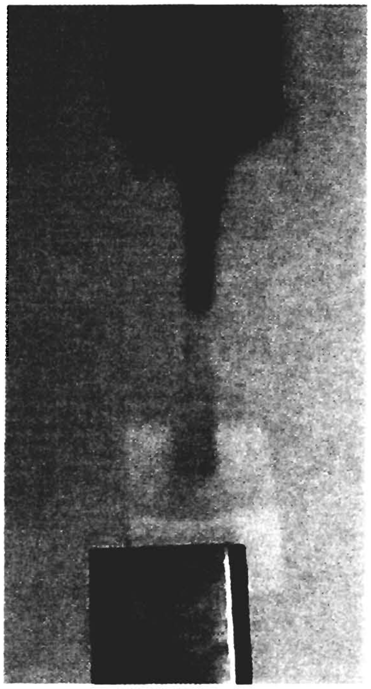

Figure 6.1: Dogbone punched hydrogel strips loaded in mechanical tester for interface strength determination. The stiff layer can be seen in purple at the top, and the soft layer has the faint violet tint at the bottom.

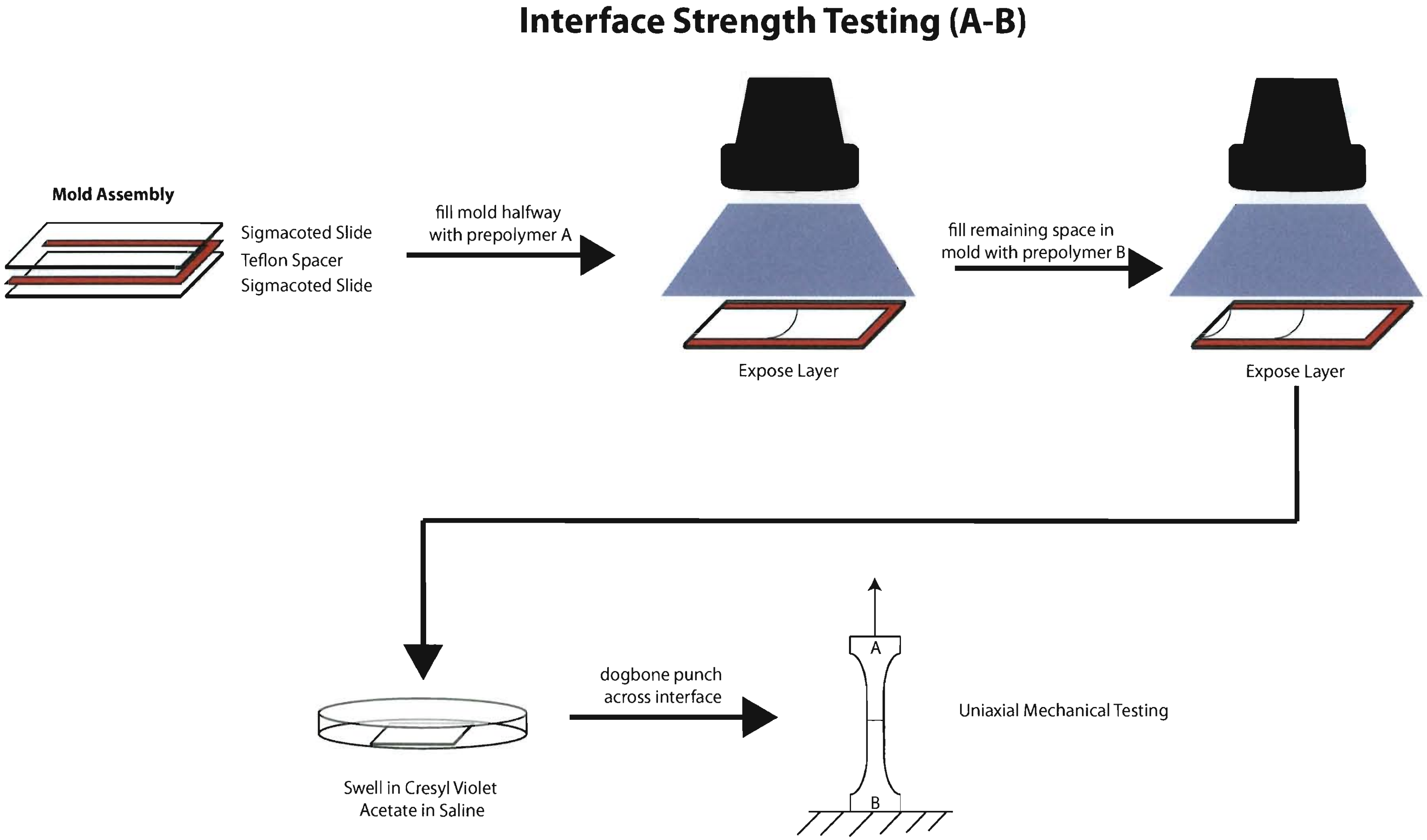
Interface Strength Testing (A-B)
Mold Assembly
Sigmacoted Slide
Teflon Spacer
Sigmacoted Slide
fill mold halfway with prepolymer A
Expose Layer
fill remaining space in mold with prepolymer B
Expose Layer
Swell in Cresyl Violet Acetate in Saline
dogbone punch across interface
A
B
Uniaxial Mechanical Testing

Figure 6.2: Schematic depicting interface strength testing of quasilaminates. Samples were imaged during testing and pulled to failure.

6.3.5 Layering

Trilayer quasilaminate gels were fabricated with A-B-A architecture, where the A layers were of different composition than the B layer. The A layers were of higher stiffness due to their lower molecular weight and higher weight fraction than the B layer. A was composed of 12.5% (w/v) 3400 kDa PEGDA and B was composed of 10% (w/v) 6000 kDa PEGDA. Single layer controls were prepared for both the A and B formulations. Since the B layer was the only layer to be cellularized in the quasilaminate, acellular and cellular single layer controls were prepared for this formulation to elucidate the effect of cell encapsulation on stiffness.

6.3.5.1 Serial Layering

Quasilaminate gels were prepared using a serial layering technique when desired layer thickness was greater than 1.0 mm (Figure 6.3). First, molds were prepared by coating 3" x 2" glass slides with Sigmacote (Sigma, St. Louis, MO), a silicone surface-coating lubricant in heptane, yielding glass slides with a tough, slick coating. The slides and PTFE spacers were then steam sterilized in an autoclave. Spacers with desired strip geometry and thickness were placed between two coated slides. The resulting well was filled with the first prepolymer solution and exposed to UV light for 7 minutes. One slide was removed, an additional spacer was added, and the slide was replaced. The resulting space was filled with the next prepolymer solution, which was allowed to diffuse into the gel for a minimum of 4 hours. The next layer was fully crosslinked with UV exposure for 7 minutes. This process can be iterated stepwise to achieve the desired number of layers.

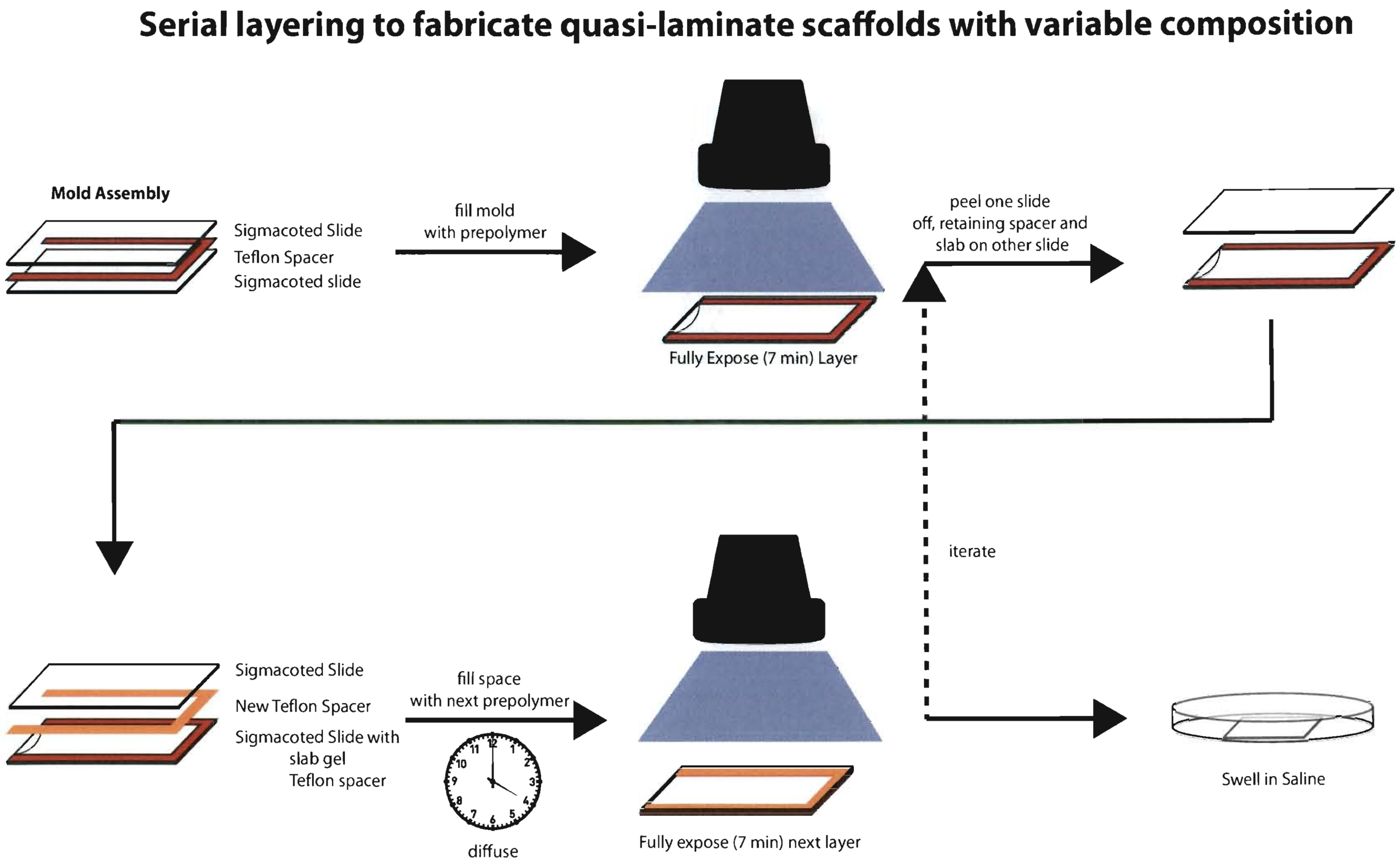
Serial layering to fabricate quasi-laminate scaffolds with variable composition
Mold Assembly
Sigmacoted Slide
Teflon Spacer
Sigmacoted slide
fill mold
with prepolymer
Fully Expose (7 min) Layer
peel one slide
off, retaining spacer and
slab on other slide
iterate
Sigmacoted Slide
New Teflon Spacer
Sigmacoted Slide with
slab gel
Teflon spacer
fill space
with next prepolymer
diffuse
Fully expose (7 min) next layer
Swell in Saline

Figure 6.3: Schematic depicting multilayer quasilaminate scaffold fabrication with serial layering approach. This fabrication technique can be used to generate scaffolds with layers between 1.0-2.0 mm and differing composition

6.3.5.2 Sandwich Layering

When desired layer thickness was below 1.0 mm, a sandwich layering technique was used to ensure reliable bonding between layers. Again, molds were prepared by coating 3" x 2" glass slides with Sigmacote (Sigma, St. Louis, MO), a silicone surface-coating lubricant in heptane, yielding glass slides with a tough, slick coating. The slides and PTFE spacers were then sterilized in an autoclave. Spacers with the desired strip geometry and thickness were sandwiched between one untreated slide and one slide coated with Sigmacote (Figure 6.4). Prepolymer solution A was pipetted into the molds and two filled molds were exposed to longwave UV light at the same time. The untreated slide was placed closest to the illumination source for 4.5 minutes. Following exposure, the slide coated with Sigmacote was removed; resulting in an underexposed (gelatinous) slab remaining adhered to the untreated slide. Next, another PTFE spacer was added and the two slides with underexposed gels were brought together (yielding an A-empty-A assembly, 3 spacers used total). This technique is shown in Figure 6.4. Prepolymer B was added to the void between slab gels and the assembly was exposed to UV irradiation for 10 minutes, rotating 180° about the length and width of the slide at 5 minutes.

6.3.6 Photolithographic Patterning

Photolithographic patterning was used to impart regions of stiffness to hydrogel scaffolds. Pilot studies to investigate feasibility of various pattern geometries and contribution of reinforcement to bulk stiffness were performed. Masks used in pilot studies were created from custom MATLAB code to generate biologically inspired

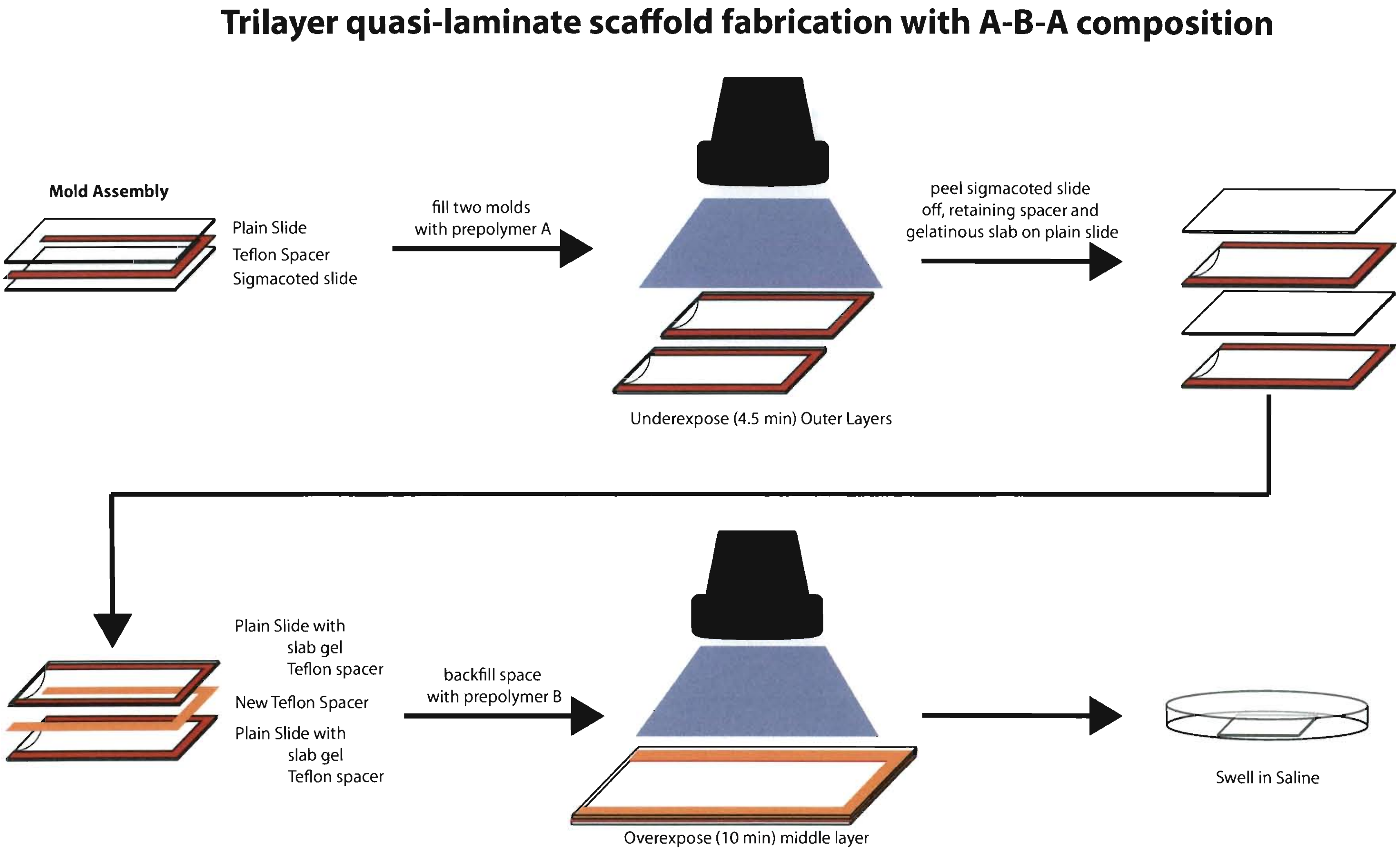
Trilayer quasi-laminate scaffold fabrication with A-B-A composition
Mold Assembly
Plain Slide
Teflon Spacer
Sigmacoted slide
fill two molds with prepolymer A
Underexpose (4.5 min) Outer Layers
peel sigmacoted slide off, retaining spacer and gelatinous slab on plain slide
Plain Slide with slab gel Teflon spacer
New Teflon Spacer
Plain Slide with slab gel Teflon spacer
backfill space with prepolymer B
Overexpose (10 min) middle layer
Swell in Saline

Figure 6.4: Schematic depicting trilayer quasilaminate scaffold fabrication with A-B-A composition. This fabrication technique can be used to generate thin (less than 1.5 mm thick) scaffolds with different stiffnesses and cellularity in each layer.

patterns including linear reinforcement, “skewed” reinforcement (random linear stripes with ± 25° from the long axis of the mask), and sinusoidal reinforcement. Pilot data suggested that stripe and sinusoidal patterns were the most likely to demonstrate anisotropic tensile behavior, so these were tested more rigorously while holding total coverage fixed. For final PLP studies, patterns were created using Adobe Illustrator. Parameters that were varied for both linear and sinusoidal patterns were stripe thickness, stripe spacing (as a function of total coverage). Negative (inverted polarity) versions of these patterns were then transferred to acetate sheets by CAD/Art Services (Bandon, OR) at 10,000 dpi, resulting in high-resolution photomasks (Figure 6.5).

To create pattern-reinforced gels, slab gels were generated by pipetting polymer B (5% w/v, 8 kDa) into a mold comprised of two slides coated with Sigmacote separated by a 0.5 mm PTFE spacer. This was exposed to UV light for 7 minutes, rotating 180° about the length and width of the slide at 3.5 minutes. These slabs were then swelled in a solution of prepolymer A (15% w/v, 3.4 kDa) supplemented with initiator under argon at 22 °C on a shaker table overnight. To pattern, molds were prepared by taping either a pure black strip or patterned piece of acetate (both 1” x 3”) emulsion side up to a plain slide to give a black background and the patterned mask. A PTFE spacer with the thickness of the swollen gel was placed on top of the black background, the slab gel positioned inside the spacer (trimmed to fit), and the patterned slide was then laid on this assembly with the patterned acetate in direct contact with the hydrogel (Figure 6.6). This assembly was then exposed to UV light for 10 minutes, rotating 180° about the length and width of the slide at 5 minutes. The uncrosslinked prepolymer was diffused out by placing the patterned gel in PBS on a rocker table for 48 hours (changes of PBS at 1, 2, 12, and 24 hours). Patterns were visualized by soaking the gels in a solution of cresyl violet acetate (0.2 mg/mL, Sigma, St. Louis, MO) in PBS for 4 hours.

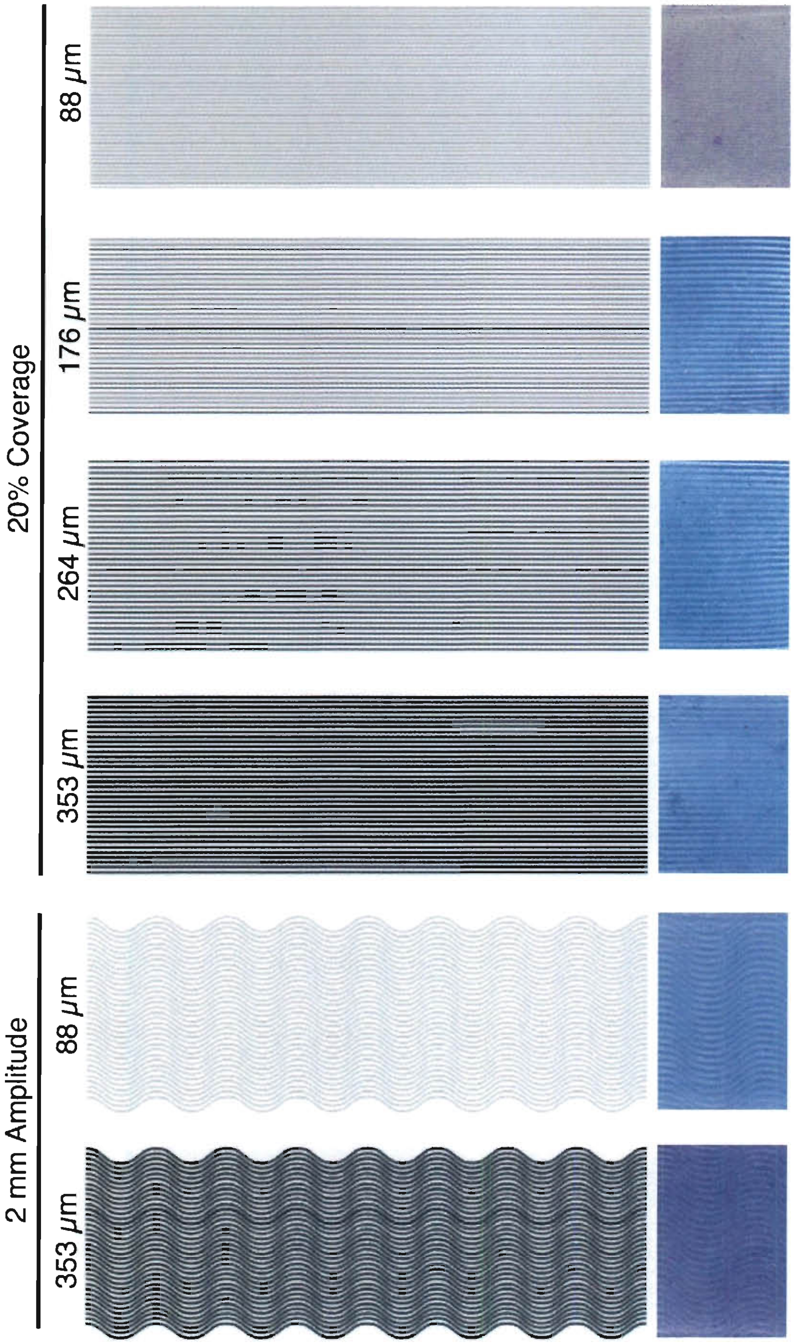
20% Coverage
88 μm
176 μm
264 μm
353 μm
2 mm Amplitude
88 μm
353 μm

Figure 6.5: Photomask patterns tested for generating anisotropic gels. The first four linear patterns have the same level of total coverage, while varying the thickness of the patterned stripes (number shown in microns); as a result, spacing between stripes changes. The sinusoidal patterns have the same amplitude and period, but thickness of the pattern is varied.

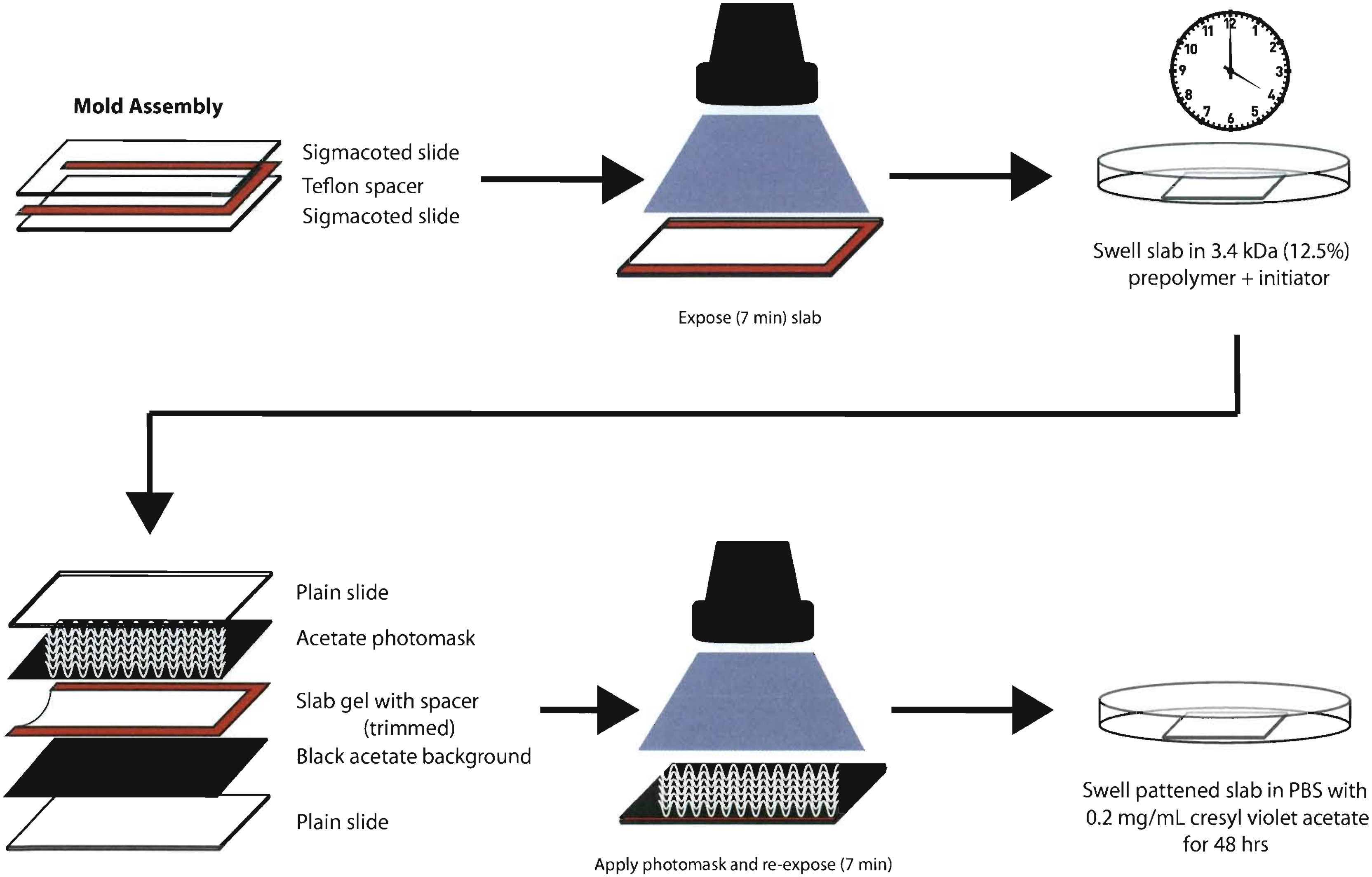
Mold Assembly
Sigmacoted slide
Teflon spacer
Sigmacoted slide
Expose (7 min) slab
11 12 1 10 2 9 3 8 4 7 6 5
Swell slab in 3.4 kDa (12.5%) prepolymer + initiator
Plain slide
Acetate photomask
Slab gel with spacer (trimmed)
Black acetate background
Plain slide
Apply photomask and re-expose (7 min)
Swell pattened slab in PBS with 0.2 mg/mL cresyl violet acetate for 48 hrs

Figure 6.6: Schematic depicting photolithographic patterning of hydrogels to yield bulk anisotropy.

6.3.7 Modeling of Photolithographically Patterned Gels

Since the potential number of parameters that could be varied for the PLP gels was quite high, particularly the sinusoidally patterned gels, simple finite element modeling with COSMOSWorks (Dassault Systèmes, Concord, MA) was performed in an attempt to predict bulk material behavior. Known material properties for PEGDA hydrogel formulations were input to SolidWorks as custom materials. Sinusoidal amplitude, spacing, and number of features was varied. The gels were then set with fixed geometry on the left edge, and a planar boundary on the right that could translate in one-dimension (similar to a uniaxial mechanical tester). Von Mises stress was used to probe the stress distribution throughout the gel. Additionally, "simulated mechanical testing" was performed by running a series of simulations with applied loads ranging from 9.81×10^{-3} to 3.924 N and then calculating the bulk strain in the gel. The applied stress was calculated and the simulated stiffness of the bulk was calculated. This simulated testing was performed to determine if the sinusoidally patterned gels deformed in a non-linear manner.

6.3.8 Flexure Testing of Quasilaminates

Flexure tests of the quasilaminates were preformed as in Section 5.2.5. To briefly summarize, samples were loaded in a custom 3-point bending tester and deformed at a rate of 1.5 mm/min to a maximum linear deformation of 6 mm. Sample deformation was tracked optically with a Canon Rebel T2i recording high definition video at 60 frames per second. The resulting video was demultiplexed into 24-bit TIFF images and analyzed with parallel Matlab code that performed digital image correlation similar to what was described in Chapter 5. Because these calculations were extremely computationally demanding, they were performed using the distributed computing feature of Matlab on SUG@R (Shared University Grid @ Rice).

6.3.9 Mechanical Testing of Photolithographically Patterned Gels

Uniaxial tensile testing was performed as above (Section 6.3.4) with the following modification. Patterned gels were punched with the dogbone punch at either 0° (along the length of the 1" x 3" slab, hereby referred to as "with" direction) or 90° (along the width of the slab, hereby referred to as "perp" direction). These gels were then loaded into the tensile testing system as described in section 6.3.4 and tested in the same fashion.

6.4 Results

6.4.1 Layering Results

Pilot studies using the serial layering method yielded quasilaminates that were strongly adherent at layer thicknesses that were greater than 1.0 mm (Figure 6.7), however, when this was scaled down to a thickness that was appropriate for flexure testing, spontaneous delamination of one or more layers was commonly observed.

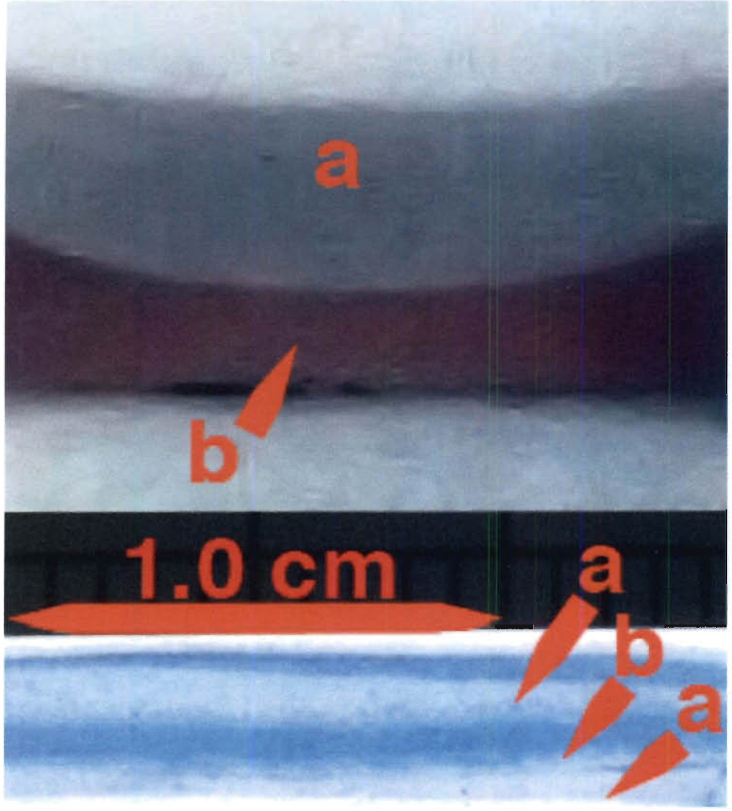

Figure 6.7: Quasiaminates formed with serial layering method. Bilayer and trilayer quasilaminates could be formed with this method, however, they could not be formed with layers under 1.0 mm in thickness. "a" a higher molecular weight polymer, and "b" is a lower molecular weight polymer. Preferential cresyl violet staining can be seen in the higher stiffness layers. The top gel was formed in a steel mold, and the curving interface was a result of surface tension.

Regardless of the formulation chosen for the "soft" layer (prepolymer B), gels did not fail at the layer interface when prepared using the sandwich layering method (Figure 6.8A) Since the gels with soft layers having low molecular weight and high weight fraction (6 kDa/10%) showed a much higher failure stress than the gels with high molecular weight and low weight fraction (8 kDa/5%), the low molecular weight with high weight fraction (6 kDa/10%) formulation was chosen for layering studies (Figure 6.8B). The higher failure stress could be accounted for by the increased stiffness shown by the low molecular weight-high weight fraction gels, resulting in a higher stress at analogous deformations.

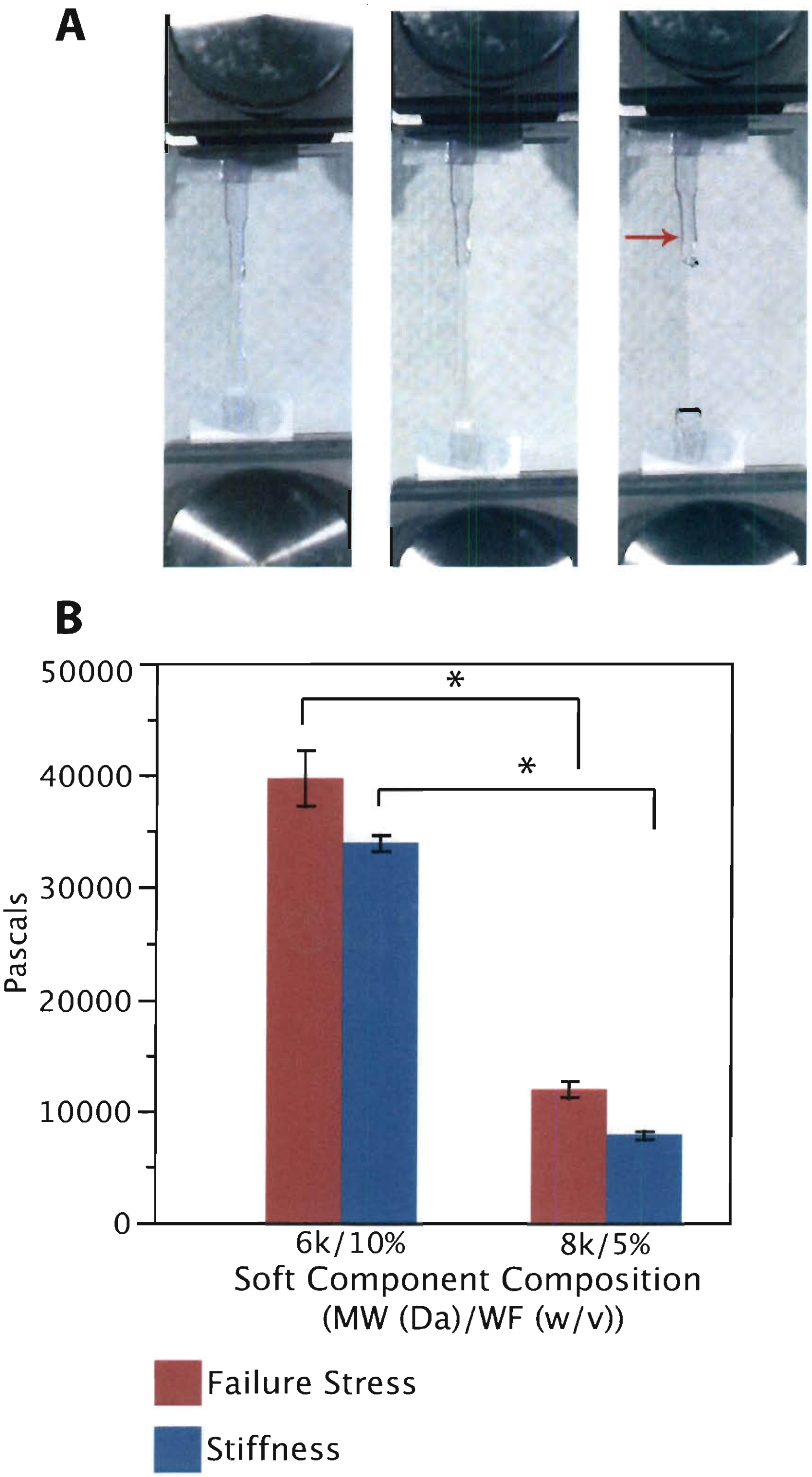

Figure 6.8: A) Representative images of tensile interface strength test demonstrating that failure does not occur at the interface between layers. The interface between layers is highlighted with the red arrow in the far right panel. B) Mean failure stress and bulk modulus for uniaxial tensile testing of quasilaminates. N≥10 for all samples. * denotes significance with $p < 0.0001$.

Quasilaminates prepared with the sandwich layering method were significantly stiffer than both of the single-layer, single component gels (Figure 6.9). Since the inner layer of the quasilaminates was the only PEGDA formulation that was to be cellularized (in the experimental design), single layer controls were prepared both with cells and acellularly. In doing so, the effect of encapsulated cells on the flexural stiffness could be probed. Since the outer layer of the quasilaminates was not to be cellularized, this step was omitted for a single layer control. The encapsulation of cells at the concentrations used in this study did not significantly alter stiffness of the gels, so the acellular and cellular samples were pooled for comparisons of means. At cell densities above $10 * 10^6$ cells/mL, cell encapsulation significantly impacts scaffold modulus, but at lower cell densities this appears to not be significant (as evidenced by Chou *et al.* and confirmed in data presented in Chapter 5 and here).[176] Additionally, PEGDA can not be remodeled by the cells, and the culture durations were too short (2 days) for significant ECM synthesis to occur. Quasilaminates swelled to a mean thickness of 1.93 mm (1.5 mm original thickness, 128% of original), 3.4k/12.5% single layer controls swelled to a thickness of 1.0288 mm (1.0 mm original thickness, 103% of original), and 6k/10% single layer controls swelled to a thickness of 1.1053 mm (1.0 mm original thickness, 111% of original).

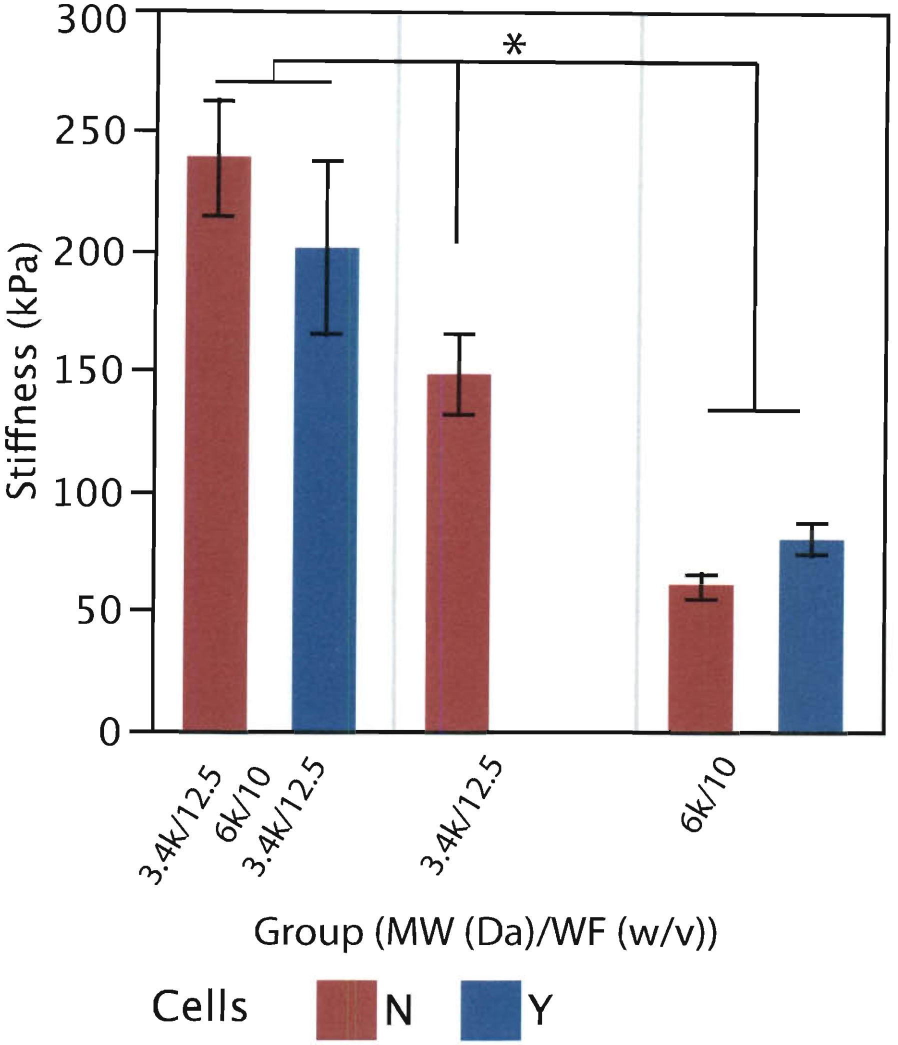

Figure 6.9: Flexure testing of quasilaminate hydrogels. The bulk flexural modulus of trilayer gels was higher than for the single layer bulk slab gels. The inclusion of cells did not significantly affect scaffold stiffness for either the softer single layer gels or the quasilaminate gels (in which cells were embedded in the softer inner layer only). Quasilaminates were significantly stiffer than both single layer gels and * denotes $p < 0.05$.

6.4.2 Behavior of Modeled Photolithographic Patterned Gels

Internal stress analysis demonstrated that because of the vast difference in stiffness between the matrix (soft component) and the “fiber” (stiffer pattern), the reinforcement bore most of the stress due to bulk applied load (Figure 6.10). As the number of patterned reinforcement elements was increased, the matrix bore nearly zero load. It is important to note that the model assumed that there was no slip between the reinforcement and the bulk matrix.

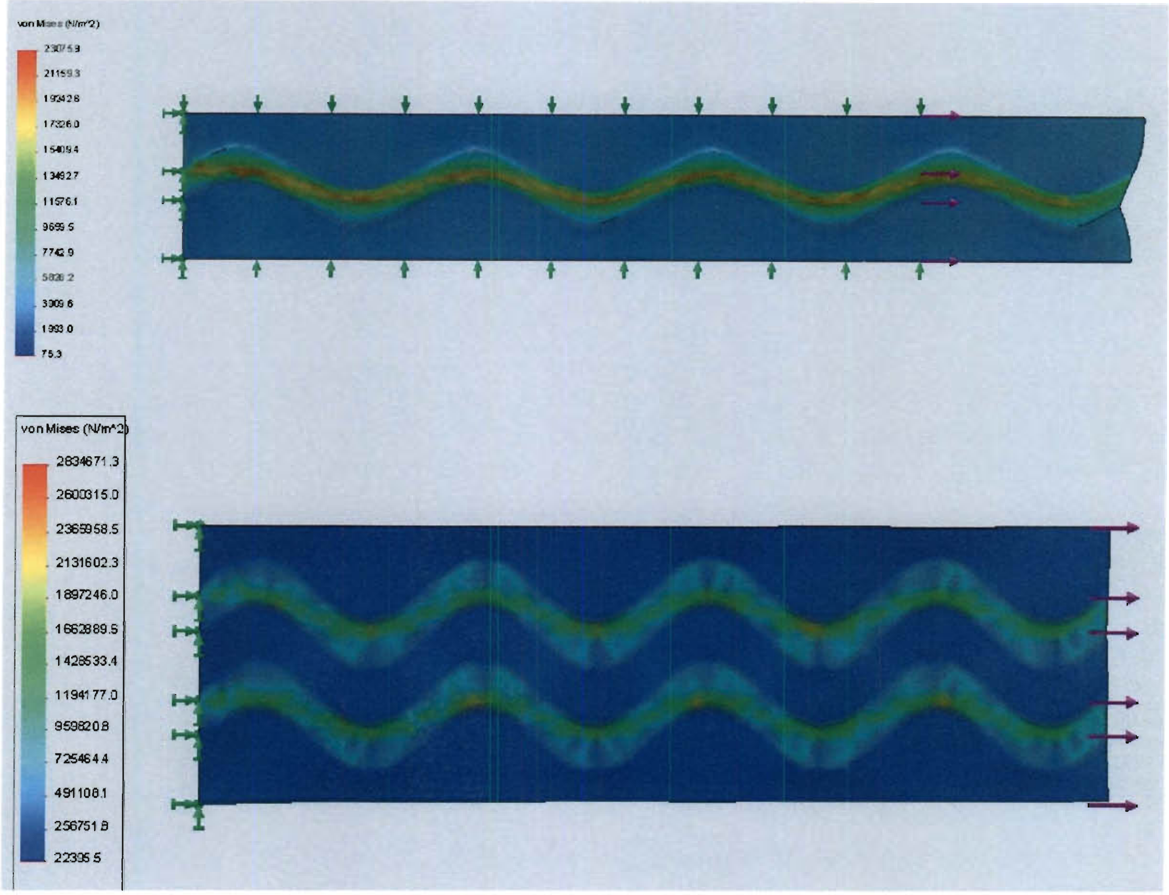
von Mises (N/m^2)
23075.9
21159.3
19242.6
17326.0
15409.4
13492.7
11576.1
9659.5
7742.9
5826.2
3909.6
1993.0
75.3
von Mises (N/m^2)
2834671.3
2600315.0
2365958.5
2131602.3
1897246.0
1662889.5
1428533.4
1194177.0
959820.8
725464.4
491108.1
256751.8
22395.5

Figure 6.10: Simplified finite element analysis of scaffold deformation when reinforced with sinusoidal patterns of increased stiffness. The patterned regions bear the majority of the load applied to the bulk.

Simulated mechanical testing showed that the sinusoidally patterned gel models showed linearly elastic behavior over the range of loads applied (Figure 6.11), in contrast to the desired nonlinear behavior. This behavior was confirmed when actual uniaxial tensile testing was performed on pattern-reinforced hydrogels, where the physical gels demonstrated linear-elastic behavior from 0-100% strain (as shown in the following section).

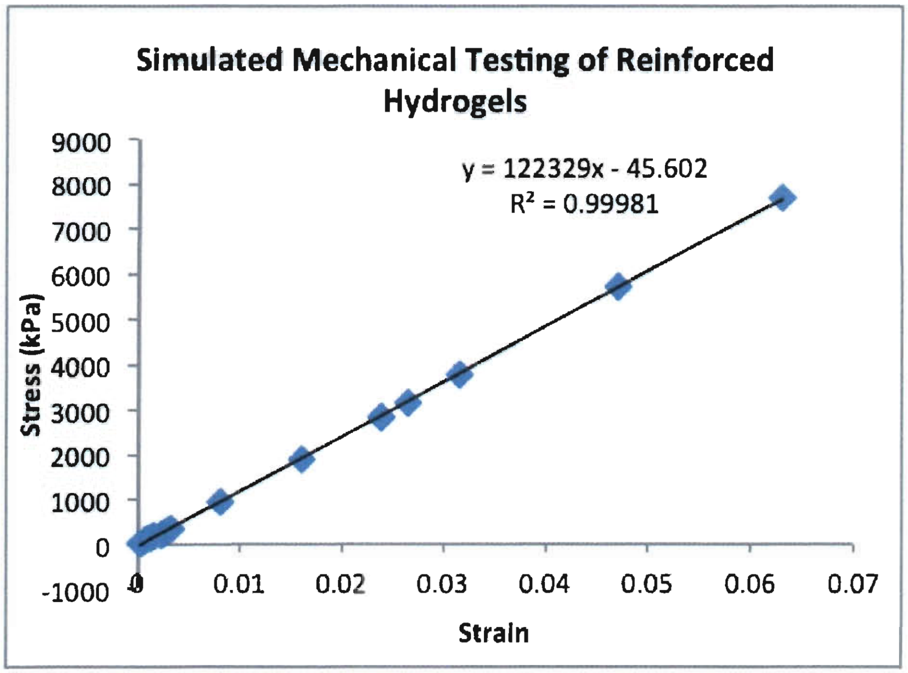

Figure 6.11: Simulated loads ranging from 9.81 x 10-3 to 3.92 N were applied to a FEA model of sinusoidally reinforced hydrogel. Bulk strain was calculated and the resulting stress-strain curve was plotted. In contrast to expected results, no nonlinear behavior was observed (linear fit r2=0.99981).

6.4.3 Mechanical Properties of Photolithographically Patterned Gels

Pilot studies were performed to investigate the feasibility of fabricating desired patterns (particularly sinusoidal patterns, Figure 6.12) at the feature size desired and to gain insight as to what parameters were most influential parameters on bulk stiffness. The patterns were imaged with cresyl violet acetate, which preferentially remains in the patterned (interpenetrating network) part of the gel. Initial samples showed that patterns of desired geometry and size yielded a range of stiffnesses in the bulk material (Figure 6.13).

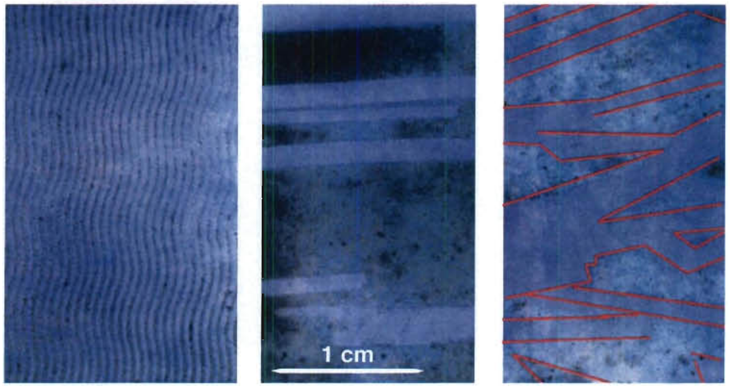

Figure 6.12: Patterns used to investigate feature size and geometry. Pattern on right ("skewed fibers") was highlighted with red lines to aid in visualization. Patterns were generated with custom MATLAB code available in Appendix VII. Dark purple indicates regions of pattern reinforcement and light purple is unpatterned gel.

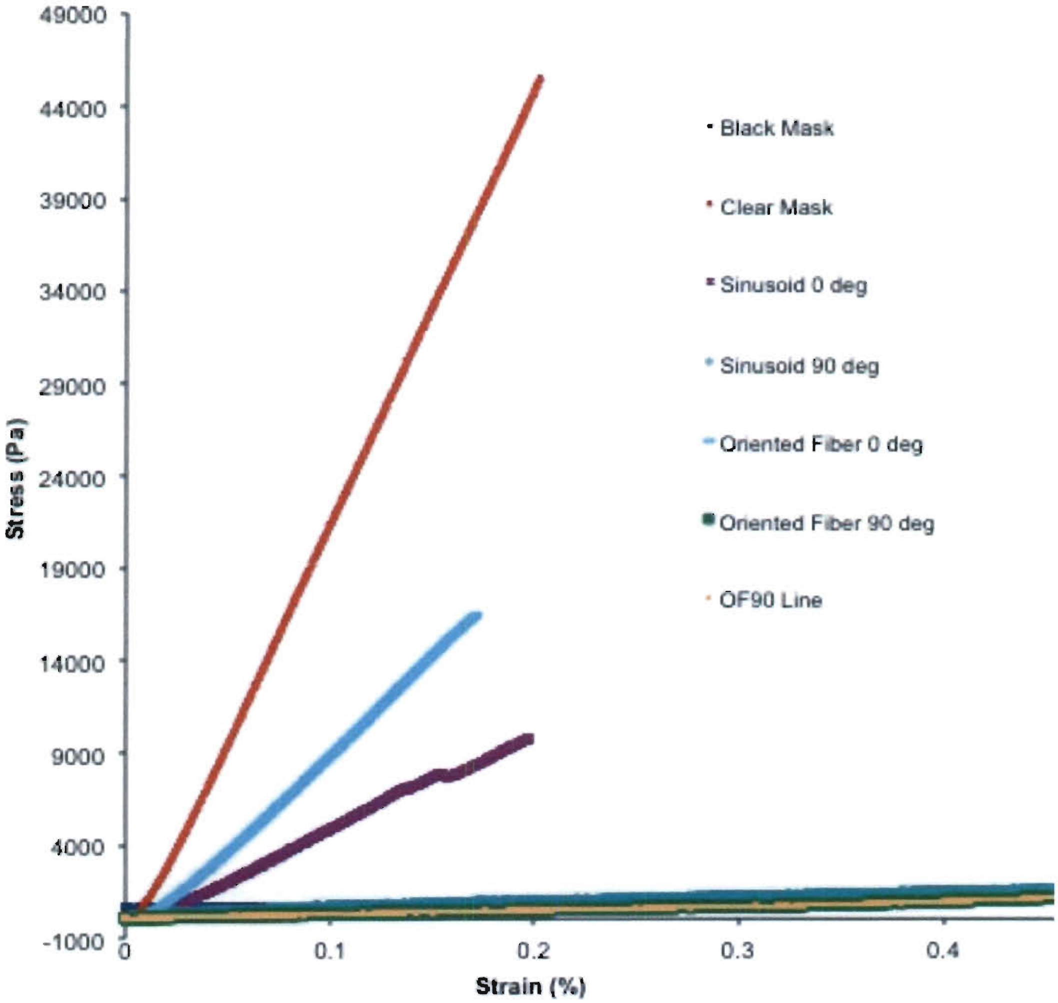

Figure 6.13: Stress strain curves for a variety of patterns used in pilot study to investigate feasibility of desired feature size and geometry.

Patterned gels tended to be stiffer as pattern thickness increased while holding the total amount of pattern coverage fixed (Figure 6.14A). For gels patterned with stripes, the 353 μm pattern showed the highest stiffness (significantly stiffer than all other stripe groups except 264 μm, where anisotropy was observed). For gels patterned with sinusoidal patterns, stiffness also significantly increased with increasing feature thickness ($p < 0.0001$). Anisotropy was demonstrated in the 264 μm stripe patterned group, where the "with reinforcement" direction was stiffer than in the perpendicular direction. Additionally, the unpatterned controls (black mask) and fully reinforced (clear film) controls were significantly less and more stiff than all samples, respectively ($p < 0.0001$). The relative contribution of pattern to stiffness could be observed when stiffness was normalized to the unpatterned control (Figure 6.14B). Generally, the trend of increased stiffness with pattern thickness was observed, regardless of sine or stripe patterning.

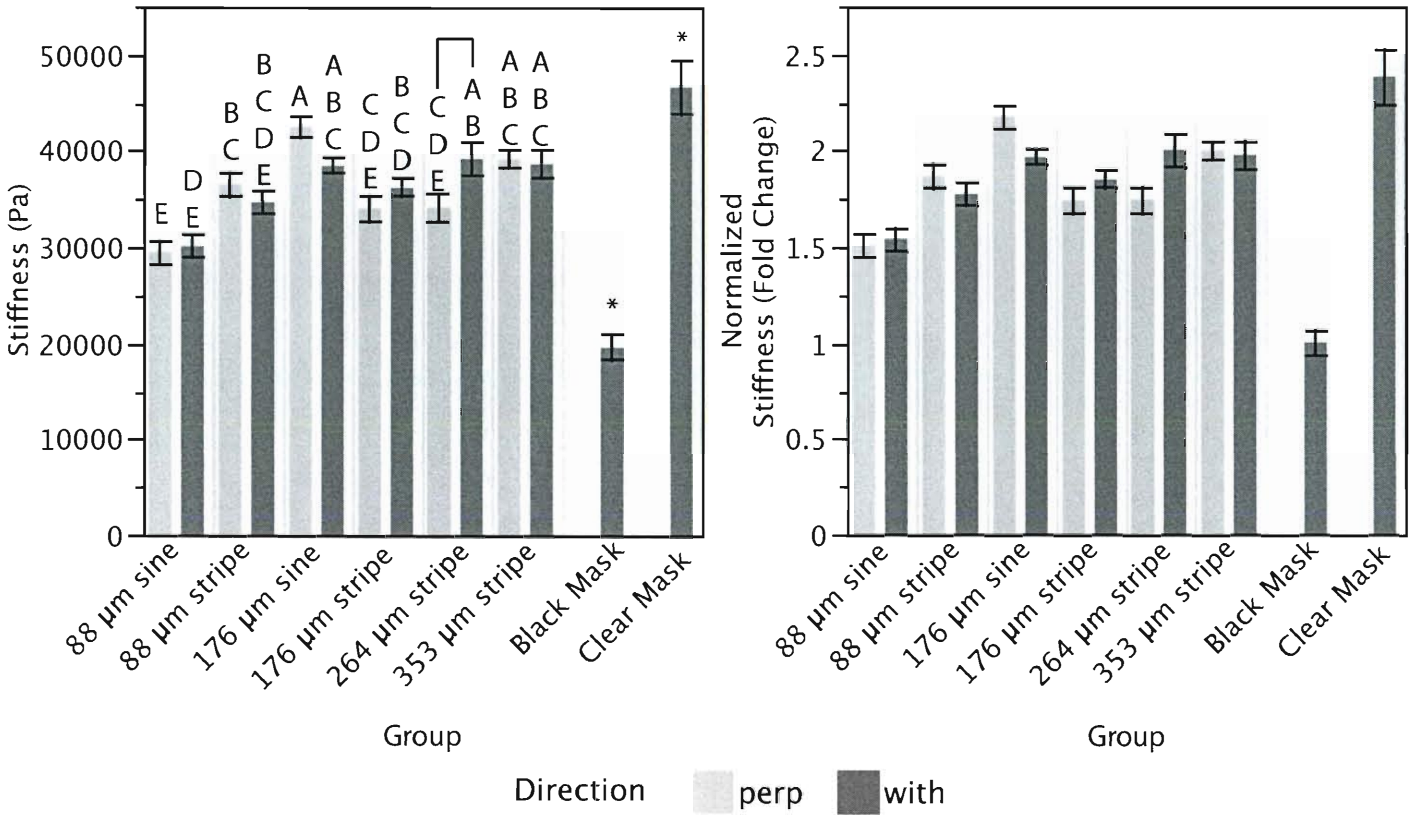

Figure 6.14: A) Tensile modulus of patterned gels. "Perp" indicates the samples were punched across (perpendicular) to the direction of the patterned features. "With" indicates samples were punched in the direction (0° to the long axis of the pattern) of the patterns. Anisotropy was observed in the 264 μm stripe group. All patterned groups were significantly stiffer than the unpatterned control (black mask) and significantly less stiff than the fully reinforced control (clear mask). * denotes significance with a $p < 0.001$ and samples marked with different letters are significantly different with $p < 0.05$. $N \geq 12$ for all groups (Subgroups, which are the directional group within each feature type, have $n \geq 6$). B) Modulus normalized to stiffness of unpatterned slab gel. Reinforcement significantly increases the modulus in comparison with control, and relative stiffening contribution as a function of pattern can be seen. Statistical significance is identical to A.

6.5 Discussion

The methods developed and implemented in the studies described in this chapter are the first to demonstrate strongly-bonded photocrosslinked multiphase hydrogels that remain well adhered after swelling. These methods allowed the development of a biphasic, trilayered composite hydrogel with distinct layers of stiffness and cellularity. Through empirical testing, a "swelling envelope" was determined that allowed the successful layering of hydrogel formulations with different material properties. Additionally, new patterns of reinforcement that demonstrate bulk anisotropic behavior in a fundamentally elastic, isotropic material were developed.

6.5.1 Interface Testing

In developing and optimizing the layering strategy, interface strength testing was performed to determine if different hydrogel formulations could indeed be successfully bonded in a serial or sandwich fashion. This study allowed the author to determine the formulations most likely to remain bonded after composite swelling. Since the 6k/10% formulation showed higher mean failure strength than the 8k/5% formulation, the 6k/10% formulation was selected for the quasilaminate flexure studies. Additionally, the bulk stiffness of this composition was higher than that of the 8k/5% as expected. This data demonstrated that biphasic layered hydrogels could reliably be fabricated using standard photopolymerization methods, and that strong interfacial bonding was retained even post-swelling.

6.5.2 Development of Serial and Sandwich Layering Methods and Practical Setbacks

Development of the layering methods had several practical setbacks due to unexpected phenomena. The serial layering method was used to create gels with thick spacers (1.0 mm or greater) in order to refine the methods using hydrogel geometries that were easy to handle. This method was presumed to use interpenetration of the polymer chains. Studies performed in Chapter 5 demonstrated that the mesh size increases with increasing molecular weight of the polymer. Also, Flory-Rehner theory shows that lower molecular weight polymers have lower effective hydrodynamic radii. Therefore, to achieve layer-layer bonding with this methodology, a layer with high molecular weight was first polymerized. The next layer to be added, with lower molecular weight was added to the polymerized high molecular weight "slab" gel and allowed to diffuse in. This was repeated on the other side to yield the desired "stiff-soft-stiff" quasilaminate. These gels were ultimately too thick to test using the 3-point bending apparatus in our laboratory, and they had to be reduced in thickness to test the bending properties. When thinner spacers were machined and the gels were prepared according to the serial layering method, many gels "delaminated" after swelling. It was observed in a pilot study (data not shown) that when preparing gels for interface strength testing (where the gels are exposed "in cross-section" as described in section 6.3.4) very low diffusion times (<30 minutes) for interpenetration were needed to obtain firmly adhered layers. Diffusion time of the interpenetrating layer did not appear to have a significant effect on adhesion at the times measured. This may be because interpenetration occurs so quickly that it is difficult to measure or that interpenetration was not the main factor that governed delamination of the quasilaminates prepared with the serial method. Results published by Cuchiara *et al.* showed that molecules with similar diffusivity to formulations tested in this chapter can penetrate more than 100 μm at times as low as 60 minutes.[79] Deep interpenetration of hydrogel prepolymer may not be necessary to achieve entanglement, and this may be why biphasic gels prepared in the serial manner showed adequate interface strength. Due to the strong adhesion that was apparent independent of interpenetration time and the difference in exposure profile (cross-sectionally vs. through the layer) for interface testing it was concluded that chain entanglement was not the actual cause of strong layer-layer adhesion. It was then speculated that if scattering of UV irradiation was occurring in thicker quasilaminates at the side opposite the UV lamp, many unreacted acrylates could remain. Therefore, the sandwich layering method was tested to determine empirically if unreacted acrylates could be used as a method to achieve strong layer-layer adhesion. This method yielded strong adhesion for the range of thicknesses tested (total initial thickness 0.75-1.5 mm) with no "delamination" of A-B-A quasilaminates. Another important factor in successful development of the quasilaminates was matching the swelling of the different layers. It was empirically observed that the mass swelling ratios for the formulations chosen needed to be within 5 (±2.5) of one another to ensure that the quasilaminates did not curl. This need to match swelling limited the potential formulations that could be used to form layers, although recently published work by Cha *et al.* has shown that material properties can be decoupled from swelling by incorporation of methacrylated alginate.[177] In the future, such decoupling methods should enable a vast range of potential formulations to be used with the layering techniques described in this work.

6.5.3 Interpretation of Quasilaminate Stiffness

Although it was expected that the quasilaminates would have a bending stiffness between that of the single layer controls, the quasilaminates were actually stiffer than single layer gels. There are several possible explanations for this finding. The first explanation considers the effects of differential swelling on the sample geometry. We observed that the B layer ("soft", 6k/10% formulation) swelled to 111% of original thickness and the A layer ("stiff", 3.4k/12.5% formulation) swelled to 103% of original thickness in single layer samples. If we assume that the swelling was similar in the quasilaminates, it follows that the two stiffer outer layers were located further from the neutral axis of bending than if all layers swelled equally, which could increase the "effective stiffness" of the composite. However, in a homogenous beam in bending this should be accounted for by the moment of inertia calculation in the Bernouilli-Euler equation (Equation 4.4). It is important to note that using an additive formula laminate composite moment of inertia yields the same moment of inertia as the standard equation for a rectangular cross section in bending.[178] These layered structures do have an axis of symmetry about the plane of bending, due to their A-B-A construction. If a layered structure with an asymmetric (i.e. A-A-B, A-B-B, A-B-C, etc.) layering scheme was to be tested, Bernoulli-Euler analysis may no longer be appropriate. However, these quasilaminates to have a uniform cross-section, and do not thin after deformation (both prerequisites for Timoshenko analysis). Additionally, since the layers in this system are covalently bonded, there probably is not free slip between layers. As a result, it is likely that there are shear deformations of the layers in addition to bending deformations. Timoshenko beam bending theory could be used to include the effect of layer shear on bulk stiffness, however this would have obfuscated comparisons with fresh tissue and single layer gels (in Chapters 4 and 5, respectively).

A more likely explanation of how thickness impacts stiffness in the quasilaminate composites follows. The thickness of the quasilaminate composite was higher than that of the single layer controls, which even when accounting for moment of inertia, will cause E_{eff} to increase since the imparted moment changes with thickness. Additionally, the quasilaminates swelled to a greater degree than their single layer controls, which could affect stiffness in two ways: (i) the actual physical increase in thickness will increase the measured stiffness since the load applied with the bending tester varies with thickness (described in Appendix II) and (ii) the changes in swelling pressure affect the polymer network (discussed below).

6.5.3.1 Consideration of Swelling on State of the Hydrogel Network and Other Potential Causes of Increased Stiffness in Quasilaminates

The second explanation above considers the effect of swelling on the hydrogel network. The quasilaminates swelled to 122% of the predicted value, based on the swelling of single layer controls (mean thickness 1.92 mm instead of 1.582 mm). This unexpected increase in one-dimensional swelling can be explained as follows. The B layer undergoes confined swelling due to the strong layer adhesions and lower stiffness of B layer when compared to the A layer. This B layer has been planarly confined to only swell across the thickness of the scaffold since the A layers (layered on top and bottom of the B layer) restrict its swelling in the length and width directions. This explanation is confirmed by the literature, where increased one-dimensional swelling is seen in thin hydrogel films when surface-coupled rather than free swelling.[179] In the hydrogel systems described in that work, the degree of linear swelling in surface-constrained hydrogels consistently exceeds the linear swelling of free hydrogels. If one considers the Flory expression for free energy, where the network is subjected to the opposing forces of thermodynamic mixing (favoring swelling) and the retractile force of the network (opposing swelling),[180] by restricting swelling to one dimension, the osmotic swelling pressure is increased, and must be opposed by higher elastic free energy. We speculate that increased swelling in quasilaminates (in comparison to single layer controls) causes a tensile "prestrain" of the hydrogel polymer mesh. This prestrain causes the quasilaminates to demonstrate higher stiffness than their single layer controls. Further characterization of layer-specific swelling will be necessary to determine the underlying cause of increased stiffness in quasilaminates. Moreover, it has been shown that a 2-fold change in volumetric swelling ratio can increase hydrogel modulus by two orders of magnitude.[110]

Another possibility that could explain the increased quasilaminate stiffness is the fabrication method. In the quasilaminates tested, each layer created had an initial thickness of 0.5 mm, whereas the single layer controls were 1.0 mm. The intent in the sandwich layer formulation approaches was to leverage UV scattering, resulting in one side of the layer having unreacted acrylates or a "sticky" gel. It may be that the UV light scattering in the central region of the single layer controls causes there to be an undercrosslinked central region. It has been shown that lowered crosslink density results in higher degree of swelling in hydrogels, which could account for the increased swelling of quasilaminates.[89] However, since PEGDA is highly transparent, it is unlikely that

UV scattering is occurring at depths of 0.5 mm, therefore making this explanation the least likely proposed here.

Regardless of the underlying cause of increased stiffness in quasilaminates, these methods allow scaffolds with distinct layers with specific cellularity and material properties to be fabricated. As shown by the flexure data, using these methods the cells' pericellular mechanical environment can be engineered to be of a lower stiffness than the overall scaffold (since the stiffness of the 6 kDa single layer controls is substantially lower than the bulk stiffness of the quasilaminate.) It has been demonstrated that VICs respond to their substrate stiffness where higher stiffness substrates accelerate calcific nodule formation, therefore the ability to culture VICs in an engineered tissue where the bulk stiffness and pericellular stiffness can be controlled will potentially result in healthier engineered tissues.[69, 113] Furthermore, when these scaffolds are flexed, a larger proportion of stress is imparted to the stiffer layers, further shielding cells from the high stresses resulting from large bending deformations, which have been correlated to sites of valve calcification. [3]

6.5.4 Interpretation of Modeled Behavior in PLP Hydrogels

Modeling of sinusoidally patterned gels was performed to attempt to identify the parameters with the most significant influence on bulk gel behavior. Modeled gels showed that the majority of applied load was borne by the reinforced areas, which was expected. However, sinusoidally patterned simulated gels showed no nonlinear behavior, regardless of period or amplitude of the sinusoid. This finding is in contrast to tissues, where collagen fiber crimp period and amplitude significantly affect tissue extensibility.[8, 168, 181] This discrepancy between model results and native valve tissues could be due to the model's use of no-slip boundary conditions between the reinforcements and the matrix, although these are likely accurate representations of these reinforcement conditions in the actual gels, they are not indicative of what happens *in vivo*. It is known that collagen and elastin fibers are able to slip through the ECM in a native aortic valve leaflet when stress is applied.[3, 182] It is likely that true fiber reinforcements that can slip within the hydrogel bulk will be necessary to achieve nonlinear behavior at strains under 100%. Our group is currently investigating the potential to replicate non-linear (tissue-like) toe regions in PEGDA hydrogels using electrospun fiber reinforcements.

6.5.5 PLP Increases Bulk Stiffness and Allows Anisotropic Behavior

The major finding in the patterning study was that patterned hydrogels demonstrated stiffness increased approximately 1.5-2 times over the stiffness of unpatterned controls. While holding total coverage fixed, as pattern feature thickness increased, the bulk stiffness increased. Only one pattern (the 264 μm stripe) resulted in anisotropy, in which the gels were stiffer along the direction length of the patterned feature (along the stripe). However, the 176 μm sinusoid pattern showed a trend of anisotropy ($p < 0.09$, Tukey-Kramer HSD; $p < 0.02$, paired t-test). The initial results showing inducement of anisotropy in photolithographically patterned hydrogels published by Nemir *et al.* did not report any effect of pattern feature width.[65] That research investigated material behavior in relation to a range of total pattern coverages (0, 25, 33, 50, and 100% coverage), and gels with total pattern coverage of 25 and 33% were the only to demonstrate anisotropy. This was the rationale for holding total pattern coverage fixed in this study and also informed the choice of probing other parameters (feature thickness, non-linear patterns) while holding total pattern coverage fixed at 20%. Further optimization of this patterning scheme, potentially employing approaches that permit fiber reinforcement "slip", it is anticipated that sinusoidal patterning will be able to generate a hydrogel with anisotropic, nonlinear stress-strain behavior. Although this work has employed patterning to create anisotropy in a material that is fundamentally isotropic and linearly elastic, a limitation of the PLP technique is that it only allows the creation of 2D patterns of reinforcement. This limitation could be overcome through two-photon adsorption methods, which allow 3D patterns to be created since there is minimal scattering due to the focal cone of the laser employed. It should be noted that two-photon adsorption methods are significantly more complex to implement and require longer patterning times [66] than the PLP strategy employed in this work. PLP of a reinforcing, interpenetrating polymer network is not the only method available to yield anisotropic material behavior in a fundamentally linearly elastic, isotropic hydrogel. Recently Zawko *et al.* demonstrated that photopatterning of secondary crosslinks in a chemically crosslinked gel yielded anisotropic swelling and viscoelastic bulk behavior.[89] The PLP methods described in this chapter could be used in an analogous method to enable patterning of secondary crosslinks that would yield differential swelling and potentially exhibit anisotropic behavior in photopolymerizable hydrogel materials. Applications of hydrogel patterning are rapidly expanding, and are not limited to purely mechanically inspired uses. Several applications of hydrogel patterning (both using PLP and soft lithography) currently under investigation include biosensors, cell-substrate studies, control of scaffold porosity, and microfluidic channels.[79, 183-187]

6.5.6 Applications and Utility of Layering and PLP Methods

The methods described in this chapter allow the fabrication of increasingly complex architectures in hydrogel scaffolds. These methods will likely find their first utility in tissue engineering, where layered, anisotropic structures are difficult or impossible to create with existing synthetic hydrogel fabrication techniques. The most obvious application is to recapitulate the layered, anisotropic structure of a heart valve, from which the studies described in this chapter derived their inspiration. By controlling the prepolymer formulation, bioactivity of each layer and the direct encapsulation of a specific cell type is possible. The result is a fabrication technique that allows simple, simultaneous control of mechanical properties, bioactivity, and cell type, and potentially the control of permeability (if the recently described methods of Cha *et al.* can easily be translated to this process.) In the future, an ideal hydrogel-based TEHV could be comprised of layers with varying bulk stiffness, cellularity, and tethered biochemical functionalization. The layers could also be patterned with layer-specific reinforcements (such as recapitulating collagen fiber orientation in the fibrosa) derived from new studies detailing layer specific ECM orientation.[188] This would allow regions of stiffness across the engineered leaflet that best mimicked native tissue. Furthermore, these methods can be translated to controlled release applications, since pericellular stiffness could be designed to be appropriate for the desired cell type, while the surface could modified by adherence of a high stiffness, low diffusivity layer. These methods permit the mimicry of tissue-specific anatomical features in hydrogels, which can in turn yield superior performance of resulting scaffolds and may enable diverse functional engineered tissues to be created.

6.6 Conclusions

Interface testing showed that strong layer bonding in mixed composition photopolymerized hydrogels was achieved by using the sandwich layering method. This study is the first to demonstrate this phenomena in PEGDA and more generally using photopolymerization to provide crosslinking. These studies showed that using the developed layering methods, a "stiff-soft-stiff" quasilaminate architecture yielded higher flexural stiffness than its constituent components separately. Photolithographic patterning with anatomically inspired patterns resulted in anisotropic tensile behavior. Additionally, all tested patterns served to reinforce the material and increase the bulk tensile modulus. This is in agreement with results published by Nemir *et al.* and these studies establish new patterns that can be used for reinforcement and the inducement of anisotropic behavior in hydrogel scaffolds.[65]

6.7 Acknowledgements

This work was supported by the March of Dimes; and in part by the Shared University Grid at Rice funded by NSF under Grant EIA-0216467, and a partnership between Rice University, Sun Microsystems, and Sigma Solutions, Inc. Thanks to Roger

Moye for assistance with supercomputing. Thanks should be paid to Hubert Tseng for discussions of mathematical proof of the thickness and stiffness relationship.

Chapter 7: Conclusions and Future Directions

7.1 Thesis Summary

The promise of a tissue engineered heart valve has yet to be realized. A living engineered valve that grows with the patient and is able to remodel in response to the *in vivo* environment would sidestep the current problems associated with clinical therapies – especially the limited supply and durability concerns of homografts, drawbacks arising from the use of systemic anticoagulation with mechanical valves, degeneration of bioprosthetics, and sizing and reoperation concerns for pediatric patients regardless of the prosthetic used. While many groups are pursuing a diversity of strategies to generate a TEHV, no one has had clinical success in the aortic position. This work took a ground-up approach to the tissue engineered heart valve, and tools and techniques for the creation of a TEHV were investigated. The design and evaluation of a system that is capable of providing necessary mechanical stimuli to developing tissues was detailed in Chapters 3 and 4. This system also has utility outside of purely tissue engineering of heart valves, and can be used for *ex vivo* organ culture of whole aortic roots, as it was in the studies in Chapter 4. This application will allow researchers to study valve biology in a more controlled and less costly fashion than large animal experiments. Information about aortic valve tissues obtained in the studies in Chapter 4 also served as design criteria for the ground-up hydrogel scaffold applications executed in Chapters 5 and 6. The hydrogel studies were the first to investigate the flexure behavior of PEGDA hydrogels in both single layer and quasilaminate structures. Furthermore, the studies in Chapter 6 were the first to show quasilaminate structures with well-adhered layers having different compositions in a photopolymerized system. The studies described in this thesis form the basis for fabricating and mechanically conditioning advanced hydrogel-based TEHV scaffolds with anatomically-inspired architectures that will address some of the mechanical shortcomings of existing approaches.

7.2 Conclusions

The design of the first simple, scalable bioreactor system that can perform both organ culture of native AV tissue and mechanical conditioning of engineered AVs is detailed in Chapter 3. Many AV bioreactor designs exist and have been reported in the literature, but did not satisfy the design goal of allowing low-cost, high-replicate culture with simple control systems. Another novel feature of our bioreactor is that it was the first to allow rapid loading of aortic valve roots since it employs a spring-locked stent. The bioreactor system can be pre-assembled into two main subassemblies and left under UV light in a biological safety cabinet (to preserve sterility) before dissection of the tissue. This feature allowed tissues to be loaded rapidly after dissection, since it did not need to be completely disassembled to load the samples.

The evaluation of medium-term (up to 14 days) organ culture of porcine aortic valves in the novel bioreactor is described in Chapter 4. The primary findings were that the tissue appeared to be best maintained to day 7 (in comparison with fresh tissue) and that optimization of the imparted dynamic culture regimen should be performed for dynamic *ex vivo* organ culture with durations longer than 7 days. At seven days, the flexural stiffness, hydroxyproline content and GAG content was unchanged from fresh tissue. Additionally, this culture regimen showed that when compared to statically cultured leaflets at the same time point, the dynamic regimen resulted in significantly better retention of flexural stiffness and hydroxyproline content. Histologically, leaflets cultured in the dynamic environment showed better retention of their characteristic layered structure, and proper distribution of collagen III and elastin. The benefits of the dynamic culture regimen were less obvious at day 14, and further optimization of the culture regimen needs to be performed before attempting cultures with this duration. Increased shear stresses and optimization of the imparted flow regimen will be necessary for long term *ex vivo* cultures. It is important to note that the bioreactor proved capable of maintaining AV organ cultures for 14 days in a sterile environment, which to our knowledge is the longest *ex vivo* organ culture of AV leaflets in a bioreactor system (published studies on whole AV organ culture have yet to extend past 96 hours).[109] Additionally, this system can certainly provide the subphysiologic forces that are thought to yield better tissue development in engineered tissues. The flexural properties of native AV leaflets that were determined in these studies served as design criteria for the flexural hydrogel work performed in Chapter 5.

The first study investigating the flexural stiffness of PEGDA hydrogels was described in Chapter 5. A variety of formulations were tested and compared with the more widely-reported compressive moduli of these formulations. Additionally, these studies demonstrated the effect of hydrogel formulation on encapsulated VIC phenotype within the gel using two well-known phenotypic markers. Much work has been performed characterizing VICs within the more prevalent mesh or foam-based TEHV scaffolds, but to-date only 7 other papers have been published detailing work with VICs and synthetic hydrogels.[1, 57, 69, 87, 112, 113, 189] Therefore, the studies in Chapter 5 significantly contribute to the nascent study of hydrogel scaffold applications for TEHV. Additionally, since flexural deformations are large in native valves and can frequently be the source of the maximum stress present in the valve[3], it is necessary to characterize this behavior for any potential TEHV scaffold. The effect of methacrylated heparin incorporation on gel material properties was another novel finding in this study. Recently published studies showed that PEGylated bioactive moieties increased gel stiffness rather than decreased it as expected.[160] The studies in Chapter 5 demonstrated the opposite effect with the bioactive moiety tested (Hep-MA). These results indicate that the effect of bioactive molecule incorporation on material properties may be difficult to predict due to differences in chemical structural and available crosslinking sites on the molecule of interest. The characterization of flexural stiffness and analysis of encapsulated VIC behavior in Chapter 5 underpinned the development of more complex hydrogel based TEHV constructs in Chapter 6.

Advanced hydrogel scaffolds with unique material properties inspired by native valve tissues were fabricated and tested in Chapter 6. These studies were the first to demonstrate a quasilaminate layered scaffold with strong layer-layer adhesion where each layer had distinct composition and cellularity in a photopolymerized system. Additionally, these studies tested the bending stiffness of "stiff-soft-stiff" quasilaminates inspired by native AV layer properties. Lastly these studies uncovered new patterns of reinforcement yielding anisotropy, and investigated the relative contribution of various experimenter-controllable parameters on bulk stiffness, adding to the growing body of literature on patterned regions of stiffness in hydrogels.

7.3 Future Directions

The bioreactor presented in Chapters 3 and 4 is simple to replicate, can scale easily to accommodate varying sample sizes, and uses very simple and durable drive and control systems. This system will allow experimenters to study AV tissue behavior in an environment that is far more controllable than an *in vivo* study, while simultaneously being much lower cost than a large animal study. Furthermore, the use of organ cultures sidesteps ethical concerns regarding experimental animal studies. In addition to organ culture of native AV tissue, the newly developed bioreactor also can be used for the *in vitro* development of TEHV. This system can readily generate pseudo-physiologic and subphysiologic flow rates and pressures. Since the system scales to readily accommodate large numbers of native AVs, it will be useful for mechanical conditioning of many TEHV constructs in parallel. This system could also be used to perform accelerated fatigue testing by rapidly cycling TEHV to investigate the failure modes of diverse TEHV scaffold materials. The novel bioreactor described in this thesis has wide ranging applications in the study of aortic valve biology and engineering, and will likely find multiple uses in our lab and others.

The hydrogel studies described in Chapters 5 and 6 serve to expand our fundamental understanding of hydrogel behavior in mechanical modes that are very relevant for valve tissues. These studies form a basis for heart valve tissue engineering in hydrogel scaffolds when added to the few existing papers from labs at University of Wisconsin, University of Colorado, and University of Western Ontario.[1, 2, 69, 87, 90, 111, 112, 190, 191] Bending of hydrogel structures is novel, and will need to continue to be analyzed. Currently, there is no model for bending analysis of these structures that allows for large deformations (similar to the complete reversal of curvature seen during leaflet opening and closing). Development of a model that accounts for large deformations both single layer and advanced structures would increase the analytical rigor of mechanical evaluation of native and engineered tissues. Additionally, the development of the advanced fabrication techniques allow the creation of hydrogel constructs that more closely mimic the material properties of a diverse range of native tissues. It is likely these methods will find utility in both tissue engineering applications and controlled release. Specifically for tissue engineering applications, these constructs will need to incorporate cell-degradable motifs to enable the seeded cells to synthesize matrix, migrate, and remodel the scaffold prior to implantation. Further characterization of the effects of incorporating these motifs on material properties will be necessary, although the developed methods should be able to be generalized to work with any photopolymerizable hydrogel system. Future studies with cell-degradable polymer scaffolds in an anisotropic, layered configuration could be evaluated in vivo in a sheep model to characterize their performance relative to the current state-of-the-art. The work performed here will allow better mimicry of native tissue behavior, which will in turn yield better performance of engineered tissues, and allow a diversity of new engineered tissues to be created by future investigators.

Chapter 8: Bibliography

1. Masters, K.S., D.N. Shah, G. Walker, L.A. Leinwand, and K.S. Anseth, *Designing scaffolds for valvular interstitial cells: cell adhesion and function on naturally derived materials.* J Biomed Mater Res A, 2004. **71**(1): p. 172-80.

2. Cushing, M.C., J.T. Liao, M.P. Jaeggli, and K.S. Anseth, *Material-based regulation of the myofibroblast phenotype.* Biomaterials, 2007. **28**(23): p. 3378-87.

3. Thubrikar, M.J., *The Aortic Valve*1990, Boca Raton, Fla.: CRC Press.

4. Mercer, J.L., M. Benedicty, and H.T. Bahnson, *The geometry and construction of the aortic leaflet.* J Thorac Cardiovasc Surg, 1973. **65**(4): p. 511-8.

5. Thubrikar, M.J., J.D. Deck, J. Aouad, and S.P. Nolan, *Role of mechanical stress in calcification of aortic bioprosthetic valves.* J Thorac Cardiovasc Surg, 1983. **86**(1): p. 115-25.

6. Bernacca, G.M., A.C. Fisher, R. Wilkinson, T.G. Mackay, and D.J. Wheatley, *Calcification and stress distribution in bovine pericardial heart valves.* J Biomed Mater Res, 1992. **26**(7): p. 959-66.

7. Bernacca, G.M., G. Tobasnick, and D.J. Wheatley, *Dynamic in vitro calcification of porcine aortic valves.* J Heart Valve Dis, 1994. **3**(6): p. 684-7.

8. Schoen, F.J. and R.J. Levy, *Founder's Award, 25th Annual Meeting of the Society for Biomaterials, perspectives. Providence, RI, April 28-May 2, 1999. Tissue heart valves: current challenges and future research perspectives.* J Biomed Mater Res, 1999. **47**(4): p. 439-65.

9. Fuster, V., R.W. Alexander, and R.A. O'Rourke, *Hurst's the heart.* 10th ed2001, New York: McGraw-Hill Medical Pub. Division. 2 v. (xxi, 2568, 92 p, [48] p. of plates).

10. Roberts, W.C., *Valvular, subvalvular and supravalvular aortic stenosis: morphologic features.* Cardiovasc Clin, 1973. **5**(1): p. 97-126.

11. Sauren, A.A., W. Kuijpers, A.A. van Steenhoven, and F.E. Veldpaus, *Aortic valve histology and its relation with mechanics-preliminary report.* J Biomech, 1980. **13**(2): p. 97-104.

12. Vesely, I. and R. Noseworthy, *Micromechanics of the fibrosa and the ventricularis in aortic valve leaflets.* J Biomech, 1992. **25**(1): p. 101-13.

13. Sands, M.P., E.A. Rittenhouse, H. Mohri, and K.A. Merendino, *An anatomical comparison of human pig, calf, and sheep aortic valves.* Ann Thorac Surg, 1969. **8**(5): p. 407-14.

14. Sauren, A.A., M.C. van Hout, A.A. van Steenhoven, F.E. Veldpaus, and J.D. Janssen, *The mechanical properties of porcine aortic valve tissues.* J Biomech, 1983. **16**(5): p. 327-37.

15. Ward, C., *Clinical significance of the bicuspid aortic valve.* Heart, 2000. **83**(1): p. 81-5.

16. O'Rourke, R.A., *Hurst's The Heart : Manual of Cardiology*, 2001, New York McGraw-Hill Professional.

17. Anand, R. and A.V. Mehta, *Progressive congenital valvar aortic stenosis during infancy: five cases.* Pediatr Cardiol, 1997. **18**(1): p. 35-7.

18. Otto, C.M., J. Kuusisto, D.D. Reichenbach, A.M. Gown, and K.D. O'Brien, *Characterization of the early lesion of 'degenerative' valvular aortic stenosis. Histological and immunohistochemical studies.* Circulation, 1994. **90**(2): p. 844-53.

19. Stewart, B.F., D. Siscovick, B.K. Lind, J.M. Gardin, J.S. Gottdiener, V.E. Smith, D.W. Kitzman, and C.M. Otto, *Clinical factors associated with calcific aortic valve disease. Cardiovascular Health Study.* J Am Coll Cardiol, 1997. **29**(3): p. 630-4.

20. Moller, J.H., A. Nakib, R.S. Eliot, and J.E. Edwards, *Symptomatic congenital aortic stenosis in the first year of life.* J Pediatr, 1966. **69**(5): p. 728-34.

21. Passik, C.S., D.M. Ackermann, J.R. Pluth, and W.D. Edwards, *Temporal changes in the causes of aortic stenosis: a surgical pathologic study of 646 cases.* Mayo Clin Proc, 1987. **62**(2): p. 119-23.

22. Thom, T., N. Haase, W. Rosamond, V.J. Howard, J. Rumsfeld, T. Manolio, Z.J. Zheng, K. Flegal, C. O'Donnell, S. Kittner, D. Lloyd-Jones, D.C. Goff, Jr., Y. Hong, R. Adams, G. Friday, K. Furie, P. Gorelick, B. Kissela, J. Marler, J. Meigs, V. Roger, S. Sidney, P. Sorlie, J. Steinberger, S. Wasserthiel-Smoller, M. Wilson, and P. Wolf, *Heart disease and stroke statistics--2006 update: a report from the American Heart Association Statistics Committee and Stroke Statistics Subcommittee.* Circulation, 2006. **113**(6): p. e85-151.

23. Ezekowitz, M.D., *Anticoagulation management of valve replacement patients.* J Heart Valve Dis, 2002. **11 Suppl 1**: p. S56-60.

24. Yun, K.L., D.C. Miller, K.A. Moore, R.S. Mitchell, P.E. Oyer, E.B. Stinson, R.C. Robbins, B.A. Reitz, and N.E. Shumway, *Durability of the Hancock MO bioprosthesis compared with standard aortic valve bioprostheses.* Ann Thorac Surg, 1995. **60**(2 Suppl): p. S221-8.

25. Rahimtoola, S.H., *Choice of prosthetic heart valve for adult patients.* J Am Coll Cardiol, 2003. **41**(6): p. 893-904.

26. Chambers, J.C., J. Somerville, S. Stone, and D.N. Ross, *Pulmonary autograft procedure for aortic valve disease: long-term results of the pioneer series.* Circulation, 1997. **96**(7): p. 2206-14.

27. Bechtel, J.F., C. Bartels, C. Schmidtke, W. Skibba, M. Muller-Steinhardt, H. Kluter, and H.H. Sievers, *Does histocompatibility affect homograft valve function after the Ross procedure?* Circulation, 2001. **104**(12 Suppl 1): p. I25-8.

28. Elkins, R.C., C.J. Knott-Craig, K.E. Ward, C. McCue, and M.M. Lane, *Pulmonary autograft in children: realized growth potential.* Ann Thorac Surg, 1994. **57**(6): p. 1387-93; discussion 1393-4.

29. Cannegieter, S.C., F.R. Rosendaal, and E. Briet, *Thromboembolic and bleeding complications in patients with mechanical heart valve prostheses.* Circulation, 1994. **89**(2): p. 635-41.

30. Chatterjee, S. and T.J. Gardner, *Factors determining selection of valve prosthesis--tissue or mechanical: current status.* Adv Cardiol, 2002. **39**: p. 189-94.

31. Schenke-Layland, K., F. Opitz, M. Gross, C. Doring, K.J. Halbhuber, F. Schirrmeister, T. Wahlers, and U.A. Stock, *Complete dynamic repopulation of decellularized heart valves by application of defined physical signals-an in vitro study.* Cardiovasc Res, 2003. **60**(3): p. 497-509.

32. Simon, P., M.T. Kasimir, G. Seebacher, G. Weigel, R. Ullrich, U. Salzer-Muhar, E. Rieder, and E. Wolner, *Early failure of the tissue engineered porcine heart valve SYNERGRAFT in pediatric patients.* Eur J Cardiothorac Surg, 2003. **23**(6): p. 1002-6; discussion 1006.

33. Hoerstrup, S.P., R. Sodian, J.S. Sperling, J.P. Vacanti, and J.E. Mayer, Jr., *New pulsatile bioreactor for in vitro formation of tissue engineered heart valves.* Tissue Eng, 2000. **6**(1): p. 75-9.

34. Hoerstrup, S.P., R. Sodian, S. Daebritz, J. Wang, E.A. Bacha, D.P. Martin, A.M. Moran, K.J. Guleserian, J.S. Sperling, S. Kaushal, J.P. Vacanti, F.J. Schoen, and J.E. Mayer, Jr., *Functional living trileaflet heart valves grown in vitro.* Circulation, 2000. **102**(19 Suppl 3): p. III44-9.

35. Sodian, R., S.P. Hoerstrup, J.S. Sperling, S. Daebritz, D.P. Martin, A.M. Moran, B.S. Kim, F.J. Schoen, J.P. Vacanti, and J.E. Mayer, Jr., *Early in vivo experience with tissue-engineered trileaflet heart valves.* Circulation, 2000. **102**(19 Suppl 3): p. III22-9.

36. Sodian, R., S.P. Hoerstrup, J.S. Sperling, S.H. Daebritz, D.P. Martin, F.J. Schoen, J.P. Vacanti, and J.E. Mayer, Jr., *Tissue engineering of heart valves: in vitro experiences.* Ann Thorac Surg, 2000. **70**(1): p. 140-4.

37. Sodian, R., S.P. Hoerstrup, J.S. Sperling, D.P. Martin, S. Daebritz, J.E. Mayer, Jr., and J.P. Vacanti, *Evaluation of biodegradable, three-dimensional matrices for tissue engineering of heart valves.* Asaio J, 2000. **46**(1): p. 107-10.

38. Rabkin, E., S.P. Hoerstrup, M. Aikawa, J.E. Mayer, Jr., and F.J. Schoen, *Evolution of cell phenotype and extracellular matrix in tissue-engineered heart valves during in-vitro maturation and in-vivo remodeling.* J Heart Valve Dis, 2002. **11**(3): p. 308-14; discussion 314.

39. Mol, A. and S.P. Hoerstrup, *Heart valve tissue engineering -- where do we stand?* Int J Cardiol, 2004. **95 Suppl 1**: p. S57-8.

40. Mol, A., C.V. Bouten, F.P. Baaijens, G. Zund, M.I. Turina, and S.P. Hoerstrup, *Review article: Tissue engineering of semilunar heart valves: current status and future developments.* J Heart Valve Dis, 2004. **13**(2): p. 272-80.

41. Baaijens, F., C. Bouten, S. Hoerstrup, A. Mol, N. Driessen, and R. Boerboom, *Functional tissue engineering of the aortic heart valve.* Clin Hemorheol Microcirc, 2005. **33**(3): p. 197-9.

42. Mol, A., N.J. Driessen, M.C. Rutten, S.P. Hoerstrup, C.V. Bouten, and F.P. Baaijens, *Tissue engineering of human heart valve leaflets: a novel bioreactor for a strain-based conditioning approach.* Ann Biomed Eng, 2005. **33**(12): p. 1778-88.

43. Mol, A., M.I. van Lieshout, C.G. Dam-de Veen, S. Neuenschwander, S.P. Hoerstrup, F.P. Baaijens, and C.V. Bouten, *Fibrin as a cell carrier in cardiovascular tissue engineering applications.* Biomaterials, 2005. **26**(16): p. 3113-21.

44. Schmidt, D., A. Mol, B. Odermatt, S. Neuenschwander, C. Breymann, M. Gossi, M. Genoni, G. Zund, and S.P. Hoerstrup, *Engineering of Biologically Active Living Heart Valve Leaflets Using Human Umbilical Cord-Derived Progenitor Cells.* Tissue Eng, 2006.

45. Schmidt, D., A. Mol, C. Breymann, J. Achermann, B. Odermatt, M. Gossi, S. Neuenschwander, R. Pretre, M. Genoni, G. Zund, and S.P. Hoerstrup, *Living autologous heart valves engineered from human prenatally harvested progenitors.* Circulation, 2006. **114**(1 Suppl): p. I125-31.

46. Schmidt, D. and S.P. Hoerstrup, *Tissue engineered heart valves based on human cells.* Swiss Med Wkly, 2006. **136**(39-40): p. 618-23.

47. Mol, A., M.C. Rutten, N.J. Driessen, C.V. Bouten, G. Zund, F.P. Baaijens, and S.P. Hoerstrup, *Autologous human tissue-engineered heart valves: prospects for systemic application.* Circulation, 2006. **114**(1 Suppl): p. I152-8.

48. Schmidt, D., J. Achermann, B. Odermatt, C. Breymann, A. Mol, M. Genoni, G. Zund, and S.P. Hoerstrup, *Prenatally fabricated autologous human living heart valves based on amniotic fluid derived progenitor cells as single cell source.* Circulation, 2007. **116**(11 Suppl): p. I64-70.

49. Schmidt, D., J. Achermann, B. Odermatt, M. Genoni, G. Zund, and S.P. Hoerstrup, *Cryopreserved amniotic fluid-derived cells: a lifelong autologous fetal stem cell source for heart valve tissue engineering.* J Heart Valve Dis, 2008. **17**(4): p. 446-55; discussion 455.

50. Stock, U.A., M. Nagashima, P.N. Khalil, G.D. Nollert, T. Herden, J.S. Sperling, A. Moran, J. Lien, D.P. Martin, F.J. Schoen, J.P. Vacanti, and J.E. Mayer, Jr.,

Tissue-engineered valved conduits in the pulmonary circulation. J Thorac Cardiovasc Surg, 2000. **119**(4 Pt 1): p. 732-40.

51. Stock, U.A. and J.E. Mayer, Jr., *Tissue engineering of cardiac valves on the basis of PGA/PLA Co-polymers.* J Long Term Eff Med Implants, 2001. **11**(3-4): p. 249-60.

52. Engelmayr, G.C., Jr., D.K. Hildebrand, F.W. Sutherland, J.E. Mayer, Jr., and M.S. Sacks, *A novel bioreactor for the dynamic flexural stimulation of tissue engineered heart valve biomaterials.* Biomaterials, 2003. **24**(14): p. 2523-32.

53. Engelmayr, G.C., Jr., E. Rabkin, F.W. Sutherland, F.J. Schoen, J.E. Mayer, Jr., and M.S. Sacks, *The independent role of cyclic flexure in the early in vitro development of an engineered heart valve tissue.* Biomaterials, 2005. **26**(2): p. 175-87.

54. Engelmayr, G.C., Jr., V.L. Sales, J.E. Mayer, Jr., and M.S. Sacks, *Cyclic flexure and laminar flow synergistically accelerate mesenchymal stem cell-mediated engineered tissue formation: Implications for engineered heart valve tissues.* Biomaterials, 2006. **27**(36): p. 6083-95.

55. Cummings, C.L., D. Gawlitta, R.M. Nerem, and J.P. Stegemann, *Properties of engineered vascular constructs made from collagen, fibrin, and collagen-fibrin mixtures.* Biomaterials, 2004. **25**(17): p. 3699-706.

56. Robinson, P.S., S.L. Johnson, M.C. Evans, V.H. Barocas, and R.T. Tranquillo, *Functional Tissue-Engineered Valves from Cell-Remodeled Fibrin with Commissural Alignment of Cell-Produced Collagen.* Tissue Eng, 2007.

57. Benton, J.A., C.A. Deforest, V. Vivekanandan, and K.S. Anseth, *Photocrosslinking of Gelatin Macromers to Synthesize Porous Hydrogels that Promote Valvular Interstitial Cell Function.* Tissue Eng Part A, 2009.

58. Liao, J., E.M. Joyce, and M.S. Sacks, *Effects of decellularization on the mechanical and structural properties of the porcine aortic valve leaflet.* Biomaterials, 2008. **29**(8): p. 1065-74.

59. Oudshoorn, M.H.M., R. Rissmann, J.A. Bouwstra, and W.E. Hennink, *Synthesis of methacrylated hyaluronic acid with tailored degree of substitution.* Polymer, 2007. **48**(7): p. 1915-1920.

60. Zeltinger, J., L.K. Landeen, H.G. Alexander, I.D. Kidd, and B. Sibanda, *Development and characterization of tissue-engineered aortic valves.* Tissue Eng, 2001. **7**(1): p. 9-22.

61. Eaglstein, W.H. and V. Falanga, *Tissue engineering and the development of Apligraf, a human skin equivalent.* Clin Ther, 1997. **19**(5): p. 894-905.

62. Sodian, R., J.S. Sperling, D.P. Martin, U. Stock, J.E. Mayer, Jr., and J.P. Vacanti, *Tissue engineering of a trileaflet heart valve-early in vitro experiences with a combined polymer.* Tissue Eng, 1999. **5**(5): p. 489-94.

63. Shinoka, T., P.X. Ma, D. Shum-Tim, C.K. Breuer, R.A. Cusick, G. Zund, R. Langer, J.P. Vacanti, and J.E. Mayer, Jr., *Tissue-engineered heart valves. Autologous valve leaflet replacement study in a lamb model.* Circulation, 1996. **94**(9 Suppl): p. II164-8.

64. Peltoniemi, H.H., D. Hallikainen, T. Toivonen, P. Helevirta, and T. Waris, *SR-PLLA and SR-PGA miniscrews: biodegradation and tissue reactions in the calvarium and dura mater.* J Craniomaxillofac Surg, 1999. **27**(1): p. 42-50.

65. Nemir, S., H.N. Hayenga, and J.L. West, *PEGDA hydrogels with patterned elasticity: Novel tools for the study of cell response to substrate rigidity.* Biotechnol Bioeng. **105**(3): p. 636-44.

66. Hahn, M.S., J.S. Miller, and J.L. West, *Three-dimensional biochemical and biomechanical patterning of hydrogels for guiding cell behavior.* Advanced Materials, 2006. **18**(20): p. 2679-+.

67. Lee, S.H., J.J. Moon, J.S. Miller, and J.L. West, *Poly(ethylene glycol) hydrogels conjugated with a collagenase-sensitive fluorogenic substrate to visualize collagenase activity during three-dimensional cell migration.* Biomaterials, 2007. **28**(20): p. 3163-70.

68. Burg, K.J., W.D. Holder, Jr., C.R. Culberson, R.J. Beiler, K.G. Greene, A.B. Loebsack, W.D. Roland, P. Eiselt, D.J. Mooney, and C.R. Halberstadt, *Comparative study of seeding methods for three-dimensional polymeric scaffolds.* J Biomed Mater Res, 2000. **51**(4): p. 642-9.

69. Benton, J.A., H.B. Kern, and K.S. Anseth, *Substrate properties influence calcification in valvular interstitial cell culture.* J Heart Valve Dis, 2008. **17**(6): p. 689-99.

70. Peppas, N.A., *Hydrogels in medicine and pharmacy*1986, Boca Raton, Fla.: CRC Press.

71. Nguyen, K.T. and J.L. West, *Photopolymerizable hydrogels for tissue engineering applications.* Biomaterials, 2002. **23**(22): p. 4307-14.

72. Hahn, M.S., M.K. McHale, E. Wang, R.H. Schmedlen, and J.L. West, *Physiologic Pulsatile Flow Bioreactor Conditioning of Poly(ethylene glycol)-based Tissue Engineered Vascular Grafts.* Ann Biomed Eng, 2007. **35**(2): p. 190-200.

73. Leslie-Barbick, J.E., J.J. Moon, and J.L. West, *Covalently-immobilized vascular endothelial growth factor promotes endothelial cell tubulogenesis in poly(ethylene glycol) diacrylate hydrogels.* J Biomater Sci Polym Ed, 2009. **20**(12): p. 1763-79.

74. Weber, L.M. and K.S. Anseth, *Hydrogel encapsulation environments functionalized with extracellular matrix interactions increase islet insulin secretion.* Matrix Biol, 2008. **27**(8): p. 667-73.

75. Peyton, S.R., C.B. Raub, V.P. Keschrumrus, and A.J. Putnam, *The use of poly(ethylene glycol) hydrogels to investigate the impact of ECM chemistry and mechanics on smooth muscle cells.* Biomaterials, 2006. **27**(28): p. 4881-4893.

76. Benoit, D.S., A.R. Durney, and K.S. Anseth, *The effect of heparin-functionalized PEG hydrogels on three-dimensional human mesenchymal stem cell osteogenic differentiation.* Biomaterials, 2007. **28**(1): p. 66-77.

77. Decker, C., *The use of UV irradiation in polymerization.* Polymer International, 1998. **45**(2): p. 133-141.

78. Hahn, M.S., L.J. Taite, J.J. Moon, M.C. Rowland, K.A. Ruffino, and J.L. West, *Photolithographic patterning of polyethylene glycol hydrogels.* Biomaterials, 2006. **27**(12): p. 2519-24.

79. Cuchiara, M.P., A.C. Allen, T.M. Chen, J.S. Miller, and J.L. West, *Multilayer microfluidic PEGDA hydrogels.* Biomaterials, 2010. **31**(21): p. 5491-7.

80. Xu, Z.K., F.Q. Nie, C. Qu, L.S. Wan, J. Wu, and K. Yao, *Tethering poly(ethylene glycol)s to improve the surface biocompatibility of poly(acrylonitrile-co-maleic acid) asymmetric membranes.* Biomaterials, 2005. **26**(6): p. 589-98.

81. Lee, M. and S.W. Kim, *Polyethylene glycol-conjugated copolymers for plasmid DNA delivery.* Pharm Res, 2005. **22**(1): p. 1-10.

82. Bromberg, L., *Crosslinked poly(ethylene glycol) networks as reservoirs for protein delivery.* Journal of Applied Polymer Science, 1996. **59**(3): p. 459-466.

83. Bryant, S.J., T.T. Chowdhury, D.A. Lee, D.L. Bader, and K.S. Anseth, *Crosslinking density influences chondrocyte metabolism in dynamically loaded photocrosslinked poly(ethylene glycol) hydrogels.* Ann Biomed Eng, 2004. **32**(3): p. 407-17.

84. Almany, L. and D. Seliktar, *Biosynthetic hydrogel scaffolds made from fibrinogen and polyethylene glycol for 3D cell cultures.* Biomaterials, 2005. **26**(15): p. 2467-77.

85. Temenoff, J.S., K.A. Athanasiou, R.G. LeBaron, and A.G. Mikos, *Effect of poly(ethylene glycol) molecular weight on tensile and swelling properties of oligo(poly(ethylene glycol) fumarate) hydrogels for cartilage tissue engineering.* J Biomed Mater Res, 2002. **59**(3): p. 429-37.

86. Cuchiara, M.P., A.C. Allen, T.M. Chen, J.S. Miller, and J.L. West, *Multilayer microfluidic PEGDA hydrogels.* Biomaterials. **31**(21): p. 5491-7.

87. Benton, J.A., B.D. Fairbanks, and K.S. Anseth, *Characterization of valvular interstitial cell function in three dimensional matrix metalloproteinase degradable PEG hydrogels.* Biomaterials, 2009. **30**(34): p. 6593-603.

88. Millon, L.E., H. Mohammadi, and W.K. Wan, *Anisotropic polyvinyl alcohol hydrogel for cardiovascular applications.* J Biomed Mater Res B Appl Biomater, 2006. **79**(2): p. 305-11.

89. Zawko, S.A., S. Suri, Q. Truong, and C.E. Schmidt, *Photopatterned anisotropic swelling of dual-crosslinked hyaluronic acid hydrogels.* Acta Biomater, 2009. **5**(1): p. 14-22.

90. Millon, L.E. and W.K. Wan, *The polyvinyl alcohol-bacterial cellulose system as a new nanocomposite for biomedical applications.* J Biomed Mater Res B Appl Biomater, 2006. **79**(2): p. 245-53.

91. Millon, L.E., G. Guhados, and W. Wan, *Anisotropic polyvinyl alcohol-Bacterial cellulose nanocomposite for biomedical applications.* J Biomed Mater Res B Appl Biomater, 2008. **86B**(2): p. 444-52.

92. Lu, S. and K.S. Anseth, *Photopolymerization of multilaminated poly(HEMA) hydrogels for controlled release.* J Control Release, 1999. **57**(3): p. 291-300.

93. Lu, S., W.F. Ramirez, and K.S. Anseth, *Photopolymerized, multilaminated matrix devices with optimized nonuniform initial concentration profiles to control drug release.* J Pharm Sci, 2000. **89**(1): p. 45-51.

94. Vesely, I., *Heart valve tissue engineering.* Circ Res, 2005. **97**(8): p. 743-55.

95. Altman, G.H., R.L. Horan, I. Martin, J. Farhadi, P.R. Stark, V. Volloch, J.C. Richmond, G. Vunjak-Novakovic, and D.L. Kaplan, *Cell differentiation by mechanical stress.* Faseb J, 2002. **16**(2): p. 270-2.

96. Hildebrand, D.K., Z.J. Wu, J.E. Mayer, Jr., and M.S. Sacks, *Design and hydrodynamic evaluation of a novel pulsatile bioreactor for biologically active heart valves.* Ann Biomed Eng, 2004. **32**(8): p. 1039-49.

97. Warnock, J.N., S. Konduri, Z. He, and A.P. Yoganathan, *Design of a sterile organ culture system for the ex vivo study of aortic heart valves.* J Biomech Eng, 2005. **127**(5): p. 857-61.

98. Gheewala, N., *Mitral Valve Organ Culture Provides a Novel Experimental Model*, in *Department of Bioengineering*2011, Rice University: Houston.

99. Weber, K.T., Y. Sun, L.C. Katwa, J.P. Cleutjens, and G. Zhou, *Connective tissue and repair in the heart. Potential regulatory mechanisms.* Ann N Y Acad Sci, 1995. **752**: p. 286-99.

100. Schneider, P.J. and J.D. Deck, *Tissue and cell renewal in the natural aortic valve of rats: an autoradiographic study.* Cardiovasc Res, 1981. **15**(4): p. 181-9.

101. Konduri, S., Y. Xing, J.N. Warnock, Z. He, and A.P. Yoganathan, *Normal physiological conditions maintain the biological characteristics of porcine aortic heart valves: an ex vivo organ culture study.* Ann Biomed Eng, 2005. **33**(9): p. 1158-66.

102. Stegemann, J.P. and R.M. Nerem, *Phenotype modulation in vascular tissue engineering using biochemical and mechanical stimulation.* Ann Biomed Eng, 2003. **31**(4): p. 391-402.

103. Weston, M.W. and A.P. Yoganathan, *Biosynthetic activity in heart valve leaflets in response to in vitro flow environments.* Ann Biomed Eng, 2001. **29**(9): p. 752-63.

104. Xing, Y., J.N. Warnock, Z. He, S.L. Hilbert, and A.P. Yoganathan, *Cyclic pressure affects the biological properties of porcine aortic valve leaflets in a magnitude and frequency dependent manner.* Ann Biomed Eng, 2004. **32**(11): p. 1461-70.

105. Gupta, V., J.A. Werdenberg, B.D. Lawrence, J.S. Mendez, E.H. Stephens, and K.J. Grande-Allen, *Reversible secretion of glycosaminoglycans and proteoglycans by cyclically stretched valvular cells in 3D culture.* Ann Biomed Eng, 2008. **36**(7): p. 1092-103.

106. Dumont, K., J. Yperman, E. Verbeken, P. Segers, B. Meuris, S. Vandenberghe, W. Flameng, and P.R. Verdonck, *Design of a new pulsatile bioreactor for tissue engineered aortic heart valve formation.* Artif Organs, 2002. **26**(8): p. 710-4.

107. Sucosky, P., K. Balachandran, A. Elhammali, H. Jo, and A.P. Yoganathan, *Altered shear stress stimulates upregulation of endothelial VCAM-1 and ICAM-1 in a BMP-4- and TGF-beta1-dependent pathway.* Arterioscler Thromb Vasc Biol, 2009. **29**(2): p. 254-60.

108. Merryman, W.D., I. Youn, H.D. Lukoff, P.M. Krueger, F. Guilak, R.A. Hopkins, and M.S. Sacks, *Correlation between heart valve interstitial cell stiffness and transvalvular pressure: implications for collagen biosynthesis.* Am J Physiol Heart Circ Physiol, 2006. **290**(1): p. H224-31.

109. Konduri, S., Y. Xing, J.N. Warnock, Z.M. He, and A.P. Yoganathan, *Normal physiological conditions maintain the biological characteristics of porcine aortic*

heart valves: An Ex vivo organ culture study. Ann Biomed Eng, 2005. **33**(9): p. 1158-1166.

110. Anseth, K.S., C.N. Bowman, and L. Brannon-Peppas, *Mechanical properties of hydrogels and their experimental determination.* Biomaterials, 1996. **17**(17): p. 1647-57.

111. Jiang, H., G. Campbell, D. Boughner, W.K. Wan, and M. Quantz, *Design and manufacture of a polyvinyl alcohol (PVA) cryogel tri-leaflet heart valve prosthesis.* Med Eng Phys, 2004. **26**(4): p. 269-77.

112. Masters, K.S., D.N. Shah, L.A. Leinwand, and K.S. Anseth, *Crosslinked hyaluronan scaffolds as a biologically active carrier for valvular interstitial cells.* Biomaterials, 2005. **26**(15): p. 2517-25.

113. Stephens, E.H., C.A. Durst, J.L. West, and K.J. Grande-Allen, *Mitral valvular interstitial cell responses to substrate stiffness depend on age and anatomic region.* Acta Biomater, 2011. **7**(1): p. 75-82.

114. Allison, D.D., J.A. Drazba, I. Vesely, K.N. Kader, and K.J. Grande-Allen, *Cell viability mapping within long-term heart valve organ cultures.* J Heart Valve Dis, 2004. **13**(2): p. 290-6.

115. Barzilla, J.E., A.S. McKenney, A.E. Cowan, C.A. Durst, and K.J. Grande-Allen, *Design and validation of a novel splashing bioreactor system for use in mitral valve organ culture.* Ann Biomed Eng, 2010. **38**(11): p. 3280-94.

116. Merryman, W.D., H.D. Lukoff, R.A. Long, G.C. Engelmayr, Jr., R.A. Hopkins, and M.S. Sacks, *Synergistic effects of cyclic tension and transforming growth factor-beta1 on the aortic valve myofibroblast.* Cardiovasc Pathol, 2007. **16**(5): p. 268-76.

117. Ku, C.H., P.H. Johnson, P. Batten, P. Sarathchandra, R.C. Chambers, P.M. Taylor, M.H. Yacoub, and A.H. Chester, *Collagen synthesis by mesenchymal*

stem cells and aortic valve interstitial cells in response to mechanical stretch. Cardiovasc Res, 2006. **71**(3): p. 548-56.

118. Zhang, X., X. Wang, V. Keshav, J.T. Johanas, G.G. Leisk, and D.L. Kaplan, *Dynamic culture conditions to generate silk-based tissue-engineered vascular grafts.* Biomaterials, 2009. **30**(19): p. 3213-23.

119. Lester, W.M., A.A. Damji, M. Tanaka, and I. Gedeon, *Bovine mitral valve organ culture: role of interstitial cells in repair of valvular injury.* J Mol Cell Cardiol, 1992. **24**(1): p. 43-53.

120. Lester, W.M., A.A. Damji, I. Gedeon, and M. Tanaka, *Interstitial cells from the atrial and ventricular sides of the bovine mitral valve respond differently to denuding endocardial injury.* In Vitro Cell Dev Biol, 1993. **29A**(1): p. 41-50.

121. Balachandran, K., S. Konduri, P. Sucosky, H. Jo, and A.P. Yoganathan, *An ex vivo study of the biological properties of porcine aortic valves in response to circumferential cyclic stretch.* Ann Biomed Eng, 2006. **34**(11): p. 1655-65.

122. He, Z., J. Ritchie, J.S. Grashow, M.S. Sacks, and A.P. Yoganathan, *In vitro dynamic strain behavior of the mitral valve posterior leaflet.* J Biomech Eng, 2005. **127**(3): p. 504-11.

123. Jimenez, J.H., J. Ritchie, Z. He, and A.P. Yoganathan, *Mechanics of the mitral valve: in vitro studies.* Conf Proc IEEE Eng Med Biol Soc, 2004. **5**: p. 3727-9.

124. Sacks, M.S., Z. He, L. Baijens, S. Wanant, P. Shah, H. Sugimoto, and A.P. Yoganathan, *Surface strains in the anterior leaflet of the functioning mitral valve.* Ann Biomed Eng, 2002. **30**(10): p. 1281-90.

125. Lenth, R.V., *Java Applets for Power and Sample Size [Computer software]*, 2006.

126. Gloeckner, D.C., K.L. Billiar, and M.S. Sacks, *Effects of mechanical fatigue on the bending properties of the porcine bioprosthetic heart valve.* Asaio J, 1999. **45**(1): p. 59-63.

127. Mirnajafi, A., J. Raymer, M.J. Scott, and M.S. Sacks, *The effects of collagen fiber orientation on the flexural properties of pericardial heterograft biomaterials.* Biomaterials, 2005. **26**(7): p. 795-804.

128. Pan, B., A. Asundi, H.M. Xie, and J.X. Gao, *Digital image correlation using iterative least squares and pointwise least squares for displacement field and strain field measurements.* Optics and Lasers in Engineering, 2009. **47**(7-8): p. 865-874.

129. Pan, B., K.M. Qian, H.M. Xie, and A. Asundi, *Two-dimensional digital image correlation for in-plane displacement and strain measurement: a review.* Measurement Science & Technology, 2009. **20**(6): p. -.

130. Pan, B., H. Xie, J. Gao, and A. Asundi, *Improved speckle projection profilometry for out-of-plane shape measurement.* Appl Opt, 2008. **47**(29): p. 5527-33.

131. Zhang, D. and D.D. Arola, *Applications of digital image correlation to biological tissues.* J Biomed Opt, 2004. **9**(4): p. 691-9.

132. Zhang, D.S., C.D. Eggleton, and D.D. Arola, *Evaluating the mechanical behavior of arterial tissue using digital image correlation.* Experimental Mechanics, 2002. **42**(4): p. 409-416.

133. Merryman, W.D., H.Y. Huang, F.J. Schoen, and M.S. Sacks, *The effects of cellular contraction on aortic valve leaflet flexural stiffness.* J Biomech, 2006. **39**(1): p. 88-96.

134. Vesely, I. and D. Boughner, *Analysis of the bending behaviour of porcine xenograft leaflets and of neutral aortic valve material: bending stiffness, neutral axis and shear measurements.* J Biomech, 1989. **22**(6-7): p. 655-71.

135. Vesely, I. and D.R. Boughner, *A multipurpose tissue bending machine.* J Biomech, 1985. **18**(7): p. 511-3.

136. Vesely, I., L. Gonzalez-Lavin, D. Graf, and D. Boughner, *Mechanical testing of cryopreserved aortic allografts. Comparison with xenografts and fresh tissue.* J Thorac Cardiovasc Surg, 1990. **99**(1): p. 119-23.

137. Engelmayr, G.C., Jr. and M.S. Sacks, *A structural model for the flexural mechanics of nonwoven tissue engineering scaffolds.* J Biomech Eng, 2006. **128**(4): p. 610-22.

138. Mirnajafi, A., J.M. Raymer, L.R. McClure, and M.S. Sacks, *The flexural rigidity of the aortic valve leaflet in the commissural region.* J Biomech, 2006. **39**(16): p. 2966-73.

139. Mirnajafi, A., B. Zubiate, and M.S. Sacks, *Effects of cyclic flexural fatigue on porcine bioprosthetic heart valve heterograft biomaterials.* J Biomed Mater Res A, 2010. **94**(1): p. 205-13.

140. Budynas, R.G., J.K. Nisbett, and J.E. Shigley, *Shigley's mechanical engineering design.* 8th ed. McGraw-Hill series in mechanical engineering2008, Boston: McGraw-Hill. xxv, 1059 p.

141. Sharpe, W.N., J. Pulskamp, D.S. Gianola, C. Eberl, R.G. Polcawich, and R.J. Thompson, *Strain measurements of silicon dioxide microspecimens by digital imaging processing.* Experimental Mechanics, 2007. **47**(5): p. 649-658.

142. Carew, E.O., J.E. Barber, and I. Vesely, *Role of preconditioning and recovery time in repeated testing of aortic valve tissues: validation through quasilinear viscoelastic theory.* Ann Biomed Eng, 2000. **28**(9): p. 1093-100.

143. Carew, E.O., A. Garg, J.E. Barber, and I. Vesely, *Stress relaxation preconditioning of porcine aortic valves.* Ann Biomed Eng, 2004. **32**(4): p. 563-72.

144. Bella, J., M. Eaton, B. Brodsky, and H.M. Berman, *Crystal and molecular structure of a collagen-like peptide at 1.9 A resolution.* Science, 1994. **266**(5182): p. 75-81.

145. Stegemann, H. and K. Stalder, *Determination of hydroxyproline.* Clin Chim Acta, 1967. **18**(2): p. 267-73.

146. Miller, E.J. and S. Gay, *Collagen: an overview.* Methods Enzymol, 1982. **82 Pt A**: p. 3-32.

147. Blumenkrantz, N. and G. Asboe-Hansen, *An improved method for the assay of hydroxylysine.* Anal Biochem, 1973. **56**(1): p. 10-5.

148. Blumenkrantz, N. and G. Asboe-Hansen, *New method for quantitative determination of uronic acids.* Anal Biochem, 1973. **54**(2): p. 484-9.

149. Ruifrok, A.C. and D.A. Johnston, *Quantification of histochemical staining by color deconvolution.* Anal Quant Cytol Histol, 2001. **23**(4): p. 291-9.

150. van der Loos, C.M., *Multiple immunoenzyme staining: methods and visualizations for the observation with spectral imaging.* J Histochem Cytochem, 2008. **56**(4): p. 313-28.

151. Ikhumetse, J.D., S. Konduri, J.N. Warnock, Y. Xing, and A.P. Yoganathand, *Cyclic aortic pressure affects the biological properties of porcine pulmonary valve leaflets.* J Heart Valve Dis, 2006. **15**(2): p. 295-302.

152. Balachandran, K., P. Sucosky, H. Jo, and A.P. Yoganathan, *Elevated cyclic stretch alters matrix remodeling in aortic valve cusps: implications for degenerative aortic valve disease.* Am J Physiol Heart Circ Physiol, 2009. **296**(3): p. H756-64.

153. Cloyd, J.M., N.R. Malhotra, L. Weng, W. Chen, R.L. Mauck, and D.M. Elliott, *Material properties in unconfined compression of human nucleus pulposus, injectable hyaluronic acid-based hydrogels and tissue engineering scaffolds.* Eur Spine J, 2007. **16**(11): p. 1892-8.

154. Stephens, E.H., C.K. Chu, and K.J. Grande-Allen, *Valve proteoglycan content and glycosaminoglycan fine structure are unique to microstructure, mechanical*

load and age: Relevance to an age-specific tissue-engineered heart valve. Acta Biomater, 2008. **4**(5): p. 1148-60.

155. Smeds, K.A. and M.W. Grinstaff, *Photocrosslinkable polysaccharides for in situ hydrogel formation (vol 54, pg 115, 2000).* J Biomed Mater Res B Appl Biomater, 2001. **55**(2): p. 254-255.

156. Messier, R.H., Jr., B.L. Bass, H.M. Aly, J.L. Jones, P.W. Domkowski, R.B. Wallace, and R.A. Hopkins, *Dual structural and functional phenotypes of the porcine aortic valve interstitial population: characteristics of the leaflet myofibroblast.* J Surg Res, 1994. **57**(1): p. 1-21.

157. Cruise, G.M., D.S. Scharp, and J.A. Hubbell, *Characterization of permeability and network structure of interfacially photopolymerized poly(ethylene glycol) diacrylate hydrogels.* Biomaterials, 1998. **19**(14): p. 1287-94.

158. Nilasaroya, A., L.A. Poole-Warren, J.M. Whitelock, and P. Jo Martens, *Structural and functional characterisation of poly(vinyl alcohol) and heparin hydrogels.* Biomaterials, 2008. **29**(35): p. 4658-64.

159. Jossang, T., J. Feder, and E. Rosenqvist, *Photon correlation spectroscopy of human IgG.* J Protein Chem, 1988. **7**(2): p. 165-71.

160. Beamish, J.A., J. Zhu, K. Kottke-Marchant, and R.E. Marchant, *The effects of monoacrylated poly(ethylene glycol) on the properties of poly(ethylene glycol) diacrylate hydrogels used for tissue engineering.* J Biomed Mater Res A. **92**(2): p. 441-50.

161. Jones, R.M., *Mechanics of Composite Materials.* 1975: p. 355.

162. Nguyen, T.D., R.E. Jones, and B.L. Boyce, *Modeling the anisotropic finite-deformation viscoelastic behavior of soft fiber-reinforced composites.* International Journal of Solids and Structures, 2007. **44**(25-26): p. 8366-8389.

163. Mohan, D. and J.W. Melvin, *Failure properties of passive human aortic tissue. II--Biaxial tension tests.* J Biomech, 1983. **16**(1): p. 31-44.

164. Fujita, Y., D.R. Wagner, A.A. Biviji, N.A. Duncan, and J.C. Lotz, *Anisotropic shear behavior of the annulus fibrosus: effect of harvest site and tissue prestrain.* Med Eng Phys, 2000. **22**(5): p. 349-57.

165. Ebara, S., J.C. Iatridis, L.A. Setton, R.J. Foster, V.C. Mow, and M. Weidenbaum, *Tensile properties of nondegenerate human lumbar anulus fibrosus.* Spine (Phila Pa 1976), 1996. **21**(4): p. 452-61.

166. Humzah, M.D. and R.W. Soames, *Human intervertebral disc: structure and function.* Anat Rec, 1988. **220**(4): p. 337-56.

167. Guerin, H.L. and D.M. Elliott, *Quantifying the contributions of structure to annulus fibrosus mechanical function using a nonlinear, anisotropic, hyperelastic model.* J Orthop Res, 2007. **25**(4): p. 508-16.

168. Hansen, K.A., J.A. Weiss, and J.K. Barton, *Recruitment of tendon crimp with applied tensile strain.* J Biomech Eng, 2002. **124**(1): p. 72-7.

169. Stephens, E.H., N. de Jonge, M.P. McNeill, C.A. Durst, and K.J. Grande-Allen, *Age-related changes in material behavior of porcine mitral and aortic valves and correlation to matrix composition.* Tissue Eng Part A, 2010. **16**(3): p. 867-78.

170. Diamant, J., A. Keller, E. Baer, M. Litt, and R.G. Arridge, *Collagen; ultrastructure and its relation to mechanical properties as a function of ageing.* Proc R Soc Lond B Biol Sci, 1972. **180**(60): p. 293-315.

171. Nguyen, T.D., R.E. Jones, and B.L. Boyce, *A nonlinear anisotropic viscoelastic model for the tensile behavior of the corneal stroma.* Journal of Biomechanical Engineering-Transactions of the Asme, 2008. **130**(4): p. -.

172. Shirazi-Adl, A., *On the fibre composite material models of disc annulus--comparison of predicted stresses.* J Biomech, 1989. **22**(4): p. 357-65.

173. Fung, Y.C., N. Perrone, M. Anliker, University of California San Diego., and United States. Office of Naval Research., *Biomechanics, its foundations and objectives*1972, Englewood Cliffs, N.J.,: Prentice-Hall. xiii, 641 p.

174. Pham, Q.P., U. Sharma, and A.G. Mikos, *Electrospinning of polymeric nanofibers for tissue engineering applications: a review.* Tissue Eng, 2006. **12**(5): p. 1197-211.

175. Pham, Q.P., U. Sharma, and A.G. Mikos, *Electrospun poly(epsilon-caprolactone) microfiber and multilayer nanofiber/microfiber scaffolds: characterization of scaffolds and measurement of cellular infiltration.* Biomacromolecules, 2006. **7**(10): p. 2796-805.

176. Chou, A.I., S.O. Akintoye, and S.B. Nicoll, *Photo-crosslinked alginate hydrogels support enhanced matrix accumulation by nucleus pulposus cells in vivo.* Osteoarthritis Cartilage, 2009. **17**(10): p. 1377-84.

177. Cha, C., S.Y. Kim, L. Cao, and H. Kong, *Decoupled control of stiffness and permeability with a cell-encapsulating poly(ethylene glycol) dimethacrylate hydrogel.* Biomaterials, 2010. **31**(18): p. 4864-71.

178. Wagner, H.D., I. Roman, and G. Marom, *Analysis of Elastic Properties of Symmetrically Laminated Beams in Bending.* Fibre Science & Technology, 1982. **16**(4): p. 295-308.

179. Toomey, R., D. Freidank, and J. Ruhe, *Swelling behavior of thin, surface-attached polymer networks.* Macromolecules, 2004. **37**(3): p. 882-887.

180. Flory, P.J., *Principles of polymer chemistry.* The George Fisher Baker non-resident lectureship in chemistry at Cornell University1953, Ithaca,: Cornell University Press. 672 p.

181. Valente, M., M. Minarini, A.F. Maizza, U. Bortolotti, and G. Thiene, *Heart valve bioprosthesis durability: a challenge to the new generation of porcine valves.* Eur J Cardiothorac Surg, 1992. **6 Suppl 1**: p. S82-90.

182. Liao, J., L. Yang, J. Grashow, and M.S. Sacks, *The relation between collagen fibril kinematics and mechanical properties in the mitral valve anterior leaflet.* J Biomech Eng, 2007. **129**(1): p. 78-87.

183. Lee, W.J., D.K. Choi, Y. Lee, D.N. Kim, J.W. Park, and W.G. Koh, *Preparation of micropatterned hydrogel substrate via surface graft polymerization combined with photolithography for biosensor application.* Sensors and Actuators B-Chemical, 2008. **129**(2): p. 841-849.

184. Suri, S. and C.E. Schmidt, *Photopatterned collagen-hyaluronic acid interpenetrating polymer network hydrogels.* Acta Biomater, 2009. **5**(7): p. 2385-97.

185. Sarkar, S., G.Y. Lee, J.Y. Wong, and T.A. Desai, *Development and characterization of a porous micro-patterned scaffold for vascular tissue engineering applications.* Biomaterials, 2006. **27**(27): p. 4775-82.

186. Khademhosseini, A., G. Eng, J. Yeh, P.A. Kucharczyk, R. Langer, G. Vunjak-Novakovic, and M. Radisic, *Microfluidic patterning for fabrication of contractile cardiac organoids.* Biomed Microdevices, 2007. **9**(2): p. 149-57.

187. Papenburg, B.J., L. Vogelaar, L.A. Bolhuis-Versteeg, R.G. Lammertink, D. Stamatialis, and M. Wessling, *One-step fabrication of porous micropatterned scaffolds to control cell behavior.* Biomaterials, 2007. **28**(11): p. 1998-2009.

188. Sacks, M.S., D.B. Smith, and E.D. Hiester, *A small angle light scattering device for planar connective tissue microstructural analysis.* Ann Biomed Eng, 1997. **25**(4): p. 678-89.

189. Shah, D.N., S.M. Recktenwall-Work, and K.S. Anseth, *The effect of bioactive hydrogels on the secretion of extracellular matrix molecules by valvular interstitial cells.* Biomaterials, 2008. **29**(13): p. 2060-72.

190. Nuttelman, C.R., S.M. Henry, and K.S. Anseth, *Synthesis and characterization of photocrosslinkable, degradable poly(vinyl alcohol)-based tissue engineering scaffolds.* Biomaterials, 2002. **23**(17): p. 3617-26.

191. Flanagan, T.C., B. Wilkins, A. Black, S. Jockenhoevel, T.J. Smith, and A.S. Pandit, *A collagen-glycosaminoglycan co-culture model for heart valve tissue engineering applications.* Biomaterials, 2006. **27**(10): p. 2233-46.

Appendix I: Design Evolution of Bioreactor and Bending Tester

A.1 Bioreactor Design Evolution

The designed bioreactor system and bending tester underwent a series of revisions as prototypes were fabricated and new discoveries regarding their performance were made. First, a crude bench top system with a sliding disk in a tub was made (Figure A1.1). This disk was aligned by 4 stainless steel wires, and motion of the disk was generated by a pulley, weights, and a strong closing spring. Mechanical valves were loaded into this system, it was filled with water, and the system was used to validate the "sliding piston" idea for valve opening and closure. In particular, this model system was evaluated to determine if changing direction caused significant "fluttering" or repeated opening and closing of the valve. This was not seen, so a simple system using a brass rack and pinion that slid on a Teflon track was fabricated to test the sliding disk within the culture chamber (Figure A1.2). The doctoral candidate used this prototype to ensure that no "water-hammer" effect was present by enclosing the sliding disk in a chamber, and that valve opening and closing proceeded as was observed in the first prototype.

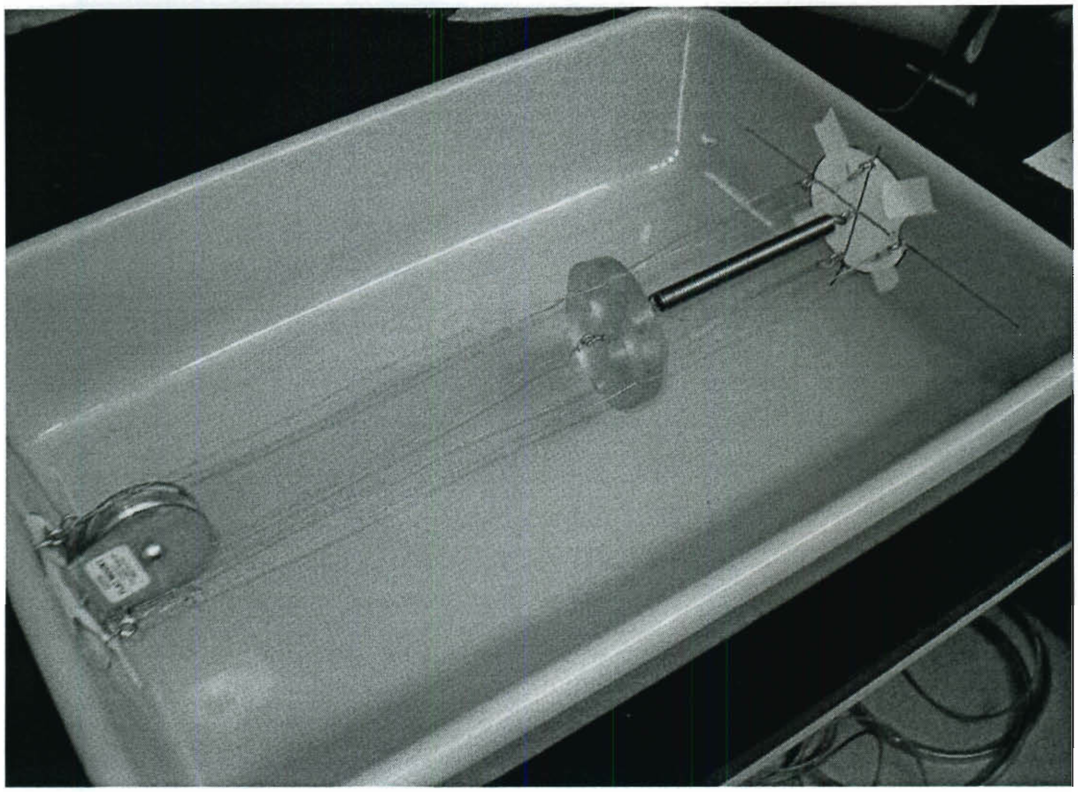

Figure A1.1: First bench top prototype to investigate sliding piston/disk design for valve opening and closure.

The first full bioreactor system can be seen in Figure A1.3, where the parts were initially fabricated to test fit and general system performance. Fluid resistance was similar to modeled behavior so the motor and gearbox selections could be made. The parts were then machined further for less binding when the piston slid (the circularity of the culture chambers was improved, since the extruded blue tubing was not sufficiently round) and material was removed from parts to reduce assembled and filled system weight. The first bioreactor that was loaded with porcine tissue and used experimentally can be seen in Figure A1.4. This bioreactor was subject to the bearing lockup and resulting sheared part problems described in Chapter 3. This was the final prototype design before the bioreactor design was deemed suitable for experimental cultures (the final design can be seen in Figure 3.1).

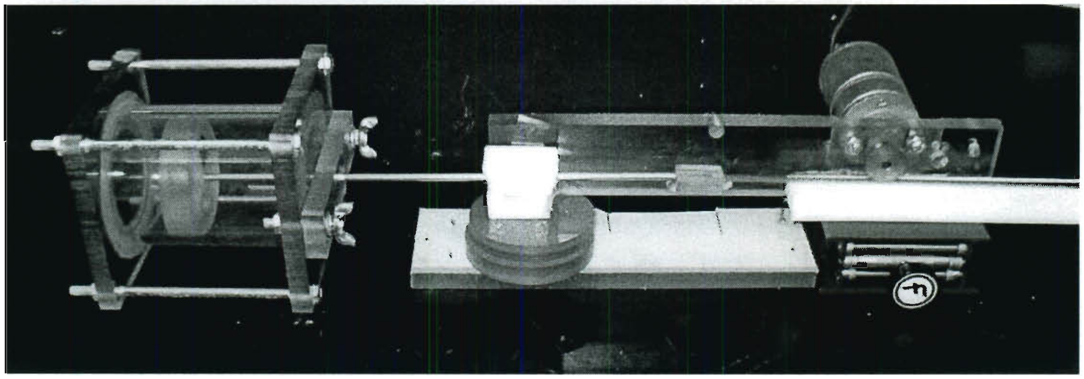

Figure A1.2: Motor-driven brass rack and pinion was used to achieve linear motion. This system investigated the effect of enclosing the piston in a culture chamber.

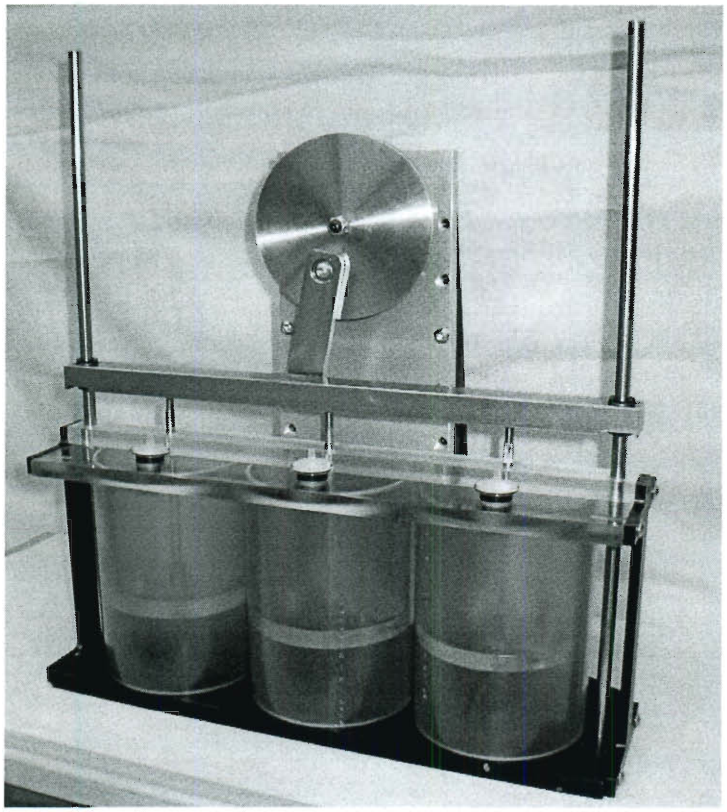

Figure A1.3: Prototype full assembly for fit testing and final drive confirmation.

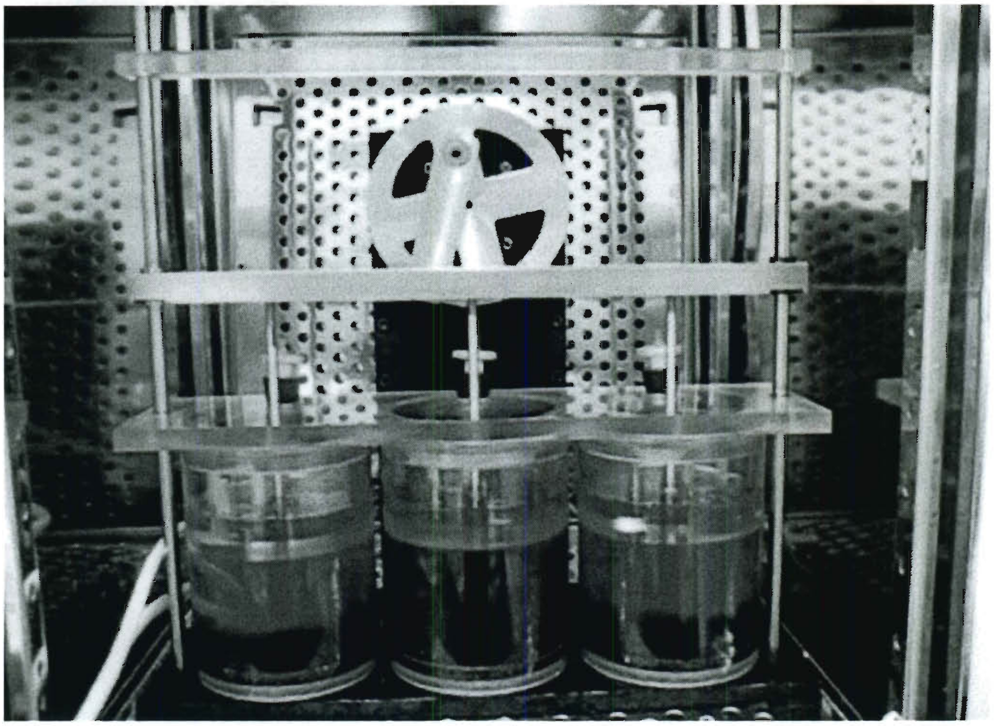

Figure A1.4: First completed version of the custom bioreactor that was used for organ culture. This system frequently became unstable, leading to bearing lockup that inspired the current design to account for alignment shaft deflection and increase the effective bearing length/diameter relationship.

A.2 Bending Tester Prototype and Evolution

The prototype bending tester was initially hand driven by a Newport micropositioner, this system was designed with Rice undergraduate Alex Brewer (Figure A1.5). The method for use was to pull an experimental sample a set deflection and measure the total resulting deformation of the flexure bar. This was the method employed by Gloeckner *et al.[126]* Since valve tissues are viscoelastic and strain rate dependent, it was determined that automation of the system was performed with a stepper motor to gain better control of the strain rate (Figure A1.6). The physical design of the motorized revision was performed with another Rice Undergraduate, Steve Xu.

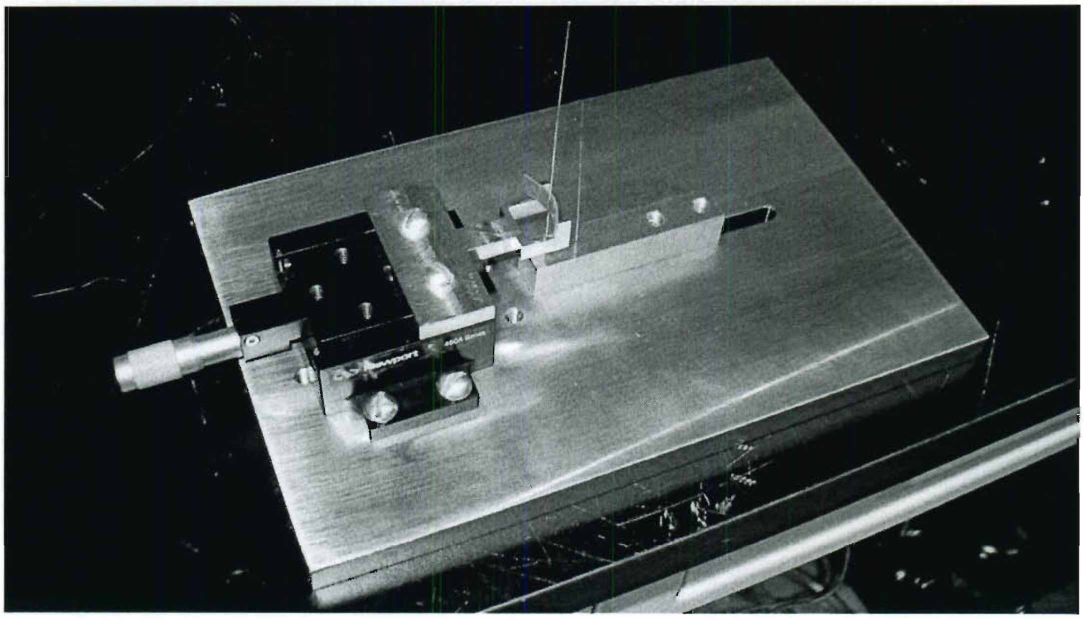

Figure A1.5: Prototype bending tester that was hand driven.

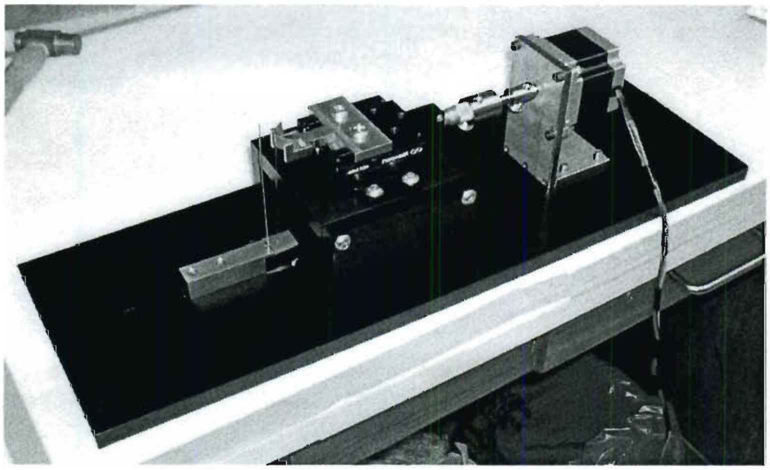

Figure A1.6: Bending tester with stepper motor to allow strain rate control and greater precision of displacement.

This system was initially used with a Leica dissection illuminator and microscope CCD, however this did not yield high enough frame rate or even enough lighting for repeatable automatic marker tracking on samples (Figure A1.7). Superior image tracking was realized by using conventional photography flood lamps and a consumer digital single lens reflex camera capable of shooting high-speed high definition video (1280x720 pixels with 60 frames per second). The final iteration of the designed bending tester can be seen in Figure 4.2.

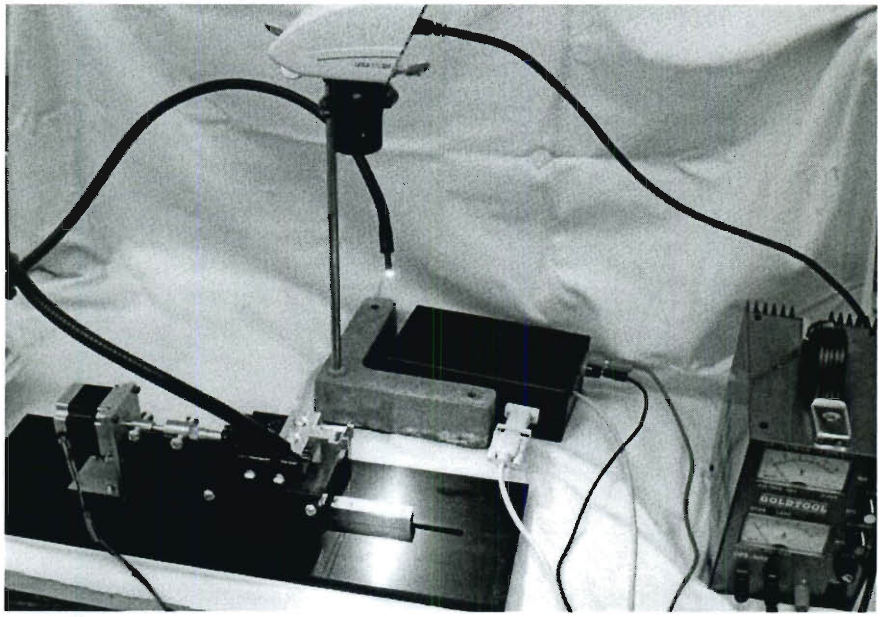

Figure A1.7: Initial bending tester experimental setup, with Leica dissection scope illumination, Leica CCD, and stepper amplifier and controller visible.

Appendix II: Additional Hydrogel Network Information

A2.1 Synthesis Verification

^{1}H-NMR was performed to verify that methacrylation of heparin was successful and therefore that it would be covalently linked to the PEGDA used in studies in Chapter 5. Percent methacrylation was calculated as 6.8% by comparing the peaks at 6.2 and 5.8 ppm to the peaks on the disaccharide repeat unit of heparin (Figure A2.1).[158]

A2.2 Additional Network Property Information

Hydrogel network properties (studied in Chapter 5) were represented in Table 5.1. Although the data is present in the table, the visual relationships of formulation on network properties is difficult to discern from that presentation, so the three main parameters have been displayed in Figure A2.2, Figure A2.3, and Figure A2.4.

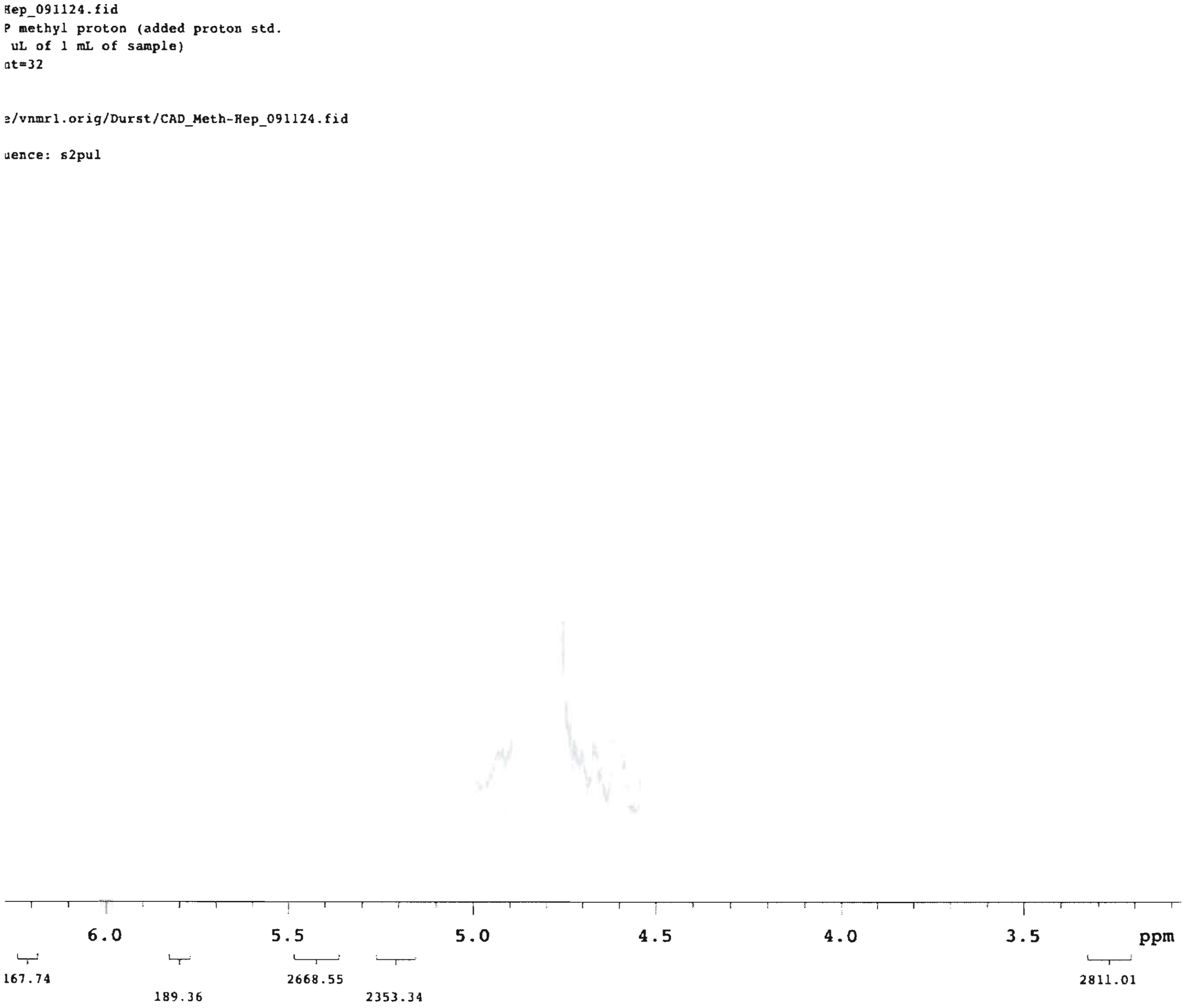

```
Hep_091124.fid
P methyl proton (added proton std.
 uL of 1 mL of sample)
nt=32

e/vnmrl.orig/Durst/CAD_Meth-Hep_091124.fid

uence: s2pul
```

Figure A2.1: Representative Hep-MA NMR Spectra

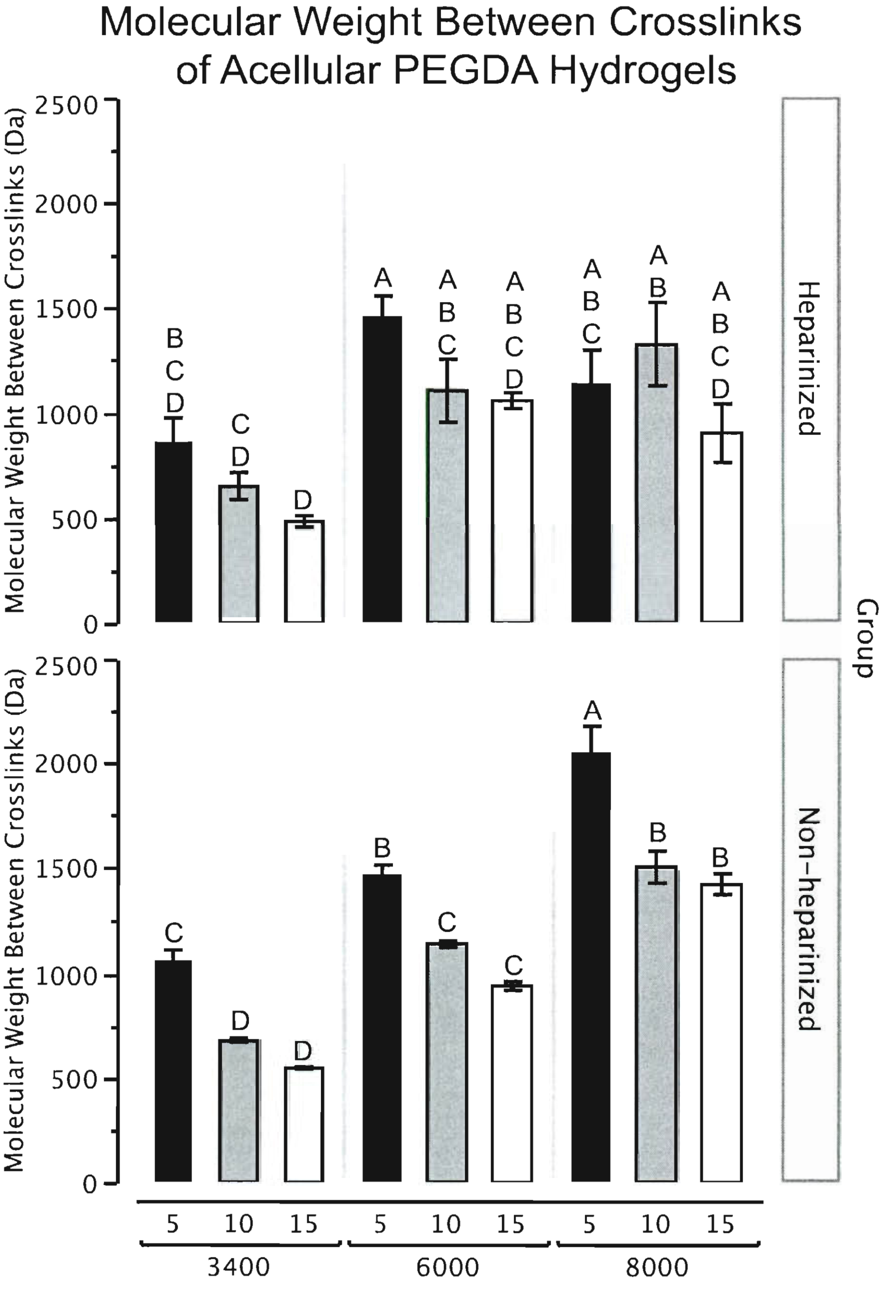

Figure A2.2: Molecular weight between crosslinks of acellular hydrogels. In both heparinized and non-heparinized gels, with increasing weight fraction, molecular weight between crosslinks decreases. In non-heparinized gels, molecular weight between crosslinks increases with increasing molecular weight. In heparinized gels, this trend is observed from 3400 to 6000 Da, but is not seen at higher molecular weights. Samples marked with different letters are significantly different at α=0.05.

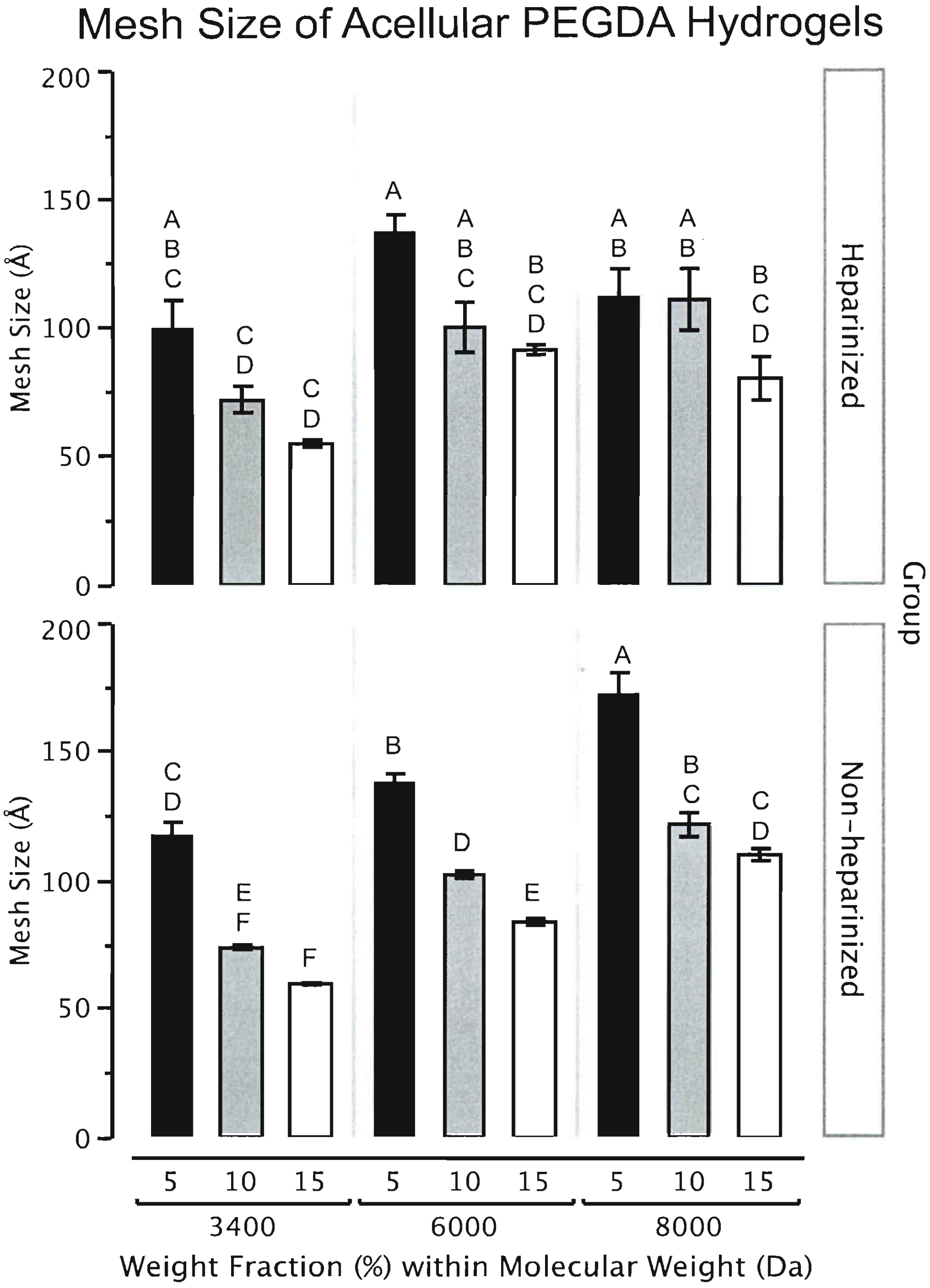

Figure A2.3: Mesh size of acellular hydrogels. In both heparinized and non-heparinized gels, with increasing weight fraction, mesh size decreases. In non-heparinized gels, mesh size increases with increasing molecular weight. Samples marked with different letters are significantly different at α=0.05.

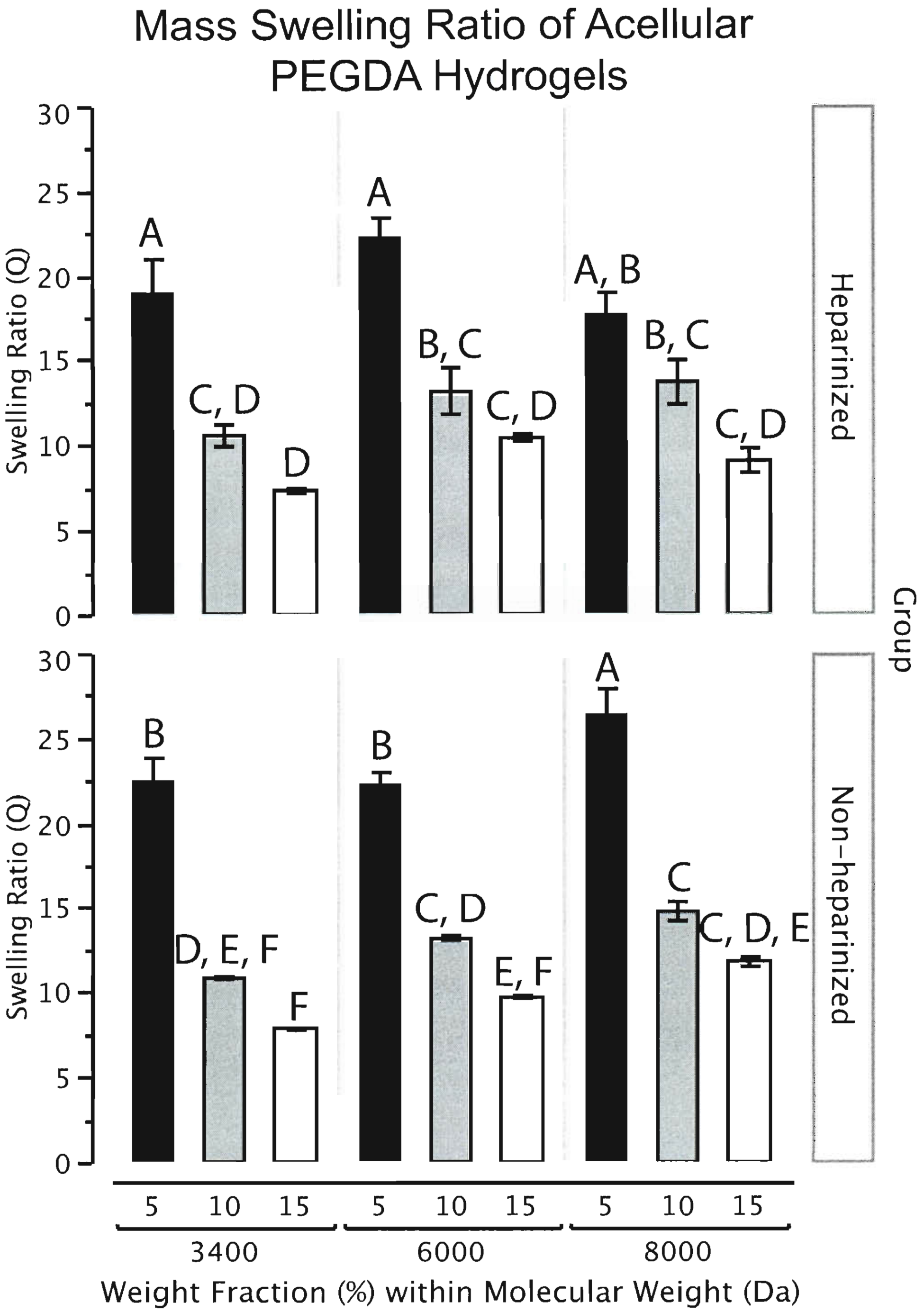

Figure A2.4: Mass swelling ratio of acellular PEGDA hydrogels functionalized with 0.5 mM Hep-MA. Samples marked with different letters are significantly different at α=0.05.

A2.3 Explanation of Moment Calculation

Bending moment is calculated as described in Figure A2.5. This moment is used in the derived relationship between thickness and stiffness in Section A2.4. If a simply supported beam undergoing three point bending is considered, and application of load P occurs at point R, the moment about a cross section at point R is PL/4. This is the point of maximum moment in the sample, and is calculated by multiplying the reaction force at Q (P/2) by the length of the arm (L/2).

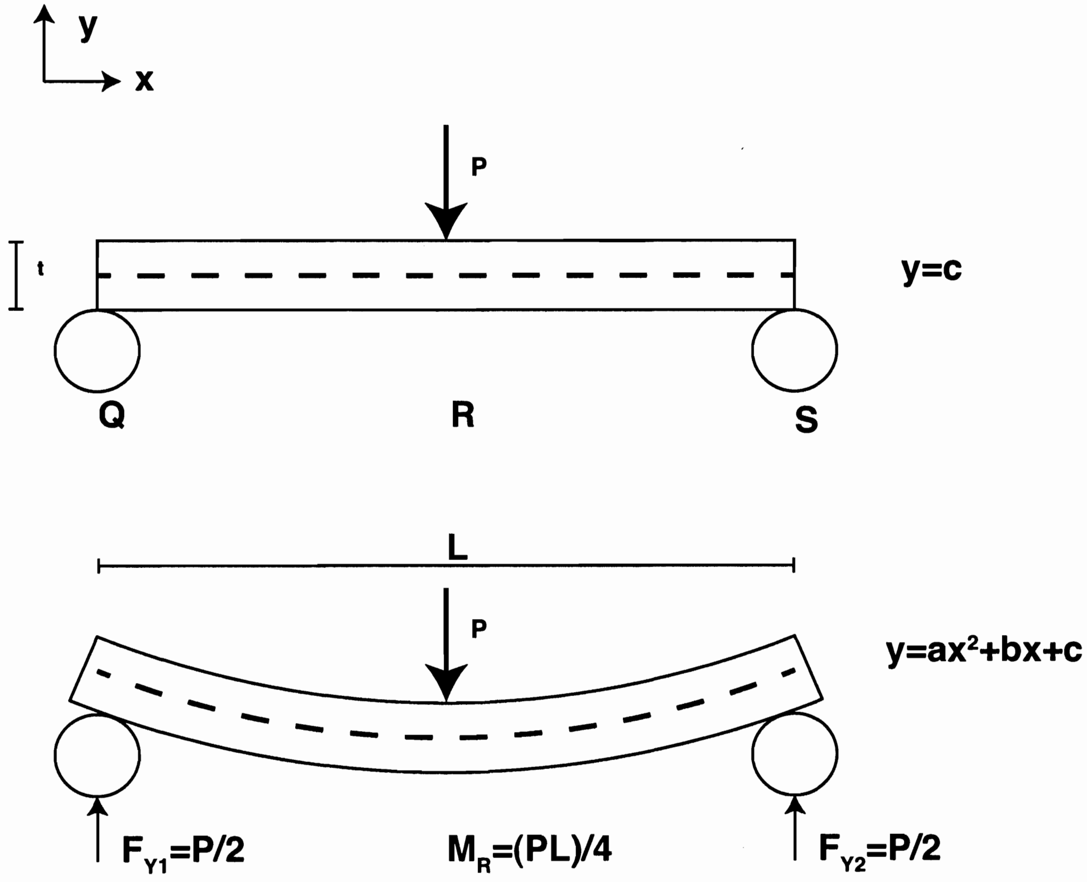

Figure A2.5: Illustration showing calculation of moment, quadratic line (fit at neutral axis), application of load, and maximum moment.

Appendix III: Confocal Tissue Strainer

This appendix features work in which I participated and was a co-author on the manuscript; however the work was led by other researchers. A brief description of the my primary contributions is given below and a reprint of the manuscript follows. This was published as Stephens EH, Durst CA, Swanson JC, Grande-Allen KJ, Ingels NB, Miller DC. Functional Coupling of Valvular Interstitial Cells and Collagen Via α2β1 Integrins in the Mitral Leaflet. Cellular and Molecular Bioengineering, 2010 Dec; 3(4):428-437

This research sought to characterize the mechanisms of mitral leaflet force generation by investigating actin-mediated VIC force generation coupled to collagen via α2β1 integrins. High-resolution confocal microscopy was intended to be used to study this phenomena and the study required a device to apply strain and measure load to mitral valve tissue while being directly imaged, however this was not available. I then designed a novel device to apply strain and measure load to mitral valve leaflets while being directly imaged with confocal microscopy. My secondary contribution was to train and assist the first author with confocal microscopy and 2nd harmonic imaging of collagen fiber. Figures representing the my primary contributions to the manuscript are shown below (Figure A3.1 and Figure A3.2)

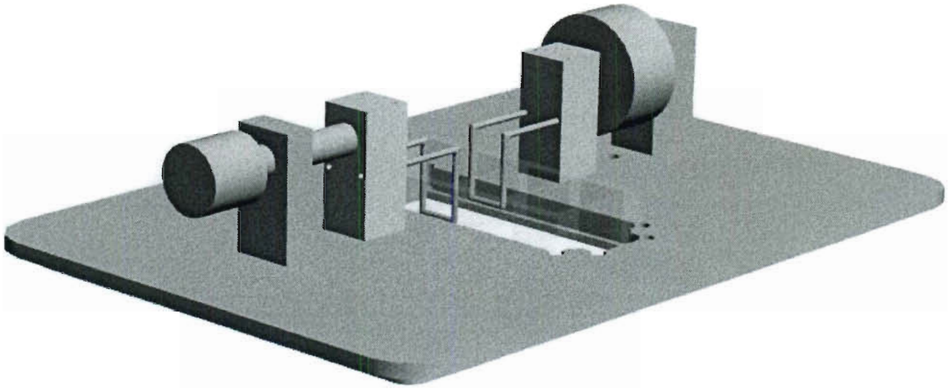

Figure A3.1: Isometric rendering of custom strain load device. The device fit into a motorized Zeiss LSM confocal microscope stage to allow direct imaging of tissue while applying strain and measuring load.

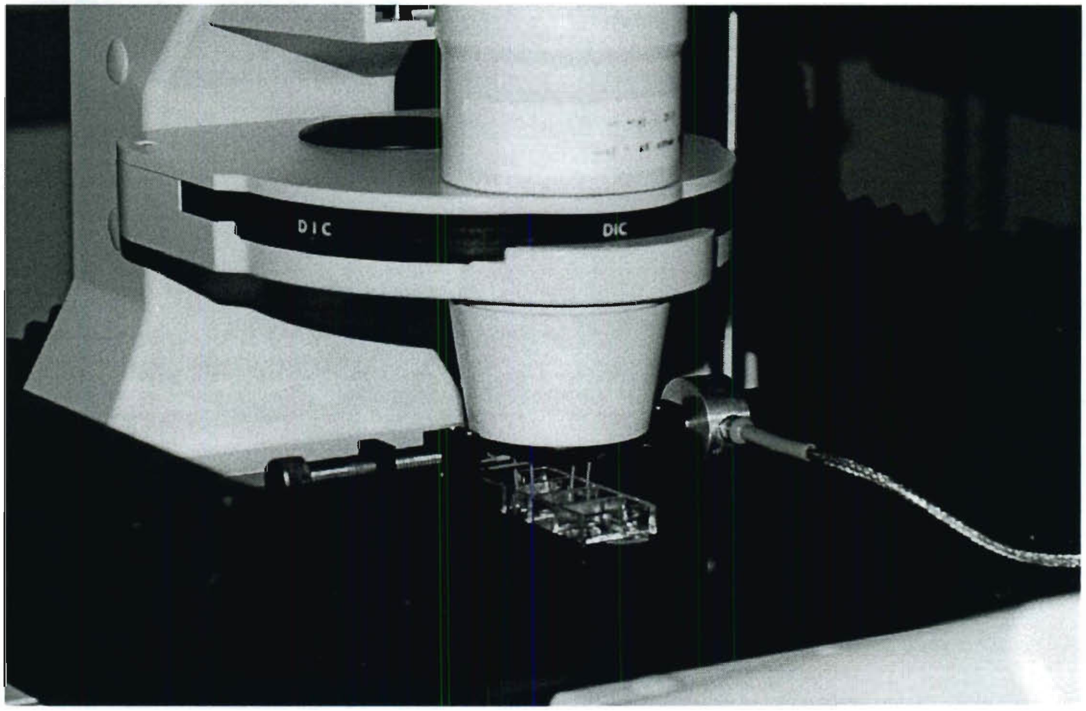

Figure A3.2: Photograph of system in use on a Zeiss LSM confocal microscope. Thumbscrew to apply strain can be seen on left of device with load cell acquiring force data on right side.

Cellular and Molecular Bioengineering (© 2010)
DOI: 10.1007/s12195-010-0139-6

Author Proof

Functional Coupling of Valvular Interstitial Cells and Collagen Via $\alpha_2\beta_1$ Integrins in the Mitral Leaflet

ELIZABETH H. STEPHENS,[3] CHRISTOPHER A. DURST,[3] JULIA C. SWANSON,[1] K. JANE GRANDE-ALLEN,[3]
NEIL B. INGELS JR.,[1,2] and D. CRAIG MILLER[1,2,4]

[1]Department of Cardiothoracic Surgery, Stanford University School of Medicine, Stanford, CA, USA; [2]Department of Cardiovascular Physiology and Biophysics, Research Institute, Palo Alto Medical Foundation, Palo Alto, CA, USA; [3]Department of Bioengineering, Rice University, Houston, TX, USA; and [4]Department of Cardiothoracic Surgery, Falk Cardiovascular Research Center, 300 Pasteur Drive, Stanford, CA 94305-5247, USA

(Received 20 February 2010; accepted 12 August 2010)

Associate Editor Chwee Teck Lim oversaw the review of this article.

Abstract—Once considered passive flaps, we now understand that mitral leaflets are dynamic structures with their own vasculature and innervation that actively remodel and even generate force in response to their environments. Valvular interstitial cells (VICs) are contractile and could underlie mitral leaflet force generation, but the exact mechanisms for VICs in mitral leaflet force generation are not understood. This study tested the hypothesis that actin-mediated VIC force generation coupled to collagen via $\alpha_2\beta_1$ integrins is necessary for force generation in the mitral leaflet. High magnification fluorescent imaging of freshly excised porcine mitral leaflets revealed VIC cytoplasm tightly conforming to collagen fibers, with actin within VIC cytoplasmic processes appearing to attach to the collagen fibers. Functional studies of isometric force development demonstrated that while control samples developed force in response to KCl, either blocking $\alpha_2\beta_1$ integrins or blocking actin polymerization via cytochalasin abolished KCl-induced force development ($p < 0.001$). These results strongly suggest that VIC-collagen coupling, mediated by $\alpha_2\beta_1$ integrins, is necessary for KCl-induced force generation in the mitral leaflet. This functional coupling between collagen and VICs via $\alpha_2\beta_1$ integrins may play a role for *in vivo* mitral valve function.

Keywords—Extracellular matrix, Force generation, Cell contraction, Integrin, Cytochalasin, Actin, Heart valve, Second harmonic generation, Confocal microscopy.

INTRODUCTION

While mitral valves were once regarded as passive flaps, a growing body of evidence continues to revise this notion. Mitral leaflets have their own vasculature,[2,13,31,42] innervation,[3,10,13,28,38] remodel in response to various stresses,[6,11,39,40] and recent studies suggest that there are multiple contractile systems within the leaflets.[23] *Ex vivo* studies have demonstrated that mitral leaflets generate force in response to vasoactive agents.[16,38] Valvular interstitial cells (VICs) are a dynamic, active component within leaflets that enable valves to remodel and mitral leaflet VICs are known to contract in response to vasoactive agents.[16] Given the contractile properties of VICs and evidence that the same vasoactive agents that cause mitral VIC contraction also result in force generation in mitral leaflets,[16,38] it appears that mitral VIC contraction could be one component of mitral leaflet force generation. However, the means by which mitral VIC contraction is transferred into mitral force generation has not been studied.

Transmission electron micrographs of mitral leaflets show VICs closely associated with collagen fibers,[16] suggesting an interaction between VICs and collagen in the leaflet, perhaps even acting together as a functional unit. Given that integrins are the primary proteins attaching cells to the surrounding matrix,[48] a potential interaction between VICs and collagen likely occurs through one of the integrins. Of the known collagen binding integrins, only $\alpha_2\beta_1$ and $\alpha_{11}\beta_1$ show higher affinity for type I collagen (the predominant collagen in heart valves[9]) than type IV.[1] Based on fibroblast–collagen gel contraction[12] and fibroblast collagen fiber transport[30] studies, we hypothesized that $\alpha_2\beta_1$ integrins may be a mechanism by which VICs attach to collagen within the mitral valve leaflet. Given the critical role that $\alpha_2\beta_1$ integrins play in fibroblast–collagen interactions,[12,30] their demonstrated presence on mitral VICs,[26] and the tools available to probe $\alpha_2\beta_1$ integrin

---

Address correspondence to D. Craig Miller, Department of Cardiothoracic Surgery, Falk Cardiovascular Research Center, 300 Pasteur Drive, Stanford, CA 94305-5247, USA. Electronic mail: dcm@stanford.edu

© 2010 Biomedical Engineering Society

Journal : **CMBE**	MS Code : **12195**	PIPS No. : **139**	☐ TYPESET	☑ DISK	☐ LE	☑ CP Dispatch : **17-8-2010**	Pages : **10**

Author Proof

function, this study chose to investigate $\alpha_2\beta_1$ integrins. While a variety of integrins have been shown to be present on enzymatically isolated mitral VICs, including $\alpha_2\beta_1$[26,27] the potential functional role of integrins in valves, however, has not been studied.

Based on the hypothesized roles of cellular contraction and $\alpha_2\beta_1$ integrins in this proposed VIC-collagen mechanotransduction within the mitral valve, the aim of this study was to test the specific hypothesis that actin-mediated VIC contraction coupled to collagen via $\alpha_2\beta_1$ integrins was necessary for force generation in mitral leaflets.

MATERIALS AND METHODS

Immunofluorescence

Porcine hearts (Yosemite Meat, Modesto, CA) were obtained within 1 h of animal slaughter and transported in cold saline (0.9% sodium chloride, Hospira, Lake Forest, IL). The central bare area (central region devoid of chordal attachments) of each mitral anterior leaflet was dissected within 4 h of animal slaughter and stained to visualize VIC cytoplasm, nucleus, and F-actin. VIC cytoplasm was stained using calcein AM (Invitrogen Molecular Probes, Eugene, OR) and VIC nuclei were stained using Syto85 (Invitrogen Molecular Probes). Cytoplasmic F-actin was stained using AlexaFluor 488 phalloidin (Invitrogen Molecular Probes) in tissues fixed in 10% formalin for 30 min and permeabilized with 0.5% Triton-X100 (Sigma-Aldrich, St. Louis, MO). Tissue was only fixed for actin staining; all other staining and force generation experiments utilized fresh tissues without fixation or permeabilization.

Confocal Microscopy

A Zeiss Leica 510 LSM confocal microscope (Zeiss, Oberkochen, Germany) with a Mira tunable Ti:Sa laser (Coherent, Santa Clara, CA) was used to visualize the fluorescent probes and the second-harmonic generated collagen signal (excitation at 820 nm, maximum emission at 410 nm). Specifically, calcein was visualized using a 488 nm Ar laser and 500–530 nm band pass (BP) filter, Syto85 was visualized using a 543 nm HeNe laser and 565–615 BP filter, and AlexaFluor 488 phalloidin was visualized using a 488 nm Ar laser and 500–530 nm BP filter. Second-harmonic generated collagen signal was obtained using an 820 nm wavelength on the tunable Ti:Sa laser and emission captured using a 390–465 nm BP filter, similar to previously reported techniques.[37] A key advantage of using second harmonic generation in these studies is that it allowed visualization of collagen without interfering with the potential VIC-collagen interaction, such as may have occurred with a fluorescent probe conjugated collagen antibody. Images were taken with the 20× objective lens, while higher magnification images used 25×, 40×, 63×, and 100× oil immersion objective lenses. Images were processed using Zeiss LSM Image Browser software (Zeiss).

Custom-Built Strain-Load Device

Using computer assisted design software (SolidWorks, Dassault Systèmes, Lowell, MA), a strain-load device (Fig. 1) was built to fit, spring-loaded, into a motorized Zeiss Leica 510 LSM confocal microscope stage replacing the standard microscope slide holder. The device was fabricated from 6061 aluminum that was anodized for corrosion resistance. Tissue samples were placed in a 4-well cover glass chamber (LabTek II, Nalgene Nunc International, Naperville, IL) and sutured to plastic mesh attached to wire struts. These wire struts were secured with set screws in blocks on either side of the wells. The blocks slid freely in one dimension in recessed channels. The 4-well cover glass chamber was suspended above the microscope objective using a small metal lip. An adjustable screw, coupled with the freely-sliding left block, allowed manipulation of strain on the tissue. A miniature tension load cell (Omega, Stamford, CT) was fit in-line with the sutured tissue. The load cell was powered using a 12 V battery that delivered 10 V DC to the load cell through the use of a voltage divider. Output from the load cell was captured by a USB data acquisition kit (USB 6008, National Instruments, Austin, TX) and recorded using a custom-designed virtual instrument (Lab View Signal Express, National Instruments).

Force Generation Studies

Small (~1 cm × 5 mm) circumferential strips of the central, bare area of the anterior mitral leaflet were sutured into the custom-designed strain-load device fit upon the microscope stage, as described above. After suturing the tissue in place, the tissue was allowed to equilibrate in Kreb's solution for at least 20 min (136.9 mM NaCl, 11.9 mM $NaHCO_3$, 2.7 mM KCl, 0.4 mM NaH_2PO_4, 2.5 mM $MgCl_2$, 2.5 mM $CaCl_2$, 11.1 mM glucose, 0.04 mM disodium EDTA, pH 7.4). Potassium chloride (95 mM) was added to control samples ($n = 10$) and the load-cell output recorded using the custom-designed software described above. To investigate the roles of $\alpha_2\beta_1$ integrins and actin in VIC-mediated leaflet contraction, VIC cytoplasmic and nuclear staining was performed as described above, and tissues were incubated with either 10 μg/mL $\alpha_2\beta_1$ monoclonal blocking antibody (Chemicon[40]) for 2 h ($n = 5$) or 25 μM cytochalasin (which prevents

Author Proof

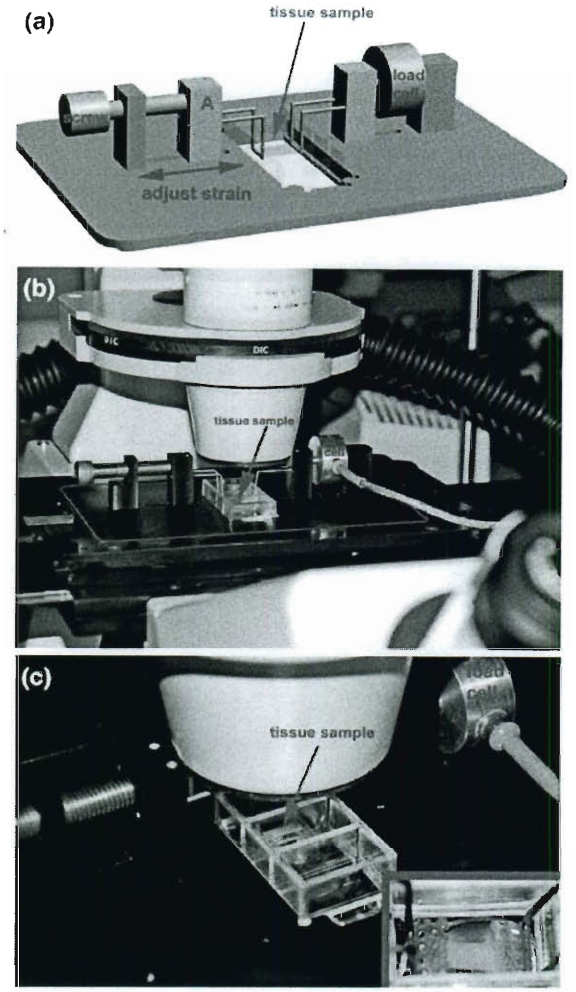

FIGURE 1. Custom-built strain-load device. (a) Diagram illustrating strain-load device built to fit into a motorized confocal stage. Adjustable screw is shown at left; this screw, coupled with a block (labeled "A") that could freely slide in cut-out channel, allowed manipulation of strain on tissue as indicated by red arrow. Chamber glass, which held tissue sample in buffer, appears ghosted in on this diagram. The chamber glass was held above objective by virtue of a small metal lip. Placement of tissue sample within the set-up is indicated by the beige rectangle and load cell is labeled. (b) Photo illustrating custom-built strain-load device diagrammed in (a) set in place on confocal stage. Edges of strain load device are outlined in red, tissue sample and load cell are labeled. Microscope objectives are located under the black stage (hidden from view) and microscope eye piece is evident in foreground of photo. Signal output from load cell is carried by silver cable to electronics not pictured. (c) Close-up photo of *in situ* strain-load device. Note valve tissue sutured to plastic mesh between green wire struts. Microscope objective can be seen beneath cover glass. Tissue sample and load cell are labeled. Inset: view of tissue sample from above (microscope head piece removed) demonstrating tissue sutured in place within the chamber. Microscope objective can be seen below.

filamentous actin polymerization) (Sigma-Aldrich) for 1 h ($n = 4$) before the addition of 95 mM KCl. All experiments were performed at room temperature.

Statistics

Statistical comparisons between groups were made with one-way ANOVAs using SigmaStat software (SPSS, Chicago, IL). For data sets that were not normally distributed, ANOVA on ranks was performed. Post-hoc pair-wise comparisons were performed using Dunn's method. The level of significance was set at $p = 0.05$. Data is represented as mean ± SEM.

RESULTS

VICs Aligned and Integrated with Collagen Fibers

Fluorescent imaging of VICs revealed that VIC cell bodies were highly aligned in parallel with collagen fibers (Fig. 2). VIC cytoplasm and nuclei were elongated, with their long axis coinciding with that of the collagen fibers. High magnification images demonstrated the VIC cytoplasm tightly conforming to the undulating contour of the crimped collagen fibers (Fig. 3). Fluorescent imaging of VIC cytoskeletal actin revealed VIC actin similarly aligned with collagen fibers, and actin within VIC cytoplasmic processes appeared to attach to collagen fibers (Fig. 4). VICs in $\alpha_2\beta_1$ integrin-blocked samples tended to show less alignment relative to collagen fibers compared to control samples taken from the same region of the same leaflet (Fig. 5). Alignment of collagen fibers, as well as alignment of VICs with each other, also tended to appear less in integrin-blocked samples.

Blocking $\alpha_2\beta_1$ Integrins or Actin Polymerization Prevented Force Generation

Consistent with previous studies,[4,7,16,24,32,38,45,47] the addition of 95 mM KCl resulted in force generation (Fig. 6) in the circumferential strip of mitral valve tissue. Blocking of either $\alpha_2\beta_1$ integrins or actin polymerization (via cytochalasin) was sufficient to prevent force generation in response to 95 mM KCl (control: 3.30 ± 0.23 mN, integrin-blocked: 0.04 ± 0.09 mN, cytochalasin 0.20 ± 0.06 mN, $p < 0.001$, Fig. 6).

DISCUSSION

The imaging results of this study, taken together with the leaflet force data, support the hypothesis that

Author Proof

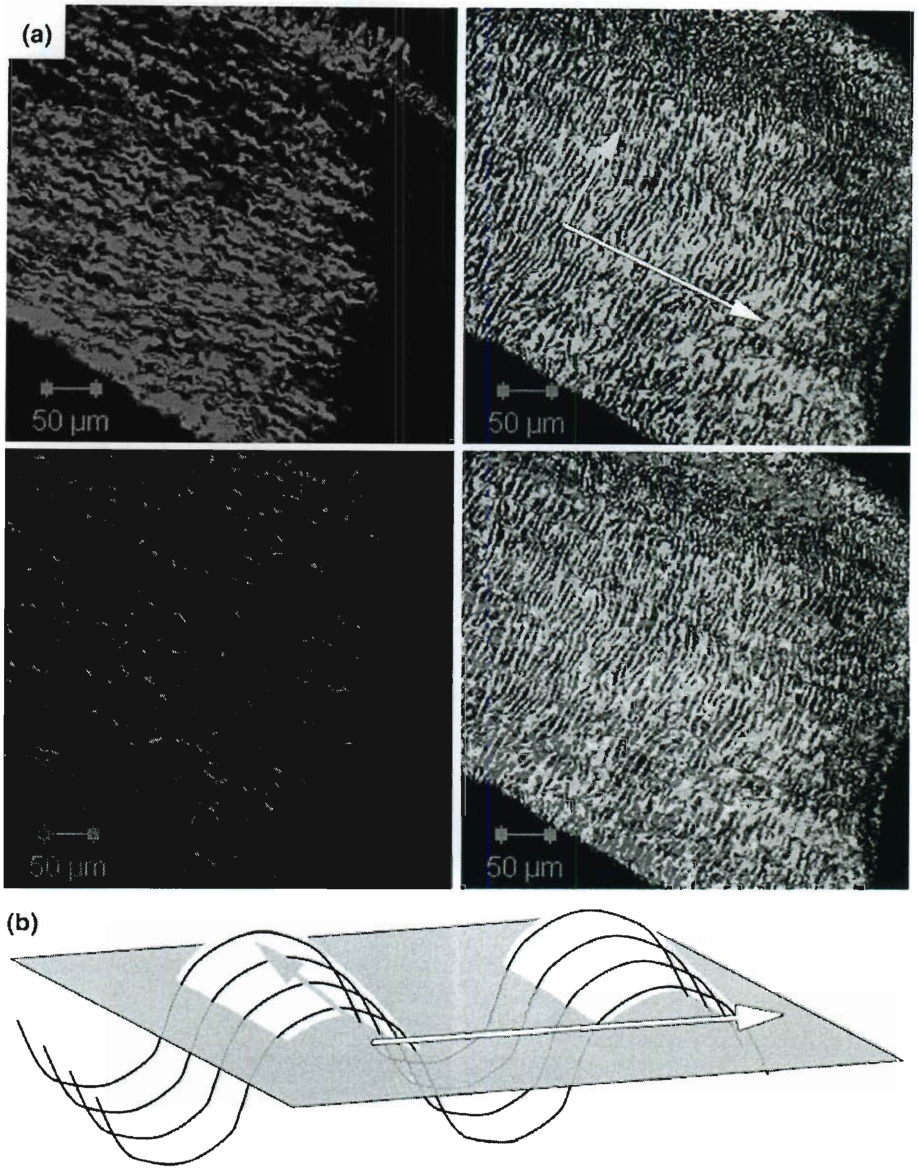

FIGURE 2. (a) Image demonstrating VIC alignment with respect to collagen fibers. Blue (upper left panel) indicates the VIC cytoplasm, green (upper right panel) indicates collagen fibers, red (lower left panel) indicates VIC nuclei, and lower right panel is the merged image of the 3 other panels. The yellow arrow in the upper right panel indicates the orientation of collagen ridges, and correlates to the yellow arrow in the schematic in part B. The white arrow in the upper right panel indicates the orientation of collagen fibers, and is analogous to the white arrow in the schematic of part b (*Note*: in all remaining figures collagen fiber alignment is indicated by a white arrow). Scale bar indicates 50 μm. (b) Schematic illustrating how undulating collagen fibers at this magnification appear as lines perpendicular to the direction of collagen fibers. White portions of undulating fibers above green plane represent portions of fibers in focus. The yellow arrow indicates the ridges visualized in the upper right panel of part a (and corresponds to the yellow arrow in part a), whereas the white arrow indicates the orientation of collagen fibers. *Note*: in all remaining figures, collagen fiber alignment is indicated by a white arrow.

VIC-collagen coupling, mediated by $\alpha_2\beta_1$ integrins, underlies leaflet force generation. Confocal microscopy imaging provided a structural foundation for a proposed VIC-collagen functional unit. Functional studies, utilizing KCl to elicit VIC contraction, built on this foundation, and demonstrated the necessary components of this functional unit for mitral valve force generation: VIC actin polymerization, collagen fibers, and $\alpha_2\beta_1$ integrins.

Author Proof

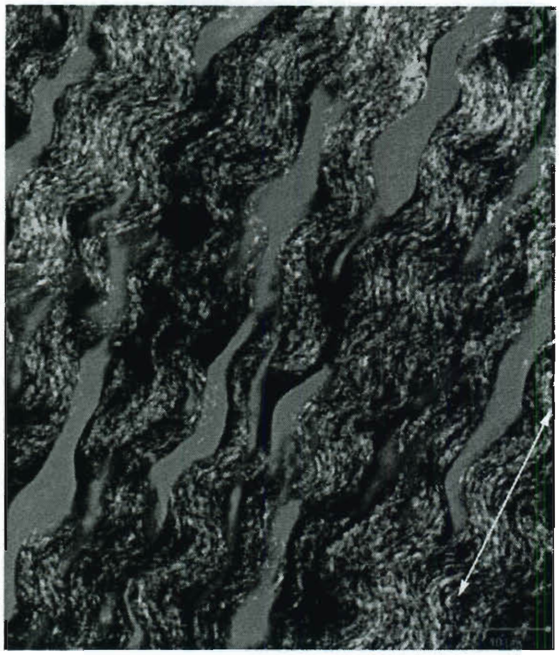

FIGURE 3. Image demonstrating VICs nestled into the curves of the collagen fibers. Green indicates collagen fibers, blue indicates VIC cytoplasm, and pink indicates VIC nuclei. White arrow indicates the direction of collagen fibers. Scale bar indicates 10 μm.

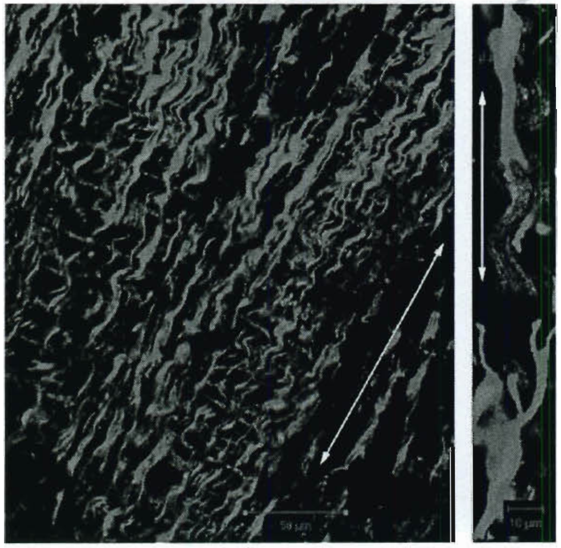

FIGURE 4. Left panel demonstrates alignment of VIC actin with collagen fibers at lower magnification. Green indicates collagen fibers, blue indicates VIC actin, and pink indicates VIC nuclei. Scale bar indicates 50 μm. Right panel demonstrates VIC actin processes "grasping" collagen fibers at higher magnification. Scale bar indicates 10 μm. White arrow in both portions of the figure indicates orientation of collagen fibers.

Structural Interaction Between VICs, Integrins, and Collagen Fibers

The second harmonic-generated collagen signal allowed visualization of the structural relationship between collagen fibers and viable VICs in freshly excised leaflets without altering their spatial arrangement with tissue fixation and processing, or disrupting potential interactions between VICs and collagen fibers, as can occur with antibodies or other probes. This method of visualizing viable cells in freshly excised tissues is in contrast to the limited number of previous studies in which transmission electron microscopy demonstrated VICs abutting collagen fibers.[16,21] While these previous studies were important to our understanding of VICs within the valve matrix, such imaging modalities have significant limitations related to specimen preparation, which make interpretation of their results in the context of *in vivo* leaflets difficult.

Of particular note was the parallel alignment of VICs relative to collagen fibers. While leaflet anisotropy has largely been attributed to collagen fiber alignment in the past,[25] the observed alignment of VICs in conjunction with the functional findings of this study and studies demonstrating that VIC contraction caused greater circumferential as opposed to radial force generation in aortic cusps,[24] suggests that VIC alignment may contribute to the anisotropic material properties of valves.

VIC cytoplasm was not only observed to closely follow the contours of the crimped collagen fibers, in what could be considered a space-filling manner, but apparent direct attachments were observed between cytoplasmic processes and collagen fibers, suggesting a structural link between VICs and collagen fibers. Imaging in this study also suggested a potential functional role for these $\alpha_2\beta_1$ integrins: attaching VICs to adjacent collagen fibers. When $\alpha_2\beta_1$ integrins were blocked, VICs were less aligned with collagen fibers as compared with VICs in control samples taken from the same leaflet region.

VIC-Integrin-Collagen Functional Unit

This study demonstrated that blocking $\alpha_2\beta_1$ integrins abolished leaflet force development; this result suggests that VICs are functionally coupled with collagen via $\alpha_2\beta_1$ integrins allowing the force generated by VIC contraction to be transmitted to collagen, and thereby the mitral leaflet. Similarly, when actin polymerization was blocked via cytochalasin,[17,18] leaflet force generation did not occur. This result suggests that leaflet force is developed by actin-dependent VIC contraction. Therefore, when either the actin portion

Author Proof

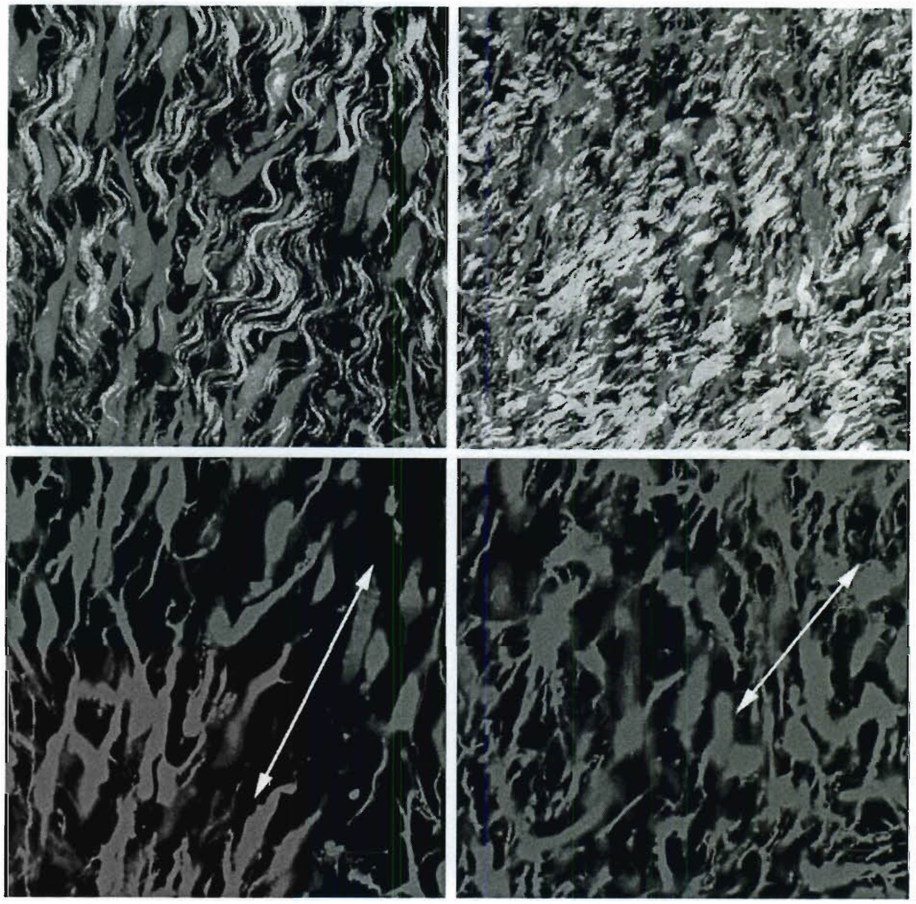

Control Sample

Integrin-Blocked Sample

FIGURE 5. VICs after blocking alpha$_2$ beta$_1$ integrins tended to show less alignment with collagen fibers. Left panel demonstrates control sample, right panel demonstrates sample from adjacent region of the same leaflet in which alpha$_2$ beta$_1$ integrins were blocked. The upper panels are merged images in which green indicates collagen fibers, blue indicates VIC cytoplasm, and pink indicates VIC nuclei. Lower images are identical to merged images above, but illustrate cytoplasm staining alone to better visualize VIC alignment relative to collagen fiber orientation (indicated by white arrows), demonstrating less alignment of VICs in alpha$_2$ beta$_1$ integrin-blocked samples relative to collagen fibers. Scale bar indicates 20 μm.

of the functional unit or the integrin portion of the functional unit is blocked, force is not generated in the leaflet.

Integrin Signaling and Mechanotransduction

Composed of transmembrane α and β heterodimers, integrins act as connectors from the cell's outside world to its cytoskeleton, usually actin.[1] Integrin signaling is complex, including both outside-in and inside-out signaling effecting short-term and long-term (i.e., gene expression) changes.[1] Upon ligand binding integrins undergo a conformational change that includes its cytoplasmic domains and initiates intracellular signaling events (outside-in signaling).[22] But intracellular signaling can also act to alter the extracellular conformation of the integrins (inside-out signaling) via cytoplasmic proteins such as FAK (focal adhesion kinase), ILK (integrin-linked kinase), filamin, talin, kindlins, and migfilin.[1] With respect to the β_1 integrin subunit specifically, four proteins are known to mediate attachment of β_1 integrin to the actin cytoskeleton: α-actinin, talin, filamin, and ILK.[5] Additionally, Rack1, caveolin, and NWASp have been shown to bind to its cytoplasmic tail.[5,41] Upon integrin binding Cdc42 and Rac are activated,[33] which leads to actin polymerization and Rho activation.[15] Integrin binding also leads to tyrosine phosphorylation of many proteins and modulation of protein tyrosine phosphatases, which among other roles regulate Rho

Author Proof

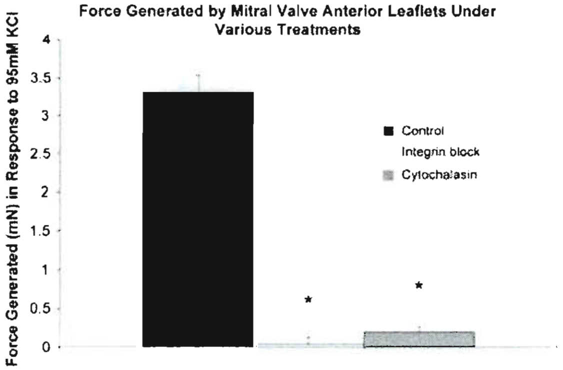

FIGURE 6. Force generated by mitral valve anterior leaflets exposed to various treatments in response to 95 mM KCl after 10 min. Overall comparison between groups by one-way ANOVA: $p < 0.001$; pair-wise comparison (Dunn's method): * $p < 0.05$ vs. control. Error bars indicate standard error of the mean.

activity.[15] Among the kinases activated with integrin binding are FAK and src, whose substrates include Rac and Cdc42.[15] In terms of actin assembly, upon integrin binding Arp2/3 is recruited to vinculin, which in turn is recruited to integrins via talin; the association of Arp2/3 and vinculin is regulated by phosphatidylinositol-3-kinase and Rac.[14] Other key regulators of Arp2/3 include the WASP family of proteins, which in turn are regulated by proteins such as Nck, Cdc42, and ptdIns(4,5)P_2.[15] Specifically in response to a contractile stimulus, N-WASp activates Arp2/3, a process that also involves Cdc42 and CrkII.[44] During contraction paxillin binds FAK and both are phosphorylated; paxillin phorphorylation may regulate downstream signaling via CrkII.[43]

VIC-Integrin-Collagen Force Generation—Relevance to Valve Function

The primary goal of this study was to demonstrate this VIC-integrin-collagen functional unit, however a natural question that arises from this work is how this unit and the forces it generates could impact valve function. Clearly the forces we measured are much lower than the forces externally applied to the valve *in vivo*, but evidence suggests that VIC contraction could impact valve function, principally by altering the valve's material properties, i.e., stiffness. Merryman *et al.*[29] demonstrated that VIC contraction increased aortic cusp flexural stiffness by 48% and elimination of VIC basal tone caused a 2–4 fold decrease in flexural stiffness. Thus, the VIC-integrin-collagen unit described here could serve to help align as well as stiffen the collagen matrix, and vary this stiffness to meet changing demands. Other work suggests that VICs could be involved in collagen fiber alignment and VIC contraction could be important in valve function in cases of low strain.[36] Given that collagen fibers are important tensile, load bearing elements in the valve and their material properties are highly dependent on fiber alignment, VIC regulation of collagen alignment could have important functional consequences. Studies in aortic cusps have also shown regional variation in force generation,[24] therefore VIC contraction could be important for regional stress distribution and/or modulating shape. Chester *et al.*[8] demonstrated that circulating vasoactive agents in an *ex vivo* setting led to aortic valve incompetence, suggesting that vasoactive agents and potentially VIC contraction within this functional unit could impact valve performance.

Implications

This study confirms and builds upon a proposed model of the mitral valve (MV) that included 3 contractile elements including cardiac muscle, smooth muscle, and VICs to explain the dynamic MV stiffness changes that occur *in vivo*.[23] The results of this study confirm that VICs are a contractile element in the MV, and add to this proposed model by demonstrating how VICs generate force in concert with collagen via integrin coupling.

A number of factors could affect the proposed VIC-integrin-collagen unit and potentially valve function in pathophysiological conditions. For example, changes in collagen fiber cross-linking and packing, as well as collagen turnover, could affect the ability of VICs to bind to collagen and transduce force. Circulating factors, including cytokines, inflammatory mediators, vasoactive agents, and pharmaceutical agents, could affect both the contractile and adhesive capabilities of VICs. Changes in VIC cell phenotype, as occur via alterations in the mechanoenvironment and chemical mediators, would also likely affect the ability of VICs to produce and transduce force. Lastly, sympathetic and parasympathetic innervation could affect this functional unit either directly or through paracrine mechanisms.

In fact, valve diseases demonstrate alterations in these factors. Changes in MV collagen content, collagen turnover, and matrix metalloproteinase expression have been documented in diseases such as dilated cardiomyopathy and functional mitral regurgitation.[19,39,40] VICs in a number of valve diseases, such as myxomatous mitral valve disease, also demonstrate a more myofibroblastic cell phenotype including greater smooth muscle α actin expression,[34] which directly relates to force generation in myofibroblasts.[20] Changes in myocardial integrin expression and activation have been demonstrated in cardiac diseases,[35] and may

Author Proof

be altered in pathological valves as well. Therefore, the proposed functional unit may be impacted by, or even contribute to valve pathologies, although considerable work in this area is needed.

The results of this study may also have implications for the design of a tissue engineered heart valve (TEHV). Creating a TEHV complete with living VICs may be necessary not only for the TEHV to successfully adapt (via matrix remodeling) to changes in valve stresses, for example as the patient grows, or as cardiac pressures change with age, but living VICs within a TEHV will be important at a more fundamental level to provide these VIC-collagen functional units and their contributions to tonus, anisotropy, and stiffness modulation.

Limitations and Future Studies

While this study represents an important step forward in examining the relationship between structure and function in the mitral leaflet, a number of limitations should be noted. Tighter control of temperature and carbon dioxide, such as with a closed chamber system more analogous to an organ bath set-up, would be ideal; however this was not feasible in the present set-up. More precise control of pre-load and of strain, perhaps using a micropositioner, would also enhance this set-up. Regardless, given the dramatic change in force generation with blocking agents, these limitations did not affect the ultimate interpretation of the study.

Studying other vasoconstrictive reagents and changes in mitral leaflet stiffness caused by these agents would also add to our understanding of VIC/leaflet contractility and how it relates to function. Further work examining the structural interaction of integrins, linking proteins, collagen, and VICs would add to our understanding of this functional unit. While much remains to be done in this area, this study is an important step in furthering our understanding of the roles played by VICs and collagen in mitral valve force generation.

In conclusion, this study demonstrated that VIC-collagen coupling via integrins contributes to force generation in mitral valves and supports the concept of multiple contractile systems in the mitral valve. Together with other studies demonstrating that the mitral valve possesses its own vasculature and innervation, and remodels in response to a variety of stimuli, this study adds to a growing body of evidence that the mitral valve is an active, dynamic entity as opposed to a passive flap. VICs, in concert with the extracellular matrix in which they are not only embedded, but also interact with and regulate the composition of, are a key component to this revised notion of the valve. As our concept of the valve continues to be refined, so too will our definition of valve diseases and therapeutic approaches to them.

ACKNOWLEDGMENTS

The authors wish to acknowledge all the members of the Stanford Cardiovascular Surgical Physiology Research Laboratory, especially Kathy N. Vo and Paul Chang, as well as microscopy assistance from Kitty Lee, Dr. Robert Raphael, and John Wright, and machining assistance from Dwight Dear. The authors also wish to thank Dr. L. Scott Baggett for his statistical expertise. Funding for this project came in part from an AATS Summer Internship Scholarship (EHS), as well as a Hertz Foundation Graduate Fellowship (EHS), NIH Ruth-Kirschstein (F30) National Research Service Award (EHS), and a Post-Doctoral Fellowship from the Western States Affiliate of the American Heart Association (JCS).

REFERENCES

[1] Barczyk, M., S. Carracedo, and D. Gullberg. Integrins. *Cell Tissue Res.* 339:269–280, 2010.

[2] Bayne-Jones, S. The blood-vessels of the heart valves. *Am. J. Anat.* 21:449–463, 1917.

[3] Borin, C., D. Vanhercke, and A. Weyns. Innervation of the atrioventricular and semi-lunar heart valves: a review. *Acta Cardiol.* 61:463–469, 2006.

[4] Bowen, I., C. Marr, A. Chester, C. Wheeler-Jones, and J. Elliott. In vitro contraction of the equine aortic valve. *J. Heart Valve Dis.* 13:593–599, 2004.

[5] Brakebusch, C., and R. Fassler. Beta 1 integrin function in vivo: adhesion, migration and more. *Cancer Metastasis Rev.* 24:403–411, 2005.

[6] Chaput, M., M. D. Handschumacher, F. Tournoux, L. Hua, J. L. Guerrero, G. J. Vlahakes, and R. A. Levine. Mitral leaflet adaptation to ventricular remodeling: occurrence and adequacy in patients with functional mitral regurgitation. *Circulation* 118:845–852, 2008.

[7] Chester, A., M. Misfeld, and M. Yacoub. Receptor-mediated contraction of aortic valve leaflets. *J. Heart Valve Dis.* 9:250–254, 2000.

[8] Chester, A. H., M. Misfeld, H. H. Sievers, and M. H. Yacoub. Influence of 5-hydroxytryptamine on aortic valve competence in vitro. *J. Heart Valve Dis.* 10:822–825, 2001.

[9] Cole, W. G., D. Chan, A. J. Hickey, and D. E. Wilcken. Collagen composition of normal and myxomatous human mitral heart valves. *Biochem. J.* 219:451–460, 1984.

[10] Cooper, T., L. M. Napolitano, M. J. Fitzgerald, K. E. Moore, W. M. Daggett, V. L. Willman, E. H. Sonnenblick, and C. R. Hanlon. Structural basis of cardiac valvar function. *Arch. Surg.* 93:767–771, 1966.

[11] Dal-Bianco, J. P., E. Aikawa, J. Bischoff, J. L. Guerrero, M. D. Handschumacher, S. Sullivan, B. Johnson, J. S. Titus, Y. Iwamoto, J. Wylie-Sears, R. A. Levine, and A. Carpentier. Active adaptation of the tethered mitral valve:

Author Proof

insights into a compensatory mechanism for functional mitral regurgitation. *Circulation* 120:334–342, 2009.

[12]Dallon, J., and H. Ehrlich. A review of fibroblast-populated collagen lattices. *Wound Repair Regen.* 16:472–479, 2008.

[13]De Biasi, S., L. Vitellaro-Zuccarello, and I. Blum. Histochemical and ultrastructural study on the innervation of human and porcine atrio-ventricular valves. *Anat. Embryol.* 169:159–165, 1984.

[14]DeMali, K. A., C. A. Barlow, and K. Burridge. Recruitment of the Arp2/3 complex to vinculin: coupling membrane protrusion to matrix adhesion. *J. Cell Biol.* 159:881–891, 2002.

[15]DeMali, K. A., K. Wennerberg, and K. Burridge. Integrin signaling to the actin cytoskeleton. *Curr. Opin. Cell Biol.* 15:572–582, 2003.

[16]Filip, D., A. Radu, and M. Simionescu. Interstitial cells of the heart valve possess characteristics similar to smooth muscle cells. *Circ. Res.* 59:310–320, 1986.

[17]Flanagan, M. D., and S. Lin. Cytochalasins block actin filament elongation by binding to high affinity sites associated with F-actin. *J. Biol. Chem.* 255:835–838, 1980.

[18]Goddette, D. W., and C. Frieden. Actin polymerization. The mechanism of action of cytochalasin D. *J. Biol. Chem.* 261:15974–15980, 1986.

[19]Grande-Allen, K. J., A. G. Borowski, R. W. Troughton, P. L. Houghtaling, N. R. Dipaola, C. S. Moravec, I. Vesely, and B. P. Griffin. Apparently normal mitral valves in patients with heart failure demonstrate biochemical and structural derangements: an extracellular matrix and echocardiographic study. *J. Am. Coll. Cardiol.* 45:54–61, 2005.

[20]Hinz, B., G. Celetta, J. Tomasek, G. Gabbiani, and C. Chaponnier. Alpha-smooth muscle actin expression upregulates fibroblast contractile activity. *Mol. Biol. Cell.* 12:2730–2741, 2001.

[21]Huang, H., J. Liao, and M. Sacks. In situ deformation of the aortic valve interstitial cell nucleus under diastolic loading. *J. Biomech. Eng.* 129:880–889, 2007.

[22]Hynes, R. O. Integrins: bidirectional, allosteric signaling machines. *Cell* 110:673–687, 2002.

[23]Itoh, A., G. Krishnamurthy, J. C. Swanson, D. B. Ennis, W. Bothe, E. Kuhl, M. Karlsson, L. R. Davis, D. C. Miller, and N. B. Ingels, Jr. Active stiffening of mitral valve leaflets in the beating heart. *Am. J. Physiol. Heart Circ. Physiol.* 296:H1766–H1773, 2009.

[24]Kershaw, J., M. Misfeld, H. Sievers, M. Yacoub, and A. Chester. Specific regional and directional contractile responses of aortic cusp tissue. *J. Heart Valve Dis.* 13: 798–803, 2004.

[25]Kunzelman, K. S., and R. P. Cochran. Stress/strain characteristics of porcine mitral valve tissue: parallel versus perpendicular collagen orientation. *J. Card. Surg.* 7:71–78, 1992.

[26]Latif, N., P. Sarathchandra, P. Taylor, J. Antoniw, and M. Yacoub. Molecules mediating cell-ECM and cell-cell communication in human heart valves. *Cell Biochem. Biophys.* 43:275–287, 2005.

[27]Latif, N., P. Sarathchandra, P. S. Thomas, J. Antoniw, P. Batten, A. H. Chester, P. M. Taylor, and M. H. Yacoub. Characterization of structural and signaling molecules by human valve interstitial cells and comparison to human mesenchymal stem cells. *J. Heart Valve Dis.* 16:56–66, 2007.

[28]Marron, K., M. H. Yacoub, J. M. Polak, M. N. Sheppard, D. Fagan, B. F. Whitehead, M. R. de Leval, R. H. Anderson, and J. Wharton. Innervation of human atrioventricular and arterial valves. *Circulation* 94:368–375, 1996.

[29]Merryman, W. D., H. Y. Huang, F. J. Schoen, and M. S. Sacks. The effects of cellular contraction on aortic valve leaflet flexural stiffness. *J. Biomech.* 39:88–96, 2006.

[30]Meshel, A., Q. Wei, R. Adelstein, and M. Sheetz. Basic mechanism of three-dimensional collagen fibre transport by fibroblasts. *Nat. Cell Biol.* 7:157–164, 2005.

[31]Montiel, M. M. Muscular apparatus of the mitral valve in man and its involvement in left-sided cardiac hypertrophy. *Am. J. Cardiol.* 26:341–344, 1970.

[32]Pompilio, G., G. Rossoni, A. Sala, G. L. Polvani, F. Berti, L. Dainese, M. Porqueddu, and P. Biglioli. Endothelial-dependent dynamic and antithrombotic properties of porcine aortic and pulmonary valves. *Ann. Thorac. Surg.* 65:986–992, 1998.

[33]Price, L. S., J. Leng, M. A. Schwartz, and G. M. Bokoch. Activation of Rac and Cdc42 by integrins mediates cell spreading. *Mol. Biol. Cell.* 9:1863–1871, 1998.

[34]Rabkin, E., M. Aikawa, J. R. Stone, Y. Fukumoto, P. Libby, and F. J. Schoen. Activated interstitial myofibroblasts express catabolic enzymes and mediate matrix remodeling in myxomatous heart valves. *Circulation* 104:2525–2532, 2001.

[35]Ross, R. S. The extracellular connections: the role of integrins in myocardial remodeling. *J. Card. Fail.* 8:S326–S331, 2002.

[36]Sacks, M. S., W. David Merryman, and D. E. Schmidt. On the biomechanics of heart valve function. *J. Biomech.* 42:1804–1824, 2009.

[37]Schenke-Layland, K., N. Madershahian, I. Riemann, B. Starcher, K. J. Halbhuber, K. Konig, and U. A. Stock. Impact of cryopreservation on extracellular matrix structures of heart valve leaflets. *Ann. Thorac. Surg.* 81:918–926, 2006.

[38]Sonnenblick, E., L. Napolitano, W. Daggett, and T. Cooper. An intrinsic neuromuscular basis for mitral valve motion in the dog. *Circ. Res.* 21:9–15, 1967.

[39]Stephens, E. H., T. C. Nguyen, A. Itoh, N. B. Ingels, Jr., D. C. Miller, and K. J. Grande-Allen. The effects of mitral regurgitation alone are sufficient for leaflet remodeling. *Circulation* 118:S243–S249, 2008.

[40]Stephens, E. H., T. A. Timek, G. T. Daughters, J. J. Kuo, A. M. Patton, L. S. Baggett, N. B. Ingels, D. C. Miller, and K. J. Grande-Allen. Significant changes in mitral valve leaflet matrix composition and turnover with tachycardia-induced cardiomyopathy. *Circulation* 120:S112–S119, 2009.

[41]Sturge, J., J. Hamelin, and G. E. Jones. N-WASP activation by a beta1-integrin-dependent mechanism supports PI3K-independent chemotaxis stimulated by urokinase-type plasminogen activator. *J. Cell. Sci.* 115:699–711, 2002.

[42]Swanson, J. C., L. R. Davis, K. Arata, E. P. Briones, W. Bothe, A. Itoh, N. B. Ingels, and D. C. Miller. Characterization of mitral valve anterior leaflet perfusion patterns. *J. Heart Valve Dis.* 18:488–495, 2009.

[43]Tang, D. D., C. E. Turner, and S. J. Gunst. Expression of non-phosphorylatable paxillin mutants in canine tracheal smooth muscle inhibits tension development. *J. Physiol.* 553:21–35, 2003.

[44]Tang, D. D., W. Zhang, and S. J. Gunst. The adapter protein CrkII regulates neuronal Wiskott-Aldrich syndrome protein, actin polymerization, and tension development during contractile stimulation of smooth muscle. *J. Biol. Chem.* 280:23380–23389, 2005.

Author Proof

[45] Taylor, P., S. Allen, and M. Yacoub. Phenotypic and functional characterization of interstitial cells from human heart valves, pericardium and skin. *J. Heart Valve Dis.* 9:150–158, 2000.

[46] Wang, X. Q., and W. A. Frazier. The thrombospondin receptor CD47 (IAP) modulates and associates with alpha2 beta1 integrin in vascular smooth muscle cells. *Mol. Biol. Cell.* 9:865–874, 1998.

[47] Wassenaar, C., W. A. Bax, R. J. van Suylen, V. D. Vuzevski, and E. Bos. Effects of cryopreservation on contractile properties of porcine isolated aortic valve leaflets and aortic wall. *J. Thorac. Cardiovasc. Surg.* 113:165–172, 1997.

[48] Zamir, E., and B. Geiger. Molecular complexity and dynamics of cell-matrix adhesions. *J. Cell Sci.* 114: 3583–3590, 2001.

UNCORRECTED PROOF

Appendix IV: Computational Fluid Model of ELSIE Bioreactor

This appendix features work in which the I and was a co-author on the manuscript; however the work was led by other researchers. A brief description of the my primary contributions is given below and a reprint of the manuscript follows. This was published as Barzilla JE, McKenny AS, Cowan AE, Durst, CA, Grande-Allen KJ. Design and Validation of a Novel Splashing Bioreactor System for Use in Mitral Valve Organ Culture. Annals of Biomedical Engineering, 2010 Nov; 38(11):3280-3294.

It was decided during the final stages of manuscript preparation that a characterization of the *in vitro* dynamic mechanical environment and corresponding tissue strains would substantially enhance the impact of the work. I then joined the project to create a computational fluid dynamics model to simulate the fluid flow and resulting shear forces as a result of the dynamic culture regimen. Figures representing the my primary contributions are shown below (Figure A4.1 and Figure A4.2)

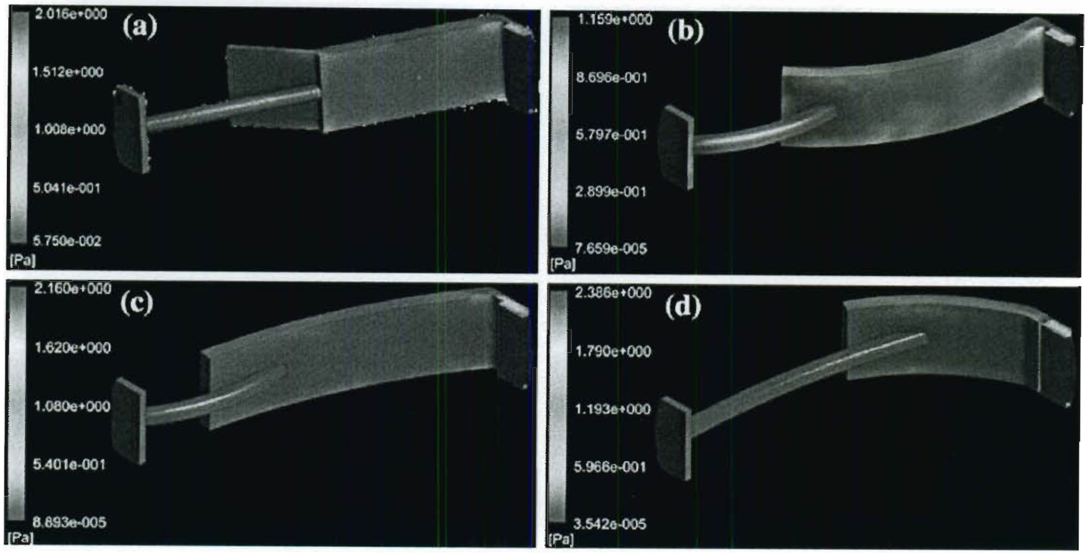
2.016e+000
1.512e+000
1.008e+000
5.041e-001
5.750e-002
[Pa]
(a)
1.159e+000
8.696e-001
5.797e-001
2.899e-001
7.659e-005
[Pa]
(b)
2.160e+000
1.620e+000
1.080e+000
5.401e-001
8.693e-005
[Pa]
(c)
2.386e+000
1.790e+000
1.193e+000
5.966e-001
3.542e-005
[Pa]
(d)

Figure A4.1: Plot of shear stress on the surface of the leaflet. Shear stress was averaged over the shown surface of the leaflet. Shear stress at system orientation: (a) 0° (straight up and down), (b) 45° , (c) 90° (horizontal), (d) 135°.

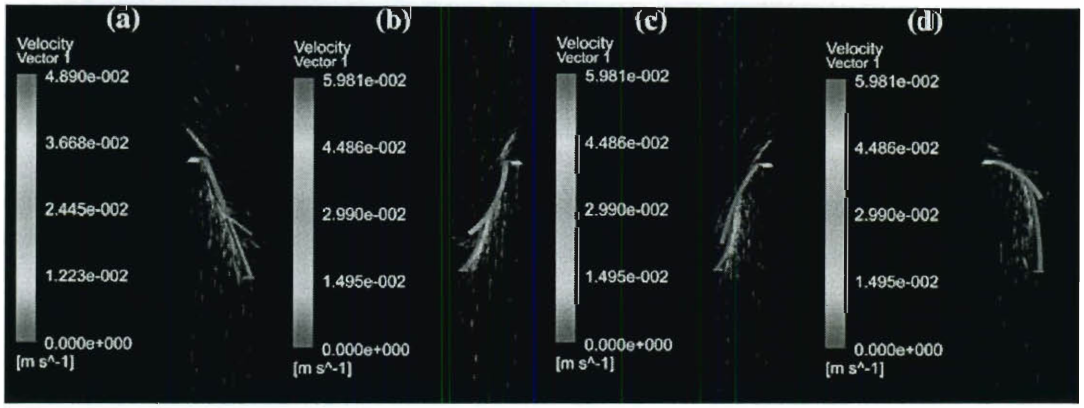

Figure A4.2: Vector plot of fluid velocity in the mid-plane of the culture chamber. Fluid velocity peaks at ~4 cm/s near the area of chordal attachment to the leaflet. Eddies can be observed near the free edge. Velocity vectors at system orientation: (a) 0°, (b) 45°, (c) 90°, (d) 135°.

Annals of Biomedical Engineering, Vol. 38, No. 11, November 2010 (*© 2010*) pp. 3280–3294
DOI: 10.1007/s10439-010-0129-9

Design and Validation of a Novel Splashing Bioreactor System for Use in Mitral Valve Organ Culture

JANET E. BARZILLA,[1] ANNA S. MCKENNEY,[2] ASHLEY E. COWAN,[3] CHRISTOPHER A. DURST,[1]
and K. JANE GRANDE-ALLEN[1]

[1]Department of Bioengineering, MS-142, Rice University, P.O. Box 1892, Houston, TX 77251-1892, USA; [2]Department of Biomedical Engineering, Rensselaer Polytechnic Institute, Troy, NY 12180, USA; and [3]Department of Biological Sciences, Murray State University, Murray, KY 42071-3361, USA

(Received 19 September 2009; accepted 12 July 2010; published online 27 July 2010)

Associate Editor Peter E. McHugh oversaw the review of this article.

Abstract—Previous research in our lab suggested that heart valve tissues cultured without mechanical stimulation do not retain their *in vivo* microstructure, i.e., cell density decreased within the deep tissue layers and increased at the periphery. In this study, a splashing rotating bioreactor was designed to apply mechanical stimulation to a mitral valve leaflet segment. Porcine valve segments ($n = 9$–10 per group) were cultured in the bioreactor for 2 weeks (dynamic culture), negative controls were cultured without mechanical stimulation (static culture), and baseline controls were fresh uncultured samples. Overall changes in cellularity and extracellular matrix (ECM) structure were assessed by H&E and Movat pentachrome stains. Tissues were also immunostained for multiple ECM components and turnover mediators. After 2 weeks of culture, proliferating cells were distributed throughout the tissue in segments cultured in the bioreactor, in contrast to segments cultured without mechanical stimulation. Most ECM components, especially collagen types I and III, better maintained normal expression patterns and magnitudes (as found in baseline controls) over 2 weeks of dynamic organ culture compared to static culture. Lack of mechanical stimulation changed several aspects of the tissue microstructure, including the cell distribution and ECM locations. In conclusion, mechanical stimulation by the bioreactor maintained tissue integrity, which will enable future *in vitro* investigation of mitral valve remodeling.

Keywords—Extracellular matrix, Collagen, Proteoglycans, Matrix metalloproteinases, Lysyl oxidase, Prolyl-4-hydroxylase, Heat shock protein 47.

ABBREVIATIONS

BGL	Biglycan
COLL	Collagen
DCN	Decorin
ECM	Extracellular matrix
GAG	Glycosaminoglycan
HSP47	Heat shock protein 47
LOX	Lysyl oxidase
MMP	Matrix metalloproteinase
P4H	Prolyl-4-hydroxylase
PCNA	Proliferating cell nuclear antigen
PG	Proteoglycan
TIMP	Tissue inhibitor of matrix metalloproteinase
VC	Versican

INTRODUCTION

The successful creation of an *in vitro* experimental model of the mitral valve would provide a powerful tool for investigating the underlying mechanisms behind and possible treatments for mitral valve disease. Although animal models have been used with great success in studying many forms of cardiovascular disease, these surgeries are invasive and costly. In addition, a large number of animals would be required to study multiple early timepoints. Alternatives to surgical methods, such as molecular imaging to monitor valve remodeling, are being explored.[14] Cell studies offer a less expensive alternative to animal studies; many recent studies of valvular biology and remodeling have employed cultures of valvular cells maintained in monolayers.[35,37,40] This widely accepted protocol, however, does not allow investigators to investigate the basis for changes to the layered structure of the native valve, which can be greatly altered in valve disease.[11] Additionally, a monolayer culture imposes a drastic

---

Address correspondence to K. Jane Grande-Allen, Department of Bioengineering, MS-142, Rice University, P.O. Box 1892, Houston, TX 77251-1892, USA. Electronic mail: grande@rice.edu

0090-6964/10/1100-3280/0 © 2010 Biomedical Engineering Society

change in environmental stimuli for the cells, and thus may not accurately elicit the *in vivo* response.

To avoid the shortcomings of animal and cell models, we have chosen to investigate organ cultures, which maintain the valvular cells within the native physical structure of the tissue. Ideally, the organ cultures would be grown in conditions engineered to mimic the native environment. Organ cultures have successfully been established for a variety of tissues, including vascular intima,[25] canine leptomeninges,[29] mouse gallbladder epithelium,[36] brain hippocampal slices,[31] and human lacrimal gland tissue.[13] In human and mammalian heart valve tissues, short-term (6 days) organ cultures have been used to investigate wound healing responses.[19–21]

Heart valve tissues are particularly appropriate for organ culture research because the cells within adult valves are nourished primarily through diffusive transport of oxygen and nutrients (as opposed to through vascularization[4]). It was therefore believed that designing a valvular organ culture system might be much simpler than designing systems for more complicated fully vascularized tissues. Previous work in our laboratory used a simple static system for organ culture (after Lester *et al.*[19–21]) to demonstrate that the cells within the cultured valve tissues remained alive during long-term culture periods (up to 7 weeks).[1] The aforementioned work also suggested, however, that static culture techniques alone did not maintain cell location. Fewer endothelial cells were noted on the cultured tissue. Although valvular interstitial cells were still present and viable after 7 weeks, fewer cells were located deep within the tissue, suggesting migration of these cells to the periphery to obtain nutrients.[1]

Since heart valves are continuously exposed *in vivo* to a variety of mechanical stresses from both myocardial motion and blood flow, it was further supposed that an *in vitro* system incorporating similar mechanical forces could maintain the valve structure. A number of bioreactor designs including flow loops,[12,15] cyclic pressure,[28,42] and cyclic flexure[5–8,26] systems are available for organ culture and tissue engineering applications. Many of these designs have specialized in the culture of semi-lunar (aortic and pulmonary) valves for a short period of time (approximately 48 h). Although these bioreactor systems have been successful for their intended function, this study was focused on the culture of atrioventricular (mitral and tricuspid) valve leaflets and their associated chordae tendinae. This study was also designed for a longer timeframe (approximately 2 weeks).

To that end, a bioreactor was designed to provide cyclic, dynamic mechanical stimulation to an organ culture via sub-physiological fluid movement against the valve surfaces. These data were compared to porcine mitral and tricuspid valves cultured without mechanical stimulation to qualify valve remodeling over a period of several weeks. We hypothesized that the perfusion and gentle stretch provided by the dynamic un-quantified mechanical environment of the splashing bioreactor would be sufficient to maintain tissue structure and prevent cell migration. The successful validation of this system will allow future use of this bioreactor in both organ culture and tissue engineering applications.

METHODS

Pilot Long-Term Static Culture Study

To determine the phenotypic effects of organ culturing without mechanical stimulation on heart valve tissue, organ cultures were established[20] for periods of time ranging from 0 to 8 weeks. Porcine tricuspid valves were used to prepare the valvular organ cultures in this study; porcine valves are widely used and accepted as anatomic[18,32] and biological models[37] for human valves. Valves ($n = 5$) were obtained from a commercial abattoir, and the tricuspid valves were dissected from the hearts within 24 h of removal from the body.

After removal of chordae tendinae and cardiac muscle tissue, the valve leaflets were dissected into 100 mm^2 blocks, yielding 5–10 blocks per individual valve. At each stage of culture establishment, care was taken to prevent physical disruption of the endothelial tissue layers. The organ culture blocks were then transferred into a sterile flow hood, gently rinsed in sterile phosphate-buffered saline (PBS), and placed into individual wells of 24-well tissue culture plates containing Medium 199 with modified HEPES buffer (Sigma, St. Louis, MO, USA) supplemented with 15% fetal bovine serum, 100 U/mL penicillin, 100 μg/mL streptomycin, and 0.25 μg/mL amphotericin B (all reagents from Invitrogen, Carlsbad, CA, USA). The organ cultures were maintained in a humidified incubator at 37 °C with 5% CO_2 for up to 8 weeks. Culture medium was changed every 2–3 days. The resulting organ cultured blocks were removed before and after establishment of culture, and subsequently at weekly intervals for analysis.

At the specified time points, tissue blocks were removed from culture, fixed in Histochoice^{TM} (Amresco, Solon, OH, USA), and embedded in paraffin. Tissue sections were stained with H&E and Movat pentachrome to identify the cell nuclei and extracellular matrix (ECM) components. Changes in the location of endothelial cells and in collagen (COLL) synthesis were evaluated immunohistochemically using antibodies against von Willebrand Factor (vWF, Sigma) and the enzyme prolyl-4-hydroxylase (P4H, Chemicon, Temecula, CA, USA), respectively. The sample was first rehydrated using graded dilutions of Flex (Richard-Allen Scientific, Kalamazoo, MI, USA). Antigen decloaking was performed using a citrate buffer, and the sample was exposed to a 10% solution of goat serum at room temperature for 1 h to limit indiscriminate binding of the secondary antibody. After removing the goat serum, the appropriate primary antibody was applied and incubated at 37 °C for 1 h. Negative controls for each sample were exposed to the secondary antibody only. The primary antibody was then removed and the sample exposed to the biotinylated secondary goat anti-mouse antibody (Jackson ImmunoResearch, West Grove, PA, USA) at room temperature for 1 h. The samples were then exposed to an avidin–biotin complex for 30 min and tagged using a 3,3′-diaminobenzidine kit for 10 min (both from Vector Labs, Burlingame, CA, USA). All samples were counterstained with hematoxylin to localize cells within the tissue.

Bioreactor Design

The bioreactor chamber design consisted of three polycarbonate segments (McMaster-Carr, Chicago, IL, USA), each 2″ in diameter (Fig. 1a). The segments were clamped together via four 4″-long, ¼″–28 partially threaded screws and nuts spaced 90° around the circumference of the bioreactor. The two ends of each segment each had three 1/16″ neoprene washers (McMaster-Carr) mounted using cyanoacrylate glue. The washers were wrapped with Teflon® tape upon chamber construction to prevent leaks. The main body of segment A was 1.5″ tall and had a ½″ hole in the center to accommodate fluid flow. The top of A was 1″ height and threaded to fit the vented filter cap from a 25-cm^2 tissue culture flask (BD Biosciences, San Jose, CA, USA) in order to allow gas exchange in the bioreactor. Segment B was 5/8″ height and had a ½″ hole in the center. Polyester mesh squares (Sefar America Inc., Depew, NY, USA) approximately 0.5 × 1 mm^2 were glued between the neoprene washers to provide a mounting location for the mitral valve. Segment C was 1.25″ height, and a ½″ hole was cut through the top 1″ for fluid flow. The bottom ¼″ of the segment was solid.

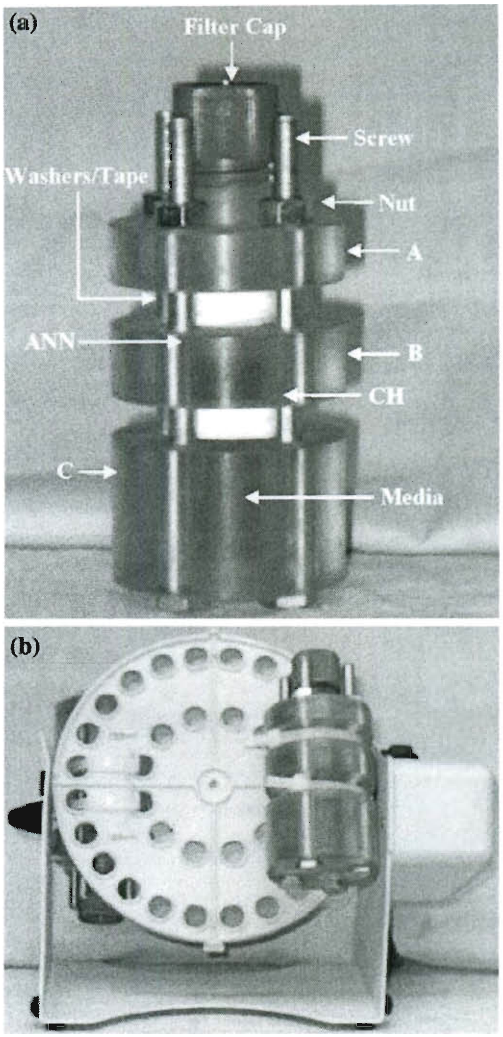

FIGURE 1. (a) Splashing bioreactor chamber. The chamber is comprised of three hollow segments (A)–(C) into which the valve segment is mounted. The media inside the chamber provide nutrients to the tissue. Valve attachment sites (inside chamber) are also indicated. ANN, annulus; CH, chordae. (b) Bioreactor on rotator. The pallet rotates 360°, forcing media over the valve surfaces.

Repeatable fluid motion was provided by rotating the bioreactor chambers using a Labnet Mini LabRoller™ (ISC Bioexpress, Kaysville, UT, USA). This rotator fit two bioreactors on a pallet, secured with two 3/16″ cable ties (Fig. 1b). The rotator, which was selected based on its small size and incubator compatibility, had only one available speed setting, rotating a full 360° at an approximate speed of 0.33 revolutions/s. This motion caused the media to splash across both valve surfaces, imparting a combination of normal and shear force to the valve; compression force from *in vivo* coaptation of the valve leaflet free edges would be absent (Fig. 2). Based on previously published values of heart rate and tissue deformation in normal *in vivo* animal models,[16,30] it was assumed that tissue velocities and developed shear stresses in the bioreactor would be sub-physiological. A 4.5-mL culture medium was used to fill the chamber; although this volume of media only partially bathed the tissue when the chamber was not rotating, this volume allowed greater forces to be imparted onto the valve surface than would have been possible if the chamber had been completely filled.

Maximum tensile strains in the leaflet and the chordae were estimated separately due to the differences in the ECM structure of the two tissue types. Stress was first calculated from the normal force of the fluid on the submerged tissue, as given by the specific weight of the fluid and the tissue geometry. Strain was then calculated using the pre-transition stiffness of the tissue, which was estimated to be five times greater for chordae than leaflet.[17,33] As a result, the maximum tensile strain for leaflet (0.65%) was five times greater that of chordae (0.13%).

Maximum bending strains within regions of local curvature were estimated for both the leaflet and chordae by the ratio of one-half leaflet thickness to radius of curvature. This calculation was independent of material or geometry and was therefore applicable to both valve portions. Leaflet thickness was assumed to be 1 mm. Radius of curvature was calculated from the chord length and arc length of the locally curved regions. To determine these lengths, it was assumed that the leaflet segment was straight across either one-half, two-thirds, three-fourths, or four-fifths of the annular to chordal attachment distance and the remainder of the leaflet segment was curved. These geometric conditions were estimated to generate maximal bending strains ranging from 4%, when the whole leaflet–chordal segment was bent in one smooth arc, to 25% when only one-fifth of the entire leaflet–chordal segment length was bent (Fig. 2).

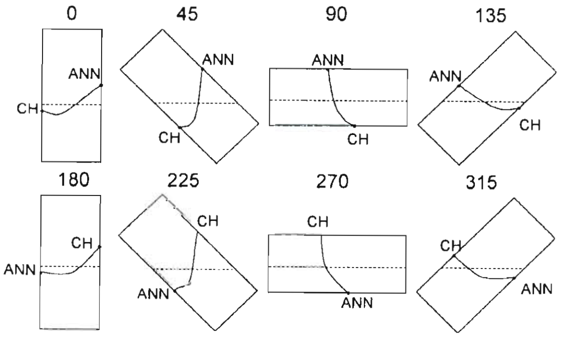

FIGURE 2. Rotation of splashing bioreactor through 360° motion. As the chamber rotates, the culture medium flows past the tissue surface, imparting normal and shear forces to the surface and causing deformation of the organ culture.

In addition, a basic computational model was used to investigate the shear forces and fluid velocities imparted to the tissue by this system. ANSYS Workbench (ANSYS Inc., Canonsburg, PA, USA) was used to run a computational fluid dynamics model of fluid flow across an idealized leaflet using the CFX code. Inlet flow rate (2.97 mL/s) was chosen from the fluid volume and rotation speed of the system. The flow was modeled as an inlet flow from the bottom surface of the lumen toward the top at four points through half of a system rotation (0°, 45°, 90°, 135° rotation). Calculations were performed using a shear-stress transport model, which improves accuracy in the boundary region thereby increasing accuracy of wall shear stress calculations. This method employs a k–ω model at the wall and then blends it with a k–ε model.[24] Tissue wall shear stress was visualized on all surfaces of the leaflet, and the shear on the surface of the leaflet was determined by using a contour plot (Fig. 3). Shear stress was observed to be consistent

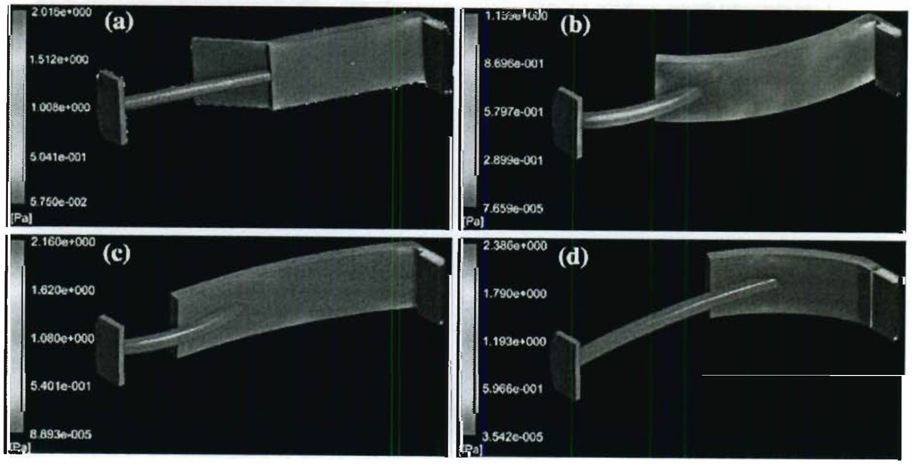

FIGURE 3. Plot of shear stress on the surface of the leaflet. Shear stress was averaged over the shown surface of the leaflet. Shear stress at system orientation: (a) 0° (straight up and down), (b) 45°, (c) 90° (horizontal), (d) 135°.

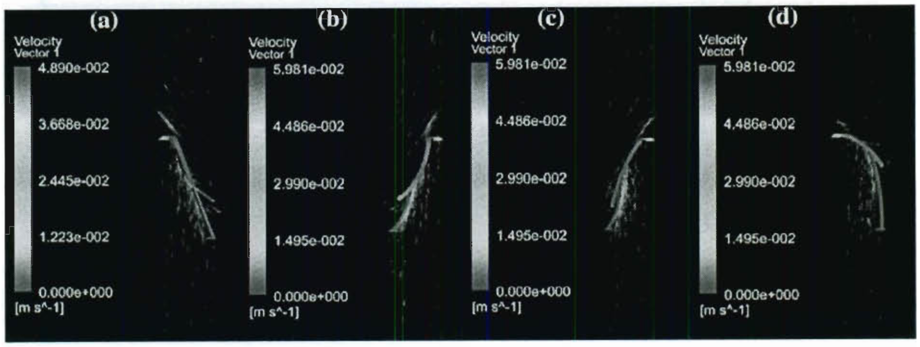

FIGURE 4. Vector plot of fluid velocity in the mid-plane of the culture chamber. Fluid velocity peaks at ~4 cm/s near the area of chordal attachment to the leaflet. Eddies can be observed near the free edge. Velocity vectors at system orientation: (a) 0°, (b) 45°, (c) 90°, (d) 135°.

over the bulk of the leaflet surface and was observed to be 0.010–0.020 Pa at all orientations. In addition, fluid velocities were investigated at the center plane of the culture chamber and visualized with a vector field (Fig. 4), showing turbulence around the leaflet free edge.

Developing a bioreactor system that could be sterilized prior to assembly, and assembled and run in a sterile manner, was a major consideration during the design process. Prior to attachment of the valve segment in the bioreactor, the bioreactor was disassembled and the individual segments washed using a 1:128 dilution of CiDecon (Decon Labs, King of Prussia, PA, USA) disinfectant. The segments were then sprayed with a 70% ethanol solution, with special attention paid to the inside surfaces, and exposed to ultraviolet light in a sterile biological hood for 30–60 min. The bioreactor pieces remained in the sterile hood until assembly. Sterility testing of the bioreactor was performed by allowing media to remain in the stationary chamber for 1 week. Initial tests were performed without valve tissue, and later tests included a mitral valve segment mounted in the bioreactor chamber. When the media were changed, a sample of the old media was placed into a 6-well plate and returned to the incubator. A sample of the fluid was also applied to an agar plate and allowed to incubate for 3 days. In addition, media were spot-checked for contamination during test runs with the valves by drawing media samples, incubating the media in a 6-well plate for 2–3 days, and examining the media using an inverted microscope.

Design Validation

Porcine mitral valves (Fisher Ham & Meat, Houston, TX, USA) from approximately 6-month-old animals were used to validate the ability of the designed bioreactor to maintain the normal condition of the valve microstructure and cell distribution. Valves were dissected from the heart within 6–10 h postmortem and rinsed in sterile PBS containing 5% antibiotic/antimycotic solution (Mediatech Inc., Herndon, VA, USA) to remove bacteria. Two 5-mm wide radial segments (one surrounding each strut chordae, Fig. 5a) were then removed from the anterior leaflets ($n = 19$ total). When preparing the tissue segments, the entire length of the leaflet (annulus to free edge) and strut chordae were used. Due to the similarity in the age of the animals from which the hearts were harvested, valve tissue segment sizes were generally consistent.

The first segment from each valve was cultured, under either static or dynamic conditions, for 2 weeks. Static cultures (negative control, $n = 10$) were placed in a T-25 tissue culture flask. As with the pilot study, static cultures were not subjected to any mechanical stimulation. Dynamic cultures ($n = 9$) were mounted in the bioreactor (Figs. 5b and 5c); anchoring on both

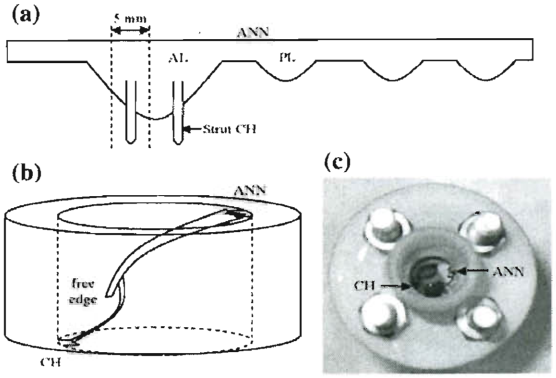

FIGURE 5. Valve insertion. (a) A 5-mm radial valve segment is removed from the AL. (b) The segment is then mounted at the ANN and CH, taking care to leave the tissue slack. The free edge is unattached. (c) Top view of valve in bioreactor. AL, anterior leaflet; ANN, annulus; CH, chordae; PL, posterior leaflet.

ends of the tissue was fixed, and did not contract as it would in the *in vivo* system. The valve segment was carefully mounted within the bioreactor in such a way that it was kept slack in order to model diastole, with the assumption that tension on the tissue culture during systole would be lower than on the *in vivo* tissue due to the lower *in vitro* fluid speed and lack of mechanical stimulation from the ventricular wall. In both test cases, the tissue was bathed in organ culture media (DMEM/Ham's F12, Mediatech Inc.; 10% bovine growth serum, HyClone Waltham, MA, USA; 1% HEPES buffer, Mediatech Inc.) containing 5% antibiotic/antimycotic solution for the first 24 h after dissection, after which it was replaced by media with 1% antibiotic/antimycotic solution. The second segment from each valve was designated a baseline control sample. All tissues were fixed in Histochoice^{TM} after 2 weeks (cultured samples) or immediately after dissection (baseline control samples). After fixation, all tissue samples were dehydrated to xylene, paraffin embedded, sectioned into 5 μm slices, and mounted on slides.

As in the pilot study, samples in the validation study were stained with H&E and Movat pentachrome. Immunohistochemical staining was employed to localize the proteoglycans (PGs) versican (VC, Seikagaku, Associates of Cape Cod, East Falmouth, MA, USA), decorin (DCN), and biglycan (BGL), as well as collagen types 1 and 3 (COLL1/COLL3), within the valve layers. Unless otherwise indicated, antibodies were generously provided by Dr. Larry Fisher (NIDCR, Bethesda, MD, USA).[9] In addition to these ECM components, the ECM synthesis mediators P4H (Millipore, Billerica, MA, USA), lysyl oxidase (LOX, Imgenex, San Diego, CA, USA), and heat shock protein 47 (HSP47, Abcam, Cambridge, MA, USA) were also localized. HSP47 is a molecular chaperone associated with COLL synthesis, whereas LOX is involved in COLL and elastin crosslinking. Immunohistochemical staining for matrix metalloproteinases (MMPs) 1, 2, 9 (all from Assay Designs, Ann Arbor, MI, USA), and 13 (Millipore) identified sites of enzymatic matrix degradation. Staining for tissue inhibitor of MMP 1 (TIMP-1, Assay Designs) stain was also performed. An antibody sensitive to proliferating cell nuclear antigen (PCNA, Abcam) determined the location of proliferating cells within the tissue. The immunohistochemical method for PGs was identical to that of the P4H method described above, except for sample pretreatment with Chondroitinase ABC (Seikagaku, Tokyo, Japan) *in lieu* of antigen decloaking to expose the core protein binding site. No antigen retrieval step was required for the COLL1, COLL3, or MMP13 primary antibodies. Sections were then treated with biotinylated secondary antibodies derived from goat (anti-rabbit or anti-mouse as appropriate, Jackson ImmunoResearch) prior to chromogenic staining.

All stained samples were imaged using a Microtek ArtixScan 4000tf slide scanner (Microtek International, Carson, CA, USA). Images were then blinded and graded for staining intensity on a scale of 0–4: 0—no stain; 1—weak stain in <50% of the area of interest; 2—weak stain in >50% or strong stain in <10%; 3—strong stain in <50%; and 4—strong stain in >50%. This semi-quantitative method has been used previously in our lab with a variability of <15%.[11] In order to determine the effect of the mechanical stimulation throughout the tissue, staining intensities were assessed in all three valve leaflet layers: the elastin-rich atrialis, located at the atrial surface; the middle spongiosa layer, comprised of PGs and glycosaminoglycans (GAGs); and the collagenous fibrosa, located near the ventricular surface. Staining intensity was also measured in the strut chordae. Co-localization of the different ECM components and turnover mediators within the valve layers was performed via comparison of the immunohistochemically stained samples to the Movat-stained samples. PCNA and H&E-stained samples were examined qualitatively to assess changes in cellular density within the different valve layers.

Statistical Analysis

Since each anterior valve leaflet had two strut chordae (Fig. 5a), each valve yielded two samples for testing. For each valve obtained during the validation study, one segment was designated a baseline control, and the second segment was cultured for 2 weeks in either the no mechanical stimulation (static) or cyclic mechanical stimulation (dynamic) condition; therefore, each test group had its own matched control. In every valve layer, staining intensity of each ECM component and turnover mediator of the cultured segment was normalized to that of the baseline control segment. A staining intensity within 20% of the baseline (normalized values of 1.0 ± 0.2) was considered to be maintenance of the component during the treatment period. Normalized staining intensities of the dynamic organ culture were compared to those of the static controls using a Student's *t*-test, with statistical significance defined as $p < 0.05$.

RESULTS

Pilot Long-Term Static Culture Study

Several general trends were identified in the Movat-stained atrioventricular valve samples cultured under static conditions over several weeks. First, COLL became more diffusely distributed in all samples. Toward the end of the culture period, COLL either dominated the cross section or shared dominance with elastin (Fig. 6a). The alcian blue stain marking the initially distinct PG layer became less well defined, then developed to a diffuse bluish haze within the COLL, and was virtually undetectable in the final week of the cultures (Fig. 6b). Finally, elastin content increased in some samples, although the final distribution of the elastin varied greatly between valve samples (Fig. 6c).

All tissue blocks taken at initial culture had an even distribution of cells on the interior, and a thin layer of endothelial cells on the outer surface (Fig. 7). Care was taking during tissue sectioning to limit damage to the endothelium, and staining performed prior to organ culture indicated that this layer was intact. In future studies, scanning electron microscopy could also be performed to confirm tissue integrity. In the first of three identified cell distribution patterns in the static cultures (Fig. 8), a *clumping pattern* was observed, in which cells became more abundant in certain areas of the valve, often less dense regions containing PGs, and less abundant in the more dense COLL-rich regions. Next, a *depletory effect* was seen, in which few cells could be detected. Finally, there was an *accumulation of cells* on the surface of many organ cultures. This accumulation, which was especially pronounced in the first 2 weeks of culture, was located mainly on the ventricular surface of the valve and in areas containing sharp protrusions or indentations that acutely and locally disrupted the endothelial layer or well-organized valve microstructure.

Cells staining for P4H were initially evenly distributed throughout the interior of the valve, but by the conclusion of culture, strong marker expression in the leaflet interior coincided with the accumulations of COLL shown in the Movat's pentachrome stain (data not shown). P4H also showed strong expression in the exterior cell accumulations. The results of the pilot study were used as a basis of comparison for the bioreactor validation studies.

Validation of Bioreactor Effectiveness

After the bioreactor was designed and built, it was tested to verify that it could maintain a sterile environment and that the mechanical stimulation would maintain ECM structure and cell viability. Sterility tests showed that the environment within the bioreactor remained free from contamination during the 2-week test period (data not shown).

The static culture results regarding the distribution of cells and the valvular-layered structure corroborated those of the pilot study. PCNA immunostaining indicated that, without mechanical stimulation, fewer proliferating cells were located deep within the tissue, although proliferating cells were found near the tissue

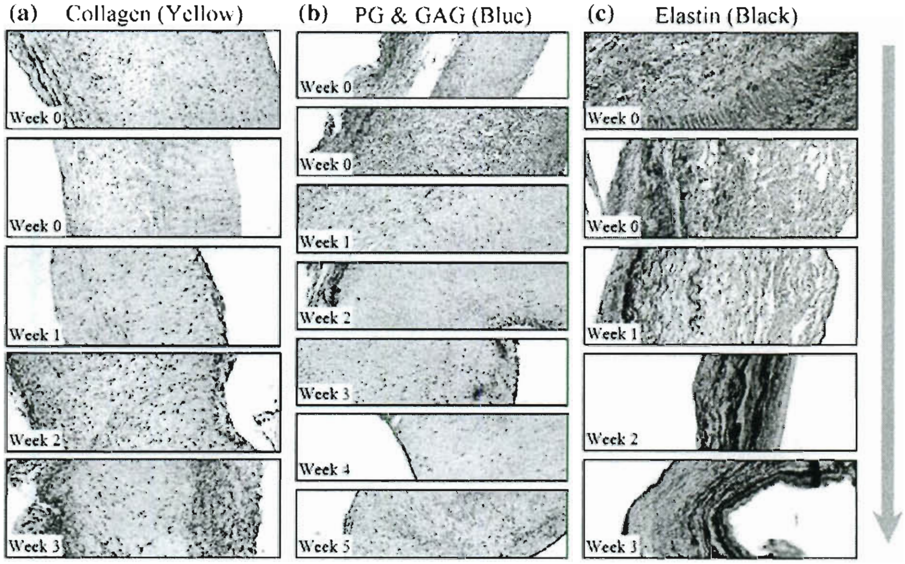

FIGURE 6. Movat pentachrome-stained sections of porcine organ-cultured valve tissue blocks (original magnification 10×). The ventricular surfaces are on the right and the atrial surfaces are on the left. (a) COLL content (yellow) clearly dispersed from the normal structure and began to dominate the valves, usually becoming the only remaining matrix protein by the conclusion of culture. (b) PG and GAG contents (blue–green) gradually disappeared, becoming just a diffuse haze in the mixture. (c) Elastin (black) became less localized and occasionally dominated the cross section, often together with COLL. Arrow indicates increase in culture duration.

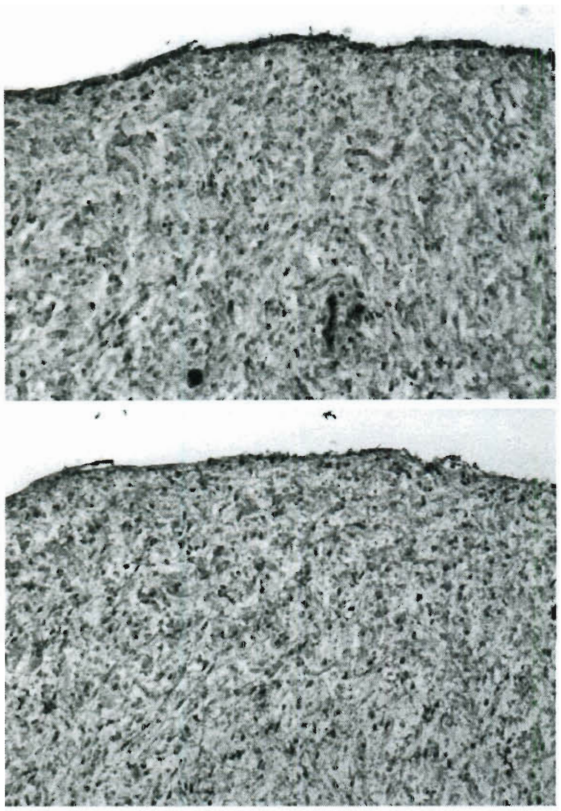

FIGURE 7. Valve section stained with vWF (top) and the corresponding negative stain (bottom) of fresh tissue immediately after sectioning into culture segments. Dark brown stain along the surfaces in the vWF section indicated the presence of an intact endothelial layer prior to organ culture.

surface. H&E staining showed the same trend (data not shown). After 2 weeks of static culture, the layered structure of the valve was also compromised. Although the Movat image showed maintenance of the atrialis, the fibrosa and spongiosa became less defined, with an increase in COLL content in the normally PG-rich free edge spongiosa.

The bioreactor appeared to counteract these static culture trends; after 2 weeks of culture, cell concentrations in the middle and periphery appeared comparable to those in control tissue, as indicated by both H&E and PCNA staining. Positive immunostaining for PCNA (Fig. 9) also suggested that these cells retained their ability to proliferate during the culture period. In addition, tissue samples cultured in the bioreactor displayed a similar ECM structure to that of the control samples; the collagenous fibrosa and elastin-rich atrialis layers of the leaflet center were clearly delineated in the Movat images (Fig. 9). The PGs in the spongiosa of the free edge were also maintained (data not shown).

The use of matched baseline controls for both the static and dynamic culture groups allowed the staining intensities of the ECM components and the turnover mediators to be normalized for comparison of differences after 2 weeks of culture. A normalized value of 1 indicated that there was no change in the component after culture, while a value <1 indicated reduced expression and a value >1 indicated greater expression. Overall, the splashing bioreactor was successful at maintaining most tested ECM components and turnover mediators (Table 1) as shown by maintenance of expression levels within 20% of baseline (normalized staining intensity of 1.0 ± 0.2). As shown in Figs. 10 and 11, static culture generally reduced expression of these factors relative to baseline controls, whereas dynamic culture resulted in more clustering of normalized expression values around 1.0. In fact, more normalized values were within 10% of baseline for dynamic culture (28 out of 52 factors) than they were with static culture (22 out of 52 factors). The most distinctive results for each layer are noted below.

In the chordae, dynamic stimulation encouraged negligible changes in component expression when compared to static culture conditions (Fig. 11a). Normal chordae consist of a COLL core surrounded by an elastin sheath. In the test samples, COLL1 content was reduced in the static culture samples and maintained in the dynamic culture samples (0.65 ± 0.21 static vs. 1.1 ± 0.27 dynamic, $p < 0.01$). Conversely, COLL3 expression was elevated in the static samples and maintained in the dynamic samples (1.5 ± 0.82 static vs. 1.1 ± 0.14 dynamic). While VC expression (which was quite low in static culture samples) tended to improve with dynamic stimulation (0.53 ± 0.14 static vs. 0.87 ± 0.54 dynamic), DCN expression remained constant among the three groups (control, static, and dynamic). Expression of MMP1, MMP2, and TIMP1 among the three culture groups was also approximately equal. HSP47, MMP9, and MMP13 results were too varied to be conclusive. Dynamic culture caused expression of P4H, LOX, and BGN that was higher than the maintenance range (1.25 ± 0.42, 1.29 ± 0.46, and 1.39 ± 0.41, respectively); in static culture conditions P4H and BGN were maintained (1.15 ± 0.46 and 0.92 ± 0.32, respectively) but LOX was reduced (0.69 ± 0.50).

The fibrosa of the normal mitral valve is also mostly comprised of COLL1 and COLL3. Normalized COLL1 expression was approximately 1.0 for both the static and dynamic cases (0.94 ± 0.45 static vs. 0.97 ± 0.25 dynamic), and COLL3 expression was elevated for both cases (1.6 ± 0.67 static vs. 1.3 ± 0.41 dynamic). BGL and P4H contents were similar among the three sample groups, whereas expression of MMP1, MMP9, LOX, and HSP47 was closer to

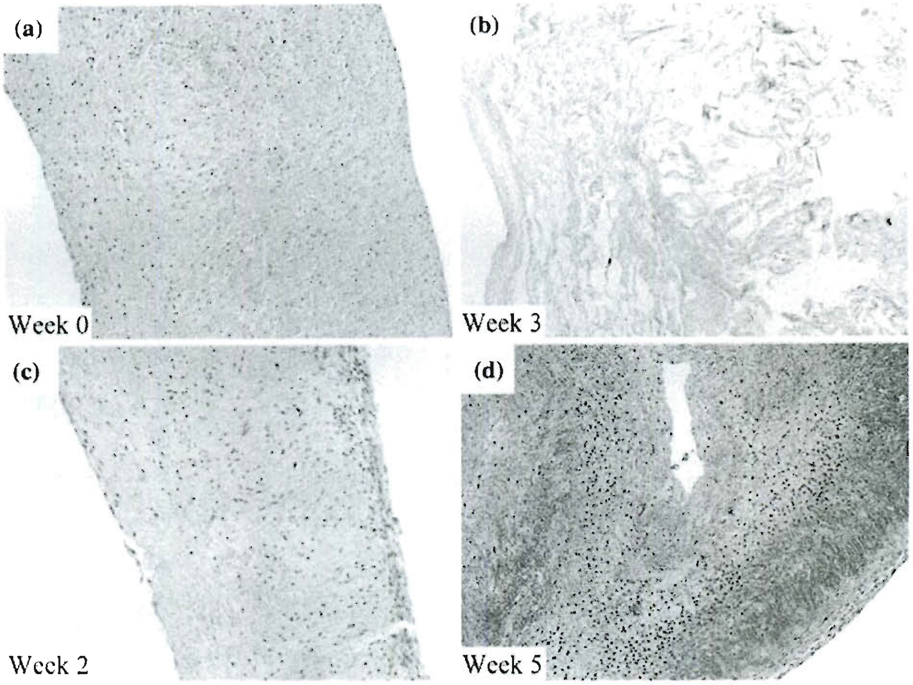

FIGURE 8. Hematoxylin and eosin-stained sections of porcine organ-cultured valve tissue blocks (original magnification 10×). The ventricular surfaces are on the right and the atrial surfaces are on the left. When compared to the control (a), valve tissue cultured without mechanical stimulation experienced (b) cell depletion pattern, (c) cell accumulation on the ventricular surface, and (d) cell clumping/migration from more dense tissue to less dense, more hydrated tissue.

baseline in dynamic samples (normalized expressions of 1.07, 1.06, 0.96, and 1.11, respectively) when compared to static samples, in which expression levels were consistently reduced (0.63, 0.69, 0.8, and 0.76). In general, use of dynamic mechanical stimulation appeared to cluster normalized component expression around 1.0 (Fig. 11b). Exceptions were VC (static 0.8 ± 0.31, dynamic 0.70 ± 0.25), COLL3 (static 1.59 ± 0.68, dynamic 1.32 ± 0.41), MMP2 (static 0.58 ± 0.39, dynamic 2.6 ± 0.89), and MMP13 (static 1.33 ± 0.52, dynamic 2.6 ± 1.6).

In normal valve tissue, the atrialis is mostly comprised of elastin. Although immunostaining for elastin was not performed, Movat images (Fig. 9) show that the elastin layer is maintained after 2 weeks of dynamic culture. While normalized COLL1 expression was reduced in static culture, it was maintained within normal values with dynamic culture (0.75 ± 0.25 static vs. 0.98 ± 0.27 dynamic, $p = 0.03$). Although normalized COLL3 expression was slightly greater with dynamic culture than static culture (0.88 ± 0.25 static vs. 1.2 ± 0.37, $p = 0.06$), baseline production of this ECM component was maintained in both cases. Expression of all PGs remained constant compared to baseline with both static and dynamic cultures, as did COLL3, MMP1, MMP2, MMP9, and LOX content; this tendency of both treatments to maintain atrialis composition is illustrated in Fig. 11c. TIMP1 expression was too varied between samples (0.68 ± 0.32 static vs. 0.74 ± 0.45 dynamic) to draw a conclusion. Dynamic stimulation caused the expression of two factors away from the maintenance range: HSP47 (static 1.32 ± 1.08, dynamic 0.77 ± 0.26) and MMP13 (static 1.16 ± 0.44, dynamic 1.6 ± 0.57).

The spongiosa of a healthy mitral valve mostly contains DCN, VC, and BGL. As shown in Fig. 11d, dynamic stimulation did not induce a marked overall improvement of component expression over static treatment; selected improvements, however, are highlighted below. Normalized expression of DCN and VC were normal in both the static and dynamic treatments (DCN: 0.92 ± 0.30 static vs. 0.95 ± 0.33 dynamic and VC: 0.91 ± 0.27 static vs. 0.98 ± 0.14 dynamic), whereas BGL expression was reduced in both culture groups (0.82 ± 0.43 static vs. 0.79 ± 0.28 dynamic). Normalized expression of MMP9 (0.55 ± 0.31 static vs. 1.2 ± 0.72, $p = 0.01$) and TIMP1 (0.79 ± 0.46 vs. 1.3 ± 0.65, $p = 0.04$) in the spongiosa was both greater with dynamic culture and reduced with static culture. MMP2, MMP9, and HSP47 expression were constant between the dynamic culture samples and baseline controls. Their resulting normalized stain

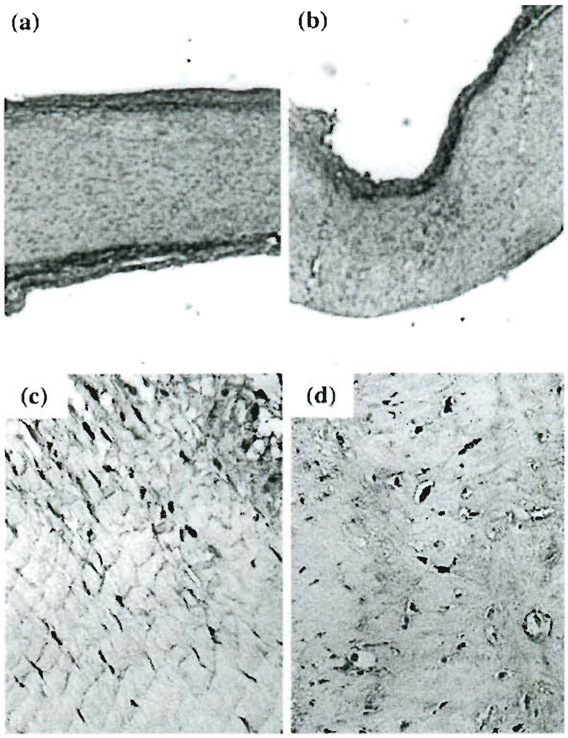

FIGURE 9. Comparison of a mitral valve center before (a, c) and after (b, d) 2 weeks of dynamic organ culture. When compared to the uncultured fresh control (a), Movat staining shows maintenance of atrialis (top black) and fibrosa (yellow) layers after 2 weeks of culture (b). PCNA stain in the fresh control (c) and the cultured (d) tissues shows the presence of proliferating cells (in brown) throughout the tissue. Atrial surface at top. Magnification = 5× (a, b) or 20× (c, d).

TABLE 1. Change in abundance of ECM component/precursor after culture.

	Atrialis	Spongiosa	Fibrosa	Chordae
BGL	–/–	–/–	–/–	–/↑
DCN	–/–	–/–	–/↑	–/–
VC	–/–	–/–	–/↓	↓/–
COLL1	↓/–	↓/↓	–/–	↓/–
COLL3	–/–	↓/↓	↑/↑	↑/–
P4H	–/↑	–/–	–/–	–/↑
MMP1	–/–	–/↓	↓/–	–/–
MMP2	–/–	–/–	↓/↑	–/–
MMP9	–/–	↓/–	↓/–	↑/–
MMP13	–/↑	–/–	↑/↑	–/–
TIMP1	↓/↓	–/↑	–/↓	–/–
LOX	–/–	–/–	–/–	↓/↑
HSP47	↑/–	↓/–	–/–	↑/–

Symbols before or after slash mark indicate changes in specified component after 2 weeks of static/dynamic culture relative to fresh tissue.

–, No change in normalized content expression (1.0 ± 0.2); ↑, increase in normalized content expression; ↓, decrease in normalized content expression.

intensity, which was approximately 1.0, was greater than and an improvement over that of the static samples. Normalized staining intensity was approximately 1.0 for MMP13, P4H, and LOX in both static and dynamic samples. Dynamic culture caused a reduction in the normalized staining intensity of three factors in the spongiosa to outside the maintenance range: COLL1 (static 0.73 ± 0.32, dynamic 0.71 ± 0.28), MMP2 (static 0.58 ± 0.39, dynamic 0.53 ± 0.27), and MMP1 (static 1.16 ± 0.61, dynamic 0.54 ± 0.57).

DISCUSSION

This study demonstrated that the splashing bioreactor provided mechanical stimulation necessary to preserve normal mitral valve-layered structure and ECM composition. In samples cultured without mechanical stimulation, proliferating cells deep within the tissue were depleted, and the layered structure noted in the normal valve became less defined with increased culture time. Fluid movement against tissue surfaces initiated by rotation of the bioreactor chamber provided perfusion and gentle tension, maintaining tissue integrity. This cyclic fluid motion was verified as sufficient to maintain valve structure for the 2-week period of interest by assessing stain intensity of PGs, COLL, and ECM turnover mediators before and after culture. This novel bioreactor, though simple in design and construction, could become a powerful tool for both tissue engineering and organ culture applications.

In the pilot study, we found that several major microstructural alterations occur when native heart valve tissue is placed in simple floating organ culture for several weeks. First, there was a dramatic upregulation of COLL and dissipation of PGs and GAGs. An increased abundance of COLL in the longer duration valve organ cultures could be caused by many cellular phenotypic changes, such as the upregulation of COLL producing enzymes and the downregulation of COLL degrading enzymes such as MMPs. A specific phenotypic analysis of the cells in the valve showed stronger P4H expression corresponding to areas of higher COLL content. We speculated that this apparent COLL upregulation and the rapid disorganization of the COLL layers could be attributed to the absence of mechanical stretch-induced perfusion of the tissues with our organ culture system. The dissipation of PGs could also be caused by the disorganization of the tissue, allowing the water-binding PGs and GAGs to leach out over time.

In addition to ECM changes, cells within the static cultured valves appeared to either migrate or dissipate with time, corroborating earlier static organ culture studies.[1] There were also large buildups of surface

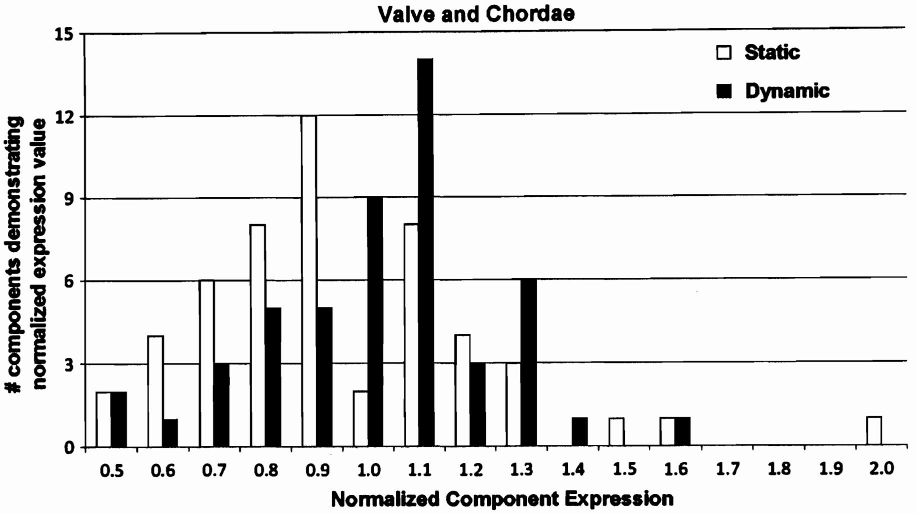

FIGURE 10. Histogram showing normalized component expression throughout the mitral valve. To generate the above histogram, the expression levels for all examined components (each of which was normalized to its matched fresh control) for all layers/chordae of the mitral valve samples were categorized into increments of 0.1. Samples cultured under static (white) and dynamic (black) conditions were compared using this histogram to gain a picture of the overall status of ECM within the cultured valves. In general, dynamic culture conditions contributed to component maintenance as defined by 1.0 ± 0.2 (100 ± 20%), after 2 weeks of culture. Not shown: normalized expression of MMP13 (2.3) and MMP2 (2.6) in fibrosa of dynamically cultured valves.

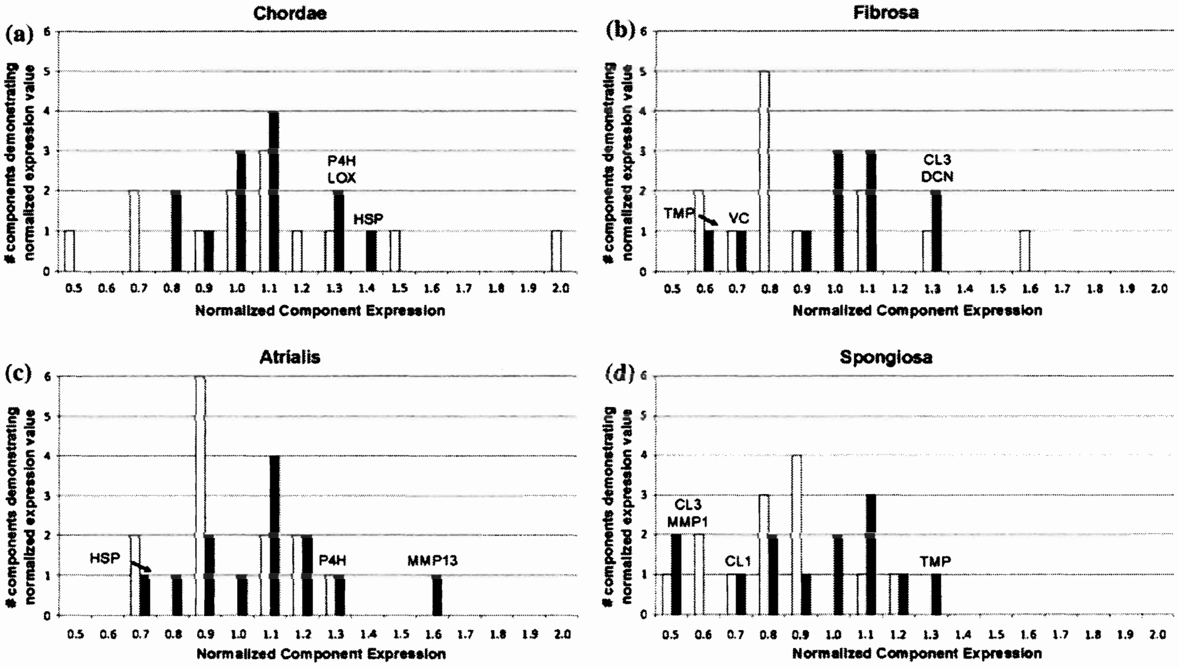

FIGURE 11. Histogram showing normalized component expression in the mitral valve chordae (a), fibrosa (b), atrialis (c), and spongiosa (d) to permit comparison of the samples cultured under static (white) and dynamic (black) conditions. These histograms were generated in the same manner as that described in the legend to Fig. 10. In general, dynamic culture conditions contributed to component maintenance as defined by 1.0 ± 0.2 (100 ± 20%) after 2 weeks of culture; the components considered to be maintained are described in the text and shown in Table 1 by the "–" symbol. ECM components and synthesis/turnover mediators not maintained by dynamic culture are indicated above bars, and are also indicated in Table 1 by the up or down arrows. Not shown: normalized expression of MMP13 (2.3) and MMP2 (2.6) in fibrosa of dynamically cultured valves. Abbreviations are as given in text except for HSP47, heat shock protein 47; CL1, collagen type 1; CL3, collagen type 3; TMP, tissue inhibitor of metalloproteases.

cells, especially on the ventricular surface. Over several weeks, the cells gradually became less abundant in the denser fibrosa layer and more abundant in the less dense spongiosa layer. Migration of cells within the organ cultured tissue blocks may have been a means to compensate for deficiencies in diffusive nutrient transport. In normal adult heart valves, cells throughout the leaflets are nourished by diffusion of oxygen and nutrients as opposed to a vascular supply.[4] Normal diffusion, however, is likely facilitated through the cyclic-stretch-induced perfusion of the tissues, which was not present in the static organ culture system.

A splashing bioreactor was therefore designed for perfusing and applying gentle stretch to a valve organ culture. Prior to using the bioreactor as a system for *in vitro* testing of valvular disease mechanisms, however, the cyclic mechanical stimulation provided by the fluid motion had to be verified as sufficient for maintaining both the layered valve structure and cell viability. The shear stress and velocity profile of flow was determined computationally, and the observed shear stress was 0.017 Pa. Furthermore, the velocity profile showed turbulence around the free edge of the leaflet. Functional evaluation of the biomechanical signals provided by this system was evident from the maintenance of tissue structure. This was illustrated by overall maintenance in elastin, PG, and COLL expression shown by immunohistostaining and histology (Movat) in dynamically cultured tissue. The lack of change in staining intensity of the ECM turnover mediators also indicated limited turnover of the ECM during the culture time. Proliferating cells were found throughout both the fresh and dynamically cultured tissues, indicating that the bioreactor was also successful in maintaining cell viability within the valve layers. These results showed that the mechanical stimulation provided by the splashing bioreactor was sufficient to maintain the valve layered structure and cell viability characteristics that were lost with static organ culture methods.

Valve cultured under static conditions tended to display excessive COLL production, and a successful bioreactor would maintain normal COLL composition. P4H has a role in the early non-helical phase of COLL synthesis,[34] BGL assists in regulation of fibril diameter,[10] and LOX catalyses the cross-links in the COLL fibers.[23] Increased normalized expression of these three components indicated additional COLL remodeling within the chordae with mechanical stimulation. Overall COLL content in the chordae, however, did not change; dynamic culture expression of COLL1 and COLL3 was almost equivalent to baseline in this highly collagenous tissue. Regulation of COLL remodeling was also noted within the valve leaflet. Considering the general increases in normalized expression of MMP13 (which degrades COLL) as well as COLL1 and COLL3, these data suggest that mechanical stimulation upregulated COLL production in the atrialis, maintaining COLL content via the appropriate turnover mediators. The increase in normalized COLL3 expression, which is also upregulated in myxomatous valves,[3] lends particular weight to this remodeling interpretation. It is also interesting to note that although MMP13 is responsible for cleaving COLL1[27,41] there was no significant decrease in COLL1 staining intensity corresponding to increased MMP13 staining intensity in the fibrosa; this result suggests that after 2 weeks there was only limited COLL remodeling in the fibrosa of dynamic culture samples. Since MMP13 is associated with COLL turnover,[41] this may have been an attempt to limit the excess COLL deposition noted in the earlier study. TIMP1 is an inhibitor of most MMPs[27,41]; its decrease in the fibrosa was possibly responsible for the increase in MMP expression.

Although the mechanical stimulation appeared to alter PG and COLL expression in the rest of the mitral valve, normalized BGL, COLL1, and COLL3 remained lower than normal in the spongiosa in both the static and dynamic culture conditions. Lack of dynamic culture-based improvement in BGL and COLL content in the spongiosa was potentially due to the lack of coaptation in the leaflet-free edge; while the bioreactor supplied mechanical stimulation from fluid flow, the tissue did not make contact with the opposing posterior leaflet as occurs *in vivo*. Elevated TIMP1 expression suggested that remodeling of the tissue might transpire given a longer culture time.

There were some apparent discrepancies between the COLL results in the two static culture studies (the pilot study and the static culture controls for the bioreactor validation study). The mitral valve tissue cultured statically in the bioreactor validation study demonstrated less staining for COLL1 (the most abundant COLL in normal valves) than baseline after 2 weeks of static culture, whereas the tissue from the pilot study showed more total COLL with increased culture time, as evidenced by the Movat safran yellow-stained regions (Fig. 6). One possible explanation is that the pilot study employed tricuspid valve tissue; the two valves may have had different responses to the culture environment. The greater accumulation of COLL in the pilot study could also be attributed to the longer culture time (up to 8 weeks). In addition, the Movat stain used in the pilot study could not be used to distinguish between the different COLL types present in the valve. In the validation study, both COLL1 and COLL3 were measured via immunostaining, and results suggested that an increase in COLL may have been due to COLL3 upregulation. COLL3 has been shown previously to be greater than normal in patients with myxomatous[3] and rheumatic[22] heart valve disease and has been presumed to indicate valve pathological remodeling; the increase in COLL3 noted in this study suggests an ongoing repair process within the tissue.

The exact role of the mechanical stimulation provided by the splashing bioreactor in maintaining ECM components and precursors should be explored in a future study. It is possible that the fluid motion directly impacted mechanical signaling in the tissue. The role of the fluid motion could be further clarified by providing mechanical stimulation in another manner, such as mounting the valve tissue in tension instead of the relaxed state used above, or by employing a different speed of rotation or a different rotation pattern (i.e., rocking vs. continuous). Another possibility is that the splashing of the culture media indirectly improved nutrient diffusion, which should be assessed in future work by comparing glucose, L-glutamine, ammonia, and lactate content in cell culture medium throughout the culture period. It is also highly likely that the rotating movement of the bioreactor improves transport of oxygen across the gas–fluid interface, thereby increasing the levels of dissolved oxygen in the medium. This improvement in oxygen levels would be beneficial to the valve as it would prevent hypoxia, which can occur when dissolved oxygen levels fall below 20%.[38] Therefore, in the future it will be important to compare the dissolved oxygen content in the culture media between static and dynamic culture conditions.

This bioreactor design validation study was novel compared to those used to validate previous heart valve tissue engineering bioreactor designs,[39] using a longer time course for the study as well as qualitative and quantitative tissue analysis methods. Previous heart valve bioreactor studies have often focused on demonstrating upregulation of ECM components or precursors after 48 h.[15,28,39] Conversely, this study employed a longer culture time, which is more useful for modeling a long-term pathology or for examining the effects of an extended tissue culture period. Furthermore, most heart valve tissue engineering bioreactor studies have used biochemical methods or qualitative immunohistochemical and histological analyses of the overall valve to assess ECM modeling.[26,42] The current research is one of few bioreactor studies[15,28] that focused on changes of specific ECM components and synthesis mediators within the individual layers, which is important due to their different structure and function. While the results from this study cannot be directly compared to those of the previous bioreactor studies, when the results are combined, a more complete picture of valvular remodeling can be drawn.

Limitations of this project include the subjectivity of the semi-quantitative immunohistochemical analysis. To eliminate potential bias, all samples were blinded prior to analysis. Repeatability was assessed by a second analysis of the tissues. This method has been previously documented to have a variability of $<15\%$,[11] and this study had a similar level of precision. It is also possible that cell migration noted in the static culture studies was due to a wound response during the initial sample preparation as opposed to nutrient access.[20] To mitigate the effect of this preparation artifact on the data, samples sectioned for staining were located deep within the tissue, away from the original cut. Another limitation was that the tissue was only examined at the study endpoint. In the future, an increased study duration with multiple timepoints could track the activity and consequences of ECM turnover mediators that were not preserved, such as MMP2 in the fibrosa. The ECM itself may remodel due to the effects of these mediators.

CONCLUSION

The development and validation of organ culture systems makes available powerful tools to study physiological systems and pathological mechanisms *in vitro* that would otherwise be nearly impossible to observe. This study describes the design of a novel bioreactor with a splashing motion that is intended to cause light stretch and perfusion of the mitral valve tissue to maintain tissue structure. Validation is an important step; maintenance of both ECM structure and cell concentration within the different layers of the tissue indicated successful organ culture when the bioreactor was used, whereas valve tissue cultured without mechanical stimulation displayed loss of the layered structure, cell loss deep within the tissue, altered COLL content, and reduced PG content. With this successful design, this bioreactor can be used to study the early mechanisms of valvular heart disease. Alternately, the design could be modified for use toward the tissue engineering of heart valves with the introduction of a treated scaffold material and donor cells.[2] The size of the entire system could also be scaled up to accommodate an entire valve, which would more faithfully reproduce the coaptation of the leaflet-free edges. In the future, this straightforward system can be used in a myriad of applications to promote further investigation of heart valve biology, pathology, and therapies.

ACKNOWLEDGMENTS

The authors acknowledge funding from the National Science Foundation (Grant #0502342). J.E.B. was supported by an NSF graduate research supplement. A.E.C. was supported by an NSF REU supplement. A.S.M. was supported by an institutional NSF REU program at the Cleveland Clinic Foundation.

REFERENCES

[1] Allison, D. D., J. A. Drazba, I. Vesely, K. N. Kader, and K. J. Grande-Allen. Cell viability mapping within long-term heart valve organ cultures. *J. Heart Valve Dis.* 13:290–296, 2004.

[2] Barzilla, J. E., T. L. Blevins, and K. J. Grande-Allen. Age-related structural changes in cardiac valves: implications for tissue-engineered repairs. *Am. J. Geriatr. Cardiol.* 15:311–315, 2006.

[3] Cole, W. G., D. Chan, A. J. Hickey, and D. E. Wilcken. Collagen composition of normal and myxomatous human mitral heart valves. *Biochem. J.* 219:451–460, 1984.

[4] Duran, C. M., and A. J. Gunning. The vascularization of the heart valves: a comparative study. *Cardiovasc. Res.* 2:290–296, 1968.

[5] Engelmayr, Jr., G. C., D. K. Hildebrand, F. W. Sutherland, J. E. Mayer, Jr., and M. S. Sacks. A novel bioreactor for the dynamic flexural stimulation of tissue engineered heart valve biomaterials. *Biomaterials* 24:2523–2532, 2003.

[6] Engelmayr, Jr., G. C., E. Rabkin, F. W. Sutherland, F. J. Schoen, J. E. Mayer, Jr., and M. S. Sacks. The independent role of cyclic flexure in the early in vitro development of an engineered heart valve tissue. *Biomaterials* 26:175–187, 2005.

[7] Engelmayr, Jr., G. C., V. L. Sales, J. E. Mayer, Jr., and M. S. Sacks. Cyclic flexure and laminar flow synergistically accelerate mesenchymal stem cell-mediated engineered tissue formation: implications for engineered heart valve tissues. *Biomaterials* 27:6083–6095, 2006.

[8] Engelmayr, Jr., G. C., L. Soletti, S. C. Vigmostad, S. G. Budilarto, W. J. Federspiel, K. B. Chandran, D. A. Vorp, and M. S. Sacks. A novel flex-stretch-flow bioreactor for the study of engineered heart valve tissue mechanobiology. *Ann. Biomed. Eng.* 36:700–712, 2008.

[9] Fisher, L. W., J. D. Termine, and M. F. Young. Deduced protein sequence of bone small proteoglycan I (biglycan) shows homology with proteoglycan II (decorin) and several nonconnective tissue proteins in a variety of species. *J Biol Chem.* 264:4571–4576, 1989.

[10] Grande-Allen, K. J., A. Calabro, V. Gupta, T. N. Wight, V. C. Hascall, and I. Vesely. Glycosaminoglycans and proteoglycans in normal mitral valve leaflets and chordae: association with regions of tensile and compressive loading. *Glycobiology* 14:621–633, 2004.

[11] Gupta, V., J. E. Barzilla, J. S. Mendez, E. H. Stephens, E. L. Lee, C. D. Collard, R. Laucirica, P. H. Weigel, and K. J. Grande-Allen. Abundance and location of proteoglycans and hyaluronan within normal and myxomatous mitral valves. *Cardiovasc. Pathol.* 18:191–197, 2009.

[12] Hildebrand, D. K., Z. J. Wu, J. E. Mayer, Jr., and M. S. Sacks. Design and hydrodynamic evaluation of a novel pulsatile bioreactor for biologically active heart valves. *Ann. Biomed. Eng.* 32:1039–1049, 2004.

[13] Hunt, S., M. Spitznas, P. Seifert, and M. Rauwolf. Organ culture of human main and accessory lacrimal glands and their secretory behaviour. *Exp. Eye Res.* 62:541–554, 1996.

[14] Jaffer, F. A., M. Nahrendorf, D. Sosnovik, K. A. Kelly, E. Aikawa, and R. Weissleder. Cellular imaging of inflammation in atherosclerosis using magnetofluorescent nanomaterials. *Mol. Imaging* 5:85–92, 2006.

[15] Konduri, S., Y. Xing, J. N. Warnock, Z. He, and A. P. Yoganathan. Normal physiological conditions maintain the biological characteristics of porcine aortic heart valves: an ex vivo organ culture study. *Ann. Biomed. Eng.* 33:1158–1166, 2005.

[16] Krishnamurthy, G., D. B. Ennis, A. Itoh, W. Bothe, J. C. Swanson, M. Karlsson, E. Kuhl, D. C. Miller, and N. B. Ingels, Jr. Material properties of the ovine mitral valve anterior leaflet in vivo from inverse finite element analysis. *Am. J. Physiol. Heart Circ. Physiol.* 295:H1141–H1149, 2008.

[17] Kunzelman, K. S., and R. P. Cochran. Stress/strain characteristics of porcine mitral valve tissue: parallel versus perpendicular collagen orientation. *J. Card. Surg.* 7:71–78, 1992.

[18] Kunzelman, K. S., R. P. Cochran, E. D. Verrier, and R. C. Eberhart. Anatomic basis for mitral valve modelling. *J. Heart Valve Dis.* 3:491–496, 1994.

[19] Lester, W. M., A. A. Damji, I. Gedeon, and M. Tanaka. Interstitial cells from the atrial and ventricular sides of the bovine mitral valve respond differently to denuding endocardial injury. *In Vitro Cell Dev. Biol.* 29A:41–50, 1993.

[20] Lester, W. M., A. A. Damji, M. Tanaka, and I. Gedeon. Bovine mitral valve organ culture: role of interstitial cells in repair of valvular injury. *J. Mol. Cell. Cardiol.* 24:43–53, 1992.

[21] Lester, W. M., and A. I. Gotlieb. In vitro repair of the wounded porcine mitral valve. *Circ. Res.* 62:833–845, 1988.

[22] Lis, Y., M. C. Burleigh, D. J. Parker, A. H. Child, J. Hogg, and M. J. Davies. Biochemical characterization of individual normal, floppy and rheumatic human mitral valves. *Biochem. J.* 244:597–603, 1987.

[23] Maki, J. M., R. Sormunen, S. Lippo, R. Kaarteenaho-Wiik, R. Soininen, and J. Myllyharju. Lysyl oxidase is essential for normal development and function of the respiratory system and for the integrity of elastic and collagen fibers in various tissues. *Am. J. Pathol.* 167:927–936, 2005.

[24] Menter, F. R. Zonal two equation k-ω turbulence models for aerodynamic flows. In: 24th AIAA Fluid Dynamics Conference, 1993; Orlando, FL, 1993, AIAA Paper 93-2906.

[25] Merrick, A. F., L. D. Shewring, S. A. Cunningham, K. Gustafsson, and J. W. Fabre. Organ culture of arteries for experimental studies of vascular endothelium in situ. *Transpl. Immunol.* 5:3–9, 1997.

[26] Merryman, W. D., H. D. Lukoff, R. A. Long, G. C. Engelmayr, Jr., R. A. Hopkins, and M. S. Sacks. Synergistic effects of cyclic tension and transforming growth factor-beta1 on the aortic valve myofibroblast. *Cardiovasc. Pathol.* 16:268–276, 2007.

[27] Nagase, H., R. Visse, and G. Murphy. Structure and function of matrix metalloproteinases and TIMPs. *Cardiovasc. Res.* 69:562–573, 2006.

[28]Platt, M. O., Y. Xing, H. Jo, and A. P. Yoganathan. Cyclic pressure and shear stress regulate matrix metalloproteinases and cathepsin activity in porcine aortic valves. *J. Heart Valve Dis.* 15:622–629, 2006.

[29]Prior, R., D. D'Urso, R. Frank, I. Prikulis, G. Wihl, and G. Pavlakovic. Canine leptomeningeal organ culture: a new experimental model for cerebrovascular beta-amyloidosis. *J. Neurosci. Methods* 68:143–148, 1996.

[30]Sacks, M. S., Y. Enomoto, J. R. Graybill, W. D. Merryman, A. Zeeshan, A. P. Yoganathan, R. J. Levy, R. C. Gorman, and J. H. Gorman, III. In vivo dynamic deformation of the mitral valve anterior leaflet. *Ann. Thorac. Surg.* 82:1369–1377, 2006.

[31]Sadgrove, M. P., J. E. Chad, and W. P. Gray. Kainic acid induces rapid cell death followed by transiently reduced cell proliferation in the immature granule cell layer of rat organotypic hippocampal slice cultures. *Brain Res.* 1035: 111–119, 2005.

[32]Sands, M. P., E. A. Rittenhouse, H. Mohri, and K. A. Merendino. An anatomical comparison of human pig, calf, and sheep aortic valves. *Ann. Thorac. Surg.* 8:407–414, 1969.

[33]Stephens, E. H., N. de Jonge, M. P. McNeill, C. A. Durst, and K. J. Grande-Allen. Age-related changes in material behavior of porcine mitral and aortic valves and correlation to matrix composition. *Tissue Eng. A* 16:867–878, 2010.

[34]Tasab, M., M. R. Batten, and N. J. Bulleid. Hsp47: a molecular chaperone that interacts with and stabilizes correctly-folded procollagen. *EMBO J.* 19:2204–2211, 2000.

[35]Taylor, P. M., S. P. Allen, and M. H. Yacoub. Phenotypic and functional characterization of interstitial cells from human heart valves, pericardium and skin. *J. Heart Valve Dis.* 9:150–158, 2000.

[36]Veranic, P., and M. Psenicnik. A mini organ culture as a model for studying the gallbladder epithelium of mouse. *Biol. Cell.* 88:145–151, 1996.

[37]Walker, G. A., K. S. Masters, D. N. Shah, K. S. Anseth, and L. A. Leinwand. Valvular myofibroblast activation by transforming growth factor-beta: implications for pathological extracellular matrix remodeling in heart valve disease. *Circ. Res.* 95:253–260, 2004.

[38]Warnock, J. N., S. Konduri, Z. He, and A. P. Yoganathan. Design of a sterile organ culture system for the ex vivo study of aortic heart valves. *J. Biomech. Eng.* 127:857–861, 2005.

[39]Weston, M. W., and A. P. Yoganathan. Biosynthetic activity in heart valve leaflets in response to in vitro flow environments. *Ann. Biomed. Eng.* 29:752–763, 2001.

[40]Wiester, L. M., and C. M. Giachelli. Expression and function of the integrin alpha9beta1 in bovine aortic valve interstitial cells. *J. Heart Valve Dis.* 12:605–616, 2003.

[41]Woessner, J. F., and H. Nagase. Matrix Metalloproteinases and TIMPs. New York: Oxford University Press, 223 pp, 2000.

[42]Xing, Y., J. N. Warnock, Z. He, S. L. Hilbert, and A. P. Yoganathan. Cyclic pressure affects the biological properties of porcine aortic valve leaflets in a magnitude and frequency dependent manner. *Ann. Biomed. Eng.* 32:1461–1470, 2004.

Appendix V: Mitral Valve Function on Substrates with Varying Stiffness

This appendix features work in which I participated and was a co-author on the manuscript; however the work was led by other researchers. A brief description of the my primary contributions is given below and a reprint of the manuscript follows. This was published as Stephens EH, Durst CA, West JL, Grande-Allen KJ. Mitral Valvular Interstitial Cell Responses to Substrate Stiffness Depend on Age and Anatomic Region. Acta Biomaterialia, 2011 Jan; 7(1):75-82.

This manuscript described the characterization of valve cell behavior to substrate stiffness while probing the anatomic region and age from which the valve cells were derived. I assisted with and performed the synthesis and characterization of PEGDA, PEG-RGDS, and Hep-MA. Additionally, I assisted with the interpretation of data regarding biofunctional moiety incorporation into gels.

Acta Biomaterialia 7 (2011) 75–82

Contents lists available at ScienceDirect

Acta Biomaterialia

journal homepage: www.elsevier.com/locate/actabiomat

Mitral valvular interstitial cell responses to substrate stiffness depend on age and anatomic region

Elizabeth H. Stephens, Christopher A. Durst, Jennifer L. West, K. Jane Grande-Allen *

Department of Bioengineering, Rice University, P.O. Box 1892 - MS142, Houston, TX 77251-1892, USA

ARTICLE INFO

Article history:
Received 6 May 2010
Received in revised form 1 July 2010
Accepted 2 July 2010
Available online 17 July 2010

Keywords:
Heart valve
Age/aging
Stiffness
Hydrogel
Surface modification

ABSTRACT

The material properties of heart valves depend on the subject's age, the state of the disease and the complex valvular microarchitecture. Furthermore, valvular interstitial cells (VICs) are mechanosensitive, and their synthesis of extracellular matrix not only determines the valve's material properties but also provides an adhesive substrate for VICs. However, the interrelationship between substrate stiffness and VIC phenotype and synthetic properties is poorly understood. Given that the local mechanical environment (substrate stiffness) surrounding VICs differs among different age groups and different anatomic regions of the valve, it was hypothesized that there may be an age- and valve-region-specific response of VICs to substrate stiffness. Therefore, 6-week-, 6-month- and 6-year-old porcine VICs from the center of the mitral valve anterior leaflet (MVAC) and posterior leaflet (PML) were seeded onto poly(ethylene) glycol hydrogels of different stiffnesses and stained for markers of VIC activation (smooth muscle alpha-actin (SMaA)) and collagen synthesis (heat shock protein-47 (HSP47), prolyl 4-hydroxylase (P4H)). Six-week-old MVAC demonstrated decreased SMaA, P4H and HSP47 on stiffer gels, while 6-week-old PML only demonstrated decreased HSP47. Six-month-old MVAC demonstrated no difference between substrates, while 6-month-old PML demonstrated decreased SMaA, P4H and HSP47. Six-year-old MVAC demonstrated decreased P4H and HSP47, while 6-year-old PML demonstrated decreased P4H and increased HSP47. In conclusion, the age-specific and valve-region-specific responses of VICs to substrate stiffness link VIC phenotype to the leaflet regional matrix in which the VICs reside. These data provide further rationale for investigating the role of substrate stiffness in VIC remodeling within diseased and tissue engineered valves.

© 2010 Acta Materialia Inc. Published by Elsevier Ltd. All rights reserved.

1. Introduction

Valve disease afflicts a substantial portion of the population: 1–2% of 26- to 84-year-olds are afflicted by mitral valve disorders [1]. Valve disease incurs significant morbidity and mortality, requiring over 100,000 surgeries in the USA each year [2]. In many of these disease states the mechanical properties of these valves are altered, often contributing to the poor valve function requiring surgical intervention. Valvular interstitial cells (VICs) are the dynamic, living component of heart valves responsible for synthesizing and maintaining the valve matrix composition, which in turn determines the valve's material behavior. VICs and valves are known to be responsive to changes in their mechanical environment [3–5]. However, the interplay between matrix-driven material properties such as stiffness and the phenotype and synthetic behavior of VICs, particularly in the mitral valve (MV), has largely been overlooked. Recent work has demonstrated age-related significant changes in valve composition [6–8] and material properties [9]; other studies have shown substantial heterogeneity in material behavior among the different anatomic regions of the MV [10]. Given that different aged VICs and VICs from different regions of the MV reside in valve tissues with distinct stiffnesses [9], it was hypothesized that there may be an age- and valve-region-specific response of VICs to substrate stiffness.

In order to test this hypothesis, separate groups of VICs from three distinct age groups and from two different regions of the MV were cultured on poly(ethylene) glycol (PEG) hydrogels of two different stiffnesses. After 48 h, the resulting VIC expression of cell phenotype and collagen synthesis markers was assessed using immunocytochemistry (ICC).

PEG hydrogels were chosen for this experiment based on their promise as a potential platform for the design of scaffolds for tissue-engineered heart valves. PEG hydrogels are extremely hydrophilic, providing prevention against protein adsorption, a critical step in the immunogenicity and degradation of bioprosthetics [11]. They are also highly permeable, allowing the exchange of nutrients and waste materials [12]. Their stiffness can be regulated by changing the molecular weight and concentration of PEG [13]. However, one of the factors that makes these gels particularly

---

* Corresponding author. Tel.: +1 713 348 3704; fax: +1 713 348 5877.
E-mail address: grande@rice.edu (K.J. Grande-Allen).

1742-7061/$ - see front matter © 2010 Acta Materialia Inc. Published by Elsevier Ltd. All rights reserved.
doi:10.1016/j.actbio.2010.07.001

attractive is the ability to customize them by conjugating to the PEG backbone various peptides, including cell ligands and growth factors, as well as incorporating enzyme-degradable sequences allowing tunability of the degradation rate of the hydrogel. This designer biofunctionality makes PEG hydrogels advantageous for the tissue engineering of heart valves. In the present study PEG hydrogels were conjugated with an Arg–Gly–Asp–Ser (RGDS) peptide, enabling VIC attachment to the hydrogel, and methacrylated heparin, which is necessary for normal VIC morphology [14,15]. These functionalized PEG hydrogels of two different stiffnesses were formulated to keep the concentration of biological cues constant, thus isolating the effect of stiffness on VIC phenotype.

2. Materials and methods

2.1. Synthesis of PEG hydrogel components

PEG-diacrylate (PEG-DA) of 3400 Da MW was synthesized from PEG (Sigma–Aldrich, St. Louis, MO) as previously described [13]. ^{1}H nuclear magnetic resonance (NMR) analysis revealed >95% acrylation. Methacrylated heparin was synthesized as described previously [14]. Briefly, a 10 mg ml^{-1} solution of heparin (Sigma–Aldrich) dissolved in ultrapure water was reacted with 40 molar excess methacrylic anhydride (Sigma–Aldrich). The pH of the solution was adjusted to 7.5 using 4 M NaOH and stirred for 24 h. Methacrylated heparin was then precipitated using cold 95% ethanol. The precipitate was then filtered, dried and dialyzed against ultrapure water using a 1000 Da MWCO membrane (Spectrum Laboratories, Rancho Dominguez, CA). The product was then lyophilized. ^{1}H NMR analysis revealed 5% methacrylation per disaccharide.

The RGDS peptide (Bachem, Bubendorf, Switzerland) was attached to hetero-bifunctional PEG (PEG-SCM; Laysan Bio, Arab, AL) by reacting the peptide with hetero-bifunctional PEG and catalyst diisopropylamine (Sigma–Aldrich) in dimethyl sulfoxide (DMSO; 1.2 M RGDS:1.0 M PEG-SCM:2.0 M disopropylamine) for 24 h. The product was then dialyzed against ultrapure water using a 1000 Da MWCO membrane (Spectrum Laboratories) and lyophilized. The Trp–Arg–Gly–Asp–Ser (WRGDS) peptide (GenScript, Piscataway, NJ) was similarly attached to hetero-bifunctional PEG. Evaluation of PEG-RGDS by gel permeation chromatography revealed 81% conjugation.

2.2. Polymerization of functionalized PEG hydrogels

PEG hydrogels were synthesized by dissolving the appropriate amounts of PEG-RGDS, methacrylated heparin and PEG-DA in phosphate-buffered saline. A volume of 10 µl ml^{-1} 2,2-dimethoxy-2-phenyl-acetophenone (300 mg ml^{-1} in 1-vinyl-2-pyrrolidone) was added and the solution was poured between two sterile glass slides separated by a 0.4 mm spacer and exposed to ultraviolet light for 2 min (365 nm, 10 mW cm^{-2}). Hydrogels were then removed from the mold and soaked in phosphate-buffered saline with 2% antibiotic (Mediatech, Herndon, VA) for at least 24 h allowing the hydrogels to swell to equilibrium. Hydrogel thickness was optically measured using a Leica DFC 320 CCD camera (Wetzlar, Germany) and ImagePro acquisition software (Media Cybernetics, Bethesda, MD). Hydrogel thicknesses were determined from the acquired images using ImageJ software (NIH, Bethesda, MD).

2.3. Optimization of functionalized PEG hydrogels

Optimization studies were performed to determine the concentrations of PEG-RGDS and methacrylated heparin in the pre-polymer solution necessary to yield equivalent amounts of these bioactive ligands in the swollen, polymerized gels of the two different weight-volume fractions of PEG-DA. The concentration of methacrylated heparin in polymerized, swollen gels was determined using an uronic acid assay, as described by Blumenkrantz and Asboe-Hansen [16] after gels were hydrolyzed by reacting them with 0.1 N NaOH for 34 h at 37 °C. These studies determined that 9.0 mg ml^{-1} of methacrylated heparin in the pre-polymer hydrogel solution for the 5% weight-volume PEG-DA hydrogel and 10.6 mg ml^{-1} of methacrylated heparin in the solution for the 15% weight-volume PEG-DA hydrogel yielded equivalent concentrations of methacrylated heparin in the polymerized, swollen gels of the different PEG-DA weight-volume fractions (Fig. 1). Optimization studies utilizing tryptophan (which was detected by its absorbance at 280 nm using a spectrophotometer (SpectraMax M2, Molecular Devices, Sunnyavale, CA)) in the RGDS peptide (WRGDS, conjugated to PEG using the same reaction as for RGDS; gel permeation chromatography revealed 83% conjugation), determined that 7.49 mg ml^{-1} of PEG-RGDS in the pre-polymer solutions for both weight-volume PEG-DA hydrogels yielded equivalent final concentrations of PEG-RGDS in the swollen, polymerized gels (Fig. 2).

2.4. Determination of elastic modulus of functionalized PEG hydrogels

Strips of the two weight-volume fraction PEG hydrogels (5 mm in width) were uniaxially tensile tested using an EnduraTec ELF 3200 (Bose, Eden Prairie, MN). The strain rate was 10 mm s^{-1} and load-elongation data were recorded until failure occurred. Displacement was converted to strain based on the initial hydrogel length between grips. The elastic modulus was determined as the slope of the least-squares linear fit to the stress–strain curve.

2.5. Cell culture and cell seeding onto PEG

Mitral valves were dissected from hearts from 6-week-, 6-month- and 6-year-old pigs obtained from an abattoir (the 6-week- and 6-month-olds from Fisher Ham and Meat, Spring, TX; the 6-year old from Animal Technologies, Tyler, TX). Based on previous studies demonstrating that the mitral valve anterior center (MVAC) is stiffer than the posterior leaflet [10], VICs were isolated from the MVAC (representing a stiffer valve region) and the PML (representing a less stiff valve region) from the same mitral valves according to previously published protocols [17]; cells were cultured in medium containing 10% bovine growth serum (HyClone, Logan, UT) and 2% antibiotic/antimycotic (Mediatech). The medium was changed every 2–3 days and cells were passaged after reaching

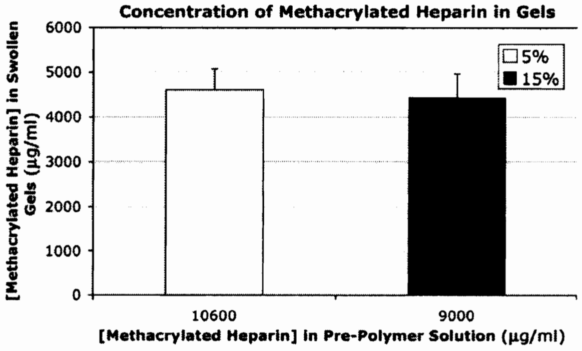

Fig. 1. Concentration of methacrylated heparin in the two different weight–volume fraction PEG swollen gels as determined by uronic acid assay. Four PEG hydrogel samples of each weight–volume fraction were tested. Error bars on all graphs indicate standard error of the mean.

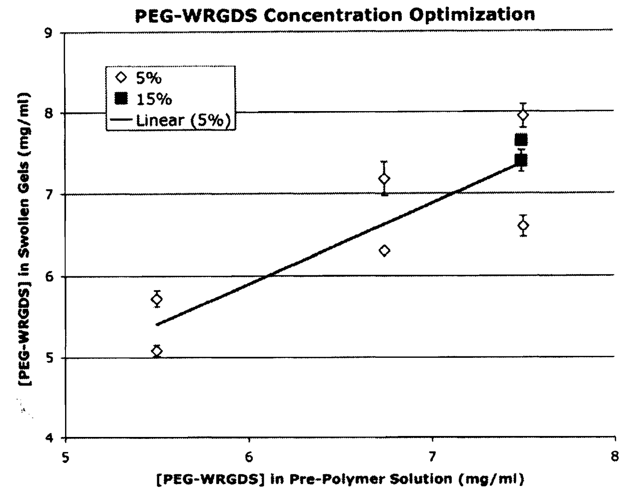

Fig. 2. Optimization of PEG-WRGDS in the two different weight-volume fraction PEG swollen gels by varying the concentration of PEG-WRGDS in the pre-polymer solutions. The concentration of PEG-WRGDS was determined by absorption at 280 nm.

80–90% confluence. Experiments were performed on cells from passages 5–6. Cells were seeded onto functionalized PEG hydrogels at a cell density of 6000 cells cm^{-2} and maintained in 10% serum medium with 2% antibiotic/antimycotic.

2.6. Immunocytochemistry

Based on previous reports demonstrating phenotypic changes in fibroblasts and VICs after 24–48 h [14,18], in the present study VICs were cultured on gels for 48 h and then fixed by incubation in 10% formaldehyde in PBS for 30 min at room temperature. Samples of dimensions 4 mm × 6 mm were cut from cell-seeded gels and transferred to the wells of an 8-well coverglass chamber (Lab-Tek II, Nalge Nunc International, Naperville, IL) for ICC staining and subsequent imaging. ICC was performed for markers of collagen synthesis prolyl 4-hydroxylase (P4H; Chemicon, Temecula, CA) and heat shock protein 47 (HSP47; Assay Designs, Ann Arbor, MI), as well as markers related to valve cell phenotype vimentin (Dakocytomation, Denmark) and the marker of VIC activation [19] smooth muscle alpha-actin (SMaA; Dakocytomation), with AlexaFluor 488 secondary antibodies (Invitrogen Molecular Probes, Eugene, OR). Stained gels were imaged using LSM 5 LIVE 5 DuoScan (Zeiss, Oberkochen, Germany) and staining intensity and cell morphology (area and circularity) were quantified using ImageJ software. For determination of staining intensity, cells were outlined and the intensity within each cell was quantified (0–255) relative to any background intensity. Multiple images (3–5) were analyzed for each marker for each VIC population cultured on the different gels.

2.7. Statistical analysis

Multifactorial analysis of variance (ANOVA) was performed using SigmaStat (SPSS, Chicago, IL). When the data for a given characteristic was normally distributed (as determined by the software), the program continued with an ANOVA. When the data set was not normally distributed, the data was rank transformed before the ANOVA was performed. In both cases the level of significance was set at 0.05.

3. Results

3.1. Stiffness of different weight-volume fraction functionalized PEG hydrogels

Uniaxial testing revealed that functionalized 5% weight-volume PEG gels had a mean modulus of 34.5 kPa, while functionalized 15% weight-volume PEG gels had a mean modulus of 323.3 kPa (Fig. 3).

3.2. SMaA expression of VICs on gels of different stiffnesses

Not all VICs stained positively for SMaA, as expected. Analysis of the fraction of VICs expressing SMaA (SMaA+ VICs) on the different gels revealed a trend towards decreased SMaA+ VICs on the 15% gels compared to the 5% in the 6-week-old MVAC VICs (Fig. 4, $p = 0.1$), but there was no difference between gels for 6-week-old PML VICs. Six-month- and 6-year-old MVAC VICs did not display a difference in the fraction of SMaA+ VICs between gels, but 6-month- and 6-year-old PML VICs showed a trend toward decreased SMaA + VICs on the 15% gels relative to the 5% gels ($p = 0.06$). Analysis of the intensity of SMaA stain in SMaA+ VICs on the different gels revealed a trend towards decreased intensity in SMaA+ VICs for 6-week-old MVAC VICs (Fig. 5, $p = 0.087$) but no difference for 6-week-old PML VICs. Six-month-old MVAC demonstrated no change in SMaA intensity in MVAC VICs but decreased SMaA intensity in PML VICs ($p < 0.05$). No difference in SMaA intensity between gels was evident for 6-year-old MVAC VICs or 6-year-old PML VICs.

3.3. P4H expression of VICs on gels of different stiffnesses

Analysis of P4H, which was expressed by all VICs, demonstrated decreased intensity in 6-week-old MVAC VICs on the 15% gels relative to the 5% gels ($p < 0.05$) but no difference between gels for 6-week-old PML VICs. Six-month-old MVAC VICs demonstrated no difference in P4H intensity between gels, but 6-month-old PML VICs demonstrated decreased intensity on the 15% gels relative to the 5% gels (Fig. 6, $p < 0.05$). Six-year-old MVAC and PML VICs both demonstrated decreased P4H intensity on the 15% gels relative to the 5% gels (MVAC $p < 0.05$, PML $p < 0.085$ (trend)).

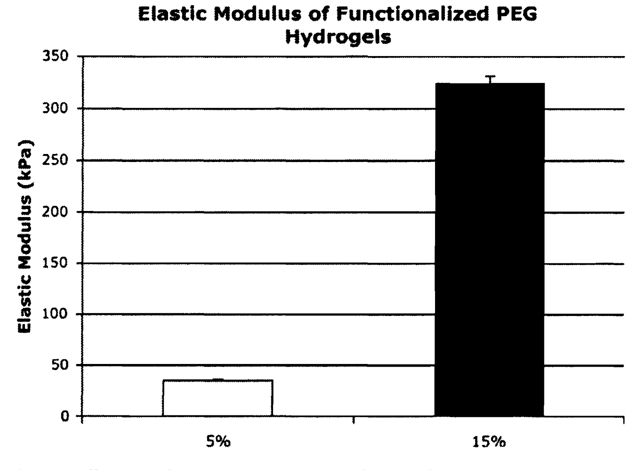

Fig. 3. Stiffness of the two weight-volume fraction functionalized PEG gels as determined by the elastic modulus during uniaxial tensile testing. Four PEG hydrogel samples of each weight-volume fraction were tested.

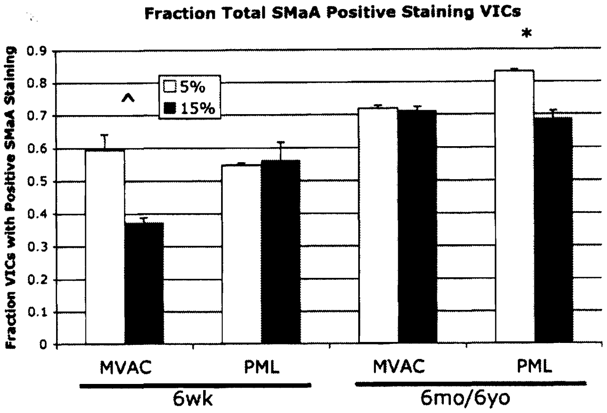

Fig. 4. Percent VICs displaying positive SMaA staining on the two gels of different stiffnesses, *$p = 0.06$, ^$p = 0.1$ 5% vs. 15% gels. Data from the 6-month-old and 6-year-old age groups were not significantly different and so were grouped together; the combined data are shown.

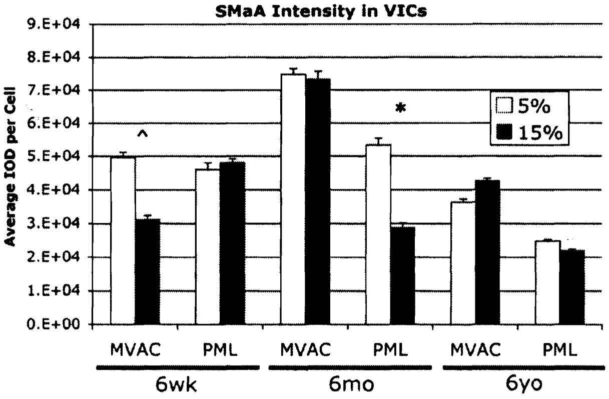

Fig. 5. SMaA staining intensity for positive SMaA staining VICs on the two gels of different stiffnesses. *$p < 0.05$, ^$p = 0.087$ 5% vs. 15% gels.

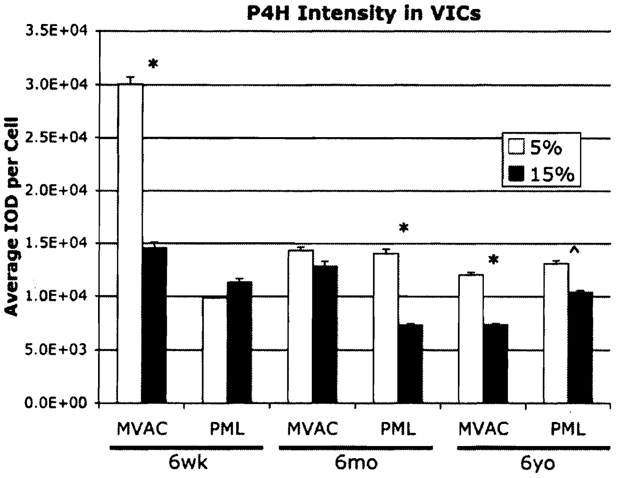

Fig. 6. P4H staining intensity of VICs on the two gels of different stiffnesses. *$p < 0.05$, ^$p < 0.085$ 5% vs. 15% gels.

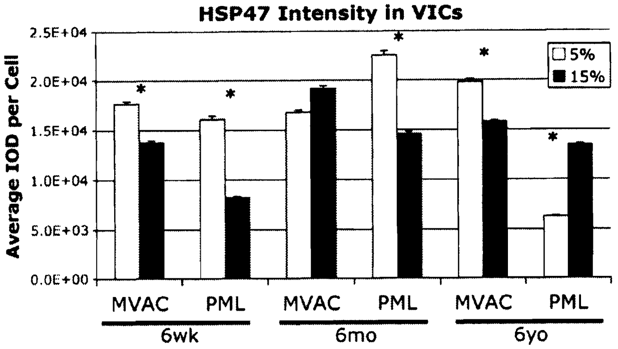

Fig. 7. HSP47 staining intensity of VICs on the two gels of different stiffnesses. *$p < 0.05$ 5% vs. 15% gels.

3.4. HSP47 expression of VICs on gels of different stiffnesses

Analysis of HSP47, which was expressed by all VICs, demonstrated decreased intensity in both 6-week-old MVAC and PML VICs on the 15% gels relative to the 5% gels (Fig. 7, both $p < 0.05$). Six-month-old MVAC VICs demonstrated no difference in HSP47 intensity between gels, but 6-month-old PML VICs demonstrated decreased HSP47 intensity on the 15% gels relative to the 5% gels ($p < 0.05$). Six-year-old MVAC demonstrated no difference in HSP47 intensity between gels, but 6-year-old PML VICs demonstrated increased HSP47 intensity on the 15% gels relative to the 5% gels ($p < 0.05$).

3.5. VIC Morphology on gels of different stiffnesses

For both MVAC and PML VICs of each age and on each gel, two populations of VICs were noted: one with a spindle-shaped cell morphology and a second with a cuboidal cell morphology (Fig. 8). Analysis of staining intensity of cuboidal and spindle-shaped subpopulations revealed that, for given age- and valve-region VICs that responded to substrate stiffness, both subpopulations demonstrated a response (data not shown). Cell morphology analysis of vimentin-stained VICs revealed a decreased cell area of 6-month-old PML VICs on the 15% gels relative to the 5% gels ($p < 0.02$). No difference was noted in circularity between VICs on PEG hydrogels of different stiffnesses.

4. Discussion

In this study, mitral VICs grown on functionalized PEG hydrogels demonstrated both age- and valve-region-specific (MVAC vs. PML) responses to substrate stiffness. These results underscore the range of unique phenotypes found in valvular cells and provide compelling motivation for further studies of heart valve mechanobiology.

4.1. Previous studies of VICs and substrate stiffness

While the response of cells to substrate stiffness has been studied extensively in cell types from many other tissues (see the excellent review by Nemir and West [20]), very limited investigation has been performed on the response of VICs to substrate stiffness. Furthermore, even though the material properties of MVs are known to be altered in diseased states [21,22] and are distinct in different MV regions [10], no studies published to date have examined the response of MV VICs to substrate stiffness. Additionally, no studies have investigated a potential age-specific response of VICs to substrate stiffness despite a growing awareness that valve

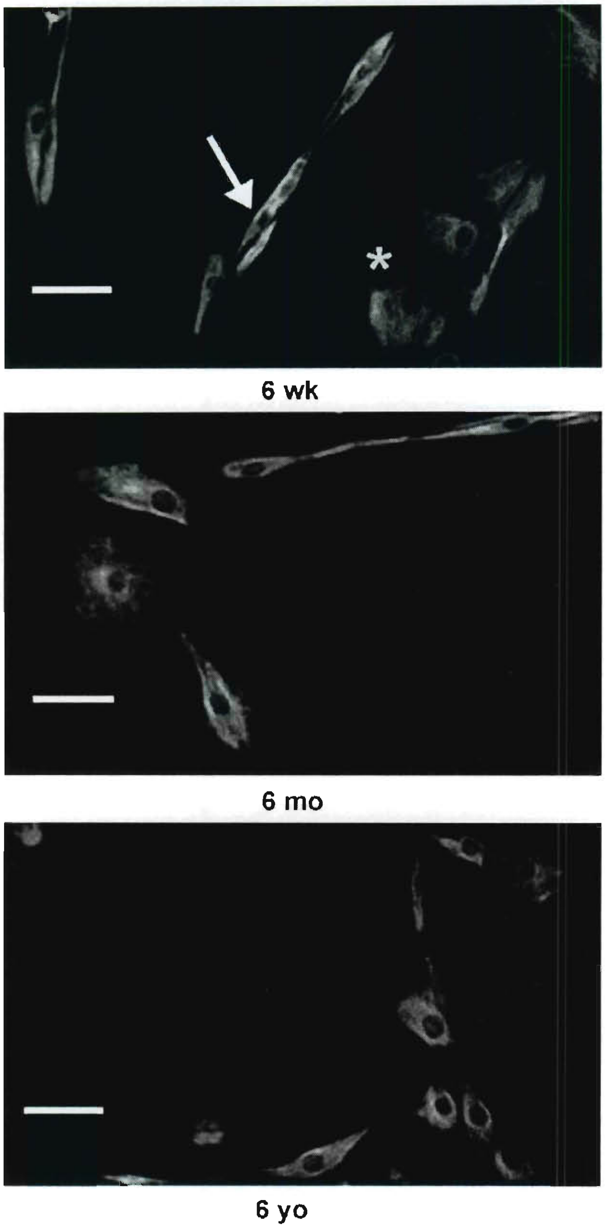

Fig. 8. Images of vimentin-stained VICs from each age group demonstrating two distinct VIC morphologic subpopulations: spindle-shaped cells (see the white arrow in the 6-week-old image) and cuboidal cells (see the yellow asterisk in the 6-week-old image). These distinct subpopulations were evident for VICs isolated from both MVAC and PML and on PEG gels of both stiffnesses. Shown here are MVAC VICs on 15% PEG gels. Scale bars indicate 50 mm.

matrix, material properties and VIC phenotype change with age [6–9].

Work on fibroblasts from different tissues examining cell phenotype and morphology changes in response to substrate stiffness has documented increased actin fibers in response to increased substrate stiffness [20], appearance of stress fibers on stiffnesses of 10 kPa and above [18], and an increase in cell spreading that was maximum on substrate stiffnesses of 8–10 kPa [18,23]. However, all of these studies were performed within a range of substrate stiffnesses that was much lower (i.e. 1–100 kPa [20]) than the stiffnesses used in the present study. While the in vivo stiffness of the MVAC continues to be debated [24,25], and the in vivo stiffness of the PML remains to be determined, these stiffnesses are certainly considerably greater than the 1–10 kPa range of substrate stiffness commonly utilized in fibroblast experiments. The two gel stiffnesses used in this study were chosen to be in the same general range that could be consistent with the in vivo stiffnesses of the MVAC and PML, yet were different enough to potentially elicit age- and valve-region-specific VIC responses.

Three previous studies aimed at identifying factors in aortic valve (AV) calcification have analyzed the effect of substrate stiffness on mineralization and activation of porcine AV VICs. One work [26] compared the calcification potential of AV VICs seeded at confluence (allowing cell-to-cell interaction) on PEG hydrogels (compressive modulus of ~100 kPa) functionalized with fibronectin or fibrin to AV VICs cultured on unmodified tissue culture polystyrene (TCPS, a much stiffer substrate) and TCPS coated with fibrin and fibronectin [26]. One of their key findings was that the response of VICs to substrate stiffness depended on the matrix coating the substrate [26]. Another study showed that porcine AV VICs cultured on collagen gels of different stiffnesses did not display any difference in calcification potential in normal medium, but in calcification medium AV VICs developed different types of calcific nodules depending on the collagen gel stiffness [27]. In an earlier study [28], SMaA expression in AV VICs was increased on stiffer collagen gels; however, in this study VICs were simultaneously exposed to different concentrations of collagen fibers and this may have confounded the interpretation of their results [28].

4.2. Age- and valve-region-specific responses of VICs to substrate stiffness

In the present study both age- and valve-region-specific responses of VICs to different substrate stiffnesses were evident. Based on ex vivo experiments of material properties of different aged porcine MVs and different regions within the porcine MV (MVAC vs. PML [10]), one would expect the 6-week-old VICs to be accustomed to a less stiff substrate relative to the 6-month- and 6-year-old VICs. Similarly, given studies demonstrating that MVAC tissues are stiffer than PML tissues [10], one would expect MVAC VICs to be accustomed to a stiffer substrate than PML VICs. Unfortunately, the actual in vivo stiffness of the MVAC remains unclear, with only a few reports citing vastly differing values [24,25]; no reports exist citing values for the in vivo stiffnesses of different aged MVAC and PML. Potentially, the results from this study could be explained by differences in "optimal" stiffness for each VIC population assessed. Just as "optimal" stiffnesses have been demonstrated for stem cell lineage specification and the expression of associated cellular markers [29], in VICs expression of myofibroblast phenotype and collagen synthesis markers may reach a maximum at a certain stiffness, and this stiffness could be unique for each VIC population. Based on the mechanical testing studies cited above, potentially the "optimal" stiffness for 6-week-old PML would be less than those for 6-month-old PML and 6-week-old MVAC. Where the stiffnesses of the 5% and 15% gels fall relative to one another upon this hypothetical marker expression–stiffness curve for a particular VIC population could explain whether differences in marker expression were observed between the VIC population seeded on the 5% and 15% gels (Fig. 9). Clearly, substantial future work is needed to investigate this hypothesis further, including a larger number and range of substrate stiffnesses. Nevertheless, the results from this study demonstrate that there are age- and valve-region-specific responses of VICs to substrate stiffness.

In terms of specific protein expression, SMaA expression and proportion of SMaA+ cells generally paralleled changes in collagen

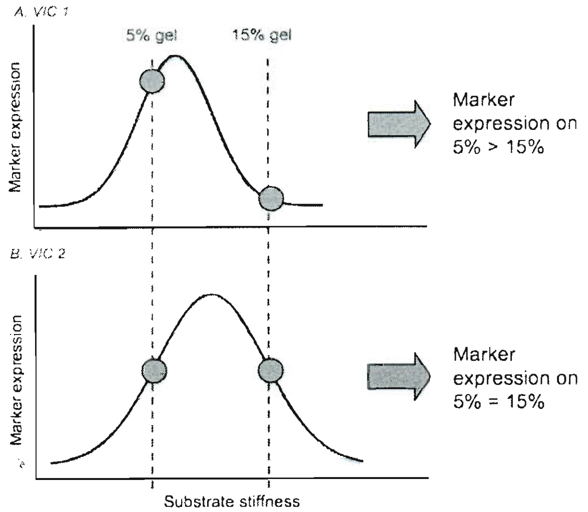

Fig. 9. Schematic illustrating how differences or lack of differences in marker expression between 5% and 15% gels may relate to a hypothetical marker expression–substrate stiffness continuum that is distinct for each VIC population (i.e. age and valve region). The stiffnesses of the 5% and 15% gels fall on the marker expression–substrate stiffness curve in A such that marker expression on 5% gels is greater than on 15% gels, whereas the 5% and 15% gels fall on the marker expression–substrate stiffness curve in B such that marker expression on the 5% gels and 15% gels are equal.

synthesis markers in 6-week-old and 6-month-old MVAC and PML VICs. However, in 6-year-old VICs changes were evident in markers of collagen synthesis despite no detectable change in SMaA intensity. Benton et al. [26] similarly found some uncoupling between stiffness-mediated changes in SMaA expression and calcification potential of AV VICs. While the results for HSP47 largely paralleled those of P4H, in 6-year-old PML VICs P4H expression was decreased on 15% gels relative to 5% gels, while HSP47 was increased. Other studies, however, confirm the potential for independent regulation of HSP47 and other markers of collagen synthesis (such as P4H) by mechanically stressed tendon cells [30] and fibroblasts treated with transforming growth factor-beta [31]. Certain enzymes, such as lysyl hydroxylase 2, have also demonstrated differential regulation of HSP47 and P4H in dermal fibroblasts [32]. Therefore, it appears reasonable for HSP47 to show distinct changes in response to substrate stiffness relative to P4H.

As anticipated, based on inherent differences between VICs from AV compared to MV [33,34], the SMaA results in this study are different from those of AV VICs reported by Pho et al. [28]. Additional distinctions between these two studies, such as cell seeding density, different adhesive substrates and range of substrate stiffnesses [28], may also have contributed to the different results. Work by Engler et al. [29] has demonstrated that for stem cells there exists a stiffness at which there is a maximum in myofibroblast marker expression, and above this stiffness myofibroblast marker expression actually decreases, which would be consistent with the findings of this study. Differences in the results between the Pho et al. study [28] and the present study may also be due to the matrix components used in the substrates of different stiffnesses.

4.3. VIC subpopulations

Distinct VIC subpopulations, including the spindle-shaped and cuboidal cell morphologies evident in this study, have been previously documented [35,36]. The spindle-shaped cells demonstrate qualities similar to fibroblasts, while those with cuboidal morphology are similar to myofibroblasts and are associated with valve remodeling and various valve pathologies [19,35–37]. These subpopulations also demonstrate differences in adhesion to different substrates and matrix components, such as fibronectin [38,39]. In the present study, when a difference in marker expression in VICs between the gels of different stiffnesses was evident, both subpopulations appeared to display this difference. Recent advances in the isolation of these subpopulations could allow a more in-depth investigation of these subpopulations with respect to substrate stiffness [39].

4.4. Implications

These distinct responses of VICs from different-aged MVs and different MV regions have important implications for our understanding of valve mechanobiology and motivate further study in the context of various diseased states. In light of the fact that these different VIC populations (from different aged valves and from different regions) reside in matrices of different stiffnesses, these results suggest that the in vivo mechanical environment in which VICs reside has a profound, fundamental impact on the responsiveness of VICs to their external environment (i.e. their baseline intracellular signaling framework), even in the ex vivo setting. In the context of normal aging, these distinct responses could relate to the ability of the valve to remodel appropriately in response to age-related changes in hemodynamics. With respect to normal physiology, the region-specific differences may relate to the different loading patterns that these regions experience. The age-specific differences could relate to the predilection of certain valve diseases to occur at certain ages, and the valve-region-specific responses could relate to the propensity of certain valve diseases to preferentially affect specific regions of the MV. Knowledge of cell–substrate interactions also has relevance for valve tissue engineering; the design of a tissue-engineered heart valve scaffold should consider how its stiffness affects the phenotype and matrix synthesis of whatever cells will be seeded within or recruited into the scaffold. The results from this study suggest that the scaffold stiffness may need to be carefully tuned depending on the cell type used.

4.5. Limitations and future studies

While the results of this study provide fundamental knowledge regarding how MV VICs respond to substrate stiffness, substantial work still needs to be done in this area and certain study limitations should be noted. While the concentrations of biological cues presented to these cells (RGDS and methacrylated heparin) were carefully orchestrated to be the same between the two substrates, there may be differences in how different aged VICs and VICs from different valve regions respond to the same concentration of these biological cues (for example, if cultured on tissue culture plastic). Future studies investigating this further, examining how these short-term changes relate to longer term changes and downstream processes, and perhaps assessing differences in how these cells interact with their substrate (i.e. expression of integrins), would add insight in this area. Additionally, the mechanism(s) by which these cells respond differently to their substrate warrants investigation. For instance, while PEG is highly hydrophilic and does not adsorb proteins, heparin is known to bind growth factors [40]. Therefore, differences in the amounts or types of growth factors produced by these different VICs in response to different substrates could then be sequestered by heparin in the gels and propagate changes in the VIC phenotype. Future investigation into inherent differences between these VIC populations could also lend insight into the results found in this study. Ultimately, a larger range of substrate stiffnesses, including stiffnesses that match those in which these different VICs reside in vivo, could allow the determination of an "optimal" substrate stiffness for each VIC population. However, this has been difficult given the limited, conflicting reports regarding the in vivo stiffnesses of the MVAC [24,25] and the lack of any in vivo studies of the PML. The goal of this set of experiments was to first determine whether there were age- and valve-region-specific responses to substrate stiffness. An exciting topic for future studies is the role of substrate stiffness in the pathogenesis of mitral valve diseases, such as myxomatous degeneration, and how age-specific and region-specific responses of VICs to substrate stiffness might relate to the incidence of myxomatous changes in particular age groups and valve regions. It should be noted that the time point of 48 h was chosen as it allowed sufficient time for cell adhesion, interaction with the matrix and phenotypic changes, while being short enough so as to not be confounded by potential differences in cell proliferation between the different VIC populations. However, it will be important in the future to examine how these short-term changes relate to downstream processes and longer term changes.

5. Conclusions

In this study, the response of MV VICs to substrate stiffness has been investigated for the first time. VIC populations taken from different regions of the same MV and VICs of different ages cultured on PEG hydrogels of different stiffnesses demonstrated age- and valve-region-specific responses to substrate stiffness. These findings should be taken into consideration in the design of an age-specific tissue-engineered heart valve and in future investigations of heart valve mechanobiology.

Acknowledgements

The authors appreciate the assistance of the members of the Grande-Allen laboratory, as well as members of the West laboratory: Michael Cuchiara, Stephanie Nemir, Ph.D., Melissa McHale, Ph.D., Maude Rowland, Jean Altus, Ph.D. and Jerome Saltarelli, Ph.D. The authors also appreciate the counsel of Scott Baggett, Ph.D. regarding statistics and the assistance of Sean Moran, Ph.D. in NMR analysis. This research was supported in part by a Hertz Foundation Graduate Fellowship (E.H.S.), a NIH Ruth Kirschstein (F30) National Research Service Award (E.H.S), and a grant from the March of Dimes (J.G.A).

Appendix A. Figures with essential colour discrimination

Certain figures in this article, particularly Figures 8 and 9, are difficult to interpret in black and white. The full colour images can be found in the on-line version, at 10.1016/j.actbio.2010.07.001.

References

[1] Rosamond W, Flegal K, Friday G, Furie K, Go A, Greenlund K, et al. Heart disease and stroke statistics – 2007 update: a report from the American Heart Association Statistics Committee and Stroke Statistics Subcommittee. Circulation 2007;115:e69–171.

[2] American Heart Association. Heart disease and stroke statistics – 2008 update. Dallas, TX, 2008.

[3] Ku CH, Johnson PH, Batten P, Sarathchandra P, Chambers RC, Taylor PM, et al. Collagen synthesis by mesenchymal stem cells and aortic valve interstitial cells in response to mechanical stretch. Cardiovasc Res 2006;71:548–56.

[4] Balachandran K, Konduri S, Sucosky P, Jo H, Yoganathan AP. An ex vivo study of the biological properties of porcine aortic valves in response to circumferential cyclic stretch. Ann Biomed Eng 2006;34:1655–65.

[5] Platt MO, Xing Y, Jo H, Yoganathan AP. Cyclic pressure and shear stress regulate matrix metalloproteinases and cathepsin activity in porcine aortic valves. J Heart Valve Dis 2006;15:622–9.

[6] Stephens EH, Chu CK, Grande-Allen KJ. Valve proteoglycan content and glycosaminoglycan fine structure are unique to microstructure mechanical load and age: relevance to an age-specific tissue-engineered heart valve. Acta Biomater 2008;4:1148–60.

[7] Stephens EH, Grande-Allen KJ. Age-related changes in collagen synthesis and turnover in porcine heart valves. J Heart Valve Dis 2007;16:672–82.

[8] Aikawa E, Whittaker P, Farber M, Mendelson K, Padera RF, Aikawa M, et al. Human semilunar cardiac valve remodeling by activated cells from fetus to adult: implications for postnatal adaptation pathology, and tissue engineering. Circulation 2006;113:1344–52.

[9] Stephens EH, De Jonge N, McNeill MP, Durst CA, Grande-Allen KJ. Age-related changes in material behavior of porcine mitral and aortic valves and correlation to matrix composition. Tissue Eng Part A 2010;16:867–78.

[10] Kunzelman KS, Cochran RP. Stress/strain characteristics of porcine mitral valve tissue: parallel versus perpendicular collagen orientation. J Cardiovasc Surg 1992;7:71–8.

[11] Gombotz W, Wang G, Horbett T, Hoffman A. Protein adsorption to poly(ethylene oxide) surfaces. J Biomed Mater Res 1991;25:1547–62.

[12] Zheng S, Liu Y, Palumbom F, Luo Y, Prestwich G. In situ crosslinkable hyaluronan hydrogels for tissue engineering. Biomaterials 2004;25:1339–48.

[13] Hahn M, McHale M, Wang E, Schmedlen R, West J. Physiologic pulsatile flow bioreactor conditioning of poly(ethylene glycol)-based tissue engineered vascular grafts. Ann Biomed Eng 2007;35:190–200.

[14] Cushing MC, Liao J, Jaeggli MP, Anseth KS. Material-based regulation of the myofibroblast phenotype. Biomaterials 2007;28:3378–87.

[15] Masters KS, Shah DN, Walker G, Leinwand LA, Anseth KS. Designing scaffolds for valvular interstitial cells: cell adhesion and function on naturally derived materials. J Biomed Mater Res A 2004;71:172–80.

[16] Blumenkrantz N, Asboe-Hansen G. New method for quantitative determination of uronic acids. Anal Biochem 1973;54:484–9.

[17] Stephens EH, Carroll JL, Grande-Allen KJ. The use of collagenase III for the isolation of porcine aortic valvular interstitial cells: rationale and optimization. J Heart Valve Dis 2007;16:175–83.

[18] Yeung T, Georges PC, Flanagan LA, Marg B, Ortiz M, Funaki M, et al. Effects of substrate stiffness on cell morphology cytoskeletal structure, and adhesion. Cell Motil Cytoskeleton 2005;60:24–34.

[19] Rabkin E, Aikawa M, Stone JR, Fukumoto Y, Libby P, Schoen FJ. Activated interstitial myofibroblasts express catabolic enzymes and mediate matrix remodeling in myxomatous heart valves. Circulation 2001;104:2525–32.

[20] Nemir S, West JL. Synthetic materials in the study of cell response to substrate rigidity. Ann Biomed Eng 2010;38:2–20.

[21] Imanaka K, Takamoto S, Ohtsuka T, Oka T, Furuse A, Omata S. The stiffness of normal and abnormal mitral valves. Ann Thorac Cardiovasc Surg 2007;13:178–84.

[22] Grande-Allen K, Barber J, Klatka K, Houghtaling P, Vesely I, Moravec C, et al. Mitral valve stiffening in end-stage heart failure: evidence of an organic contribution to functional mitral regurgitation. J Thorac Cardiovasc Surg 2005;130:783–90.

[23] Solon J, Levental I, Sengupta K, Georges PC, Janmey PA. Fibroblast adaptation and stiffness matching to soft elastic substrates. Biophys J 2007;93:4453–61.

[24] Krishnamurthy G, Itoh A, Bothe W, Swanson JC, Kuhl E, Karlsson M, et al. Stress–strain behavior of mitral valve leaflets in the beating ovine heart. J Biomech 2009;42:1906–16.

[25] Sacks MS, Enomoto Y, Graybill JR, Merryman WD, Zeeshan A, Yoganathan AP, et al. In-vivo dynamic deformation of the mitral valve anterior leaflet. Ann Thorac Surg 2006;82:1369–77.

[26] Benton JA, Kern HB, Anseth KS. Substrate properties influence calcification in valvular interstitial cell culture. J Heart Valve Dis 2008;17:689–99.

[27] Yip CY, Chen JH, Zhao R, Simmons CA. Calcification by valve interstitial cells is regulated by the stiffness of the extracellular matrix. Arterioscler Thromb Vasc Biol 2009;29:936–42.

[28] Pho M, Lee W, Watt D, Laschinger C, Simmons C, McCulloch C. Cofilin is a marker of myofibroblast differentiation in cells from porcine aortic cardiac valves. Am J Physiol Heart Circ Physiol 2008;294:H1767–1778.

[29] Engler AJ, Sen S, Sweeney HL, Discher DE. Matrix elasticity directs stem cell lineage specification. Cell 2006;126:677–89.

[30] Pan H, Halper J. Regulation of heat shock protein 47 and type I procollagen expression in avian tendon cells. Cell Tissue Res 2003;311:373–82.

[31] Sasaki H, Sato T, Yamauchi N, Okamoto T, Kobayashi D, Iyama S. Et al., Induction of heat shock protein 47 synthesis by TGF-beta and IL-1 beta via enhancement of the heat shock element binding activity of heat shock transcription factor 1. J Immunol 2002;168:5178–83.

[32] Wu J, Reinhardt DP, Batmunkh C, Lindenmaier W, Far RK, Notbohm H, et al. Functional diversity of lysyl hydroxylase 2 in collagen synthesis of human dermal fibroblasts. Exp Cell Res 2006;312:3485–94.

[33] Walker GA, Masters KS, Shah DN, Anseth KS, Leinwand LA. Valvular myofibroblast activation by transforming growth factor-beta: implications for pathological extracellular matrix remodeling in heart valve disease. Circ Res 2004;95:253–60.

[34] Liu AC, Gotlieb AI. Transforming growth factor-beta regulates in vitro heart valve repair by activated valve interstitial cells. Am J Pathol 2008;173:1275–85.

[35] Taylor PM, Batten P, Brand NJ, Thomas PS, Yacoub MH. The cardiac valve interstitial cell. Int J Biochem Cell Biol 2003;35:113–8.

[36] Messier Jr RH, Bass BL, Aly HM, Jones JL, Domkowski PW, Wallace RB, et al. Dual structural and functional phenotypes of the porcine aortic valve interstitial population: characteristics of the leaflet myofibroblast. J Surg Res 1994;57:1–21.

[37] Rabkin-Aikawa E, Farber M, Aikawa M, Schoen FJ. Dynamic and reversible changes of interstitial cell phenotype during remodeling of cardiac valves. J Heart Valve Dis 2004;13:841–7.

[38] Blevins TL, Carroll JL, Raza AM, Grande-Allen KJ. Phenotypic characterization of isolated valvular interstitial cell subpopulations. J Heart Valve Dis 2006;15:815–22.

[39] Stephens EH, Huynh TN, Cieluch JD, Grande-Allen KJ. Fibronectin-based isolation of valve interstitial cell subpopulations: relevance to valve disease. J Biomed Mater Res A 2010;92:340–9.

[40] Cushing MC, Liao JT, Anseth KS. Activation of valvular interstitial cells is mediated by transforming growth factor-beta1 interactions with matrix molecules. Matrix Biol 2005;24:428–37.

Appendix VI: Mathematical Models for Mechanical Testing of Leaflets

This appendix features work in which the I participated and was a co-author on the manuscript; however the work was led by other researchers. A brief description of the my primary contributions is given below and a reprint of the manuscript follows. This was published as Stephens EH, de Jonge N, McNeill MP, Durst CA, Grande-Allen KJ. Age-Related Changes in Material Behavior of Porcine Mitral and Aortic Valves and Correlation to Matrix Composition. Tissue Engineering Part A, 2010 Mar; 16(3):867-78.

These studies aimed to characterize valvular material properties as a function of age. I trained the other authors on and assisted with uniaxial tensile testing. Additionally, I helped interpret the viscoelastic data, identified the utility of Fung's quasilinear viscoelastic model (QLV) for this approach and applied a Maxwell-Weichert model with three elements to describe the biphasic stress relaxation behavior.

TISSUE ENGINEERING: Part A
Volume 16, Number 3, 2010
© Mary Ann Liebert, Inc.
DOI: 10.1089/ten.tea.2009.0288

Age-Related Changes in Material Behavior of Porcine Mitral and Aortic Valves and Correlation to Matrix Composition

Elizabeth H. Stephens, B.S.,[1] Nicky de Jonge, M.Sc.,[2] Meaghan P. McNeill, B.S.,[3]
Christopher A. Durst, B.S.,[1] and K. Jane Grande-Allen, Ph.D.[1]

Recent studies showing significant changes in valvular matrix composition with age offer design criteria for age-specific tissue-engineered heart valves. However, knowledge regarding aging-related changes in valvular material properties is limited. Therefore, 6-week, 6-month, and 6-year-old porcine aortic valves (AV) and mitral valves (MV) were subjected to uniaxial tensile testing. In addition to standard material parameters, the radius of transition curvature (RTC) was measured to assess the acuteness of the transition region of the tension–strain curve. Radially, the MV had greater stiffness and a smaller RTC compared with the AV. Circumferentially, the center of the MV anterior leaflet (MVAC) had the highest stiffness (MVAC > AV > MV free edge [MVF]), greater stress relaxation (MVAC > MVF/AV), lowest extensibility (MVAC < AV < MVF), and smaller RTC compared with MVF (AV < MVAC < MVF). AV and MV radial strips had a larger RTC compared with circumferential strips. Aging elevated stiffness for MV and AV radial and circumferential strips, elevated stress relaxation in AV and MVF circumferential strips, and increased RTC for MV radial and MVF circumferential strips. In conclusion, there are significant age-related differences in the material properties of heart valves, which parallel differences in tissue composition and structure, likely impact valve function, and highlight the need for age-specific design goals for tissue-engineered heart valves.

Introduction

ALTHOUGH HEART VALVE composition and microstructure are known to change with aging,[1–6] and a number of valve diseases show increased incidence with aging,[7,8] the effects of aging on valvular material properties remain largely unknown, with the exception of one study of radial failure strain of aortic valves (AVs).[9] It is likely that valve material behavior varies with age given age-related changes in valve composition, including increased collagen content[1,2] and crosslinking,[2,4] as well as changes in the abundance and turnover of specific extracellular matrix (ECM) components.[3,10,11] Potential age-related changes in the material behavior of valves likely contribute to proper physiologic function, as cardiac hemodynamics change during the normal aging process.[12] Ultimately, a properly designed tissue-engineered heart valve (TEHV) would similarly need specific material properties that allow it to withstand these different hemodynamics depending on the patient age.

Valves are considered to be quasi-viscoelastic,[13,14] highly anisotropic tissues[15–20] that demonstrate stress relaxation[14,17,20–24] but low hysteresis[13,14] and no creep.[14,23] Tensile testing of valves results in a characteristic load-elongation curve with a low slope pre-transition region in which the collagen fibers are crimped and the elastic fibers are bearing load, followed by a transition region during which loading is transferred to the collagen fibers, and then a post-transition region whose high slope reflects load bearing by the collagen fibers.[21,22,25] Valve anisotropy, in which valves are stiffer and less extensible in the circumferential direction compared with the radial direction,[15–20] is attributed to collagen fiber alignment in the circumferential direction.[15,26] Stiffness also varies regionally within the mitral valve (MV) (i.e., between the anterior center [MVAC] and the free edge [MVF]),[15] as does ECM composition in these regions.[27]

Therefore, the primary objective of this study was to assess age-related differences in the material properties of porcine MV and AV and to consider these differences in the context of valve microstructure and ECM composition. In addition to standard material parameters, we developed a novel parameter termed "radius of transition curvature" (RTC) to quantify the acuteness of the transition from the

---

[1] Department of Bioengineering, Rice University, Houston, Texas.
[2] Department of Biomedical Engineering, Eindhoven University of Technology, Eindhoven, The Netherlands.
[3] Departments of Mathematics and Biology, Baylor University, Waco, Texas.

Table 1. Sample Set

	Circumferential strips						*Radial strips*				
	MV		*AV*				*AV*				
	MVAC	*MVF*	*NC*	*LC*	*RC*	*Total*	*MV*	*NC*	*LC*	*RC*	*Total*
6-week old	6	5	7	7	6	25	7	8	7	6	28
6-month old	5	5	4	5	4	18	6	5	4	3	18
6-year old	9	11	6	6	8	31	6	8	9	9	32

MV, mitral valve; AV, aortic valve; NC, noncoronary; MVAC, MV between the anterior center; and MVF, MV between the free edge; LC, left coronary; RC, right coronary.

pre-transition to post-transition region of the tension–strain curve.

Materials and Methods

Tissue sample procurement

Based on comparable anatomy between porcine and human valves,[28–30] valves from 6-week, 6-month, and 6-year-old pigs were used (corresponding to child, young adult, and older adult ages in humans[11]). Porcine hearts were obtained from abattoirs (from Fisher Ham and Meat [Spring, TX] for 6-week-old and 6-month-old pigs; from Animal Technologies [Tyler, TX] for 6-year-old pigs) and measured to normalize leaflet thickness to heart size (maximum circumference and longitudinal length from the origin of the pulmonary artery to heart apex). MVs and AVs were dissected from the hearts, chordae were removed from the MV, and circumferential and radial strips of 5 mm diameter were cut from both MV and AV (Table 1). Given known differences between the material properties of the MVAC (defined as the central region without chordal attachments) and MVF,[15] circumferential strips were taken from both of these regions (Fig. 1A). MV radial strips spanned the entire leaflet height from annulus to free edge. Tissues were stored in phosphate-buffered saline (PBS) at 4°C until testing and tissues were tested within 4 days of harvesting (based on studies showing material properties of valves do not change in that time period[31,32]).

Mechanical testing

The thickness of the tissue was measured at four locations using a displacement gauge (Mitutoyo, Kawasaki, Japan). Tissue samples were glued to balsa wood with cyanoacrylate and clamped within an EnduraTec ELF 3200 (Bose, Minnetonka, MN) such that the edge of the balsa wood aligned with the end of the grips (Fig. 1B). The balsa wood improved traction of the tissue within the grips, thereby preventing slippage during testing. Mechanical testing was performed in a 37°C PBS bath as described previously.[33] Briefly, mechanical testing began with the tissue in an unloaded state and consisted of 25 cycles of preconditioning at 1 Hz followed by one load-elongation cycle (0.5 Hz). The tissue was then allowed to rest for 15 s before another three cycles of preconditioning and a stress relaxation test (duration 100 s).

Data analysis

Gauge length, defined as the length at which the tissue first starts bearing load, was calculated by fitting a cubic function to the pre-transition region of the load-elongation curve and then determining the tissue length corresponding to the local minimum, similar to the method used by Carew and Vesely.[34] Recorded displacement values were then divided by gauge length to calculate strains and load converted to tension by dividing by tissue width. The slope of the post-transition portion of the tension–strain curve (post-transition "stiffness") was calculated by first fitting a straight line to the maximum load and the preceding four points. Additional preceding points were added and the slope of the linear least-squares fit line was recalculated until its value changed by more than 1%. The pre-transition stiffness was determined as the slope of the linear least-squares fit between zero strain to one half of "end-transition" strain (where the end-transition point was the closest point to the origin that was used in the post-transition slope calculation).

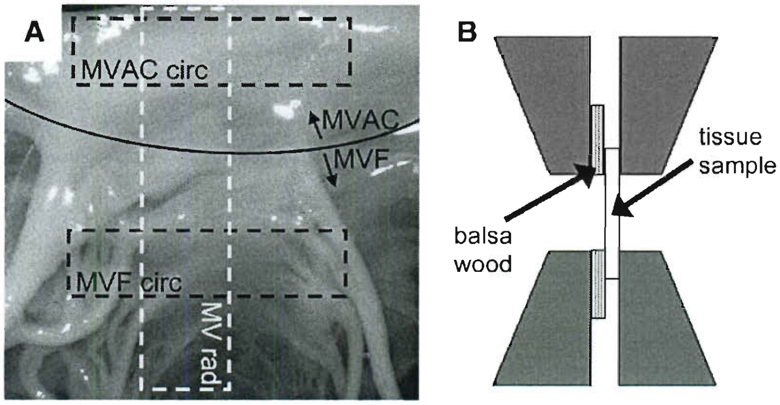

FIG. 1. (**A**) Orientation of tissue strips cut from the mitral valve (MV) (indicated by dashed boxes). Curved solid line indicates the border between the center (MVAC) and free edge (MVF) of the mitral value (MV) anterior leaflet. Rad, radial; circ, circumferential. (**B**) Diagram illustrating the placement of glued balsa/valve tissue sample construct within grips of material testing system.

Extensibility was defined as the intersection of the linear least-squares fit of the post-transition region with the x-axis (strain). The stress relaxation data were fit to the following two-phase decay equation:

$$y = y_0 + A_0 e^{-K_{\mathrm{fast}} X} + A_1 e^{-K_{\mathrm{slow}} X}$$

The K_{fast} and K_{slow} values were calculated iteratively using Graphpad Prism (GraphPad Software, La Jolla, CA). The percentage relaxation (%SR) was calculated as the difference between the initial load and the load remaining at 100 s as a percentage of the initial load. The y_0 value refers to the plateau stress in the tissue (where t is approaching 100 s). A_0 and A_1 are best-fit values from a nonlinear regression referring to the span of the fast and slow portions of the curve. The RTC was calculated by first dividing the y-axis of the tension–strain curve by 100 N/m to make both axes dimensionless and then rotating the tension–strain curve clockwise so that pre-transition and post-transition lines were at equal angles from the vertical (which converted the vertex of the transition region to a global minimum). A hyperbola was then fit to the points in the transition region (from 0 to 1.5× end-transition strain) and the RTC was calculated as the inverse of the second derivative of this global minimum.

Histology and immunohistochemistry

To evaluate the valvular material behavior in context of the ECM composition, representative tissue strips equivalent to those used for mechanical testing were fixed in 10% formalin overnight, dehydrated, paraffin embedded, and sectioned for histological examination. Movat pentachrome was used to visualize the different ECM components and leaflet layers. Immunohistochemistry was also performed as previously described[11,35] to identify and localize the proteoglycans (PGs) decorin, biglycan, and versican (decorin [LF122] and biglycan [LF104] from Dr. Larry Fisher, NIH, Bethesda, MD;[36] versican [2B1] from Associates of Cape Cod, East Falmouth, MA), the glycosaminoglycan (GAG) hyaluronan (HA, using HA-binding protein; Associates of Cape Cod), and collagen type III (Col III, which has been shown to change with age,[11] LF69; from Dr. Larry Fisher[37]). Based on studies showing that valve cell contractility can affect valvular material behavior,[38] staining was also performed for the myofibroblast marker nonmuscle myosin heavy chain-IIB (NMM; Covance, Berkeley, CA) as previously described.[39] Briefly, immunohistochemical staining consisted of antigen retrieval (citrate buffer; Biocare Medical, Concord, CA), except for PGs in which chondroitinase ABC was used[35] (Associates of Cape Cod), followed by quenching of endogenous peroxidases. Nonspecific staining was blocked using goat serum buffer, followed by application of primary antibody. Rinses in PBS were performed before application of the appropriate species-specific secondary antibody. Positive staining was visualized using Vectastain Elite ABC and diaminobenzidine kits (Vector Laboratories, Burlingame, CA), followed by hematoxylin counterstaining. Radially oriented strips of the MV and AV, which were previously stained in this same manner as described in a previous publication,[10,11] were also used to provide context.

Statistical analysis

Multifactorial analysis of variance (ANOVA) was performed using SigmaStat (SPSS, Chicago, IL). When the data were normally distributed, an ANOVA test was used. When the data set was not normally distributed, a rank transform was performed before the ANOVA. In both cases the level of significance was set at 0.05.

Results

Thickness

All test strips cut from the MV were thicker than in the AV ($p < 0.001$), whether in the circumferential direction (Fig. 2) or radial direction. For all valve strips, thickness increased with age (each $p < 0.001$), as reported previously for human valves.[40] The normalized thickness of circumferential and radial strips (whether normalized to the circumferential or longitudinal dimension of the heart) of 6-month olds was greater than for other age groups ($p \leq 0.035$ for each valve or leaflet region; thickness normalized to circumference).

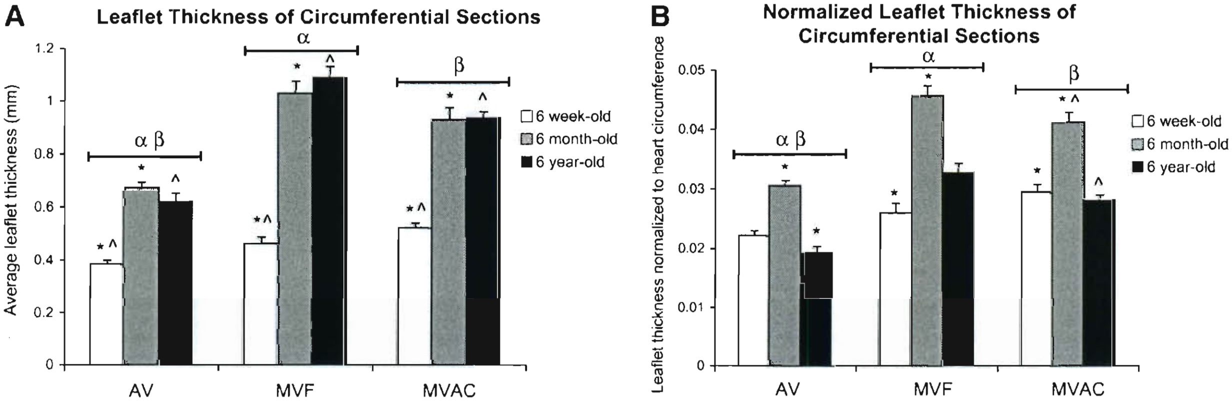

FIG. 2. (A) Thickness of circumferential valve strips with age. Results for radial strips were comparable (data not shown). (B) Thickness of circumferential valve strips with age normalized to heart size (maximum circumference of heart). *,^Significantly different between ages within a given valve region. α,βValve regions significantly different for a given direction (radial or circumferential).

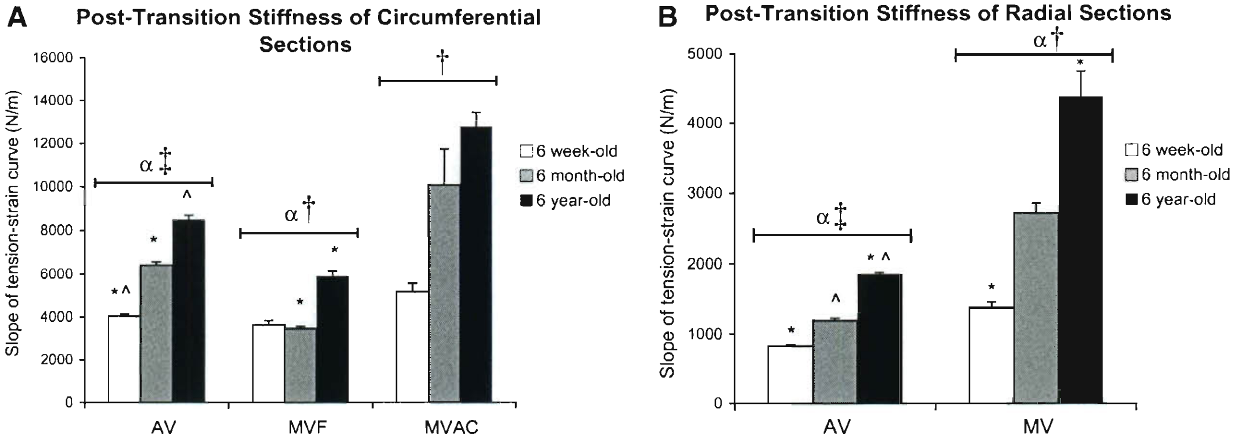

FIG. 3. Slope of post-transition region of tension–strain curves for (**A**) circumferential strips and (**B**) radial strips. *,^Significantly different between ages within a given valve region by *post hoc* ANOVA comparing all ages. $^{\alpha}$AV and MV significantly different for a given direction (radial or circumferential). ‡AV radial significantly different from AV circumferential; †MVAC circumferential, MVF circumferential, and MV radial strips each significantly different from one another. AV, aortic valve; ANOVA, analysis of variance.

Post-transition and pre-transition stiffnesses

In the post-transition region of the tension–strain curves, MV and AV radial stiffness was less than circumferential ($p < 0.001$), consistent with previously published studies.[15–20] The radial stiffness of MV was greater than for AV ($p < 0.001$; Fig. 3). Among circumferential strips, the stiffness of MVAC was greatest, followed by AV, and then MVF ($p = 0.005$). With increasing age, MV and AV radial stiffness increased (each $p \leq 0.003$), as did MV and AV circumferential stiffness (each $p \leq 0.010$).

In the pre-transition region of the curves, there were no significant differences between circumferential and radial stiffnesses in either the AV or MV. Amongst MV and AV circumferential samples, MVF pre-transition stiffness was greater than MVAC, followed by AV (Fig. 4, $p < 0.001$). With increasing age, the pre-transition stiffness of MV samples (both circumferential and radial) and AV radial samples increased (each $p < 0.001$).

Stress relaxation

In the AV, radial sections showed a higher K_{fast} but a lower K_{slow} than circumferential strips (Table 2, each $p < 0.001$). In the MV, however, the K_{fast} and K_{slow} of MVAC circumferential strips were higher than for MV radial (each $p < 0.005$). Among radially oriented sections, the AV K_{fast} and K_{slow} were both greater than for the MV (each $p \leq 0.002$). Among circumferential sections, K_{fast} of MVAC was greater than AV, followed by MVF ($p < 0.001$), but K_{slow} was greatest in AV (AV > MVAC > MVF, $p < 0.001$). With increasing age, AV circumferential K_{fast} was reduced ($p = 0.006$), as was

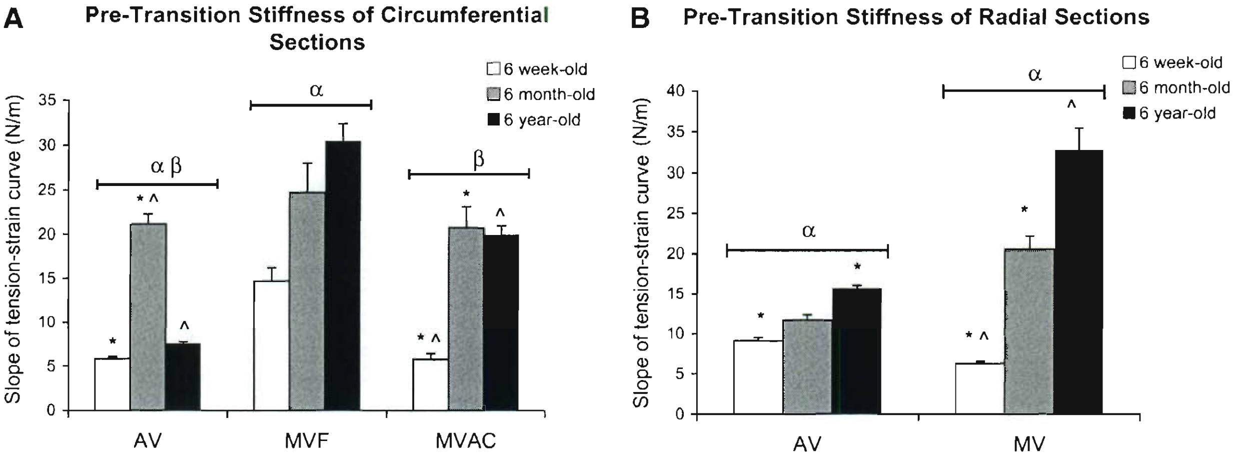

FIG. 4. Slope of the pre-transition region of tension–strain curves for (**A**) circumferential strips and (**B**) radial strips. *,^Significantly different between ages within a given valve region by *post hoc* ANOVA comparing all ages. $^{\alpha,\beta}$AV and MV significantly different for a given direction (radial or circumferential).

Table 2. Stress Relaxation Time Constants

Valve	*Valve region*	*Direction*	*Age*	K_{fast}	K_{slow}
AV	Total	Rad[1,2]	6 weeks	0.545 ± 0.025	0.0295 ± 0.0010
			6 months	0.596 ± 0.030	0.0321 ± 0.0013
			6 years	0.543 ± 0.023	0.0312 ± 0.0010
		Circ[2,5,6]	6 weeks	0.548 ± 0.023[a]	0.0361 ± 0.0010
			6 months	0.445 ± 0.030[a]	0.0329 ± 0.0013
			6 years	0.485 ± 0.023	0.0352 ± 0.0010
MV	Total	Rad[1,3]	6 weeks	0.493 ± 0.046	0.0270 ± 0.0013
			6 months	0.477 ± 0.056	0.0264 ± 0.0015
			6 years	0.463 ± 0.056	0.0240 ± 0.0015
	MVF	Circ[4,6]	6 weeks	0.457 ± 0.069	0.0307 ± 0.0019[a]
			6 months	0.468 ± 0.069	0.0270 ± 0.0019
			6 years	0.499 ± 0.044	0.0263 ± 0.0012[a]
	MVAC	Circ[3,4,5]	6 weeks	0.545 ± 0.052	0.0299 ± 0.0014
			6 months	0.566 ± 0.069	0.0330 ± 0.0019
			6 years	0.707 ± 0.046	0.0285 ± 0.0013

Units for K_{fast} and K_{slow} are N/s. Data represent mean ± standard error of the mean. Samples with the same numeric superscripts indicate significant differences between K_{fast} as well as K_{slow} values for those samples across ages, except four in which K_{fast} was only significantly different between samples and six in which only K_{slow} was significantly different between samples. All differences marked represent $p < 0.05$.

[a] Significant difference between indicated ages within a given valve region/direction.

Rad, radial; circ, circumferential.

MVF circumferential K_{slow} ($p = 0.046$). With respect to the relative magnitudes of relaxation, %SR was greater for AV circumferential than for AV radial (Fig. 5, $p < 0.001$) and greater for MVAC circumferential, followed by MVF circumferential, then MV radial ($p < 0.001$). Among circumferential strips, %SR of MVAC was greater than for either AV or MVF ($p = 0.014$). With increasing age, %SR was increased in AV circumferential strips ($p = 0.009$) and in MVF circumferential sections ($p = 0.005$).

Extensibility

In both the AV and MV, circumferential strips were less extensible than radial strips ($p < 0.001$; Fig. 6). There were no differences between extensibilities of AV and MV strips. In both MV and AV radial strips, as well as in MVAC circumferential strips, extensibility was reduced with age (each $p \leq 0.010$). There was no effect of age on the extensibility of MVF circumferential strips. Among AV circumferential strips, the 6-month-old samples were the least extensible ($p < 0.001$).

Radius of Transition Curvature (RTC)

AV circumferential RTC was less than AV radial RTC ($p < 0.001$; Fig. 7). MVAC circumferential RTC was less than MVF circumferential RTC and then MV radial RTC ($p < 0.001$). Among circumferential strips, AV RTC was less

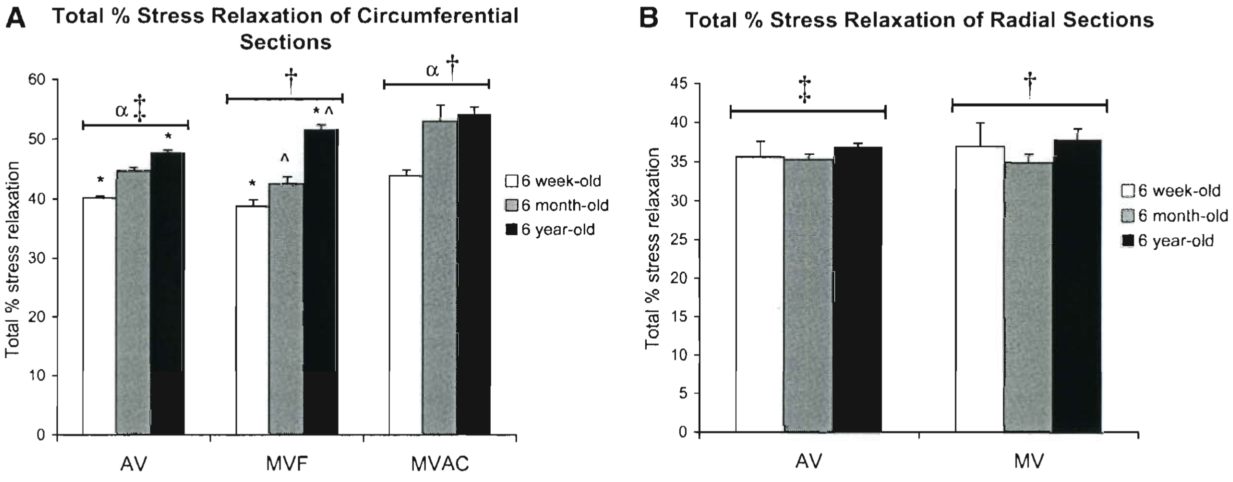

FIG. 5. Total percentage of relaxation (SR) for (**A**) circumferential strips and (**B**) radial strips. *,^Significantly different between ages within a given valve region by *post hoc* ANOVA comparing all ages. αValve regions significantly different for a given direction (radial or circumferential). ‡AV radial significantly different from AV circumferential. †MVAC circumferential, MVF circumferential, and MV radial strips each significantly different from one another.

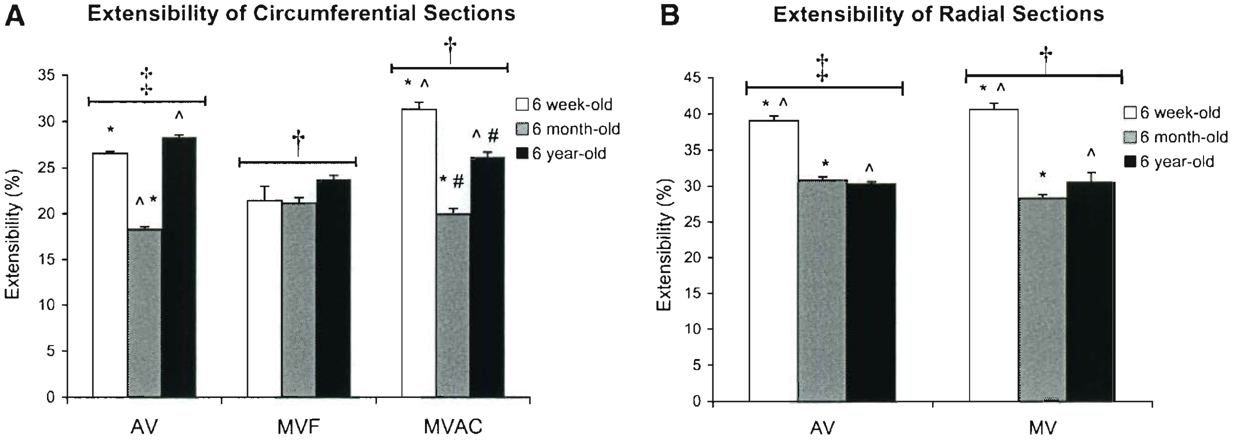

FIG. 6. Extensibility for (**A**) circumferential strips and (**B**) radial strips. $^{*,\wedge,\#}$Significantly different between ages within a given valve region by *post hoc* ANOVA comparing all ages. ‡AV radial significantly different from AV circumferential. †MV radial strips are significantly different from both MVAC and MVF circumferential strips.

than MVAC RTC, which was less than MVF RTC ($p < 0.001$). With age, MVF circumferential and MV radial RTC increased ($p = 0.003$ and $p = 0.033$), but no age-associated changes were evident in AV strips.

Differences between AV leaflets

In 6-year-old AVs, the noncoronary (NC) leaflet was thicker than the left or right coronary leaflets ($p = 0.007$), as previously reported for human valves.[40,41] However, there was no significant difference in thickness between AV leaflets in the other age groups. For both radially and circumferentially oriented strips, K_{fast} of the NC leaflet was greater than for the other two leaflets (each $p \leq 0.037$). However, the circumferential %SR for the NC leaflet was less than for the other two leaflets ($p = 0.039$). RTC of AV NC leaflets was less than the coronary leaflets ($p = 0.031$).

Differences in valve matrix composition

By Movat staining, it was evident that the annulus portion of MV radial strips (corresponding to the MVAC) contained a higher proportion of the collagen-rich fibrosa layer compared with AV radial strips (Fig. 8). MVAC circumferential strips contained a much thicker fibrosa than found in MVF (Fig. 9). With age, the fibrosa thickened and collagen content increased throughout the valve layers, but this increase was particularly evident in the fibrosa layer and in the ventricularis layer, where collagen surrounded elastic fibers. Interestingly, there was also a marbling of PG/GAGs (see inset in Fig. 8) in the fibrosa of the 6-year-old MV radial annulus and MVAC circumferential section, which was not evident in the younger ages. Immunohistochemistry revealed that the PGs versican, biglycan, and decorin, as well as the GAG HA, were present within this marbling. Cir-

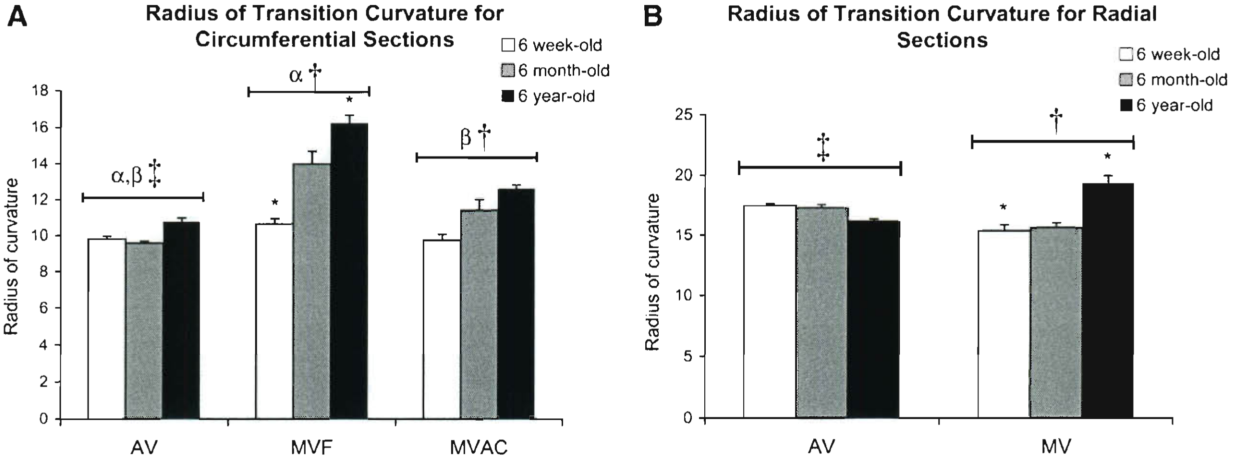

FIG. 7. Radius of transition curvature: (**A**) circumferential strips and (**B**) radial strips. *Significantly different between ages within a given valve region by *post hoc* ANOVA comparing all ages. $^{\alpha,\beta}$AV and MV significantly different for a given direction (radial or circumferential). ‡AV radial significantly different from AV circumferential. †MVAC circumferential, MVF circumferential, and MV radial strips each significantly different from one another.

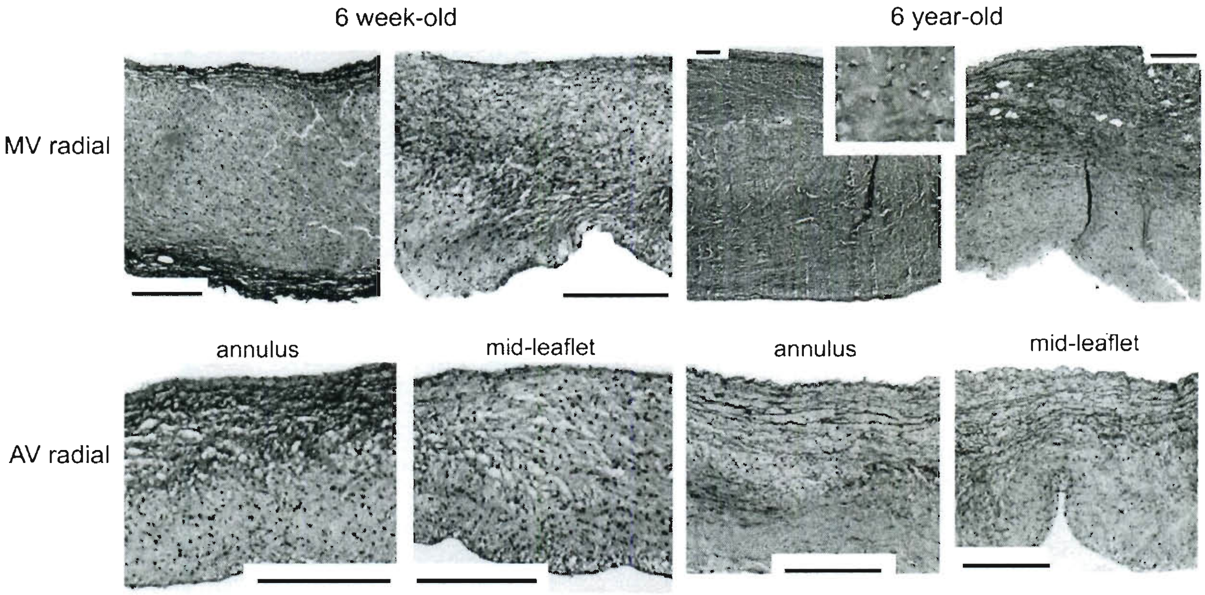

FIG. 8. Representative Movat-stained tissue sample sections for 6-week-old and 6-year-old radial strips. In Movat pentachrome-stained tissue, yellow = aligned collagen, black = elastic fibers, and green/blue = proteoglycans (PGs)/glycosaminoglycans (GAGs). To facilitate comparison between AV and MV, valves were all oriented with the fibrosa at the bottom of the image and sized to show the complete leaflet thickness allowing visualization of all leaflet layers. Because of differences in leaflet thickness (see Fig. 2), magnifications differ between images. Scale bars equal 200 μm. Note that the MV radial annulus is almost exclusively fibrosa (corresponding to the MVAC), whereas AV radial annulus shows a considerably smaller proportion of the leaflet thickness composed of fibrosa. Also of note is the marbling of PG/GAG with collagen in the fibrosa of 6-year-old MV radial annular strips (see close-up view in inset) and MVAC circumferential strips compared with 6-week-old strips. This marbling may, in part, account for the increase in SR seen with age (see Discussion section). Color images available online at www.liebertonline.com/ten.

cumferential strips also contained more Col III with age (Fig. 10), as found previously for radial strips.[11] The myofibroblast marker NMM was more strongly expressed in 6-year-old strips of MVAC than in younger valves.

Discussion

This study showed for the first time that there are significant age-related differences in numerous material properties of MV and AV. At each age, the valves were more extensible and less stiff radially than circumferentially, as is well known.[15–20] All valves, however, demonstrated age-associated increases in post-transition stiffness and most also showed increased pre-transition stiffness. In general, extensibility was reduced with age, especially radially. Stress relaxation parameters also varied with age, particularly circumferentially. The overall shape of the tension–strain curves also changed with age, as demonstrated by the novel parameter RTC, which generally increased with age in the MV and was larger radially than circumferentially. These age-related changes in material properties paralleled an increase in collagen content, particularly in the fibrosa and ventricularis (which is normally rich in elastic fibers), and a marbling appearance of the fibrosa, in which PG/GAGs were interspersed throughout the collagen. Because this study tested MV and AV from the same hearts, it was also possible to demonstrate differences in material properties between MV and AV.

With increasing age, the leaflets showed greater post-transition stiffness both radially and circumferentially. This finding is consistent with age-related stiffening of other connective tissues such as cartilage[42] and tendon,[43] which are mainly attributed to increased collagen crosslinking.[43] Leaflet composition explains much of the differences in stiffness among sample groups. For example, the preponderance of the collagenous fibrosa layer within the MV annulus likely contributes to the greater radial stiffness of MV compared with AV and the greater circumferential stiffness of MVAC compared with MVF. Age-related increases in fibrosa thickness and collagen content shown here for numerous valve regions, as well as previously reported increases in collagen[1,2] and in crosslinking[2,4] in aging valves, could explain the increased stiffness with age. A greater proportion of cells in the 6-year-old MVAC expressed the activated myofibroblast phenotype, which has been linked with increased leaflet stiffness.[38] In addition, collagen crosslinking has been directly correlated with the stiffness of circumferential strips of human AV, although no such correlation was found for radial strips.[26] Combined with evidence suggesting that the ventricularis is a key contributor to valvular material behavior in the radial direction,[22,44] the age-related increase in radial stiffness could be due to increased collagen in the ventricularis, as observed in the Movat-stained sections.

Interestingly, the pre-transition stiffness also significantly increased with age. This parameter may be due in part to the stiffness of the elastic fibers,[45] but is not often

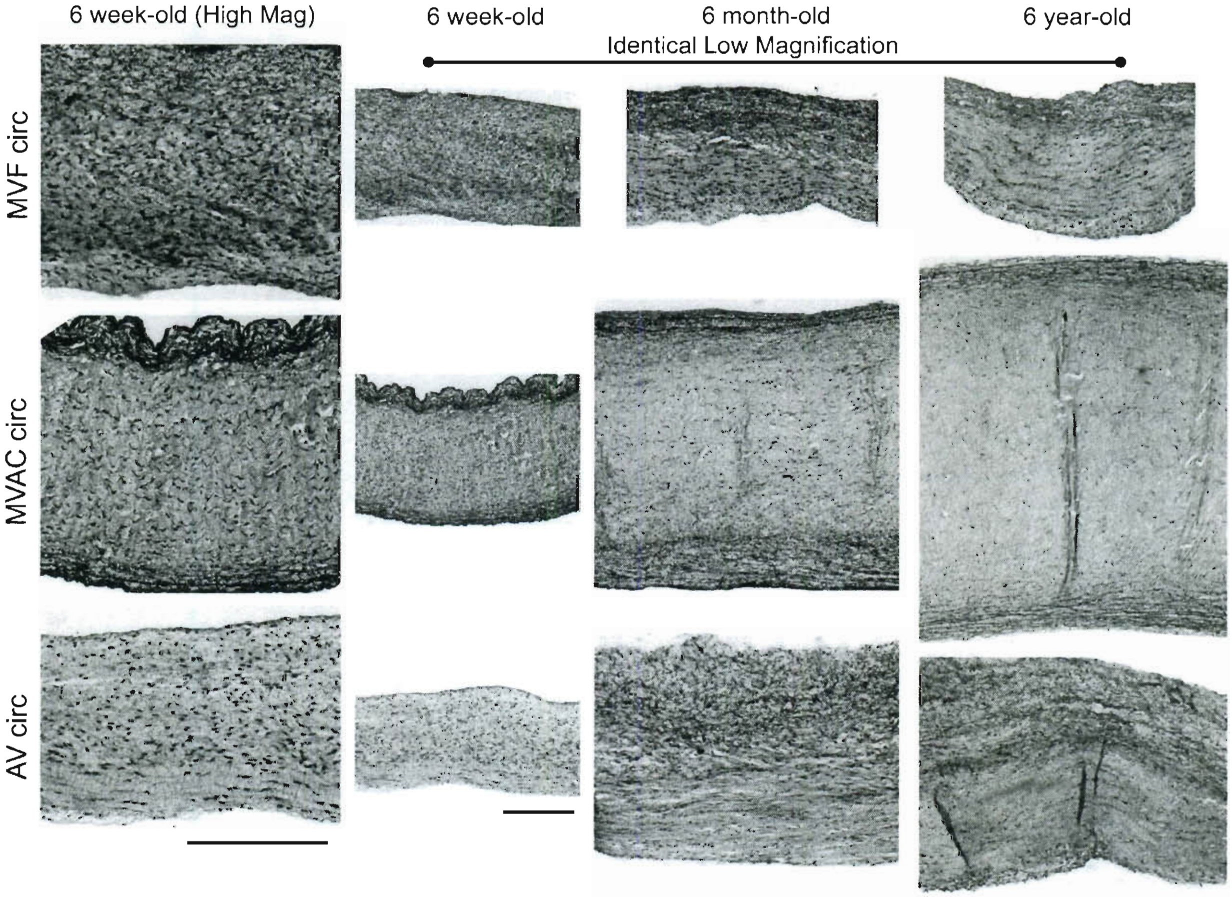

FIG. 9. Representative Movat-stained tissue sample sections for 6-week-old, 6-month-old, and 6-year-old circumferential strips. In Movat pentachrome-stained tissue, yellow = aligned collagen, black = elastic fibers, and green/blue = PGs/GAGs. To facilitate comparison between AV and MV, valves were all oriented with the fibrosa at the bottom of the image. Images in column 1 show high magnification of 6-week-old valves (all images in column 1 are the same magnification). Images in columns 2–4 are lower magnification to demonstrate the differences in leaflet thickness (all images in columns 2–4 are the same magnification). Scale bars equal 200 μm. Compared with MVF, MVAC circumferential sections contain much higher proportion of fibrosa. For all valve regions an increase in collagen was noted throughout the valve layers with age, but most particularly in the fibrosa and ventricularis. Color images available online at www.liebertonline.com/ten.

reported[15,16,18,46] and has never previously been studied with respect to age. The increase in pre-transition stiffness with age could reflect the stiffening of aging elastic fibers,[43] as well as increased collagenous reinforcement of the elastic fibers, which was observed in Movat-stained sections. It was also noteworthy that the age-related increases in the thickness of the valve leaflets[40] were not proportional to the increase in heart size, possibly due to the ventricular hypertrophy found in older animals.[47,48]

Accompanying the age-related increase in the post-transition stiffness was a pronounced reduction in radial extensibility of older valves. Extensibility assesses the amount of tissue that can stretch before the collagen fibers are fully uncrimped and able to bear load;[21] its magnitude reflects both collagen fiber crimp and alignment. The finding that extensibility is greater radially than circumferentially confirms previous reports;[16–18,20] this anisotropy permits the leaflets to stretch radially during valve closure. These findings are also consistent with a previous report on an age-related reduction in maximal radial stretch of human cryopreserved valves.[9] A reduction in extensibility with age could be attributed to factors that impact collagen uncrimping, such as increased collagen crosslinking[2,4] or elastic fiber fragmentation,[43] which can lead to gradual permanent tissue stretch and less-crimped collagen fibers. Indeed, in tendon collagen, crimp amplitude decreases and crimp wavelength increases with age;[49] these extensibility changes motivate future study of collagen crimp in aging heart valves. Similarly, heart valves subjected to glutaraldehyde fixation (crosslinking) under pressure demonstrated reduced collagen crimp and extensibility.[50]

The novel finding of an increase in the percentage of circumferential stress relaxation (in AV and MVF) with age could be due to many factors. First, there is more HA with age[10] as well as marbling of PGs/GAGs in the collagenous fibrosa, which would allow more sliding of collagen bundles relative to one another.[51] Alternatively, the greater numbers of the PGs decorin and biglycan,[10] which bind to the surface of collagen fibrils,[52] could be transferring more load from

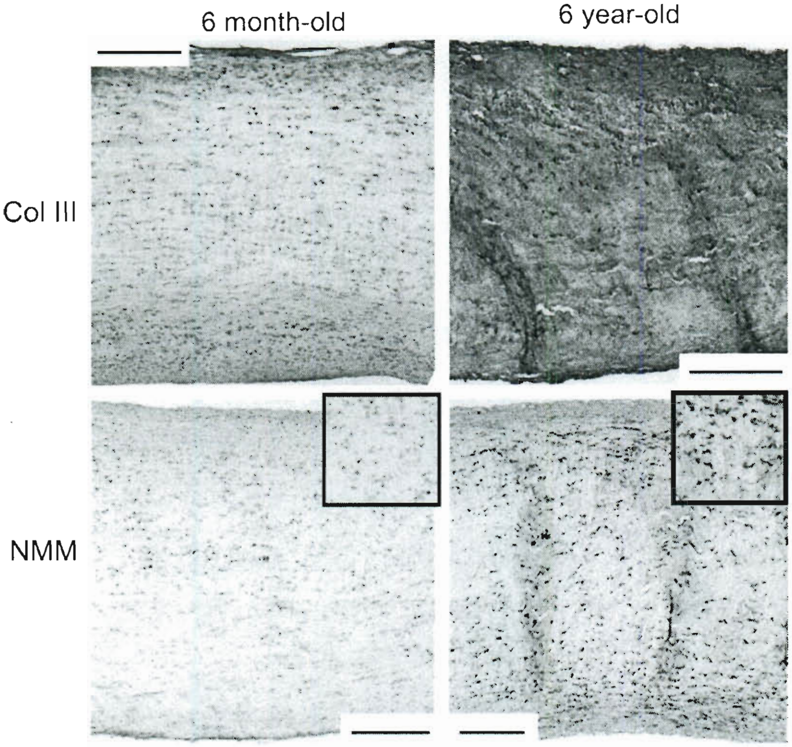

FIG. 10. MVAC circumferential sections showing increased Col III and NMM in 6-year-old sections compared with 6-month-old sections. Similar differences were noted for the staining of Col III for other valve regions between the 6-year-old aged sections and the younger ages. Scale bar equals 200 µm. Insets in NMM images are 1.5× higher magnification for improved visualization of cells. Col III, collagen type III; NMM, nonmuscle myosin heavy chain-IIB. Color images available online at www.liebertonline.com/ten.

collagen to other matrix components, resulting in greater %SR. Indeed, age-related changes in %SR were most evident in the circumferential direction, the predominant collagen fiber direction.[53] Reductions in the functionality[43] and content[10] of elastic fibers could also increase stress relaxation, according to studies on pericardium.[54] Lastly, the greater abundance of Col III, which dissipates more energy than does collagen type I,[55] could have contributed to the greater %SR with age. There is some disagreement in the heart valve literature regarding anisotropy in stress relaxation.[14,17,20,23,24] Our finding of greater %SR in circumferential strips compared with radial strips corroborates the work by Lee *et al.*, who measured the %SR of fresh leaflets over 1000 s using uniaxial testing.[20]

The viscoelasticity of valve tissues has been examined using a wide variety of constitutive models,[17,19,33,56–59] but the effects of age have not been previously investigated. In particular, the quasi-linear viscoelastic (QLV) model developed by Fung[60] has been applied to fresh and fixed valve tissues;[19,33,56] analysis using this technique, however, is computationally intense. In this study, a Maxwell–Weichert model with three elements was used to examine biphasic decay behavior of the stress relaxation curve.[61,62] The age-related decreases in K_{fast} of AV circumferential samples and in K_{slow} of MVF samples both indicate more viscous behavior, which could relate to the increased abundance of PGs and GAGs.[10] The K_{fast} and K_{slow} values reported in this study also serve as baseline parameters for evaluating mechanical properties of TEHVs. While current TEHV studies have focused primarily on linear material properties, understanding the viscoelastic properties will continue to be of significant value, especially as more advanced materials are developed.

The novel parameter RTC, which quantifies the acuteness of the transition region of the tension–strain curve, can be compared across samples for any soft tissues that display bilinear tension–strain or stress–strain curves. Collagen fibers that are highly aligned and uniformly crimped will have a very acute transfer of load bearing from elastic fibers to the straightened collagen fibers, and hence a very small RTC. If collagen fibers are not uniformly crimped, their transition to load bearing would be more gradual, resulting in a greater RTC. A larger RTC would also result from a random fiber alignment, in which some fibers would be initially aligned with the applied load and begin bearing load at low strains, but the remaining collagen bundles would require varying amounts of additional strain and/or rotational realignment before bearing load.[21] Indeed, the angular distribution of collagen fibers significantly changes within this transition region.[21] The smaller RTC of MVAC circumferential strips compared with MVF likely indicates greater alignment[53] and homogeneity of collagen fiber crimping in MVAC compared with the other valve regions. In the valve, collagen bundles are predominantly oriented circumferentially,[53] and therefore, RTC would be lower circumferentially than radially, as found here. The age-related increase in RTC of MVF and MV radial strips could be due to greater collagen crosslinking[2,4] and a greater abundance of network-forming Col III. In future, it will be important to relate this parameter to changes in the soft tissue microstructure during this transition region of loading.

This study is also the first to show differences in material properties between NC and coronary AV leaflets, such as lower %SR and RTC in the NC leaflet. These differences may be due to the lack of coronary blood flow within the NC sinus; simulations of human AVs have shown that NC experiences higher stress[63] and greater diastolic pressure loading than the other leaflets.[64] The NC leaflet also contains smaller diameter collagen fiber bundles,[65] which may permit easier rotation of collagen fibers as they align in the direction of loading, and hence contribute to a lower RTC. An additional subset of valves was frozen at −20°C for 2 months before testing; as previously demonstrated by Clark,[18] significant differences were found between fresh AV and previously frozen AV (data not shown).

Conclusion

In this study, AV and MV from the same porcine hearts were subjected to tensile testing. In the analysis of the tensile testing data, we developed a novel parameter, RTC, which may be useful in quantifying the dynamic stress–strain behavior of biological tissues. Overall, our results showed that between AV and MV, and within each valve, there are profound heterogeneities and age-related changes that reflect the ECM and microstructural composition. In addition, the effects of age on the heart valve tissues differ between valves, valve regions, and material testing orientations. Given the documented similarities between porcine and human valves, these results provide further justification (as well as baseline data) for the development of age-specific TEHVs. These age-related changes in valve material properties likely contribute to proper physiologic function of valves at different ages. For instance, the age-related increase in leaflet stiffness likely allows the AV and MV to withstand the increase in cardiac pressures and concomitant decrease in aortic compliance with age.[12] Clearly, considerable work remains in understanding the structural and mechanical complexity of heart valves, their ECM and cell composition, and the contributions of these characteristics to valve function.

Acknowledgments

The authors thank Janet Barzilla, Ph.D., Joyce J. Kuo, B.S., and Daniel Laucirica in the Grande-Allen lab, and Anita Mol, Ph.D., and Martijn Cox, M.Sc., from the Eindhoven University of Technology exchange program. Special thanks also to Scott Baggett, Ph.D., for statistical expertise; Benjamin K. Stephens, Ph.D., for mathematical consultation regarding curve fitting and radius of curvature analysis; Roman M. Natoli, Ph.D., for consultation on constitutive modeling; and Larry Fisher, Ph.D., for the generous gift of multiple antibodies.

Disclosure Statement

No competing financial interests exist.

References

1. Keller, F., and Leutert, G. [Age dependence of collagen structures of the human heart]. Z Gerontol **27**, 186, 1994.
2. Angrist, A. Aging heart valves and a unitary pathological hypothesis for sclerosis. J Gerontol **19**, 135, 1964.
3. Aikawa, E., Whittaker, P., Farber, M., Mendelson, K., Padera, R.F., Aikawa, M., and Schoen, F.J. Human semilunar cardiac valve remodeling by activated cells from fetus to adult: implications for postnatal adaptation, pathology, and tissue engineering. Circulation **113**, 1344, 2006.
4. Bashey, R.I., Torii, S., and Angrist, A. Age-related collagen and elastin content of human heart valves. J Gerontol **9**, 203, 1967.
5. Sell, S., and Scully, R.E. Aging changes in the aortic and mitral valves. Histologic and histochemical studies, with observations on the pathogenesis of calcific aortic stenosis and calcification of the mitral annulus. Am J Pathol **46**, 345, 1965.
6. McDonald, P.C., Wilson, J.E., McNeill, S., Gao, M., Spinelli, J.J., Rosenberg, F., Wiebe, H., and McManus, B.M. The challenge of defining normality for human mitral and aortic valves: geometrical and compositional analysis. Cardiovasc Pathol **11**, 193, 2002.
7. Goldbarg, S.H., Elmariah, S., Miller, M.A., and Fuster, V. Insights into degenerative aortic valve disease. J Am Coll Cardiol **50**, 1205, 2007.
8. Aronow, W.S. Heart disease and aging. Med Clin North Am **90**, 849, 2006.
9. Christie, G.W., and Barratt-Boyes, B.G. Age-dependent changes in the radial stretch of human aortic valve leaflets determined by biaxial testing. Ann Thorac Surg **60**, S156, 1995.
10. Stephens, E.H., Chu, C.-K., and Grande-Allen, K.J. Valve proteoglycan content and glycosaminoglycan fine structure are unique to microstructure, mechanical load and age: relevance to an age-specific tissue-engineered heart valve. Acta Biomaterialia **4**, 1148, 2008.
11. Stephens, E.H., and Grande-Allen, K. Age-related changes in collagen synthesis and turnover in porcine heart valves. J Heart Valve Dis **16**, 672, 2007.
12. VanAuker, M.D. Age-related changes in hemodynamics affecting valve performance. Am J Geriatr Cardiol **15**, 277, 2006.
13. Grashow, J., Yoganathan, A.P., and Sacks, M.S. Biaxial stress-stretch behavior of the mitral valve anterior leaflet at physiologic strain rates. Ann Biomed Eng **34**, 315, 2006.
14. Stella, J., Liao, J., and Sacks, M.S. Time-dependent biaxial mechanical behavior of the aortic heart valve leaflet. J Biomech **40**, 3169, 2007.
15. Kunzelman, K.S., and Cochran, R.P. Stress/strain characteristics of porcine mitral valve tissue: parallel versus perpendicular collagen orientation. J Card Surg **7**, 71, 1992.
16. May-Newman, K., and Yin, F. Biaxial mechanical behavior of excised porcine mitral valve leaflets. Am J Physiol **269**, H1319, 1995.
17. Leeson-Dietrich, J., Boughner, D., and Vesely, I. Porcine pulmonary and aortic valves: a comparison of their tensile viscoelastic properties at physiological strain rates. J Heart Valve Dis **4**, 88, 1995.
18. Clark, R. Stress-strain characteristics of fresh and frozen human aortic and mitral leaflets and chordae tendineae. Implications for clinical use. J Thorac Cardiovasc Surg **66**, 202, 1973.
19. Sauren, A., van Hout, M., van Steenhoven, A., Veldpaus, F., and Janssen, J. The mechanical properties of porcine aortic valve tissues. J Biomech **16**, 327, 1983.
20. Lee, J., Courtman, D.W., and Boughner, D. The glutaraldehyde-stabilized porcine aortic valve xenograft. I. Tensile viscoelastic properties of the fresh leaflet material. J Biomed Mater Res **18**, 61, 1984.
21. Liao, J., Yang, L., Grashow, J., and Sacks, M.S. The relation between collagen fibril kinematics and mechanical properties in the mitral valve anterior leaflet. J Biomech Eng **129**, 78, 2007.

22. Vesely, I., and Noseworthy, R. Micromechanics of the fibrosa and the ventricularis in aortic valve leaflets. J Biomech **25,** 101, 1992.
23. Grashow, J., Sacks, M.S., Liao, J., and Yoganathan, A.P. Planar biaxial creep and stress relaxation of the mitral valve anterior leaflet. Ann Biomed Eng **34,** 1509, 2006.
24. Vesely, I., Boughner, D., and Leeson-Dietrich, J. Bioprosthetic valve tissue viscoelasticity: implications on accelerated pulse duplicator testing. Ann Thorac Surg **60,** S379, 1995.
25. Merryman, W.D., Engelmayr, G.C., Jr., Liao, J., and Sacks, M.S. Defining biomechanical endpoints for tissue engineered heart valve leaflets from native leaflet properties. Prog Pediatr Cardiol **21,** 153, 2006.
26. Balguid, A., Rubbens, M., Mol, A., Bank, R., Bogers, A., van Kats, J., de Mol, B., Baaijens, F., and Bouten, C. The role of collagen cross-links in biomechanical behavior of human aortic heart valve leaflets—relevance for tissue engineering. Tissue Eng **13,** 1501, 2007.
27. Grande-Allen, K.J., Calabro, A., Gupta, V., Wight, T.N., Hascall, V.C., and Vesely, I. Glycosaminoglycans and proteoglycans in normal mitral valve leaflets and chordae: association with regions of tensile and compressive loading. Glycobiology **14,** 621, 2004.
28. Crick, S., Sheppard, M., Ho, S., Gebstein, L., and Anderson, R. Anatomy of the pig heart: comparisons with normal human cardiac structure. J Anat **193,** 105, 1998.
29. Sands, M.P., Rittenhouse, E.A., Mohri, H., and Merendino, K.A. An anatomical comparison of human pig, calf, and sheep aortic valves. Ann Thorac Surg **8,** 407, 1969.
30. Sim, E.K., Muskawad, S., Lim, C.S., Yeo, J.H., Lim, K.H., Grignani, R.T., Durrani, A., Lau, G., and Duran, C. Comparison of human and porcine aortic valves. Clin Anat **16,** 193, 2003.
31. Patel, J. Effect of absolute specimen size on the tensile properties of porcine aortic valve tissues [masters thesis]. Case Western Reserve, Cleveland, OH, 2003.
32. Grande-Allen, K., Barber, J., Klatka, K., Houghtaling, P., Vesely, I., Moravec, C., and McCarthy, P. Mitral valve stiffening in end-stage heart failure: evidence of an organic contribution to functional mitral regurgitation. J Thorac Cardiovasc Surg **130,** 783, 2005.
33. Carew, E., Barber, J., and Vesely, I. Role of preconditioning and recovery time in repeated testing of aortic valve tissues: validation through quasilinear viscoelastic theory. Ann Biomed Eng **28,** 1093, 2000.
34. Carew, E., and Vesely, I. A new method of estimating gauge length for porcine aortic valve test specimens. J Biomech **36,** 1039, 2003.
35. Gupta, V., Barzilla, J.E., Mendez, J.S., Stephens, E.H., Lee, E.L., Collard, C.D., Laucirica, R., Weigel, P.H., and Grande-Allen, K.J. Abundance and location of proteoglycans and hyaluronan within normal and myxomatous mitral valves. Cardiovasc Pathol **18,** 191, 2009.
36. Fisher, L.W., Stubbs, J.T., III, and Young, M.F. Antisera and cDNA probes to human and certain animal model bone matrix noncollagenous proteins. Acta Orthop Scand Suppl **266,** 61, 1995.
37. Bernstein, E.F., Chen, Y.Q., Kopp, J.B., Fisher, L., Brown, D.B., Hahn, P.J., Robey, F.A., Lakkakorpi, J., and Uitto, J. Long-term sun exposure alters the collagen of the papillary dermis. Comparison of sun-protected and photoaged skin by northern analysis, immunohistochemical staining, and confocal laser scanning microscopy. J Am Acad Dermatol **34,** 209, 1996.
38. Merryman, W., Huang, H., Schoen, F., and Sacks, M. The effects of cellular contraction on aortic valve leaflet flexural stiffness. J Biomech **39,** 88, 2006.
39. Stephens, E.H., Nguyen, T.C., Itoh, A., Ingels, N.B., Jr., Miller, D.C., and Grande-Allen, K.J. The effects of mitral regurgitation alone are sufficient for leaflet remodeling. Circulation **118,** S243, 2008.
40. Sahasakul, Y., Edwards, W.D., Naessens, J., and Tajik, A. Age-related changes in aortic and mitral valve thickness: implications for two-dimensional echocardiography based on an autopsy study of 200 normal human hearts. Am J Cardiol **62,** 424, 1988.
41. Silver, M., and Roberts, W.C. Detailed anatomy of the normally functioning aortic valve in hearts of normal and increased weight. Am J Cardiol **55,** 454, 1985.
42. Charlebois, M., McKee, M.D., and Buschmann, M.D. Nonlinear tensile properties of bovine articular cartilage and their variation with age and depth. J Biomech Eng **126,** 129, 2004.
43. Bailey, A.J. Molecular mechanisms of ageing in connective tissues. Mech Ageing Dev **122,** 735, 2001.
44. Stella, J., and Sacks, M.S. On the biaxial mechanical properties of the layers of the aortic valve leaflet. J Biomech Eng **129,** 757, 2007.
45. Vesely, I. The role of elastin in aortic valve mechanics. J Biomech **31,** 115, 1998.
46. Ghista, D.N., and Rao, A.P. Mitral-valve mechanics—stress-strain characteristics of excised leaflets, analysis of its functional mechanics and its medical application. Med Biol Eng **11,** 691, 1973.
47. Safar, M. Ageing and its effects on the cardiovascular system. Drugs **39,** 1, 1990.
48. Gardin, J., Savage, D., Ware, J., and Henry, W. Effect of age, sex, and body surface area on echocardiographic left ventricular wall mass in normal subjects. Hypertension **9,** II36, 1987.
49. Diamant, J., Keller, A., Baer, E., Litt, M., and Arridge, R.G. Collagen; ultrastructure and its relation to mechanical properties as a function of ageing. Proc R Soc Lond B Biol Sci **180,** 293, 1972.
50. Broom, N.D., and Thomson, F.J. Influence of fixation conditions on the performance of glutaraldehyde-treated porcine aortic valves: towards a more scientific basis. Thorax **34,** 166, 1979.
51. Scott, J. Elasticity in extracellular matrix shape modules of tendon, cartilage, etc. A sliding proteoglycan-filament model. J Physiol **553,** 335, 2003.
52. Kinsella, M.G., Bressler, S.L., and Wight, T.N. The regulated synthesis of versican, decorin, and biglycan: extracellular matrix proteoglycans that influence cellular phenotype. Crit Rev Eukaryot Gene Expr **14,** 203, 2004.
53. Cochran, R.P., Kunzelman, K.S., Chuong, C.J., Sacks, M.S., and Eberhart, R.C. Nondestructive analysis of mitral valve collagen fiber orientation. ASAIO Trans **37,** M447, 1991.
54. Rabkin, S., Berghause, D.G., and Bauer, H.F. Mechanical properties of the isolated canine pericardium. J Appl Physiol **36,** 69, 1974.
55. Silver, F., Horvath, I., and Foran, D. Mechanical implications of the domain structure of fiber-forming collagens: comparison of the molecular and fibrillar flexibilities of the alpha1-chains found in types I-III collagen. J Theor Biol **216,** 243, 2002.
56. Carew, E.O., Talman, E.A., Boughner, D.R., and Vesely, I. Quasi-Linear Viscoelastic theory applied to internal shearing of porcine aortic valve leaflets. J Biomech Eng **121,** 386, 1999.

57. Carew, E., Garg, A., Barber, J., and Vesely, I. Stress relaxation preconditioning of porcine aortic valves. Ann Biomed Eng **32,** 563, 2004.
58. Duncan, A.C., Boughner, D., and Vesely, I. Dynamic glutaraldehyde fixation of a porcine aortic valve xenograft. I. Effect of fixation conditions on the final tissue viscoelastic properties. Biomaterials **17,** 1849, 1996.
59. Duncan, A.C., Boughner, D., and Vesely, I. Viscoelasticity of dynamically fixed bioprosthetic valves. II. Effect of glutaraldehyde concentration. J Thorac Cardiovasc Surg **113,** 302, 1997.
60. Fung, Y.C. Biomechanics: Mechanical Properties of Living Tissues, 2nd edition. New York: Springer-Verlag, 1993, pp. 277–292.
61. Peleg, M., and Normand, M. Comparison of 2 methods for stress-relaxation data presentation of solid foods. Rheol Acta **22,** 108, 1983.
62. Mayne, A.S., Christie, G.W., Smaill, B.H., Hunter, P.J., and Barratt-Boyes, B.G. An assessment of the mechanical properties of leaflets from four second-generation porcine bioprostheses with biaxial testing techniques. J Thorac Cardiovasc Surg **98,** 170, 1989.
63. Grande, K.J., Cochran, R.P., Reinhall, P.G., and Kunzelman, K.S. Stress variations in the human aortic root and valve: the role of anatomic asymmetry. Ann Biomed Eng **26,** 534, 1998.
64. Lin, S., Liu, C., Young, S., Lin, M., and Chiou, C. Age-related changes in aortic valve with emphasis on the relation between pressure loading and thickened leaflets of the aortic valves. Int J Cardiol **103,** 272, 2005.
65. Doehring, T., Kahelin, M., and Vesely, I. Mesostructures of the aortic valve. J Heart Valve Dis **14,** 679, 2005.

Address correspondence to:
K. Jane Grande-Allen, Ph.D.
Department of Bioengineering
Rice University
PO Box 1892–MS142
Houston, TX 77251–1892

E-mail: grande@rice.edu

Received: April 27, 2009
Accepted: October 7, 2009
Online Publication Date: November 20, 2009

Appendix VII: Custom MATLAB Code

1. prodcata_sugar.m

The following script allows the determination of bending stiffness from samples where the digital image correlation (marker tracking) was run on SUG@R. The script requires the matrix of marker positions as a function of image to be local. Sample parameters such as thickness of the sample and width between the loading posts are measured visually. Stiffness, length and diameter of the flexure bar are also input. The script then shows a graph of marker positions, sample information like thickness and moment of inertia are output. A graph of bending moment versus change in curvature is then displayed and the linear fit can be calculated.

```
%Script for Processing Data Run on Sugar. Samples should be
in folders with
% Commented lines near end of script can be used to
automate fits instead of using curve fitting toolbox
initial image, grid data, validx and validy (tracked data),
and filelist.
%clear all;
% use speckle tracking algorithms
% filelist_generator;
% %makegray;
% grid_generator;
% automate_image;

%------------
% calculate the sample thickness and width, conversion
factor (pixels to mm), and moment of inertia

%if exist('FileNameBase')==0
[FileNameBase,PathNameBase] = uigetfile( ...
    {'*.bmp;*.tif;*.jpg;*.TIF;*.BMP;*.JPG','Image files
(*.bmp,*.tif,*.jpg)';'*.*',  'All Files (*.*)'}, ...
    'Open base image thickness calculation');
```

```
%end

cd(PathNameBase)
imtool(FileNameBase);
menu(sprintf('Click OK when t1-t5, mm, wp (btwn posts), and
s have been measured.'),'Ok');
prompt={'Enter the height of the gel (mm)'};
   name='Input for MoI calculation';
   numlines=1;
   defaultanswer={''};
   options.Resize='on';

answer=inputdlg(prompt,name,numlines,defaultanswer,options)
;

   wreal=str2num(answer{1});


tp=(t1+t2+t3+t4+t5)/5;
treal=tp/mm;
inertia=(1/12)*treal^3*wreal;
wppost=wp/mm;

sprintf('\n Sample thickness %.2f mm \n Sample height %.2f
mm \n Moment of inertia %.2f', treal, wreal, inertia)

displacement;

%-----------
% calculate the curvature
load('filenamelist.mat');
load('validx_corr.dat');
load('validy_corr.dat');
[q,r]=size(filenamelist);
%colors=['b.';'g.';'r.';'m.';'k.'];
% x_init= load('grid_x.dat')/mm;
% y_init=load('grid_y.dat')/mm;
sx=load('validx_corr.dat')/mm;
sy=load('validy_corr.dat')/mm;

%creates matrix of dots from each image, fits quadratic
line, calculates
%change in curvature (delK)

for i=1:q-1
     x_fin(:,i)=sx(:,i);
     y_fin(:,i)=sy(:,i);
     coeff(:,i)=polyfit(x_fin(:,i),y_fin(:,i),2);
```

```
    yprime(:,i)=polyder(coeff(:,i));
    ydprime(i)=polyder(yprime(:,i));

%k(:,i)=(polyval(ydprime(i),sx(:,1)))./((1+(polyval(yprime(
:,i),sx(:,1))).^2).^(3/2));

delk(:,i)=polyder((ydprime(:,i)./(1+yprime(:,i).^2).^(3/2))
);
    y2(:,i)=polyval(coeff(:,i),sx(:,i));
    SSE(i)=sum((y_fin(:,i)-y2(:,i)).^2);
    SST(i)=sum((y_fin(:,i)-mean(y_fin(:,i))).^2);
    r2(i)=1-(SSE(i)/SST(i));
end
delk=polyder(k);
sprintf('R-squared values for each fit: \n%.2f   %.2f
%.2f   %.2f   %.2f',r2)

%plots tracked dots/fitted lines to ensure good tracking
figure(1)
hold on;
%plot(x_init,y_init,'y.');
xlabel('x position (mm)');
ylabel('y position (mm)');
%for l=1:q-1
    plot(x_fin,y_fin,'x')%,colors(l,:));
    plot(sx,y2,'.')%,colors(l));
%end

%find displacements between ref rod and bending rod
% filelist_generator2;
% grid_generator2;
% automate_image2;
%calculate distance between ref rod and bending rod
mx_init=load('grid_x2.dat');
my_init=load('grid_y2.dat');

mx=load('validx2.dat');
my=load('validy2.dat');
[a,b]=size(filenamelist);
spread_init=((mx_init(1)-mx_init(2))^2+(my_init(1)-
my_init(2))^2)^.5;

for i=1:a-1
    spread(i)=((mx(1,i)-mx(2,i))^2+(my(1,i)-my(2,i))^2)^.5;
end

spread=spread-spread_init;
spread=spread/mm;
```

```
prompt={'Enter the stiffness of the flexure bar
(MPa)','Enter the flexure bar length (mm)','Enter the
diameter of the flexure bar (mm)'};
   name='Input for force calculation';
   numlines=1;
   defaultanswer={'164351','81','0.508'};
   options.Resize='on';

answer=inputdlg(prompt,name,numlines,defaultanswer,options)
;

   E=str2num(answer{1});
   L=str2num(answer{2});
   dia=str2num(answer{3});

%this moment of inertia is for a rectangle
I=pi/4*(dia/2)^4;
%sreal=s/mm;
%d=size(x_fin);
% post1=median(x_fin(:,1))-wreal/2;
% post2=median(x_fin(:,1))+wreal/2;

%calculate force applied by rod in each image
%p is in newtons
P=(spread*3*(E*I))/(L^3);
%
% Fx=(P(1:69)/2).*((y2(d(1),[1:69])-y2(d(1)-
1,[1:69]))./(x_fin(d(1),[1:69])-x_fin(d(1)-1,[1:69])));
% Fy=P(1:69)/2;
% M=Fy*wreal+Fx.*spread(1:69);
%init=1;
%fin=80;
M=P/4*wppost;
%stiffness=M./(inertia*mean(delk(:,[init:fin])));
%oldstiffness=(P*L^3)./(48*inertia*spread);
figure(2)
hold on;
plot(delk,M,'.');
xlabel('change in curvature (mm^-1)');
ylabel('Moment (N-mm)');
% stifffit=polyfit(delk(1,[1:fin]),M,1);
% stiffy=polyval(stifffit,delk(1,[1:fin]));
% plot(mean(delk(:,[1:fin])),stiffy,'r')
% SSE2=sum((M-stiffy).^2);
% SST2=sum(((M-mean(M))).^2);
% r22=1-(SSE2/SST2);
```

2. sugarprep.m

This script is used to prepare bending samples to have SUG@R run the marker tracking. On local machine, the gridpoints for the sample, reference rod, and flexure bar are created. These can then be uploaded along with the image sequence.

```
%local preparation for sample before uploading to sugar
%generates list of files in a folder
% creates initial grid points on sample
% creates initial grid points on flexure bar and reference
rod
% save everything in each samples folder
% using default filenames makes things easier
filelist_generator;
grid_generator;
grid_generator2;
```

3. sample11.m

This is an example script used to start a job in a “-nodisplay” command line version of MATLAB to automate tracking on SUG@R.

```
% call to matlab on sugar to automate image tracking
% needs image stack with grid data and filelist in the
folder with the
% images
% helps to separate samples in folders
% 3000 tiffs at 500x500 should take ~1.5 hours with 8
processor cores
cd
/shared.scratch/cd5012/PreppedForAnalysis/Cropped_Images/Sa
mple_11
automate_image_mp_2009b;
automate_image_mp_2009b2;
```

4. tensproc.m

This is a script used to process uniaxial tensile testing samples. The bounds of strain range where the material is linear needs to be known and put in the respective i and j parameters in the script.

```
%filelist_generator;
%automate with this and filenamelist length
%ensure that strain range in loop is appropriate and linear
for your samples
%files need to be incrementally numbered text files with
displacement (mm) in column 1, load (kN)
%in column 2, and sample thickness needs to be in a user
created vector
%called thick (in mm)
% commented functions can be used in place of fitting,
interactive toolbox
% can also be used
filelist_generator_txt;
if exist('filenamelist')==0
    load('filenamelist')              % file with the list of
filenames to be processed
end

numfiles=length(filenamelist);
prompt={'Enter the gauge length (mm)','Enter the neck width
(mm)'};
       name='Input for stress strain calculations';
       numlines=1;
       defaultanswer={'10','2'};
       options.Resize='on';

answer=inputdlg(prompt,name,numlines,defaultanswer,options)
;

       gl=str2num(answer{1});
       nw=str2num(answer{2});

 output=zeros(length(filenamelist),4);
 output(:,2)=thick';
for p=1:numfiles
    m=dlmread(filenamelist(p,:));
    offset=0;
    %thick=m(1,3);
    strain=(m(:,1))/gl;
    stress=(m(:,2))*1000/(nw/1000*thick(p)/1000);
    strain=round(strain*1000)/1000;
    i=find(strain==0.2);
    j=find(strain==0.6);
    linfit=polyfit(strain(i:j),stress(i:j),1);
    linfity=polyval(linfit,strain(i:j));
    correlation=corrcoef(stress(i:j),linfity);
    output(p,1)=p;
    output(p,3)=linfit(1,1);
    output(p,4)=correlation(1,2);
end
figure(1)
plot(output(:,4),output(:,3))
figure(2)
[n,xout]=hist(output(:,4),20);
bar(xout,n)
success=xlswrite('analyzed_samples.xls',output);
if success==1;
    sprintf('Data analyzed and file successfully written')
else
    sprintf('Data not written, check output matrix for
information')
end

    % figure(1)
    % plot(strain);
    % lowstrain=[];
    %     lowstrain(:,1)=strain(strain<0.25);
    %     lowstrain(:,2)=stress(strain<0.25);
    % medstrain=[];
    % z=find(strain<0.5);
    %
medstrain(:,1)=strain(find(strain>0.25):z(length(z)));
    %
medstrain(:,2)=stress(find(strain>0.25):z(length(z)));
    % highstrain=[];
    % y=find(strain<1);
    %
highstrain(:,1)=strain(find(strain>0.5):y(length(y)));
    %
highstrain(:,2)=stress(find(strain>0.5):y(length(y)));
    % subplot(3,1,1)
    %     plot(lowstrain(:,1),lowstrain(:,2))
    % hold on;
    % llinfit=polyfit(lowstrain(:,1),lowstrain(:,2),1);
    % llinfity=polyval(llinfit,lowstrain(:,1));
    % plot(lowstrain(:,1),llinfity,'r');
    % xlabel('Strain (%)')
% ylabel('Stress (Pa)')
% title('Low strain region')
% subplot(3,1,2)
% plot(medstrain(:,1),medstrain(:,2))
% hold on;
% mlinfit=polyfit(medstrain(:,1),medstrain(:,2),1);
% mlinfity=polyval(mlinfit,medstrain(:,1));
% plot(medstrain(:,1),mlinfity,'r');
% xlabel('Strain (%)')
% ylabel('Stress (Pa)')
% title('Mid-strain region')
% subplot(3,1,3)
% plot(highstrain(:,1),highstrain(:,2))
% hold on;
% hlinfit=polyfit(highstrain(:,1),highstrain(:,2),1);
% hlinfity=polyval(hlinfit,highstrain(:,1));
% plot(highstrain(:,1),hlinfity,'r');
% xlabel('Strain (%)')
% ylabel('Stress (Pa)')
% title('High strain region')
% if abs(mlinfit(1)-llinfit(1))<2000
%     avg_E=(mlinfit(1)+llinfit(1))/2
% end
% l=llinfit(1)
% m=mlinfit(1)
% h=hlinfit(1)
subplot(2,1,1)
plot(strain,stress)
subplot(2,1,2)
plot(strain(i:j),stress(i:j),'b.')
hold on;
plot(strain(i:j),linfity,'r')
```

5. pegpatgen.m

This script can be used to generate photomasks with oriented or chopped “fibers”, holes, or sinusoidal patterns. DPI of the output mask is set and the choices are made via the MATLAB GUI.

```
function pegpatgen();
```

```
% Prompt user for mask size
prompt={'Enter the mask width (in)','Enter the mask height
(in)','Enter the mask resolution (dpi)'};
   name='Mask Size';
   numlines=1;
   defaultanswer={'','',''};
   options.Resize='on';

answer=inputdlg(prompt,name,numlines,defaultanswer,options)
;

   mask_sizex=str2num(answer{1})*str2num(answer{3});
   mask_sizey=str2num(answer{2})*str2num(answer{3});
   dpi=str2num(answer{3});


gridtypesel(mask_sizex,mask_sizey,dpi);

close all

%-------------------------------
%
% Decide which type of mask you want to create

function gridtypesel(mask_sizex,mask_sizey,dpi);

gridselection = menu(sprintf('Which type of mask do you
want to use'),...
    'Oriented - Fibers','Oriented - Chopped','Random -
Fibers','Random - Chopped','Holes','Sinusoidal
Fibers','Cancel');

if gridselection==1
    lbounds=[0.5*dpi,0.75*dpi]; %Length Bounds -- currently
arbitrary
    wbounds=[0.025*dpi,0.05*dpi]; %width bounds --
currently arbitrary
    coverage=0.5*(mask_sizex*mask_sizey); %50% coverage
    maxsize=lbounds(2)*wbounds(2);
    numfibers=floor(coverage/maxsize);
    lengths=floor(lbounds(1)+(lbounds(2)-
lbounds(1)).*rand(numfibers,1));
    widths=floor(wbounds(1)+(wbounds(2)-
wbounds(1)).*rand(numfibers,1));
    originx=floor(rand(numfibers,1)*mask_sizex);
    originy=floor(rand(numfibers,1)*mask_sizey);
    skew=floor(87.5+(92.5-87.5)*rand(numfibers,1)); %fiber
skew, roughly estimated from sacks abme 1997
    dfiny=floor(lengths.*sind(skew));
    dfinx=floor(lengths.*cosd(skew));
    finx=dfinx+originx;
    finx(finx<0)=0;
    finx(finx>mask_sizex)=mask_sizex;
    finy=dfiny+originy;
    finy(finy<0)=0;
    finy(finy>mask_sizey)=mask_sizey;
    grid=ones(mask_sizey,mask_sizex);
    figure(1);
    imshow(grid)
    hold on;
    for i=1:numfibers
        line([originx(i) finx(i)],[originy(i)
finy(i)],'LineWidth',widths(i),'Color','k');
        i=i+1;
    end
    pause
    return
end


if gridselection==2
    lbounds=[0.1*dpi,0.25*dpi]; %length bounds
    wbounds=[0.075*dpi,0.125*dpi]; %width bounds
    coverage=0.5*(mask_sizex*mask_sizey); %50% coverage
    maxsize=lbounds(2)*wbounds(2);
    numfibers=floor(coverage/maxsize);
    lengths=floor(lbounds(1)+(lbounds(2)-
lbounds(1)).*rand(numfibers,1));
    widths=floor(wbounds(1)+(wbounds(2)-
wbounds(1)).*rand(numfibers,1));
    originx=floor(rand(numfibers,1)*mask_sizex);
    originy=floor(rand(numfibers,1)*mask_sizey);
    skew=floor(87.5+(92.5-87.5)*rand(numfibers,1)); %fiber
skew
    dfiny=floor(lengths.*sind(skew));
    dfinx=floor(lengths.*cosd(skew));
    finx=dfinx+originx;
    finx(finx<0)=0;
    finx(finx>mask_sizex)=mask_sizex;
    finy=dfiny+originy;
    finy(finy<0)=0;
    finy(finy>mask_sizey)=mask_sizey;
    grid=ones(mask_sizey,mask_sizex);
    imshow(grid);
    hold on;
    for i=1:numfibers
        line([originx(i) finx(i)],[originy(i)
finy(i)],'LineWidth',widths(i),'Color','k');
        i=i+1;
    end
    pause
    return
end

if gridselection==3
    lbounds=[0.5*dpi,0.75*dpi]; %Length Bounds
    wbounds=[0.025*dpi,0.05*dpi]; %width bounds
    coverage=0.5*(mask_sizex*mask_sizey); %50% coverage
    maxsize=lbounds(2)*wbounds(2);
    numfibers=floor(coverage/maxsize);
    lengths=floor(lbounds(1)+(lbounds(2)-
lbounds(1)).*rand(numfibers,1));
    widths=floor(wbounds(1)+(wbounds(2)-
wbounds(1)).*rand(numfibers,1));
    originx=floor(rand(numfibers,1)*mask_sizex);
    originy=floor(rand(numfibers,1)*mask_sizey);
    skew=floor(rand(numfibers,1)*180); %fiber skew
    dfiny=floor(lengths.*sind(skew));
    dfinx=floor(lengths.*cosd(skew));
    finx=dfinx+originx;
    finx(finx<0)=0;
    finx(finx>mask_sizex)=mask_sizex;
    finy=dfiny+originy;
    finy(finy<0)=0;
    finy(finy>mask_sizey)=mask_sizey;
    grid=ones(mask_sizey,mask_sizex);
    imshow(grid);
    hold on;
    for i=1:numfibers
        line([originx(i) finx(i)],[originy(i)
finy(i)],'LineWidth',widths(i),'Color','k');
        i=i+1;
    end
    pause
    return
end

if gridselection==4
    lbounds=[0.1*dpi,0.25*dpi]; %length bounds
    wbounds=[0.075*dpi,0.125*dpi]; %width bounds
    coverage=0.5*(mask_sizex*mask_sizey); %50% coverage
    maxsize=lbounds(2)*wbounds(2);
    numfibers=floor(coverage/maxsize);
    lengths=floor(lbounds(1)+(lbounds(2)-
lbounds(1)).*rand(numfibers,1));
    widths=floor(wbounds(1)+(wbounds(2)-
wbounds(1)).*rand(numfibers,1));
    originx=floor(rand(numfibers,1)*mask_sizex);
    originy=floor(rand(numfibers,1)*mask_sizey);
    skew=floor(rand(numfibers,1)*180); %fiber skew
    dfiny=floor(lengths.*sind(skew));
    dfinx=floor(lengths.*cosd(skew));
    finx=dfinx+originx;
    finx(finx<0)=0;
    finx(finx>mask_sizex)=mask_sizex;
    finy=dfiny+originy;
    finy(finy<0)=0;
    finy(finy>mask_sizey)=mask_sizey;
    grid=ones(mask_sizey,mask_sizex);
    imshow(grid);
    hold on;
    for i=1:numfibers
        line([originx(i) finx(i)],[originy(i)
finy(i)],'LineWidth',widths(i),'Color','k');
        i=i+1;
    end
    pause
    return
end

if gridselection==5 %holes
    return
end

if gridselection==6 %sinusoidal fibers
  prompt={'Enter the period (mm)','Enter the amplitude
(mm)','Enter the spacing (mm)'};
   name='Sinusoid Parameters';
   numlines=1;
   defaultanswer={'','',''};
   options.Resize='on';

answer=inputdlg(prompt,name,numlines,defaultanswer,options)
;

   period=str2num(answer{1})*25.4;
   amplitude=str2num(answer{2})*25.4;
   spacing=str2num(answer{3})*25.4;

   freq=2*pi/period;
```

```
    t=0:pi/(10*freq):mask_sizex;
    sinusoid=amplitude*sin(freq*t);

    numlines=floor(mask_sizey*25.4/(spacing+amplitude));
    sinmatrix(1,:)=sinusoid;
    tmat(1,:)=t;

    for i=1:numlines-1
        sinmatrix(i+1,:)=sinmatrix(i,:)+spacing;
        tmat(i+1,:)=t;
    end
    figure(1)
    hold on;
    for i=1:numlines
        plot(t,sinmatrix(i,:))
    end
     return
end

if gridselection==7

    return

end

function owpat(mask_sizex,mask_sizey,dpi);
%lbounds=[0.25*dpi,0.5*dpi]; %Length Bounds
wbounds=[0.0075*dpi,0.125*dpi]; %width bounds
coverage=0.5*(mask_sizex*mask_sizey); %50% coverage
maxsize=lbounds(2)*wbounds(2);
numfibers=floor(coverage/maxsize);
lengths=floor(lbounds(1)+(lbounds(2)-
lbounds(1)).*rand(numfibers,1));
widths=floor(wbounds(1)+(wbounds(2)-
wbounds(1)).*rand(numfibers,1));
originx=floor(rand(numfibers,1)*mask_sizex);
originy=floor(rand(numfibers,1)*mask_sizey);
skew=floor(75+(105-75)*rand(numfibers,1)); %fiber skew
dfiny=floor(lengths.*sind(skew));
dfinx=floor(lengths.*cosd(skew));
finx=dfinx+originx;
finx(finx<0)=0;
finx(finx>mask_sizex)=mask_sizex;
finy=dfiny+originy;
finy(finy<0)=0;
finy(finy>mask_sizey)=mask_sizey;
grid=ones(mask_sizex,mask_sizey);
figure(1);
```

```
imshow(grid)
hold on;
for i=1:numfibers
    line([originx(i) finx(i)],[originy(i)
finy(i)],'LineWidth',widths(i),'Color','k');
    i=i+1;
end
pause;

function ocpat(mask_sizex,mask_sizey,dpi);
lbounds=[0.1*dpi,0.25*dpi]; %length bounds
wbounds=[0.075*dpi,0.125*dpi]; %width bounds
coverage=0.5*(mask_sizex*mask_sizey); %50% coverage
maxsize=lbounds(2)*wbounds(2);
numfibers=floor(coverage/maxsize);
lengths=floor(lbounds(1)+(lbounds(2)-
lbounds(1)).*rand(numfibers,1));
widths=floor(wbounds(1)+(wbounds(2)-
wbounds(1)).*rand(numfibers,1));
originx=floor(rand(numfibers,1)*mask_sizex);
originy=floor(rand(numfibers,1)*mask_sizey);
skew=floor(75+(105-75)*rand(numfibers,1)); %fiber skew
dfiny=floor(lengths.*sind(skew));
dfinx=floor(lengths.*cosd(skew));
finx=dfinx+originx;
finx(finx<0)=0;
finx(finx>mask_sizex)=mask_sizex;
finy=dfiny+originy;
finy(finy<0)=0;
finy(finy>mask_sizey)=mask_sizey;
grid=ones(mask_sizex,mask_sizey);
imshow(grid);
hold on;
for i=1:numfibers
    line([originx(i) finx(i)],[originy(i)
finy(i)],'LineWidth',widths(i),'Color','k');
    i=i+1;

end

function ranwpat(mask_sizex,mask_sizey,dpi);
lbounds=[0.25*dpi,0.5*dpi]; %Length Bounds
wbounds=[0.075*dpi,0.125*dpi]; %width bounds
coverage=0.5*(mask_sizex*mask_sizey); %50% coverage
maxsize=lbounds(2)*wbounds(2);
numfibers=floor(coverage/maxsize);
lengths=floor(lbounds(1)+(lbounds(2)-
lbounds(1)).*rand(numfibers,1));
```

```
widths=floor(wbounds(1)+(wbounds(2)-
wbounds(1)).*rand(numfibers,1));
originx=floor(rand(numfibers,1)*mask_sizex);
originy=floor(rand(numfibers,1)*mask_sizey);
skew=floor(rand(numfibers,1)*180); %fiber skew
dfiny=floor(lengths.*sind(skew));
dfinx=floor(lengths.*cosd(skew));
finx=dfinx+originx;
finx(finx<0)=0;
finx(finx>mask_sizex)=mask_sizex;
finy=dfiny+originy;
finy(finy<0)=0;
finy(finy>mask_sizey)=mask_sizey;
grid=ones(mask_sizex,mask_sizey);
imshow(grid);
hold on;
for i=1:numfibers
    line([originx(i) finx(i)],[originy(i)
finy(i)],'LineWidth',widths(i),'Color','k');
    i=i+1;
end

function rancpat(mask_sizex,mask_sizey,dpi);
lbounds=[0.1*dpi,0.25*dpi]; %length bounds
wbounds=[0.075*dpi,0.125*dpi]; %width bounds
coverage=0.5*(mask_sizex*mask_sizey); %50% coverage
maxsize=lbounds(2)*wbounds(2);
numfibers=floor(coverage/maxsize);
lengths=floor(lbounds(1)+(lbounds(2)-
lbounds(1)).*rand(numfibers,1));
widths=floor(wbounds(1)+(wbounds(2)-
wbounds(1)).*rand(numfibers,1));
originx=floor(rand(numfibers,1)*mask_sizex);
originy=floor(rand(numfibers,1)*mask_sizey);
skew=floor(rand(numfibers,1)*180); %fiber skew
dfiny=floor(lengths.*sind(skew));
dfinx=floor(lengths.*cosd(skew));
finx=dfinx+originx;
finx(finx<0)=0;
finx(finx>mask_sizex)=mask_sizex;
finy=dfiny+originy;
finy(finy<0)=0;
finy(finy>mask_sizey)=mask_sizey;
grid=ones(mask_sizex,mask_sizey);
imshow(grid);
hold on;
for i=1:numfibers
    line([originx(i) finx(i)],[originy(i)
finy(i)],'LineWidth',widths(i),'Color','k');
    i=i+1;
end
```

Appendix VIII: Custom ImageJ Scripts

1. Macro to Quantify DAB Intensity

```
macro "dabquant [d]" {
dir = getDirectory("image")
name = getTitle;
mainimage=name;
run("Colour Deconvolution", "vectors=[H DAB]");
close();
rename("dabimage");
run("Duplicate...", "title=DAB");
//run("8-bit");
setAutoThreshold("Default");
run("Threshold...");
waitForUser("Set mask","Threshold set?");
getThreshold(lower,upper);
//setThreshold(0, 160);
run("Convert to Mask");
run("Fill Holes");
run("Set Measurements...", "area mean min display redirect=dabimage
decimal=3");
run("Analyze Particles...", "size=500-Infinity circularity=0.00-1.00 show=Outlines
display exclude include");
outlines=getTitle;
selectWindow(outlines)
run("Copy");
close();
index = lastIndexOf(name, ".");
  if (index!=-1) name = substring(name, 0, index);
  measurename = name + "-d.xls";
measurepath=dir+measurename;
saveAs("Measurements", measurepath);
run("Close");
close();
selectWindow(mainimage);
setPasteMode("AND");
run("Paste");
pathoutlines=dir+name + "-d-outlines";
saveAs("tiff", pathoutlines);
close();
close();
close();
close();
}
```

2. Macro to Count Cells Using Hematoxylin

```
macro "cell count [c]" {
dir = getDirectory("image")
name = getTitle;
mainimage=name;
run("Colour Deconvolution", "vectors=[H DAB]");
close();
close();
rename("himage");
run("Duplicate...", "H");
//run("8-bit");
setAutoThreshold("Default");
run("Threshold...");
waitForUser("Set mask","Threshold set?");
getThreshold(lower,upper);
//setThreshold(0, 160);
run("Convert to Mask");
run("Close-");
run("Watershed");
run("Set Measurements...", "area mean min display redirect=himage decimal=3");
run("Analyze Particles...", "size=5-100 circularity=0.00-1.00 show=Outlines
display exclude include");
houtlines=getTitle;
selectWindow(houtlines)
run("Copy");
close();
index = lastIndexOf(name, ".");
  if (index!=-1) name = substring(name, 0, index);
  measurename = name + "-h.xls";
measurepath=dir+measurename;
saveAs("Measurements", measurepath);
run("Close");
close();
selectWindow(mainimage);
setPasteMode("AND");
run("Paste");
pathoutlines=dir+name + "-h-outlines";
saveAs("tiff", pathoutlines);
close();
close();
close();
close();
}
```